UIDE

Powered by
Arizona State University

ING. AUTOMOTRIZ

Trabajo integración Curricular previa a la obtención del título de Ingeniero en Automotriz.

AUTORES:
Stalyn Ricardo Collaguazo Casa
Erika Geovanna Zuñiga Armijos

TUTOR:
Ing. Marcos Xavier Gutierrez Ojeda

Método para evaluar los flujos de atomizacion de combustible.

QUIITO-ECUADOR |2022

CERTIFICACIÓN

Nosotros, Stalyn Ricardo Collaguazo Casa y Erika Geovanna Zuñiga Armijos, declaramos bajo juramento, que el trabajo aquí descrito es de nuestra autoría; que no ha sido presentado anteriormente para ningún grado o calificación profesional y que se ha consultado la bibliografía detallada.

Cedemos nuestros derechos de propiedad intelectual a la Universidad Internacional del Ecuador, para que sea publicado y divulgado en internet, según lo establecido en la Ley de propiedad Intelectual, reglamento y leyes.

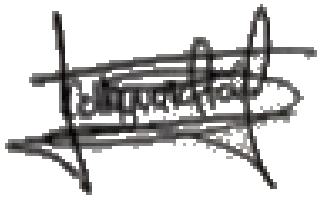

Stalyn Ricardo Collaguazo Casa

Erika Geovanna Zuñiga Armijos

Yo, Marcos Xavier Gutiérrez Ojeda, certifico que conozco al autor del presente trabajo siendo el responsable exclusivo tanto de su originalidad y autenticidad, como de su contenido.

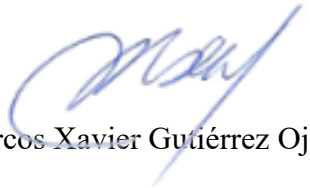

Marcos Xavier Gutiérrez Ojeda, PhD

DEDICATORIA

Al creador de todas las cosas, el que me acompaña y siempre me levanta de mis continuos tropiezos, con todas las fuerzas de mi corazón, dedicamos primeramente nuestra tesis a Dios.

De igual manera, dedicamos nuestra tesis a nuestros padres que han sabido guiarnos durante toda nuestra vida por el buen camino con sus consejos, enseñándonos a encarar las adversidades sin perder nunca la dignidad ni desfallecer en el intento.

A nuestras familias quienes por ellos somos lo que somos, por su apoyo, amor incondicional, ayuda en los momentos difíciles y por ayudarnos con los recursos necesarios para estudiar. Nos han dado todo lo que somos como personas, nuestros valores, nuestros principios, nuestro carácter, nuestro empeño, nuestra perseverancia y nuestro coraje para conseguir nuestros objetivos.

AGRADECIMIENTO

Dios, tu amor y tu bondad no tienen fin, nos permites sonreír ante todos nuestros logros que son resultado de tu ayuda, demostrándonos que todo momento estás nosotros ayudándonos a aprender de nuestros errores y a no cometerlos otra vez. Gracias, mi Dios.

A nuestras familias que todos juntos son impresionantes y su amor para nosotros es invalorable, nos enseñaron muchas cosas vitales para la vida y nos encaminaron por el buen sendero.

No obstante, resulta indispensable resaltar y agradecer a la institución de mi formación académica a nuestros maestros y autoridades por sus enseñanzas y conocimientos compartidos.

Y a todos nuestros amigos que han estado conmigo en todo momento, les agradecemos con todo nuestro corazón. Gracias.

ÍNDICE DE CONTENIDO

MÉTODO PARA EVALUAR FLUJOS DE ATOMIZACIÓN DE COMBUSTIBLE

Stalyn Collaguazo[1], Erika Zuñiga[2], Marcos Gutiérrez[3]

[1]stcollaguazoca@uide.edu.ec, Quito – Ecuador

[2]erzunigaar@uide.edu.ec, Quito – Ecuador

[3]magutierrezoj@uide.edu.ec, Quito – Ecuador

Ingeniería Automotriz Universidad Internacional del Ecuador

Resumen

El análisis de dos imágenes por medio de un método de sustracción en el lenguaje de programación Python permite encontrar las diferencias que, en condiciones normales pasarían por desapercibidas o no mostraría el detalle e impacto que de esas diferencias. La comparación de los dos flujos de atomización de combustible en modo esquemático; así como simulado para diferentes tipos de fluidos y condiciones no reactivas y de combustión, permitió visualizar las zonas de mayor densidad de combustible y concluir que la colisión de flujos de atomización puede contribuir a la mejor atomización de combustible. Los flujos de atomización bajo condiciones no reactivas y de combustión fueron simulados con el software OpenFOAM, se simularon dos tipos de fluidos y varios flujos que colisionan entre sí. El análisis de imagen muestra las diferencias de las imágenes con colores de diferente intensidad, lo que permite identificar las zonas con mayor o menor densidad de combustible.

Palabras clave: flujo de atomización, análisis por imagen, Python, PIL, ImageChops, ImageChops.difference, OpenFOAM..

Abstract

The analysis of two images by means of a subtraction method in the Python programming language allows finding the differences that, under normal conditions, would go unnoticed or would not show the detail and impact of those differences. The comparison of the two fuel atomization streams in schematic mode; as well as simulated for different types of fluids and non-reactive and combustion conditions, allowed to visualize the areas with the highest fuel density and to conclude that the collision of atomization flows can contribute to the best fuel atomization. The atomization flows under non-reactive and reacting conditions were simulated with the OpenFOAM software, two types of fluids and several flows that collide with each other were simulated. The image analysis shows the differences of the images with colors of different intensity, which allows to identify the areas with higher or lower fuel density.

Keywords: atomization flow, image analysis, Python, PIL, ImageChops, ImageChops.difference, OpenFOAM..

1. INTRODUCCION

Las investigaciones de los flujos de atomización por parte de los sistemas de inyección de combustible han sido dependientes de la capacidad de captar imágenes y de procesarlas por medio de software. La última década ha brindado dos posibilidades de hacer este tipo de análisis de modo más práctico y accesible. La primera posibilidad es la de captar imágenes de alta resolución. La segunda posibilidad es la de tener software y librerías que permiten su implementación con pocas líneas de código para ser procesadas en computadoras estándar. Estas dos posibilidades permiten enfocarse en comparar y evaluar la diferencia de las imágenes, y obtener un resultado puntual e inobjetable sobre una condición u otra.

La comparación de imágenes y el detalle de sus diferencias, ha ganado interés en aplicaciones de seguridad y en especialidad para llevar a cabo procesos de autentificación con márgenes de error y de variación bastante reducidos. Las bondades de esta tecnología son aplicadas en esta investigación para evaluar la atomización del combustible entre diferentes condiciones y configuraciones del sistema de inyección.

La evaluación y comprobación de los sistemas de inyección que se realizan de modo únicamente visual, directamente en un banco que prueba la funcionalidad de un componente, pasan por alto pequeñas e imperceptibles diferencias. En el presente trabajo, el análisis por computadora de las imágenes capturadas en video del flujo de atomización permite amplificar esas pequeñas diferencias y evaluar de modo más crítico múltiples flujos de atomización o su interacción entre ellos.

Normalmente los flujos de atomización para ser considerados correctos deben estar dentro de un patrón de medición, si esto flujos están fuera de esos rangos, entonces se considera que el flujo es defectuoso. La necesidad de expandir este enfoque de evaluación consiste en evaluar lo que pasa también dentro de ese patrón de evaluación; así como también la interacción entre flujos de atomización. En los modelos actuales, tanto los físico-matemáticos [1, 2], como los computacionales, se evalúan los flujos que se dispersan en un volumen determinado o en un espacio libre y abierto; pero, no muestran un método o técnica que evalúe su interacción.

Du et al. [3], menciona la necesidad de caracterizar los flujos de atomización para desarrollar una mejor comprensión de comportamiento de los combustibles en motores a gasolina de ignición por compresión. En esa investigación se compararon dos diferentes tipos de gasolina en condiciones no reactivas, analizando el flujo másico de la inyección, y la longitud de penetración de líquido vapor. La caracterización del flujo de atomización se llevó cabo en un recipiente a presión constante, con una condición térmica homogénea a lo largo del flujo de atomización. El procesamiento de las imágenes para caracterizar la longitud de la atomización, se lleva a cabo por el método de retroiluminación difusa, que se basa en la extinción de la luz incidente por medio del combustible en fase líquida, esto da como resultado sombras que muestran las variaciones en la densidad de los flujos de atomización. La investigación de Sharma y Agarwal [4] de modo similar caracteriza el flujo de atomización de combustibles oxigenados por medio del análisis de sombras en las imágenes; esta prueba fue llevada a cabo a cuatro presiones de inyección diferentes en la cámara de combustión y el objetivo fue observar el efecto que tiene en el flujo de atomización el oxígeno presente en el combustible. Esta última investigación resalta la importancia de estudiar los flujos de atomización y los procesos de combustión para el desarrollo de la nueva generación de motores más eficiente y limpios, en contraste

con investigaciones y enfoques anteriores, concentrados únicamente en las emisiones contaminantes y en la eficiencia del combustible. Esto refuerza la idea de que, en un futuro a mediano plazo, la implementación de nuevos tipos de combustibles que sean más ecológicos, permita explotar y aprovechar la predecible dependencia de los motores de combustión interna, y a la vez permitan la aplicación de nuevos conceptos de motor. Para ese momento, será de mucha utilidad tener herramientas que permitan evaluar y tomar decisiones, de las técnicas y métodos que garanticen una mezcla homogénea, lo que en la actualidad aún se persigue.

Los modelos computacionales de los flujos de atomización en condiciones reactivas y no reactivas, son más avanzados y complejos que los modelos experimentales, ya que cuentan con la ventaja de limitarse a ser modelados teóricamente; sin embargo su alcance es bastante amplio al estudiar los flujos de atomización desde un enfoque Euleriano, en donde el estudio del fluido es desde un punto de referencia fijo; y desde una especificación Lagrangiana, en donde una parte del fluido se estudia mientras esta parte se mueve en el espacio y el tiempo [5]. La investigación de Pillai et al., lleva a cabo simulaciones Large-eddy (LES) que son un modelo matemático de turbulencia usado en la Mecánica de Fluidos Computacional (CFD); en estas simulaciones se observa que el flujo de atomización, en especial el diámetro de las partículas atomizadas, y su posterior combustión se ven afectados cuando se ejercen fluctuaciones temporales [6].

Uno de los principales problemas que se evidenciaron en el presente estudio, de lo que se estudia en la caracterización de los flujos de atomización, es la falta del análisis y pruebas en lo que respecta a la interacción entre flujos. Investigaciones anteriores se han enfocado en modelos físicos y matemáticos de flujos individuales, con su post análisis de fotografías y videos. En referencia a la fuente [6], que menciona el efecto de las fluctuaciones; entonces, es muy concebible suponer que la interacción de los flujos mejora el nivel de atomización del combustible, y para su evaluación, es necesario que la caracterización de los flujos de atomización muestre cuáles son las diferencias entre flujos individuales y entre aquellos que interactúan entre sí. El análisis de estas diferencias, dará como resultado las zonas más y menos densas del combustible atomizado y de combustión. El propósito de esta investigación es el de mostrar estas diferencias en imagen.

2. MATERIALES Y MÉTODOS

El análisis de imagen se llevó a cabo en tres etapas; primero, con el uso de una imagen que muestre de modo extremadamente básico la diferencia entre un flujo puramente esquemático de atomización; segundo, se analiza el flujo atomizado de diésel puro comparado con aceite lubricante inyectado a 1500 bares de presión durante 0.5ms [7]; y tercero, con 1, 2, y 4 flujos de atomización [8] llevados a cabo por medio de CFD (Dinámica de Fluidos Computacional) en OpenFOAM ® [9], bajo condiciones reactivas y no reactivas; es decir, sin y con combustión.

La imagen para ser analizada en el primer caso se muestra en la figura 1, la misma que puede ser elaborada en cualquier software que permita crear imágenes.

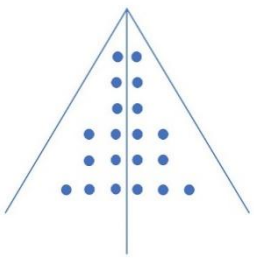

a. Flujo dentro del parámetro de atomización.

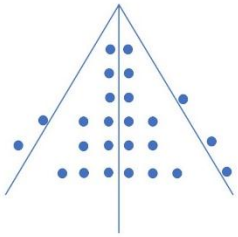

b. Flujo fuera del parámetro de atomización

Figura 1. Imagen de prueba de un flujo esquemático de atomización.

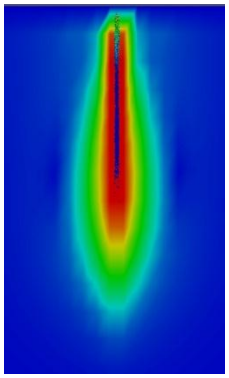

a. Flujo de atomización de diésel puro.

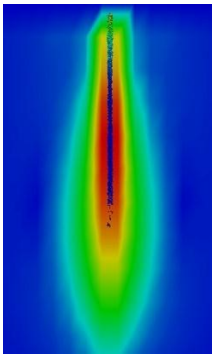

b. Flujo de atomización de aceite lubricante usado.

Figura 2. Imagen de prueba de un flujo esquemático de atomización. Las imágenes originales pueden encontrarse en el App. 1.

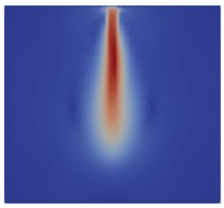

a. Flujo de atomización individual sin combustión.

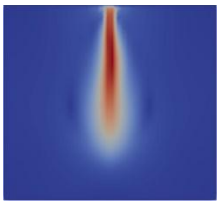

b. Flujo de atomización individual con combustión.

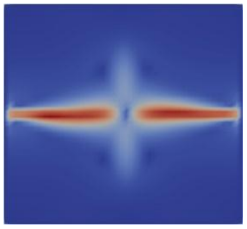

c. Doble flujo de atomización sin combustión.

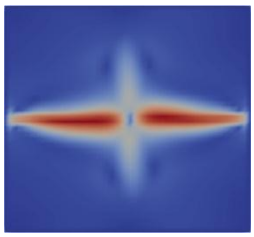

d. Doble flujo de atomización con combustión.

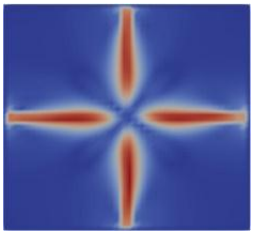

e. Cuádruple flujo de atomización sin combustión.

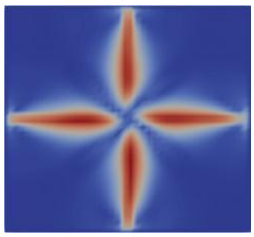

f. Cuádruple flujo de atomización con combustión.

Figura 3. Imágenes de simulación CFD bajo condiciones reactivas y no reactivas de 1, 2 y 4 flujos de atomización. Las imágenes originales pueden encontrarse en el App. 2.

3. RESULTADOS Y DISCUCIÓN

La tabla 2 muestra las diferencias entre los flujos de atomización estudiados en las figuras 1-3. La diferencia consiste en sustraer la diferencia entre las imágenes seleccionadas.

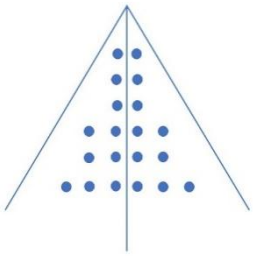

a. Flujo dentro del parámetro de atomización.

Figura 1. Imagen de prueba de un flujo esquemático de atomización.

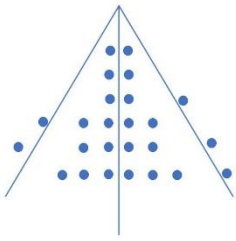

b. Flujo fuera del parámetro de atomización

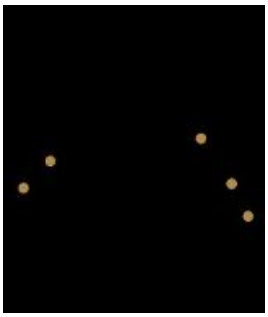

c. Diferencia del flujo de atomización.

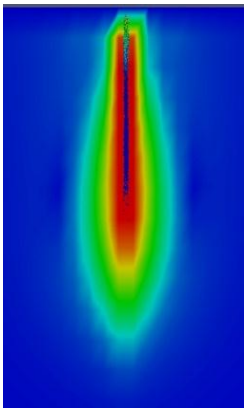

d. Flujo de atomización de diésel puro.

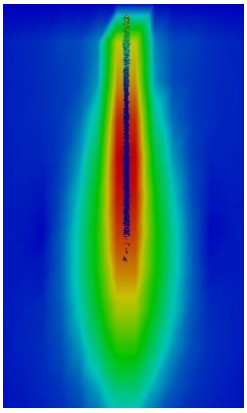

e. Flujo de atomización de aceite lubricante usado.

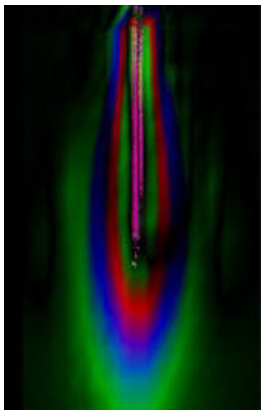

f. Diferencia del flujo de atomización.

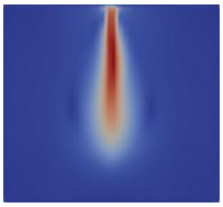

g. Flujo de atomización individual sin combustión.

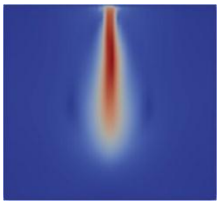

h. Flujo de atomización individual con combustión.

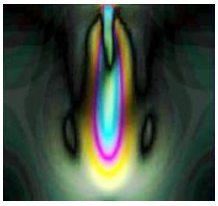

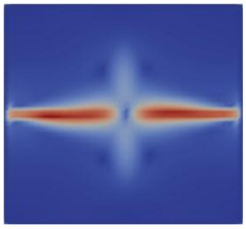

i. Doble flujo de atomización sin combustión.

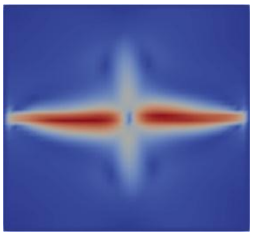

j. Doble flujo de atomización con combustión.

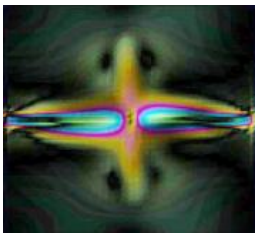

k.

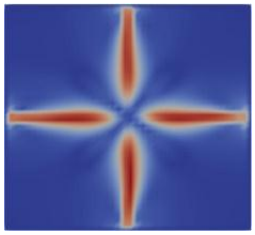

l. Cuádruple flujo de atomización sin combustión.

m. Diferencia del flujo de atomización

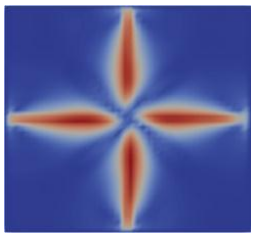

n. Cuádruple flujo de atomización con combustión.

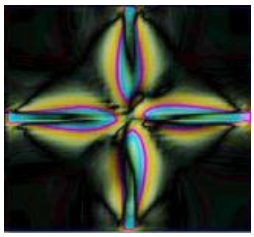

o. Diferencia del flujo de atomización

Figura 4. Análisis de imagen entre condiciones reactivas y no reactivas de atomización.

Una clara ventaja para analizar los flujos de atomización sobre las técnicas de caracterización convencionales; incluso sobre aquellas equipadas con equipos potentes en lo que se refiere a toma de datos y procesamiento de la información. Otra ventaja es la de contar con un código de programación bastante simple que permite analizar cualquier tipo de imagen. La desventaja que se encontró y que es una limitante, es la de no poder procesar las imágenes en computadores convencionales con los resultados que se esperan de supercomputadores, por lo que fue necesario contar con equipos de gran capacidad de procesar gráficos y datos. Una fuente importante de error puede ser la posición de origen y de referencia con la que se compara las imágenes, ya que una mínima diferencia de sombra, reflejo o cualquier diferencia en una imagen digitalizada, se mostrará como una diferencia del objeto que se analiza, lo que no correspondería con la realidad.

4. CONCLUSIONES

Como se menciona en la introducción, el objetivo de esta investigación es mostrar las diferencias de imagen entre los flujos de atomización que se estudian; anteriormente los flujos de atomización se caracterizaban y evaluaban en función de un patrón del flujo en el que debían encontrarse, ahora es posible evaluar las diferencias de los distintos y condiciones por los que atraviesan los flujos de atomización de combustible.

Esta investigación ha demostrado que la sustracción de imagen puede dar el detalle gráfico de las zonas con alta o baja densidad de combustible, tanto en condiciones reactivas como en condiciones sin combustión.

Los presentes hallazgos podrían ayudar analizar flujos de atomización reales, captados por medio de fotografías o videos. Los resultados analizando imágenes de simulación han sido muy prometedores por lo que es de esperar una aplicación satisfactoria de esta técnica con la ayuda de cámaras de alta resolución y con la capacidad de captar videos en cámara lenta.

El punto fuerte de este trabajo consiste en que la técnica descrita para analizar imágenes puede ser decisiva a la hora de tomar decisiones sobre técnicas y procedimientos para mejorar la atomización de combustible; esto puede conducir, a la refutación de teorías en donde la colisión de los flujos atomización de combustible pueden contribuir a la reducción del diámetro de las moléculas que colisionan y no a su coalición. Otra ventaja es que este método puede analizar de modo simultáneo varios fenómenos como la colisión de flujos en lugar de analizarlos de modo individual, como es el caso de la caracterización de los flujos de atomización.

El trabajo que queda por delante para continuar con el desarrollo de esta técnica, consiste en cuantificar las diferencias, para que la evaluación visual pueda expandirse al análisis de variaciones en propias del flujo de

atomización como en aquellas en las que estas puedan ocurrir.

5. REFERENCIAS

[1] Lahane, S., & Subramanian, K. A. (2015). Effect of different percentages of biodiesel–diesel blends on injection, spray, combustion, performance, and emission characteristics of a diesel engine. Fuel, 139, 537–545. https://doi.org/10.1016/j.fuel.2014.09.036

[2] Yu, Y., Li, G., Wang, Y., & Ding, J. (2016). Modeling the atomization of high-pressure fuel spray by using a new breakup model. Applied Mathematical Modelling, 40(1), 268–283.

[3] Du, J., Mohan, B., Sim, J., & Roberts, W. L. (2019). Experimental study on the non-reacting spray characterization of gasoline compression ignition fuel. Energy Procedia, 158, 1968–1973. https://doi.org/10.1016/j.egypro.2019.01.453

[4] Sharma, N., & Agarwal, A. K. (2021). Macroscopic spray characteristics of a gasohol fueled GDI injector and impact on Engine Combustion and particulate morphology. Fuel, 295, 120461. https://doi.org/10.1016/j.fuel.2021.120461

[5] Wen, J., Hu, Y., Nishiie, T., Iino, J., Masri, A., & Kurose, R. (2021). A flamelet les of turbulent dense spray flame using a detailed high-resolution VOF simulation of Liquid Fuel Atomization. Combustion and Flame, 111742. https://doi.org/10.1016/j.combustflame.2021.111742

[6] Pillai, A. L., Nagao, J., Awane, R., &Kurose, R. (2020). Influences of liquid fuel atomization and flow rate fluctuations on spray combustion instabilities in a backward-facing step combustor. Combustion and Flame, 220, 337–356. https://doi.org/10.1016/j.combustflame.2020.06.031

[7] Tablet School. Tablet School Journal. Nr.: 008. Vol.: 001. ISSN: 2661-6505. Art.: 2020-33-3313-0002. Feb 2021. M. Gutiérrez. “Modelling the spray development of fuel blends from recycled edible and lubricating oils using OpenFOAM®”. Retrieved November 10, 2021, from https://www.tablet-school.com/tablet-school-journal/.

[8] Tablet School. Tablet School Journal. Nr.: 008. Vol.: 001. ISSN: 2661-6505. Art.: 2020-33-3313-0001. Feb 2021. M. Gutiérrez. “Babel Project – A Multiinjector Concept”. Retrieved November 10, 2021, from https://www.tablet-school.com/tablet-school-journal/

[9] OpenFOAM. Retrieved November 11, 2021, from https://www.openfoam.com/.

[10] The world's most popular data science platform. Anaconda. Retrieved November 12, 2021, from https://www.anaconda.com/.

[11] Welcome to Python.org. Python.org. Retrieved November 12, 2021, from https://www.python.org/.

ANEXOS

ANEXOS INTRODUCCIÓN

Fuel 139 (2015) 537–545

Contents lists available at ScienceDirect

Fuel

journal homepage: www.elsevier.com/locate/fuel

Effect of different percentages of biodiesel–diesel blends on injection, spray, combustion, performance, and emission characteristics of a diesel engine

Subhash Lahane, K.A. Subramanian *

Engines and Unconventional Fuels Laboratory, Centre for Energy Studies, Indian Institute of Technology Delhi, New Delhi 110 016, India

HIGHLIGHTS

- In-line fuel injection pressure and spray penetration is higher with all biodiesel blends.
- Chance of wall impingement is to be critical with B20 but more with B25, B50, and B100.
- Ignition delay and rate of pressure rise decreased with all biodiesel blends.
- NOx emission increases with all biodiesel blends (B20: 15.6% and B100: 22.8%).
- B15 is the optimum blend based on change in NOx emission and no wall impingement.

ARTICLE INFO

Article history:
Received 9 February 2014
Received in revised form 2 June 2014
Accepted 11 September 2014

Keywords:
In-line fuel pressure
Spray penetration
Wall impingement
NOx emission
Diesel engine

ABSTRACT

A comparative study of effect of different biodiesel–diesel blends (B5, B10, B15, B20, B25, B50 and B100) on injection, spray, combustion, performance, and emissions of a direct injection diesel engine at constant speed (1500 rpm) was carried out. The penetration distance increased with increase in percentage of biodiesel in diesel due to enhanced in-line fuel pressure. The simulation results indicate the spray penetration with biodiesel–diesel blend up to B15 does not lead to wall impingement but B20 is to be a critical limit of wall impingement (within uncertainty ±1.3%). However, it is observed clearly from the simulation results that probability of wall impingement is more with higher blends (B25, B50 and B100). The ignition delay period decreased with all biodiesel blends due to higher cetane number resulting in less rate of pressure rise and the smooth engine running operation. The engine torque does not change significantly with biodiesel–diesel blends up to 20% (B20). However, the torque reduction is about 2.7% with B100 at the rated load. Carbon monoxide (CO), hydrocarbon (HC) and smoke emissions decreased with all biodiesel–diesel blends. However, oxides of nitrogen (NOx) emission increased in the range of 1.4–22.8% with all biodiesel–diesel blends at rated load due to oxygenated fuel, automatic advance in dynamic injection timing (DIT), higher penetration and higher in-cylinder temperature. A notable conclusion emerged from this study is the optimum biodiesel–diesel blend based on no wall impingement (B15: 0% and B20 ±1.3% uncertainty limit) and increase in NOx emission (B15: 4.1% and B20: 15.6%) in a conventional (unmodified) diesel engine is up to B15.

1. Introduction

The main driving force behind the implementation of biodiesel in diesel engines is due to enhancement of fuel quality, self reliance of energy need, and boosting of rural economy. The higher cetane number of Karanja biodiesel (CN:58) could provide the easy starting of the engine, lesser white smoke, shorter ignition delay, less probability of knocking and smooth running of diesel engine as compared to base diesel [1]. The sulfur and aromatics in biodiesel are lower as these properties would affect on formation of particulate matter in diesel engines. However, the bulk modulus is higher with biodiesel (1500 MPa) than base diesel (1350 MPa) as this property indicates the compressibility of the fuel that would effect on injection characteristics of diesel engines. In a diesel engine, the fuel spray characteristics which deal the interaction of the injected fuel with the surrounding hot air during ignition delay period and combustion, is mainly dependent on injection characteristics such as injection delay, in-line fuel injection pressure, dynamic injection timing (DIT), in-cylinder injection duration and injector nozzle con-

* Corresponding author. Tel.: +91 11 26591247; fax: +91 11 26581121.
E-mail address: subra@ces.iitd.ac.in (K.A. Subramanian).

http://dx.doi.org/10.1016/j.fuel.2014.09.036
0016-2361/

figuration. The fuel spray characteristics play an important role in the improvement of combustion and engine performance, because it influences the mixture formation process of fuel with air in the engine cylinder [2]. Some information on diesel fuel spray characteristics is available in literature. However, information on biodiesel spray is scanty.

1.1. Injection and spray characteristics of a diesel engine using biodiesel–diesel blends

Diesel engine process including injection, spray, mixing, ignition and combustion influences its performance and emission characteristics. Among these processes, injection and spray process are important as they are affected by the quality of fuel, resulting in alteration of combustion characteristics of diesel engines. As biodiesel has a different physico-chemical property (density, viscosity, distillation properties, bulk modulus, surface tension, etc.) as compared to base diesel, its effect on the injection [3] and spray characteristics of the engine need to be studied in order to find scopes for solving these problems.

Fuel injection system plays a vital role on enhancing engine efficiency and emission reduction of the modern diesel engine [4]. The injection characteristics of a diesel engine include injection delay, static injection timing, DIT and injection duration. The duration of injection delay is defined as the duration between DIT and static injection timing. DIT is defined as the actual injection timing where the fuel is started to inject into the cylinder. The fuel-injection process is important as it influences fuel spray characteristics (break-up length, spray cone angle, sauter mean diameter (SMD), penetration and air entrainment) and mixture formation process [2].

The numerical analysis of injection characteristics using biodiesel–diesel blends (B25, B50, B75 and B100) was carried out by Kegl and Hribernik [5] and Kegl [6]. They reported that the DIT advanced whereas injection duration and in-line pressure increased with all biodiesel–diesel blends. The process of atomization and fuel–air mixing rate could be enhanced by increasing the in-line fuel injection pressure [7]. However, it may increase penetration distance which results in more probability of wall impingement. National Renewable Energy Lab (NREL), USA reported that the automatic advance in injection timing is due to higher bulk modulus of biodiesel (1500 MPa) than diesel (1350 MPa) as it implies the compressibility of the fuel [8]. The bulk modulus of biodiesel is higher than base diesel resulting in significant increase in in-line fuel pressure. The fuel spray penetration distance increases with increase in the in-line fuel pressure resulting in increase of probability of wall impingement [9]. It may be noted that wall impingement is one of the main durable issues of a diesel engine that needs to be reduced. It could be reduced mainly by reducing the penetration distance.

Fuel quality parameters including viscosity, density, and surface tension influence the spray characteristics of diesel engines. High viscosity and surface tension of biodiesel increase SMD, which affects fuel atomization [7]. Gao et al. [10] studied the spray characteristics of three biodiesel fuels (Jatropha, palm and used fried oil). SMD and spray penetration increased with increasing percentage of biodiesel in diesel but the spray cone angle decreased resulting in poor atomization. It may be noted that the injection characteristics alter fuel spray and combustion which influence performance and emission characteristics of diesel engines for biodiesel–diesel blends. Hence, injection characteristics are a central theme of design of a diesel engine for biodiesel utilization.

1.2. Combustion characteristics of a diesel engine using biodiesel–diesel blends

The combustion characteristics are one of the important tools to optimize performance and emission characteristics of diesel engines. Due to different properties of diesel and biodiesel, both fuels exhibit different combustion characteristics with respect to change in engine load. The main aim of optimization of fuel spray characteristics is improvement of mixture formation process which influences auto ignition and combustion process of diesel engines [11,12]. Biodiesel fuel comprises of 10–11% oxygen (by weight) which would enhance the heat release rate during combustion and reduces emissions (CO, HC, and Smoke/PM) significantly except NOx [13–15]. Combustion with biodiesel fueled diesel engine starts earlier at advanced dynamic injection timing due to higher bulk modulus. The peak rate of pressure rise is lower for biodiesel due to shorter ignition delay [16]. As high ignition delay leads to high rate of pressure rise, some extend to knocking, noise and NOx emission, it is necessary to lower the ignition delay. So, the combustion characteristics such as ignition delay, start of combustion, rate of pressure rise, etc. of a diesel engine for Karanja biodiesel–diesel blend need to be studied in detail in order to find the scopes for further improvement of the performance and emission reduction.

1.3. Performance and emission characteristics of a diesel engine using biodiesel–diesel blends

Biodiesel has low carbon content than diesel fuel (Diesel: 87 and Biodiesel: 77.2 wt.%). Hence, biodiesel fueled diesel engines will emit lower carbon based emissions than base diesel. Graboski and McCormick [17] studied the performance and emission characteristics of a diesel engine fueled with biodiesel–diesel blends (B10, B20, B30, B50 and B100) as compared to base diesel. The results indicated that CO, HC, PM, smoke and Poly-Aromatic Hydrocarbon (PAH) emissions decreased with the biodiesel–diesel blends whereas brake specific fuel consumption (BSFC) and NOx increased significantly [18,19]. Rakopoulos et al. [20] reported that the BSFC increases with the oxygen enrichment in the fuel but it does not affect with oxygen enrichment in the intake air. The percentage of torque reduction was reported as 0.85%, 1.25%, 2.33% and 5.90% with B20, B35, B65 and B100 respectively.

Experimental investigation was carried out to study the performance and emission characteristics of a diesel engine fueled with different percentages of karanja biodiesel–diesel blends (B5, B10, and B15) [21]. They concluded that B10 (karanja biodiesel–diesel blend) is the optimum blend for diesel engines. However, Mahanta et al. [22] concluded that B15 and B20 could be the optimum in terms of fuel efficiency and power developed. However, the optimum biodiesel–diesel blend would depend on particular feedstock [23,24]. It was reported that the appropriate biodiesel–diesel blend required for ensuring the optimum performance and low emission. As biodiesel is produced from different feed stocks, the physico-chemical properties of biodiesel will vary with the feed stock [25]. Lin et al. [23] reported the effect of biodiesel's feedstock on a diesel engine performance. They studied engine performance characteristics with biodiesel derived from different feed stocks including soybean oil methyl ester (SOME), peanut oil methyl ester (PNOME), corn oil methyl ester (COME), sunflower oil methyl ester (SFOME), rapeseed oil methyl ester (ROME), palm oil methyl ester (POME), palm kernel oil methyl ester (PKOME), and waste fried oil methyl ester (WFOME), and these results were compared with base diesel as given in Table 1. In general, they reported that carbon, hydrogen, oxygen, and sulfur content will influence the calorific value of a fuel and hence, it would also influence the engine performance and emission characteristics. Similarly, the combustion, performance and emission characteristics of a diesel engine fueled with biodiesel derived from wasting cooking oil were compared with base diesel [26,27]. The chance of wall impingement will be more for biodiesel fueled diesel engine due to higher injection pressure. Hence, the optimum biodiesel–diesel blend has to be

Table 1
The experimental results of the engine performance and exhaust emissions from different feedstock fuels [23].

Item	PD	SOME	PNOME	COME	SFOME	ROME	POME	PKOME	WFOME
BSFC(g/MJ)	63.5	71.7	71.1	69.9	69.5	71.1	72.7	72.8	72
Power (kW)	7.22	7.18	7.13	7.18	7.32	7.25	7.28	7.2	7.14
Smoke (%)	22	9	11	10	9	10	9	6	11
NOx (ppm)	466	566	555	564	570	587	548	492	555
THC (ppm)	178	131	138	132	129	135	124	119	134
EGT (°C)	405	397	398	401	402	401	392	387	394

selected based on change in NOx emission and minimum probability of wall impingement. Therefore, the present study is aimed at the optimization of biodiesel–diesel blend based on injection, spray, combustion, performance and emission characteristics of a diesel engine.

2. Experimental details

A test diesel engine (single cylinder, four strokes, air cooled, constant speed (1500 rpm) with maximum power output of 7.4 kW (Swept volume: 947.38 cc; compression ratio: 19.5:1; nozzle diameter: 0.19 mm)) was used for the study (Fig. 1). The engine was equipped with cam-shaft driven fuel injector (mechanical fuel injector). An eddy current dynamometer was used for loading the engine. A piezoelectric strain gauge pressure transducer was mounted on the fuel line for measurement of in-line fuel pressure. A piezoelectric transducer was mounted (as flush mounted) in the cylinder head for in-cylinder pressure measurement (Measuring range: 0–250 bar, sensitivity: 45p C/bar and linearity: $\leqslant$±0.3%). The crank angle encoder was mounted on the engine shaft for crank angle measurement with an accuracy of 0.05° CA. AVL indicom system comprised of in-built charge amplifier and data acquisition system was used for acquiring of pressure-crank angle data. The injection signals were processed using the system with the signal amplifier. The engine speed (1500 rpm) was maintained as constant throughout the tests. CO, CO_2 and HC emissions were measured using AVL Di-gas analyzer (Measurement principle: Infrared measurement). NOx emission was measured using CLD analyzer (linearity: ±1%). Smoke opacity was measured using AVL smoke meter (Accuracy: ±1%, measuring range: 0–100% Opacity). The Karanja methyl ester (biodiesel) was prepared in a laboratory scale and the biodiesel of 5%, 10%, 15%, 20%, 25%, 50% and 100% (B5, B10, B15, B20, B25, B50 and B100) by volume was blended with base diesel (Bharat stage IV (equivalent of Euro IV)). The physico-chemical properties were measured (density, viscosity, flash point, cloud point, pour point, and calorific value) whereas other physico-chemical properties such as thermal conductivity, surface tension and latent heat of fuels were taken from National Renewable Energy Laboratory (NREL) and BP websites (Table 2).

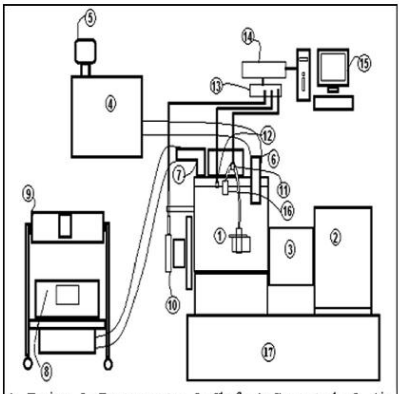

Fig. 1. Experimental set-up.

Experimental tests were conducted on the diesel engine in-order to assess injection, combustion, performance and emissions of the engine for base diesel and biodiesel–diesel blends. Each test was repeated at least three times to confirm the accuracy of measured data.

The measured injection and combustion characteristics (Injection duration, In-line fuel pressure, In-cylinder pressure) were given as input to the spray models/correlations. The measured swirl ratio of 2.20 was taken into account for calculation of spray characteristics. The spray characteristics are analyzed with respect to crank angle per cycle. The models, which are selected for calculating the spray characteristics for the present study, are based on our previous work published in literature [2]. These spray models are optimized/selected based on available measured data in the literature for spray characteristics. Furthermore, these selected models are also used by many researchers to calculate biodiesel spray characteristics. Even though the spray characteristics could be calculated with more accurate during the ignition delay period, it is very difficult to predict the spray characteristics after the start of combustion. The reasons could be due to fuel spray interaction with air at very high temperature, high pressure and unpredictable air motion (high velocity) resulting to complexity in nature of mixture formation with unburned reactant and burned product during the diffusion combustion phase. Wall impingement is defined that it would occur when the spray penetration distance is higher than the available length between piston bowl surface and nozzle tip. A study of probability wall impingement based on spray penetration and piston bowl motion with respect to crank angle was carried out. Spray penetration with respect to crank angle was calculated using model. Wall impingement would occur when the spray penetration is higher than the available length between piston bowl surface and nozzle tip. The volume of cylinder with respect to crank angle was calculated using Eqs. (1)–(4). From the known displacement volume, the stroke length can be calculated as given in Eq. (5). Injector angle was measured to predict the inclined length, i.e. actual distance from injector nozzle tip to piston bowl depth (Fig. 2) with respect to crank angle.

$$r_c = \frac{V_t}{V_c} = \frac{V_d + V_c}{V_c} \tag{1}$$

$$V_d = \frac{\pi}{4} \times D^2 \times L \tag{2}$$

where r_c = Compression ratio, D = Cylinder bore and L = Stroke length

Table 2
Physico-chemical properties of diesel and biodiesel blends.

Property	Diesel	B5	B10	B15	B20	B25	B50	B100
Density (kg/m^3)	821.5	823.1	827.5	831.3	835.6	838.9	860.7	893.6
Viscosity (cSt)	2.64	2.65	2.66	2.69	2.71	2.75	3.5	5.8
Flash point (°C)	76	85	96	101	110	117	129	147
Cloud point (°C)	6.5	7.2	8.3	9.1	10	10.3	11.1	13.6
Pour point (°C)	3.1	3.5	3.8	4.3	4.5	4.8	5.3	6.7
CV (MJ/kg)	44.05	43.89	43.25	42.90	42.60	42.00	41.73	40.750
Thermal condu. (W/mK)	0.061	–	–	–	–	–	–	0.018
Surface tension (N/m)	0.023	–	–	–	–	–	–	0.028
Latent heat (kJ/kg)	250	–	–	–	–	–	–	181

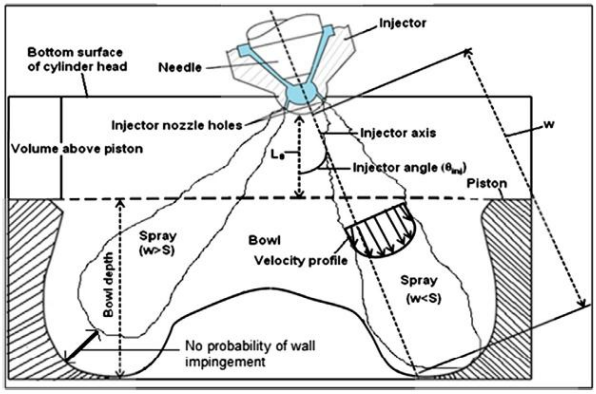

Fig. 2. Occurrence of wall impingement on the surface of piston bowl.

Cylinder volume (V) at any crank angle position θ can be calculated using Eq. (6).

$$V_\theta = V_c + \left[\frac{\pi \times D^2}{4}(l + a - s)\right] \tag{3}$$

where $s = a \times \cos\theta + (l^2 - a^2 \times \sin^2\theta)^{1/2}$ (4)

The available length (L_θ) between the nozzle tip to piston surface can be calculated using V_θ as given in Eq. (5).

$$L_\theta = \frac{4 \times V_\theta}{\pi \times D^2} \tag{5}$$

The sum of bowl depth (B_L) and L_θ is known as total length (L_t) as given in Eq. (6).

$$L_t = L_\theta + B_L \tag{6}$$

The maximum available inclined length (w) can be calculated using Eq. (7). The entire representation of wall impingement is shown in Fig. 2.

$$w = \frac{L_t}{\cos(\theta_{inj})} \tag{7}$$

The actual maximum available length (w) can be found from the distance between nozzle tip to bowl depth. If 'w' is greater than spray penetration ($w > S$), wall impingement does not occur, whereas 'w' is lesser than spray penetration ($w < S$), the probability of wall impingement would be more. If 'w' is equal to spray penetration ($w = S$), it is a critical condition.

3. Results and discussion

3.1. Analysis of injection characteristics for different biodiesel–diesel blends with comparison of base diesel

Figure 3 shows that the injection delay is lower with all biodiesel–diesel blends than base diesel due to lesser compressibility of biodiesel (higher bulk modulus) resulting in automatic advancement in dynamic injection timing (DIT). As the duration of injection delay decreased from 5.6° CA with base diesel to 5.5°, 5.4°, 5.3°, 5.2°, 5.1°, 5° CA with B10, B15, B20, B25, B50 and B100 respectively, DIT advanced from 0.4° CA before top dead center (BTDC) with base diesel to 0.5°, 0.6°, 0.7°, 0.8°, 1.1° and 1.5° CA BTDC with B10, B15, B20, B25, B50 and B100 respectively. However, there is no change in injection delay and DIT with B5. The drastic advancement can be observed from the figure for higher blends (B25, B50 and B100). It may be noted that bulk modulus is function of density (B5: 823.1, B10: 827.5, B15: 831.3, B20: 835.6, B25: 838.9, B50: 860.7 and B100: 893.6 kg/m^3) and square of sound velocity resulting in higher bulk modulus of biodiesel. In general, the advanced DIT generally leads to higher NOx emission.

The in-line fuel injection pressure increases with increase the percentage of biodiesel in diesel. It may be noted that the in-line fuel pressure fluctuates as the pressure waves generated by the mechanical injection pump propagates more rapidly toward the injector [15]. Bulk modulus is the ratio of pressure (dP) and volumetric strain (dV/V). If the volumetric strain (dV/V) is constant, the pressure (dP) is directly proportional to bulk modulus (B). Similarly, the peak in-line fuel injection pressure of all biodiesel–diesel blends (B5: 484.28, B10: 487.62, B15: 490.85, B20: 495.45,

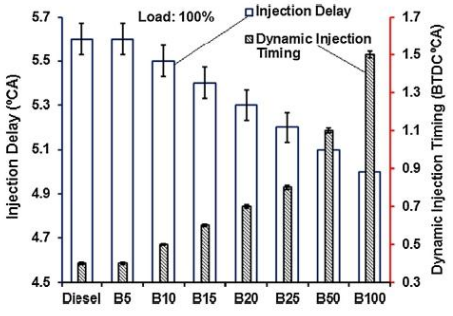

Fig. 3. Comparison of injection delay and DIT for base diesel and biodiesel blends.

B25: 493.48, B50: 496.32 and B100: 505.9 bar) is higher than base diesel (Diesel: 472.31 bar). In order to maintain same power output, the fuel flow rate needs to be enhanced more. The enhanced fuel flow rate may be one of the reasons to increase in-line fuel injection pressure with biodiesel–diesel blends.

The high in-line fuel pressure for biodiesel–diesel blends increases spray penetration distance which is discussed in latter section. The in-cylinder fuel injection duration is higher with all biodiesel–diesel blends than base diesel. In order to maintain same power output, the fuel flow rate needs to be enhanced more. The increased injection duration would affect performance characteristics of the engine mainly torque, BSFC and combustion characteristics negatively. The injection duration increases from 10.2° CA with base diesel to 10.5°, 10.7°, 10.8°, 10.9°, 11°, 11.2° and 11.4° CA with B5, B10, B15, B20, B25, B50 and B100 respectively at the rated load. The percentage change in injection duration is in the range of 5–10% for B20 to B100 whereas it is less than 5% up to B15. Hence, injection system including injection timing, plunger diameter, number of nozzle holes and its size and nozzle opening pressure has to be optimized for the overcoming of the problem of increased mass flow rate of biodiesel blends.

3.2. Analysis of spray characteristics for different biodiesel–diesel blends and base diesel

3.2.1. Spray break-up length (L_b)

The break-up length (BUL) is calculated using Hiroyasu–Arai model as shown in Eq. (8).

$$L_b = 15.8 \times \left(\frac{\rho_l}{\rho_a}\right)^{0.5} \times D_n \tag{8}$$

where ρ_l is liquid density (kg/m^3), ρ_a is air density (kg/m^3), D_n is nozzle diameter (m).

As the density of biodiesel blends (B100: 893.6 kg/m^3) is higher than base diesel (821.5 kg/m^3), the break-up length for B100 fuel is higher than base diesel (Fig. 4(a)). The peak break-up length is higher with B100 (13.9 mm) as compared to base diesel (13.5 mm) at the rated load. There is no change in break-up length with biodiesel–diesel blend (B5 to B20) as the values are within uncertainty limit (±1.3%) whereas there is a significant increase with B25, B50 and B100 blends. Break-up length preferably should be less whereas higher break-up length leads to the poor air entrainment into the fuel spray.

3.2.2. Spray cone angle (θ)

The spray cone angle (SCA) is calculated using Reitz model as given in Eq. (9).

$$\tan\left[\frac{\theta}{2}\right] = \left(\frac{1}{A}\right) \times 4 \times \pi \times \left(\frac{\rho_a}{\rho_l}\right)^{0.5} \times \left(\frac{3^{0.5}}{6}\right) \tag{9}$$

where $A = 3 + \left(\frac{(L_n/D_n)}{3.6}\right)$

The spray cone angle (θ) for biodiesel–diesel blends is lower than base diesel due to higher density of biodiesel–diesel blends than base diesel (Fig. 4(b)). At the end of spray, the spray cone angle is more divergent could be due to the momentum of spray decreases from upstream (injector tip) to downstream (spray tip). The peak spray cone angle decreased from 17.5° with base diesel to 16.8° with B100 at the rated load at 10° CA ATDC. It may be due to higher density and viscosity of biodiesel. At same spray penetration distance, if spray cone angle decreased, air entrainment would be less resulting to poor mixture formation. Even though biodiesel blend has higher in-line fuel pressure, spray cone angle does not change significantly with biodiesel because of spray cone angle is influenced mainly by fuel quality (density and viscosity).

3.2.3. Sauter mean diameter (SMD)

Sauter mean diameter is the average diameter of droplet that has same volume to surface area ratio as that of the total spray. The average diameter of droplet is used to describe the quality of atomization and SMD is a main input to calculate other spray characteristics. Hiroyasu model was used to calculate SMD (X_{32}) as given in Eqs. (10)–(12).

$$X_{32} = Max(X_{32}^{LS}, X_{32}^{HS}) \tag{10}$$

$$X_{32}^{LS} = 4.12 \times D_n \times \mathrm{Re}^{0.12} \times \mathrm{We}^{-0.75} \times \left(\frac{\mu_l}{\mu_a}\right)^{0.54} \times \left(\frac{\rho_l}{\rho_a}\right)^{0.18} \tag{11}$$

$$X_{32}^{HS} = 0.38 \times D_n \times \mathrm{Re}^{0.25} \times \mathrm{We}^{-0.32} \times \left(\frac{\mu_l}{\mu_a}\right)^{0.37} \times \left(\frac{\rho_l}{\rho_a}\right)^{-0.47} \tag{12}$$

where Re and We is Reynolds and Weber number, μ_l and μ_a is fuel and air viscosity (Pa s).

SMD is higher for the biodiesel–diesel blends than that of base diesel fuel and this is due to the higher density, viscosity and surface tension of biodiesel–diesel blends (Fig. 5). The change of increase in SMD up to B15 blend is within uncertainty limit whereas SMD increased beyond B20 blends. The Weber number is important parameter for SMD and it is function of density and surface tension. As the surface tension is higher with biodiesel [28], Weber number would be lower. Hence, lower Weber number would give larger SMD with biodiesel. A sharp peak of SMD is observed for B100 at 2° CA ATDC and it is due to change in in-line fuel pressure at particular crank angle. At the end of spray, SMD increases significantly during 9–11° CA ATDC due to decrease in in-line pressure. The larger SMD deprived the mixing rate of air and fuel.

3.2.4. Spray penetration

Spray penetration calculated using Hiroyasu–Arai model is shown in Eqs. (13), (14) as these equations were used by other researchers to calculate the spray penetration distance of a diesel engine for biodiesel–diesel blends. The penetration distance with respect to crank angle is calculated using input of measured in-line fuel pressure, in-cylinder pressure, injection duration, nozzle diameter and air density for the biodiesel–diesel blends and the results are compared with base diesel. It is observed from the results that the penetration distance increased with all biodiesel–diesel blends (Fig. 5). The peak penetration distance increased from 34.24 mm with base diesel to 34.4, 34.8, 35.1, 36.28, 36.6, 36.9 and 37.5 mm with B5, B10, B15, B20, B25, B50 and B100 at the rated load. The change in increase of spray penetration is lower than 5% up to B20 blend whereas it is higher for B25, B50 and B100.

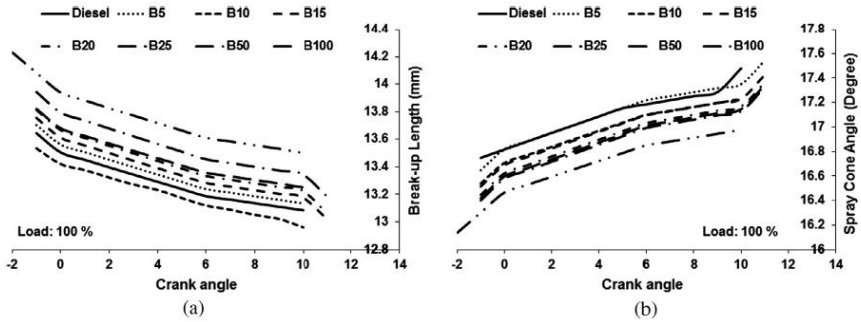

Fig. 4. Variation of (a) break-up length and (b) spray cone angle for base diesel and biodiesel blends.

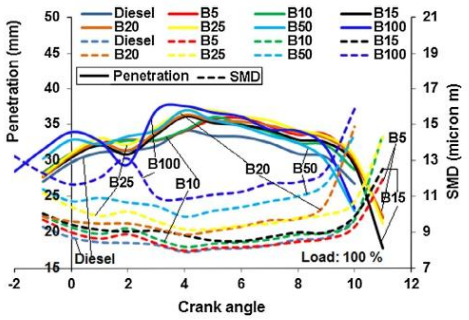

Fig. 5. Variation of SMD and spray penetration for base diesel and biodiesel blends.

In case of B100 at 2° CA ATDC, sudden drop was observed for penetration. It is mainly due to drop in in-line fuel pressure at 2° CA ATDC. At the downstream of the spray (tip), penetration decreases due to lesser momentum toward downstream. The higher penetration is beneficial for air entrainment but it may lead to wall impingement [29].

$$S = 2.95 \times \left(\frac{\Delta P}{\rho_a}\right)^{0.25} \times (D_n \times t)^{0.5} \quad \text{for } t > t_b \tag{13}$$

$$S = 0.39 \times \left(2 \times \frac{\Delta P}{\rho_a}\right)^{0.5} \times t \quad \text{for } t < t_b \tag{14}$$

where S is spray penetration (m), t is injection time (s) and t_b is break-up time (s).

3.2.5. Air entrainment

Air entrainment is defined as the process of air drawn into the fuel spray. Air entrainment calculated using Rakopoulos model/correlation is given in Eq. (15). Air entrainment is calculated with respect to crank angle using input of calculated spray cone angle, penetration and air density.

$$m_a = \left(\frac{\pi}{3}\right) \times \left(\tan\left(\frac{\theta}{2}\right)\right)^2 \times S^3 \times \rho_a \tag{15}$$

It is observed from the results that the air entrainment increased for biodiesel–diesel blends due to higher in-line fuel pressure resulting in higher penetration distance as compared to base diesel (Fig. 6). In case of B100, air entrainment suddenly drops at 2° CA ATDC as it is mainly due to sudden drop in in-line fuel pressure resulting in drop in penetration at particular crank angle. At the end of the spray, air entrainment decreased due to decrease in penetration distance. In general, as the spray cone angle decreased, air entrainment also decreased. The net result is in increased air entrainment as the penetration distance is more influencing parameter to increase in air entrainment than spray cone angle.

3.2.6. Wall impingement

Spray wall impingement is also an important post process in spray combustion. It is observed from the simulation study that the probability of wall impingement is more with higher biodiesel–diesel blends (B25, B50 and B100). This is due to increased penetration distance. The distance between nozzle tip and piston bowl decreases as piston moves toward top dead center and vice versa. The distance between nozzle tip and piston bowl depth (0–1) is shown in Fig. 7. The distance '0–1' is the highest distance as compared to the distance '0–2' and '0–3'. The distance '0–1' is considered for all calculations. When piston moves toward the top dead center (TDC), there may be a probability of fuel impingement on piston bowl at points '3' and '2' due to shorter distance of '0–2' and '0–3'. The general mathematical form of wall impingement is explained in our study that was used to calculate the wall impingement [9]. There is no wall impingement for base diesel, B5, B10, B15 and B20 as shown in Fig. 7. As the uncertainty limit of penetration is ±1.3%, there may be a probability of wall impingement with B20. However, wall impingement was observed clearly with higher

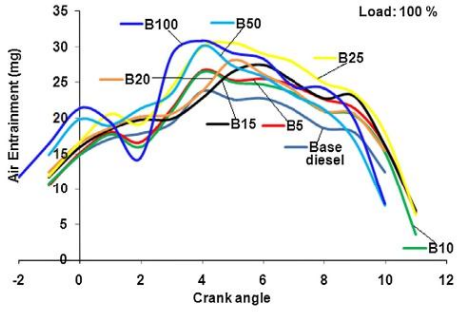

Fig. 6. Variation of air entrainment for base diesel and biodiesel blends.

biodiesel–diesel blends such as B25, B50 and B100. For B100, wall impingement is observed from 3° CA ATDC to 5° CA ATDC whereas for B25 and B50, it is observed from 3.8° CA ATDC to 4.3° CA ATDC. The wall impingement problem can be overcome by optimizing the nozzle hole size (diameter) and number of nozzle holes [29].

3.3. Analysis of combustion characteristics for different biodiesel–diesel blends and base diesel

Ignition delay, premixed combustion, mixing controlled (diffusion) combustion and late burning combustion are the vital parameters of combustion in diesel engines. The liquid fuel injected into the combustion chamber of an engine undergoes a set of physical and chemical process such as atomization, evaporation and mixing with air entrained into the spray. Ignition occurs in the periphery of the spray depending on the temperature and pressure of the in-cylinder air. The ignition delay was found lower with all the biodiesel–diesel blends (B5: 3.2°, B10: 3.2°, B15: 3°, B20:2.9°, B25: 2.8°, B50: 1.7° and B100: 1.6° CA) as compared to base diesel (3.4° CA) due to higher cetane number of biodiesel. The start of combustion advanced for all biodiesel blends (B5: 2.8°, B10: 2.7°, B15: 2.4°, B20: 2.2°, B25: 2°, B50: 0.6° and B100: 0.1° CA ATDC) than diesel (3° CA ATDC). It is mainly due to the advance in injection timing and higher cetane number of biodiesel–diesel blends which improves the ignition quality.

The peak in-cylinder temperature increased with all biodiesel–diesel blends (B20: 1742, B100: 1810 K) as compared to base diesel (1687 K) (Fig. 8). It may be due to advance in DIT resulting in early combustion process initiated. In addition to this, the presence of oxygen molecule in biodiesel tends to advance the start of combustion. The comparison of heat release rate (HRR) for diesel and biodiesel blends is shown in Fig. 9. The endothermic reaction of fuel with air initially results in negative heat release rate. HRR is one of the important tools to optimize any internal combustion engine parameters. The heat release rate can be calculated using first law of thermodynamics. The adjustment of ignition delay can control the premixed combustion phase and this phase is responsible for NOx formation and knocking. Mixing controlled combustion phase (diffusion) is responsible for smoke formation. Premixed combustion phase duration increased marginally for all biodiesel–diesel blends as compared to base diesel. As the premixed combustion phase duration is higher for biodiesel–diesel blends, it could be one of the reasons for increase in NOx emission with biodiesel–diesel blends. Mixing controlled combustion phase duration increased marginally with all biodiesel–diesel blends as compared to base diesel.

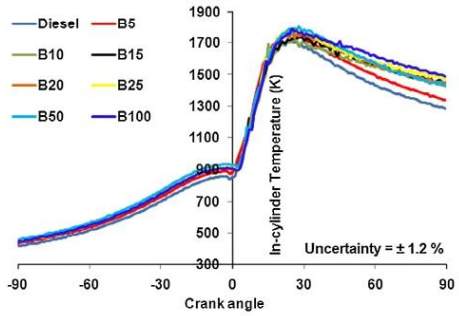

Fig. 8. Variation of in-cylinder temperature for base diesel and biodiesel blends.

The rate of pressure rise decreased with all biodiesel–diesel blends (B5: 5.9, B10: 5.4, B15: 4.35, B20: 4.3, B25: 4.26, B50: 3.25, B100: 2.2 bar/CA) as compared to base diesel (6.7 bar/CA) resulting in smoother engine running. The diesel engine with biodiesel–diesel blends has lesser ignition delay mainly due to higher cetane number resulting in lower rate of pressure rise [30]. The combustion duration is an important tool for optimizing performance and emission characteristics of the engine. The combustion duration is higher with all biodiesel–diesel blends (B20: 87.8° CA and B100: 89.9° CA) than base diesel (86° CA). The combustion duration increased marginally for lower biodiesel–diesel blends (up to B25) whereas it increased significantly for higher biodiesel–diesel blends (B50 and B100). It may be due to biodiesel has lower calorific value results in longer injection duration. In order to reduce combustion duration, a sustainable technology needs to be identified such as optimization of injection system and engine design parameters.

3.4. Analysis of performance and emission characteristics of the diesel engine for different biodiesel–diesel blends and base diesel

The brake specific energy consumption (BSEC) is calculated from the brake power output of the engine, calorific value and

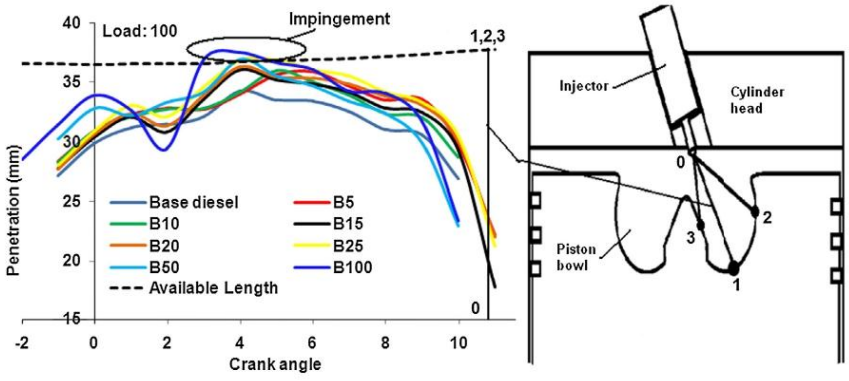

Fig. 7. Wall impingement for base diesel and biodiesel blends.

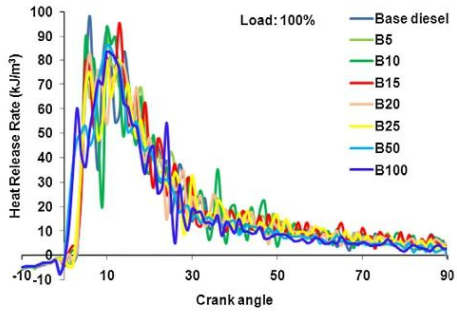

Fig. 9. Variation of heat release rate for base diesel and biodiesel blends.

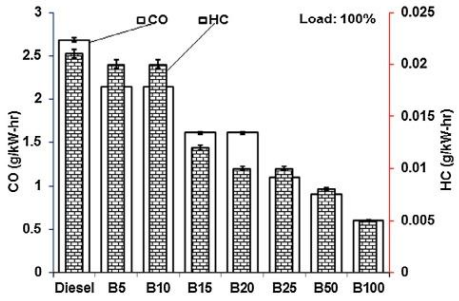

Fig. 11. Comparison of CO and HC emissions for base diesel and biodiesel blends.

the mass flow rate of the fuel. BSEC increases at lower and the rated load but it marginally decreases at 50%, 75% and 90% load (Fig. 10). The BSEC increases at lower load due to lower in-cylinder pressure and temperature. The BSEC increases with increase the biodiesel–diesel blends due to biodiesel having higher injection duration and combustion duration. BSEC increased from 12.7 MJ/kW-h with base diesel to 17.5 MJ/kW-h with B100 at the rated load. The increase in BSEC results in lower brake thermal efficiency (BTE) for biodiesel–diesel blends as compared to base diesel (Fig. 10). BTE decreased marginally with lower biodiesel–diesel blends (up to B25) whereas it decreased significantly with higher biodiesel blends (B50 and B100). It may be mainly due to biodiesel having higher density, viscosity and surface tension results in poor atomization and mixture formation (less spray cone angle) with air. It will lead to slower combustion and lower BTE. BTE at 50% and 75% loads marginally increased with all biodiesel blends as compared to diesel (within uncertainty limit). The percentage torque reduction was found to be 0.21, 0.63, 0.84, 0.9, 1.27, 2.33 and 2.76 for B5, B10, B15, B20, B25, B50 and B100 respectively as shown in Fig. 10. It is clearly seen from the figure that torque reduction is more for higher blends (B25, B50 and B100) whereas it is less for B5, B10, B15 and B20.

CO and HC emissions decreased with biodiesel–diesel blends due to higher oxygen content and lower C/H ratio (Fig. 11). The cleaner and complete combustion takes place due to oxygen content in biodiesel fuel which helps to reduce the CO and HC emissions. The automatic advancement of injection timing with biodiesel will provide more time for mixture formation resulting in decrease in CO and HC emissions. CO and HC emissions decreased from 2.68 g/kW-h and 0.02 g/kW-h with base diesel to 0.5 g/kW-h and 0.005 g/kW-h with B100 respectively at the rated load.

NOx emission increased from 6.24 g/kW-h with base diesel to 8.07 g/kW-h with B100 (Fig. 12). This is one of the major problems for use of biodiesel in diesel engine. It is due to fuel containing oxygen (10%), automatic advance in injection timing and its formation around spray periphery due to larger penetration distance. NOx emission for lower biodiesel–diesel blends (up to B20) increased marginally at all loads whereas it increased significantly for higher biodiesel–diesel blends (B25, B50 and B100) at all loads. At rated load, NOx emission increased marginally up to B15, but beyond B15, NOx emission increased significantly. In pump-line-nozzle injection system, advanced injection timing increases the residence time of fuel which results in high reaction rate and more NOx formation. The problem can be overcome using NOx reduction techniques such as exhaust gas recirculation (EGR), injection timing optimization, nozzle opening pressure, nozzle size and number of nozzle holes optimization [29].

Smoke emission decreased drastically with all biodiesel–diesel blends (B100: 15.4% opacity) as compared to base diesel (51.9% opacity) as shown in Fig. 12. It decreased due to oxygen content of the biodiesel molecule, enables more complete combustion even in regions of the fuel-rich diffusion flames in combustion chamber. Biodiesel which is an oxygenated fuel provides oxygen in the core of the spray (rich fuel) during combustion process and hence enhancing reduction in smoke formation.

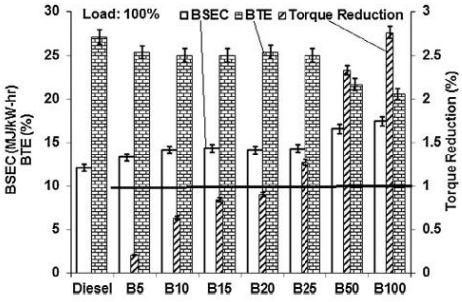

Fig. 10. Comparison of BSEC, BTE and torque reduction for base diesel and biodiesel blends.

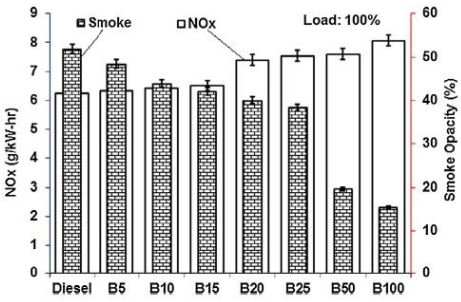

Fig. 12. Comparison of NOx and smoke emissions for base diesel and biodiesel blends.

4. Conclusions

The following conclusions are drawn based on experimental and simulation results of spray, injection, combustion, performance and emission characteristics of a diesel engine fueled with biodiesel–diesel blends with comparison of base diesel.

Dynamic injection timing (DIT) of the engine advanced at all loads for all biodiesel–diesel blends due to higher bulk modulus of biodiesel. At the rated load, the DIT advanced from 0.4° CA BTDC with base diesel to 0.7° CA BTDC and 1.5° CA BTDC with B20 and B100 respectively. Spray penetration increased with all biodiesel–diesel blends (B20: 36.28 mm, B100: 37.5 mm) than base diesel (34.28 mm) due to higher in-line fuel pressure with biodiesel. No wall impingement was observed for B5, B10, and B15 whereas wall impingement probability was observed to be critical for B20 (within uncertainty ±1.3%). However, there is more probability of wall impingement with higher biodiesel blends (B25, B50 and B100) due to higher penetration distance.

Ignition delay and rate of pressure rise (RPR) decreased with all biodiesel–diesel blends due to higher cetane number of biodiesel than base diesel. At the rated load, the peak RPR decreased from 6.7 bar/°CA with diesel to 4.3 bar/°CA and 2.2 bar/°CA with B20 and B100 respectively. The reduction of torque was observed significantly beyond B20 blends. CO, HC and smoke emissions decreased drastically from 2.68 g/kW-h, 0.021 g/kW-h and 51.9% opacity with base diesel to 0.6 g/kW-h, 0.005 g/kW-h and 15.4% opacity with B100 respectively at the rated load. NOx emission increased with all biodiesel blends as compared to diesel due to oxygen content in biodiesel, advancement in DIT, higher penetration and in-cylinder temperature. NOx emission increased from 6.24 g/kW-h with base diesel to 7.39 g/kW-h and 8.07 g/kW-h with B20 and B100 respectively at the rated load. The optimum biodiesel–diesel blend based on no wall impingement and increase in NOx emission in unmodified diesel engine is up to B15.

References

[1] Subramanian KA, Lahane S. Comparative assessment of injection, combustion, performance and emission characteristics of a diesel engine for biodiesel–diesel blends. Int J Renew Energy Tech 2013;3(4):410–29.

[2] Subramanian KA, Lahane S. Comparative evaluations of injection and spray characteristics of a diesel engine using karanja biodiesel–diesel blends. Int J Energy Res 2013;37:582–97.

[3] Choi CY, Bower GR, Reitz RD. Effects of biodiesel blended fuels and multiple injections on DI diesel engines. SAE 970218; 1997.

[4] Kegl B. Biodiesel usage at low temperature. Fuel 2007. http://dx.doi.org/10.1016/j.fuel.2007.06.023.

[5] Kegl B, Hribernik A. Experimental analysis of injection characteristics using biodiesel fuel. Energy Fuels 2006;20:2239–48.

[6] Kegl B. Numerical analysis of injection characteristics using biodiesel fuel. Fuel 2006;85:2377–87.

[7] Ejim CE, Fleck BA, Amirfazli A. Analytical study for atomization of biodiesels and their blends in a typical injector: surface tension and viscosity effects. Fuel 2007;86:1534–44.

[8] Tat ME, Gerpen JH. Measurement of biodiesel speed of sound and its impact on injection timing. Report by NREL/SR-510-31462-2003.

[9] Lahane S, Subramanian KA. Modelling and CFD simulation of effects of spray penetration on piston bowl impingement in a DI diesel engine for biodiesel–diesel blend (B20). In: Proceeding of ASME ICED Spring Technical Conference; 2012: 163–70.

[10] Gao Y, Deng J, Li C, Dang F, Liao Z, Wu Z, et al. Experimental study of the spray characteristics of biodiesel based on inedible oil. Int J Biotechnol Adv 2009;27:616–24.

[11] Sahoo PK, Das LM. Combustion analysis of Jatropha, Karanja and Polanga based biodiesel as fuel in a diesel engine. Fuel 2009;88:994–9.

[12] Rakopoulos DC. Heat release analysis of combustion in heavy-duty turbocharged diesel engine operating on blends of diesel fuel with cottonseed or sunflower oils and their bio-diesel. Fuel 2012;96:524–34.

[13] Sharma YC, Singh B, Upadhyay SN. Advancements in development and characterization of biodiesel: a review. Fuel 2008;87:2355–73.

[14] Zheng M, Mulenga MC, Reader GT, Wang M, Ting DSK, Tjong J. Biodiesel engine performance and emissions in low temperature combustion. Fuel 2008;87:714–22.

[15] Moon G, Lee Y, Choi K, Jeong D. Emission characteristics of diesel, gas to liquid, and biodiesel-blended fuels in a diesel engine for passenger cars. Fuel 2010;89:3840–6.

[16] Qi DH, Geng LM, Chen H, Bian YZH, Liu J, Ren XCH. Combustion and performance evaluation of a diesel engine fueled with biodiesel produced from soybean crude oil. Renew Energy 2009;34:2606–13.

[17] Graboski MS, McCormick RL. Combustion of fat and vegetable oil derived fuels in diesel engines. Prog Energy Combust Sci 1998;24(2):125–64.

[18] Sahoo PK, Das LM. Process optimization for biodiesel production from Jatropha, Karanja and Polanga oils. Fuel 2009;88:1588–94.

[19] Sahoo PK, Das LM, Babu MKG, Naik SN. Biodiesel development from high acid value polanga seed oil and performance evaluation in a CI engine. Fuel 2007;86:448–54.

[20] Rakopoulos CD, Hountalas DT, Zannis TC, Levendis YA. Operational and environmental evaluation of diesel engines burning oxygen-enriched intake air or oxygen-enriched fuels: a review. SAE Paper No. 2004–01-2924.

[21] Bajpai S, Sahoo PK, Das LM. Feasibility of blending karanja vegetable oil in petro-diesel and utilization in a direct injection diesel engine. Fuel 2009;88:705–11.

[22] Mahanta P, Mishra SC, Kushwah YS. An experimental study of *pongamia pinnata* L. oil as a diesel substitute. IMechE Part A: J Power Energy 2006;20:803–8.

[23] Lin B, Huang J, Huang D. Experimental study of the effects of vegetable oil methyl ester on DI diesel engine performance characteristics and pollutant emissions. Fuel 2009;88:1779–85.

[24] Caresana F. Impact of biodiesel bulk modulus on injection pressure and injection timing, the effect of residual pressure. Fuel 2011;90:477–85.

[25] No SY. Inedible vegetable oils and their derivatives for alternative diesel fuels in CI engines: a review. Renew Sustain Energy Rev 2011;15:131–49.

[26] An H, Yang WM, Chou SK, Chua KJ. Combustion and emissions characteristics of diesel engine fueled by biodiesel at partial load conditions. Appl Energy 2012;99:363–71.

[27] An H, Yang WM, Maghbouli A, Li J, Chou SK, Chua KJ. Performance, combustion and emission characteristics of biodiesel derived from waste cooking oils. Appl Energy 2013;112:493–9.

[28] Som S, Longman DE, Ramirez AI, Aggarwal SK. A comparison of injector flow and spray characteristics of biodiesel with petro diesel. Fuel 2010;89:4014–24.

[29] Lahane S, Subramanian KA. Impact of nozzle holes configuration on fuel spray, wall impingement and NOx emission of a diesel engine for biodiesel–diesel blend (B20). Appl Therm Eng 2014;64:307–14.

[30] Kuti OA, Zhu J, Nishida K, Wang X, Huang Z. Characterization of spray and combustion processes of biodiesel fuel injected by diesel engine common rail system. Fuel 2013;104:838–46.

Available online at www.sciencedirect.com

ScienceDirect

Energy Procedia 158 (2019) 1968–1973

Energy Procedia

www.elsevier.com/locate/procedia

10th International Conference on Applied Energy (ICAE2018), 22-25 August 2018, Hong Kong, China

Experimental study on the non-reacting spray characterization of gasoline compression ignition fuel

Jianguo Du[a], Balaji Mohan[a*], Jaeheon Sim[b], William L. Roberts[a]

[a]*Clean Combustion Research Center, King Abdullah University of Science and Technology, Thuwal, Makkah Province, Saudi Arabia*
[b]*Fuel Technology Division, R&DC, Saudi Aramco, Dhahran, Eastern Province, Saudi Arabia*

Abstract

Gasoline compression ignition (GCI) engines have recently become a topic of interest due to its potential for very high thermal efficiencies with significant pollution reduction. High reactivity gasoline-like fuels with shorter ignition delay and similar volatility compared to market gasoline have been identified as a viable option for the GCI engines. To fully realize the potential of gasoline-like fuels in GCI engines, spray characterization of the fuel is needed for developing a better understanding of these fuels' behavior in perspective of GCI engine applications. In this study, the spray characteristics of high reactivity gasoline-like fuel specially designed for GCI engines were investigated and compared with commercial gasoline fuel under non-reacting conditions. The new GCI fuel of RON 77 and E10 market gasoline of RON 91 were tested using a high-pressure custom-made multi-hole injector. The rate of injection, liquid and vapor penetration lengths were measured for both the fuels. It was found that the spray characteristics of GCI fuel are similar to that of the commercial E10 gasoline under non-reacting conditions.

Keywords: GCI; high reactivity low octane fuel; rate of injection; spray characteristics

1. Introduction

Gasoline Compression ignition (GCI) engines have become a popular topic among engine researchers due to its potential for very high thermal efficiencies combined with significant reduction in pollution [1]. The development of GCI engines can help obtain better NO_X-soot trade-off as well as lower fuel consumption especially with the help

* Corresponding author. Tel.: +966 54470 1875.
E-mail address: balaji.mohan@kaust.edu.sa

10.1016/j.egypro.2019.01.453

of appropriate fuels having shorter ignition delay and lower aromatic content. Therefore, there is a tremendous interest in developing gasoline-like fuels tailor-made for GCI engine applications. The fuel requirements for GCI applications are high volatility like gasoline but more reactive than the gasoline i.e., lower octane number. There are quite a few studies on using high reactivity gasoline-like fuels in GCI engine modes from our research groups in Saudi Aramco and KAUST [2–6].

The performance of internal combustion engine highly depends on liquid fuel spray atomization as this process controls the fuel evaporation rate and air-fuel mixing which in turn dictates the emission levels and engine power output. Therefore, spray characterization of fuel is significant in understanding its combustion behavior in detail [7]. For GCI applications, the required injection pressure is much higher than injection pressure of typical gasoline direct injection (GDI) injector for appropriate mixture stratification and equivalence ratio due to higher compression ratio of engine. The fuel spray atomization and air/fuel mixing controls the combustion phasing in GCI combustion modes [8]. Hence, the study of fuel spray characterization helps in better understanding the spray break-up phenomena and also provide experimental data for model development and validation. There are few spray characterization studies of high reactivity gasoline fuel under diesel like boundary conditions but no significant work has been done to characterize the spray behavior of gasoline-like fuel using gasoline multi-hole injector under GCI engine conditions [9,10]. Therefore, this study aims to characterize spray behaviors such as rate of injection, liquid length, vapor penetration under GCI engine operating conditions and create an extensive database for CFD model developments and validations.

2. Experimental setup and diagnostics

2.1. Fuel injection system

The fuel injection system used in this study consists of a commercial gasoline common rail, solenoid operated multi-hole gasoline injector and compressed air driven liquid pump. The high-pressure gasoline injector designed specifically for GCI engine application was provided by Saudi Aramco for research purposes. The injector has 10 holes of diameter 0.165 mm and an outer spray cone angle of 110°. The injector can be operated at a maximum of 500 bar injection pressure. The fuel used in this study is Aramco GCI fuel of RON 77, and commercial E10 gasoline was used for comparison.

2.2. Rate of injection rig

The rate of injection was measured by using momentum flux principle [11]. The rig shown in figure 1a consists of a chamber which can be pressurized up to 15MPa. The chamber has a provision to fit the injector and a piezoelectric force sensor on the opposite sides. The chamber provides optical access through two windows of size 35 mm in diameter and 22 mm thick placed orthogonally to the injector and the sensor. The optical access helps to capture the accurate start and end of injection events through high-speed videos. The signal from the force sensor is amplified through a charge amplifier and acquired using a DAQ card at a frequency of 100kHz. A circular target was screwed to the sensor tip to capture the entire spray jet. The gap between the injector tip and force sensor circular target was maintained at 1.5 mm. A total of 50 injections were conducted to obtain the injection rate and its standard deviation. The entire data acquisition and control were automated through an in-house LabVIEW code. The total mass of the fuel injected was measured using a mass balance for 100 injections.

2.3. Spray characterization rig

Spray characterization were conducted in a constant pressure vessel as shown in Figure 1b. The vessel is capable of operating at maximum of 1MPa pressure and 700 K temperature. To measure the actual gas temperature in the vessel, a rod with four sheathed thermocouples (probes are 12.7 mm apart) is installed through the bottom center (see Figure 1b) stretching along the vessel axis. The distance between the injector tip and the closest thermocouple probe is 10 cm. Simultaneous measurements of temperature with all probes showed that the ambient gas is thermally homogeneous in the vessel along the spray axis. Optical access was enabled by quartz windows installed on three

sides. Fuel temperature at injector tip was measured with a dummy injector based on the recommendations from the Engine Combustion Network (ECN) [12,13]. A 3 mm diameter hole is drilled through the axis of the injector, and the injector is equipped with a type K thermocouple which allows measuring the temperature in the sac volume. A water cooling house around the injector body and nozzle was implemented to prevent overheating of fuel under evaporating conditions. The fuel temperature is controlled at 90° C when ambient gas is preheated to 100° C. The injector is installed such that there are two plumes on the central vertical plane, one on the top and one on the bottom. A Mie-scatter image was taken from the front view to make sure that the plumes are aligned on the central plane as shown in Figure 2b. Injector driving current profile is shown in Figure 2a.

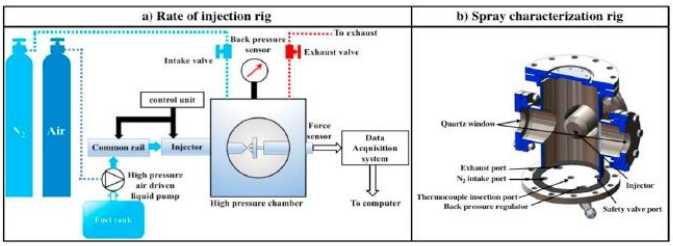

Fig. 1. Experimetnal setup (a) Schematic of rate of injection rig; (b) Cut section view of CAD model of the spray characterization rig

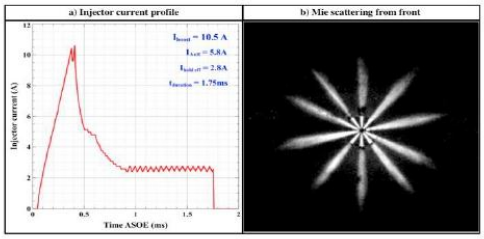

Fig. 2. (a) Injector current profile; (b) Mie-scattering from front

2.4. Imaging system

The Diffused backlit illumination (DBI) method which is based on the extinction of an incident light by the liquid-phase fuel [14] was used to characterize the liquid penetration length. The homogenous background incident light is created with a diffuser and a LED light of visible wavelength. Shadowgraph technique is employed to measure the vapor penetration length of the spray jets. The shadowgraph is the simplest form of an optical system suitable for observing flow exhibiting variation of the fluid density. The experimental setup for the DBI and shadowgraph imaging is shown in figure 3. A high-repetition rate camera (Photron SA4) was employed to capture the spray event at 20 kfps frame rate. The images were then processed with an edge recognition function in MATLAB following a threshold based binarization of the image. Detailed experimental matrix is shown in Table 1.

Table 1. Experimental conditions.

Methods	Fuel	T_{amb} (°C)	P_{amb} (bar)	T_{fuel} (°C)	P_{inj} (bar)	Duration (ms)	Repeats
Shadowgraph, DBI	Aramco GCI RON77, E10 gasoline	21 100	1, 5, 10	21 90	100, 150, 300	1.75	10

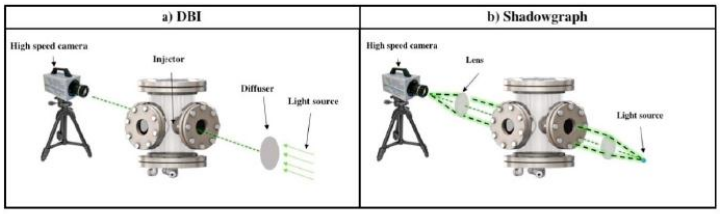

Fig. 3. Imaging system (a) Diffused back lit illumination technique; (b) Shadowgraph technique

2.5. Image processing

To find the boundary of plumes, the raw image is first converted to grayscale; and then background information is subtracted; after that, the gray image is binarized using threshold; finally, after applying a median filter, the image is ready for boundary detection. The post-processing steps are shown in figure 4. The distance between farthest point and injector tip along injector axis is regarded as penetration length. Vapor penetration and liquid penetration length were measured from shadowgraph and DBI images, respectively. Based on this definition and post-processing, the relationship between penetration length and time after the start of injection can be obtained.

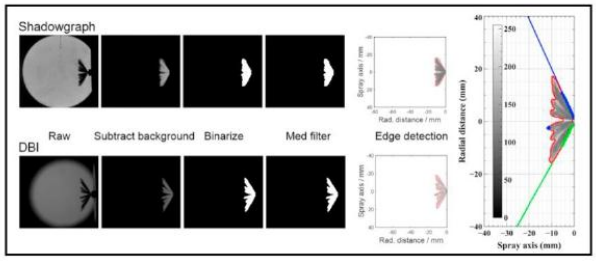

Fig. 4. Image post-processing sequence

3. Results and discussion

3.1. Rate of injection

Figure 5a shows the comparison of injection rate profile between commercial E10 gasoline and Aramco GCI fuel under non-reacting conditions. It is shown that both fuels exhibit similar rate of injection profiles under all injection pressure variations. It is also interesting to note that the hydraulic duration decreases as the injection pressure increases. This might be due to an inherent characteristic of the injector. The cumulative mass calculated from the injection rate profiles were compared with that of the total mass measured using the mass balance as shown in figure 5b. The shaded region shows a band of 8% deviation and the symbols represent the cumulative mass against the mass from the mass balance at different injections pressure keeping the injection duration constant. It can be observed that the error between the mass measurement using mass balance and the rate of injection rig falls well within 8% for all the cases reported in this study. This shows that the rate of injection obtained for both fuels was highly reliable and accurate.

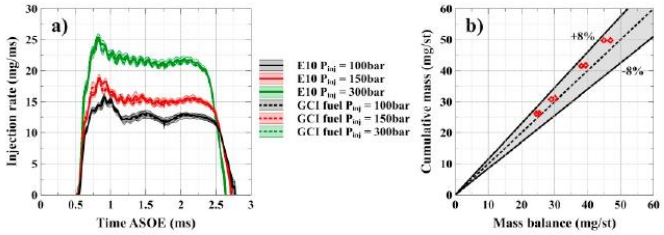

Fig. 5. Comparison of (a) the rate of injection between E10 gasoline and Aramco GCI fuel at different injection pressures; and (b) the total mass calculated from injection rate profile and measured by mass balance

3.2. Parametric variations

Comparison of different parameters' influence on penetration length is shown in Figure 6. The comparison between different injection pressures shows that higher injection pressure leads to longer penetration length. This is due to the higher momentum of the liquid. With increasing ambient gas pressure, the penetration capability is weakened.

Liquid penetration at 373 K ambient gas temperature is slightly shorter than that at room temperature of 300 K due to faster evaporation of liquid fuel. However, the ambient gas temperature at both cases are below the final boiling point (453.9K) of the fuel and the effect of evaporation rate difference is small. It should be noted that the difference in penetration is negligible among the two fuels tested in this study due to small density difference and non-reacting conditions. This can also be ascertained from the rate of injection profiles of the two fuels as shown in figure 5a. The key parameters that affect liquid spray breakup and penetration length under non-evaporating conditions are the pressure difference between injection pressure and ambient pressure, and the fuel properties like density, viscosity, surface tension and volatility. The small difference of fuel properties in these aspects results in similar spray behavior at a given injection and ambient pressure under non-reacting conditions. Figure 7 shows the transient spray boundary comparison between the two fuels under investigation. This shows that both fuel exhibit similar spray structure like its spray penetrations.

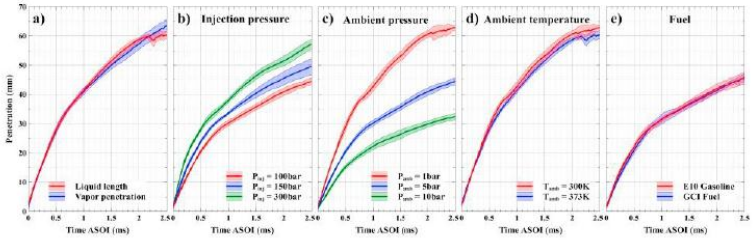

Fig. 6. Comparison of a) liquid and vapor penetration of GCI fuel and b-d) effect of injection pressure, ambient pressure, ambient temperature on vapor penetration of GCI fuel and e) effect of fuel on vapor penetration

4. Conclusions

Spray characterization of gasoline-like fuel specifically designed for GCI applications was done and compared with that of commercial E10 gasoline using a high-pressure multi-hole gasoline injector. It was found that the rate of injection of both fuels was very similar due to similar density and viscosity of fuels. It was also interesting to see the spray characteristics like liquid and vapor penetration length was similar between GCI RON 77 fuel and E10 market

gasoline fuel under non-reacting spray conditions with various ambient pressure, injection pressure and ambient temperature. This study provides valuable spray characterization of GCI fuel under non-reacting conditions and reacting spray measurement is required for complete database to cover various GCI engine operating conditions.

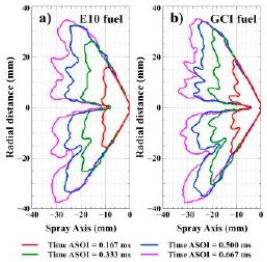

Fig. 7. Transient spray boundary evolution of a) E10 gasoline fuel b) GCI fuel

Acknowledgements

This work was sponsored by the Saudi Aramco under the FUELCOM II program and by King Abdullah University of Science and Technology.

References

[1] Zhang Y, Kumar P, Traver M, Cleary D. Conventional and Low Temperature Combustion Using Naphtha Fuels in a Multi-Cylinder Heavy-Duty Diesel Engine. SAE Int J Engines 2016;9:1021–35.

[2] Viollet Y, Chang J, Kalghatgi G. Compression ratio and derived cetane number effects on gasoline compression ignition engine running with naphtha fuels. SAE Int J Fuels Lubr 2014;7:412–26.

[3] Badra J, Elwardany A, Sim J, Viollet Y, Im H, Chang J. Effects of in-cylinder mixing on low octane gasoline compression ignition combustion. SAE Technical Paper; 2016.

[4] Zhang Y, Voice A, Tzanetakis T, Traver M, Cleary D. An Evaluation of Combustion and Emissions Performance With Low Cetane Naphtha Fuels in a Multicylinder Heavy-Duty Diesel Engine. J Eng Gas Turbines Power 2016;138:102805.

[5] Vallinayagam R, An Y, S.Vedharaj, Sim J, Chang J, Johansson B. Naphtha vs. dieseline – The effect of fuel properties on combustion homogeneity in transition from CI combustion towards HCCI. Fuel 2018;224:451–60. doi:10.1016/J.FUEL.2018.03.123.

[6] Vallinayagam R, Vedharaj S, An Y, Dawood A, Izadi Najafabadi M, Somers B, et al. Combustion Stratification for Naphtha from CI Combustion to PPC 2017. doi:https://doi.org/10.4271/2017-01-0745.

[7] Mohan B, Yang W andSiawkiang C, others. Fuel injection strategies for performance improvement and emissions reduction in compression ignition engines-A review. Renew Sustain Energy Rev 2013;28:664–76.

[8] Atef N, Badra J, Jaasim M, Im HG, Sarathy SM. Numerical investigation of injector geometry effects on fuel stratification in a GCI engine. Fuel 2018;214:580–9. doi:10.1016/J.FUEL.2017.11.036.

[9] Chang J, Viollet Y, Amer A, Kalghatgi G. Fuel economy potential of partially premixed compression ignition (PPCI) combustion with naphtha fuel. SAE Technical Paper; 2013.

[10] Mohan B, Jaasim M, Ahmed A, Hernandez Perez F, Sim J, Roberts WL, et al. Numerical Simulations of High Reactivity Gasoline Fuel Sprays under Vaporizing and Reactive Conditions. SAE Tech Pap Ser n.d.

[11] Mohan B, Yang W, Tay KL, Yu W. Macroscopic spray characterization under high ambient density conditions. Exp Therm Fluid Sci 2014;59:109–17.

[12] Payri R, García-Oliver JM, Bardi M, Manin J. Fuel temperature influence on diesel sprays in inert and reacting conditions. Appl Therm Eng 2012;35:185–95.

[13] Malbec L-M, Egúsquiza J, Bruneaux G, Meijer M. Characterization of a set of ECN spray A injectors: nozzle to nozzle variations and effect on spray characteristics. SAE Int J Engines 2013;6:1642–60.

[14] Skeen SA, Manin J, Pickett LM, Cenker E, Bruneaux G, Kondo K, et al. A Progress Review on Soot Experiments and Modeling in the Engine Combustion Network (ECN). SAE Int J Engines 2016;9:883–98. doi:https://doi.org/10.4271/2016-01-0734.

Fuel 295 (2021) 120461

Contents lists available at ScienceDirect

Fuel

journal homepage: www.elsevier.com/locate/fuel

Full Length Article

Macroscopic spray characteristics of a gasohol fueled GDI injector and impact on engine combustion and particulate morphology

Nikhil Sharma, Avinash Kumar Agarwal *

Engine Research Laboratory, Department of Mechanical Engineering, Indian Institute of Technology Kanpur, Kanpur 208016, India

ARTICLE INFO

Keywords:
Microscopic spray characterization
Shadowgraphy
MBT timing
Combustion
FE-SEM

ABSTRACT

A comprehensive understanding of renewable fuels' spray behavior leads to superior combustion and emission characteristics from internal combustion (IC) engines. This study is aimed at investigating the influence of gasoline and gasohol (E15, M15, and Bu15; 85% v/v gasoline blended with 15% v/v ethanol, methanol, and butanol) on macroscopic spray characteristics, followed by IC engine combustion characterization. Macroscopic spray investigations were performed at four different fuel injection pressures (FIPs) in a constant volume spray chamber (CVSC) for oxygenated renewable fuels vis-à-vis conventional fuels. This study was followed by engine investigations, with a focus on comparative combustion characterization for the test fuels at different load points. The engine was then optimized to find the maximum brake torque (MBT) timing for all test fuels. Towards the end, field emission-scanning electron microscopy (FE-SEM) images of soot particles were also presented along with Energy-dispersive X-ray spectroscopy (EDS) analysis to find trace metals in soot particles. Numerous studies in the open literature are available wherein researchers have shown that the presence of oxygen in fuel helps meet stringent emission legislations; however, most studies didn't investigate the effect of fuel oxygen on spray characteristics. One of the research questions debated in this manuscript is "how important is macroscopic spray characteristics, when it comes to using renewable fuels in gasoline direct injection (GDI) engines?" The database from these experimental investigations of renewable fuels may be vital in simulations of spray and combustion in the near future for developing efficient and cleaner next-generation IC engines, which is in contrast with previous researches focused on engine emissions and fuel efficiency improvement alone.

1. Introduction

As emission legislations are becoming increasingly stringent with time, a potential solution to comply with them could be either by improving internal combustion (IC) engines through improved engine design or exploring newer fuels, which contribute lesser to the air pollution [1,2]. Over the years, gasoline direct injection (GDI) engines and fuel injectors have undergone exponential improvements in delivering fuel to the engine combustion chamber at increasingly higher FIPs [3]. The need for further research in this area arose from complications in fuel-air mixture preparation at more comprehensive engine operating conditions for using renewable fuels. Several oxygenated renewable fuels (Fig. 1) are being explored for IC engine applications for transport and decentralized power generation sectors. These renewable fuels emit lower emissions because of the presence of oxygen in their molecular structure [4–8].

Alcohols are the most potent oxygenated fuels and, when blended with gasoline, lead to a higher degree of completion of engine combustion, hence lower emissions. Fig. 1 shows various oxygenated fuels as potential partial/full replacement of conventional petroleum-based fuels. Many of these alcohols are being investigated by researchers to evaluate the effect of different engine parameters such as fuel injection pressure (FIP), engine speed, and engine load on the engine performance and emission characteristics. Atilla et al. [9] investigated the effects of blending 5, 10, 15, and 20 vol% methanol with gasoline on the performance of a spark ignition (SI) engine. The authors reported that M5 exhibited the best engine performance in terms of brake mean effective pressure (BMEP), and M20 exhibited the best engine performance in terms of brake thermal efficiency (BTE). Nauwerck et al. [10] performed experiments to investigate fuel spray shape in a pressurized constant volume spray chamber (CVSC) using a multi-hole GDI injector with a nominal cone angle of 90° at FIP of up to 500 bar using gasoline as a test fuel. The authors reported that with increasing chamber pressure, spray penetration length decreased and spray width increased. However, with

* Corresponding author.
E-mail address: akag@iitk.ac.in (A.K. Agarwal).

https://doi.org/10.1016/j.fuel.2021.120461
Received 22 July 2020; Received in revised form 31 December 2020; Accepted 8 February 2021
Available online 25 March 2021

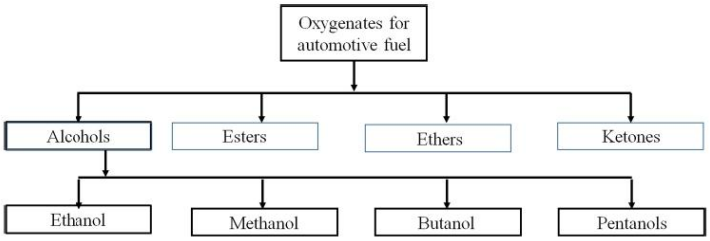

Fig. 1. Oxygenate fuel portfolio for automotive applications.

Table 1
Important properties of constituent fuels [18,19].

Properties	Gasoline	Butanol	Ethanol	Methanol
Molecular formula	C_4-C_{12}	$C_4H_{10}O$	C_2H_5OH	CH_3OH
Density @ 20 °C (g/cm^3)*	0.745	0.811	0.79	0.796
Molecular weight (Kg/Kmol)	110	74.12	46	32.04
Viscosity (mm^2/s) @40 °C*	0.6	2.544	1.08	0.59
Research octane number	95	96	108.6	108.7
Motor octane number	85	84	89.7	88.6
Cetane number	15	25	8	3
Lower heating value (MJ/Kg) *	42.7	32.7	26.8	19.9
Flash-point (°C)	−45 to −38	36	8	12
Auto-ignition temperature (°C)	300–400	343	434	470
Boiling point range (°C)	25–215	118	78.4	64.5
Oxygen content (% w/w)	< 0.05	21.6	34.8	50
Stoichiometric air/fuel ratio	14.7	11.2	9.02	6.49
Carbon content (wt. %)	86.4	64.8	52.5	37.5
Hydrogen content (% w/w)	13.6	13.6	13.1	12.5
Latent heat of vaporization (KJ/Kg)	310–320	716	920	1100
Surface tension @ 27 °C (N/m)	18.93	24.7	22.05	22.18

*Measured *at ERL, IIT Kanpur*.

Table 2
Comparison of measured important properties of blended test-fuels.

Property	Bu15	E15	M15
Calorific value (MJ/Kg)*	41.20	40.31	39.27
Density (g/cm^3) @ 30C*	0.755	0.750	0.755
Viscosity(mm^2/s) @ 40 °C *	0.891	0.672	0.598

*Measured at ERL, IIT Kanpur.

increasing chamber temperature, spray penetration length increased. Patel et al. [11] performed spray investigations of Karanja biodiesel fueled engine and reported relatively lower spray jet penetration length with increasing ambient pressure. They also reported slower spray evolution for biodiesels compared to mineral diesel. More details about spray evolution can be referred to in the open literature [12]. Chen et al. [13] investigated the effects of blending n-butanol (15, 30, and 50% v/v) with gasoline and investigated its combustion characteristics in a GDI engine. The authors reported that with increasing blending percentage of butanol in gasoline, maximum cylinder pressure (P_{max}) and heat release rate (HRR) increased, and crank angle for P_{max} advanced. Cooney et al. [14] reported that the highest P_{max} was exhibited by n-butanol (100%), probably because of faster n-butanol HRR than gasoline. In addition to this, Wallner et al. [15] performed experiments and advanced the spark timing (ST) by 5 CA for gasoline to avoid engine knocking at a higher engine load due to relatively higher octane rating of E10. Ethanol had a higher octane number than gasoline; hence the phenomenon of premature ignition was less probable. Lesser fuel atomization, dilution of engine oil, and cold-start were the significant drawbacks of using oxygenated blends/fuels [16]. Charoenphonphanich et al. [17] studied combustion behavior using pressure–time, rate of pressure rise (RoPR), and MFB data in a CVCC using 20% and 85% ethanol-gasoline blends and ethanol vis-a-vis baseline gasoline. They concluded that as the blending percentage of ethanol in gasoline increased, combustion characteristics improved. Peak HRR was higher because of acceleration in the flame evolution process. Wallner et al. [15] stated that Bu10 and gasoline were relatively more prone to knocking at higher engine loads than E10. A possible reason for such a trend could be higher flame velocity of Bu10 than E10 and baseline gasoline.

Several researchers have showed that oxygen in the test fuel helped comply with very stringent emission legislations. However, research reported in open literature on spray and combustion characteristics of renewable/oxygenated fuels in a GDI engine is somewhat limited. This investigation is therefore unique since it aims to understand the physical mechanisms involved in spray evolution and establish a relationship

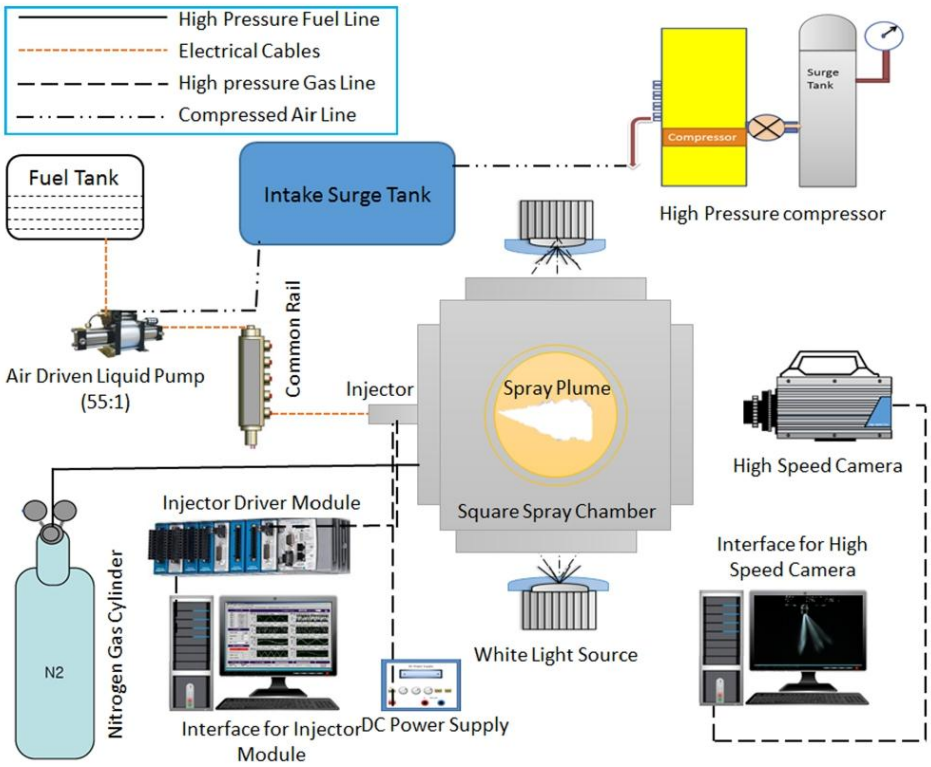

Fig. 2. Schematic of the experimental setup for macroscopic spray visualization.

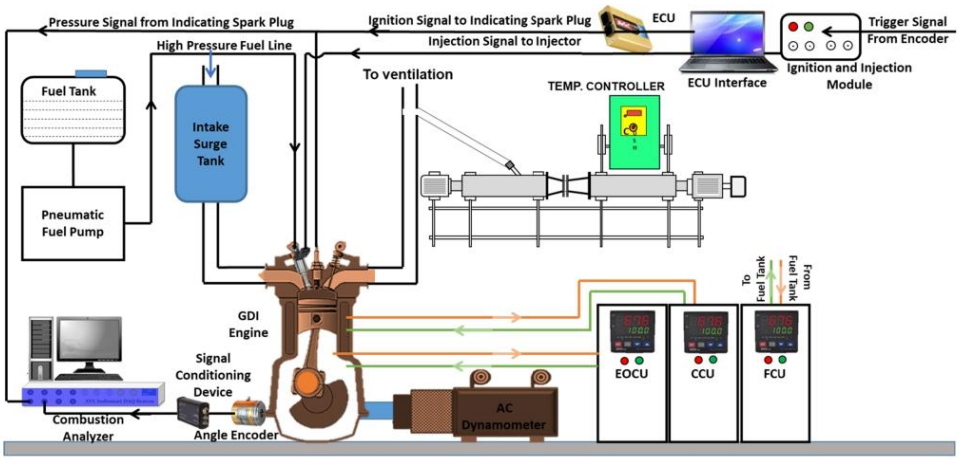

Fig. 3. Schematic of the GCI engine experimental setup.

Table 3
Technical specifications of the test engine.

Parameters	Specifications
Engine type	Gasoline Direct Injection
Number of Cylinder/s	1
Bore/Stroke	86 mm/86 mm
Compression ratio	10.5
Displacement volume	0.5 L
Connecting rod length	196 mm
Maximum power	6.28 kW @ 2000 rpm
Maximum torque	30 Nm @ 2000 rpm
Fuel injector	Six nozzle hole solenoid injector
Injector type	Direct injection
Maximum fuel injection pressure	250 bar

between macroscopic spray characteristics and combustion characteristics of the three oxygenated renewable test-fuels, namely E15, M15, and Bu15 (85% v/v gasoline blended with 15% v/v ethanol, methanol, and butanol) vis-à-vis conventional gasoline. Macroscopic spray characteristics, namely spray penetration length, spray area, and shadowgraphy images of the spray evolution, are reported in this study. GDI engine's combustion characteristics using these renewable/oxygenated were investigated, and the test engine's MBT timing was optimized. Important combustion related parameters such as in-cylinder pressure, HRR, cumulative heat release (CHR), P_{max}, maximum HRR (R_{max}), start of combustion (SoC), combustion phasing (CP), combustion duration (CD), and combustion noise for all test fuels were investigated at different engine operating conditions. Soot samples from the exhaust of the engine using different test-fuels were collected on 47 mm quartz filer papers using partial flow dilution tunnel. Field emission-transmission electron microscopic (FE-SEM) images of soot agglomerates collected on the quartz filter paper were captured. Electron dispersive spectroscopic (EDS) analysis was performed to qualitatively assess the presence of various trace metals in the soot agglomerates.

2. Experimental setup and methodology

Two experimental setups for macroscopic spray investigations and engine investigations were developed and used in this study. Four test fuels, namely gasoline, E15, M15, and Bu15, were used in this study. Important properties of constituent fuels are shown in Table 1, and the measured properties of blended test fuels are shown in Table 2.

Macroscopic spray characterization experiments were performed under non-evaporating test conditions, at ambient chamber pressure (unpressurized chamber) at four FIPs (40, 80, 120, and 160 bar). Schematic of the spray visualization experimental setup is given in Fig. 2.

The experimental setup for macroscopic spray visualization comprised of three sub-systems: (i) CVSC, (ii) fuel injection system, and (iii) spray imaging system. CVSC had optical access from all four sides via quartz windows, and a six-hole GDI injector was installed on one of the metallic side flanges, as shown in Fig. 2. The fuel injection equipment comprised of a high-pressure pneumatic amplifier pump (Hydraulic Engineering Corporation; L3-04-45), a fuel reservoir (1 L capacity), high-pressure fuel lines, and an injector driver/controller (NI; CompactRIO-9022). A standalone direct injection (SADI) system was used to control the GDI injector using CalView software interface and a direct current (DC) power supply. Two flicker-free white light sources (NaBa Green; RDL 24 W) illuminated the fuel spray and droplets, and a high-speed CCD camera (Photron; Fastcam SA1.1) was used to capture the spray evolution images in the CVSC. These images were captured using a high-speed camera at 16,000 frames per second (fps) and then analyzed to determine various macroscopic spray parameters such as the spray penetration length, spray cone angle, and spray area.

CVSC experiments were followed by GDI engine experiments, and the schematic of the engine experimental setup is shown in Fig. 3.

The test engine selected for these experiments was a 0.5L single-cylinder GDI engine (Mobiltek; GDI 0.5L) with a rated torque of 30Nm at 2000 rpm. A transient dynamometer (Dynomerk Controls; 6-2013) of 36 kW was used to motor the engine to the desired speed before conducting the experiment. Schematic of the engine experimental setup and technical specifications of the test engine are shown in Fig. 3 and table 3, respectively. An open electronic control unit (ECU) (Motec; m400) was used to change the spark timing (ST), the fuel injection timing, and the injector pulse width. This GDI injector had 6 nozzle holes. The maximum FIP achieved with the integrated pump was 250 bar. A peak and hold current driver (Zenobalti Co.; ZB-5100G) was part of the injector driver circuit. Engine oil, coolant, and fuel conditioning units (AVL; Fuel System Compact™) were also part of the engine test cell. A partial flow dilution tunnel was used to collect the particulate samples on a 47-mm quartz filter paper at a constant engine speed of 2000 rpm for further morphological investigations.

3. Experimental procedure

Spray evolution imaging at four FIPs (40, 80, 120, and 160 bar) was done in the CVSC for three gasohol blends vis-à-vis conventional

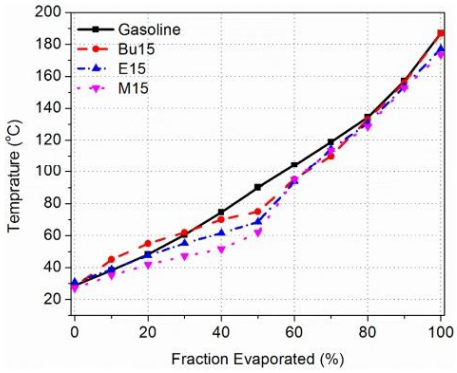

Fig. 4. Distillation characteristic curves of the test-fuels.

Table 4
Experimental test matrix.

Experiments	FIP (bar)				Load (%)						Spark Timing (°CA bTDC)				
	40	80	120	160	20	40	50	60	80	100	16	20	24	28	32
Macroscopic Spray Evolution	✓	✓	✓	✓	x	x	x	x	x	x	x	x	x	x	x
Engine Investigations	x	x	✓	x	✓	✓	x	✓	✓	✓	✓	✓	✓	✓	✓
Particulate Morphology	x	x	✓	x	x	x	✓	x	x	✓	x	x	✓	x	x

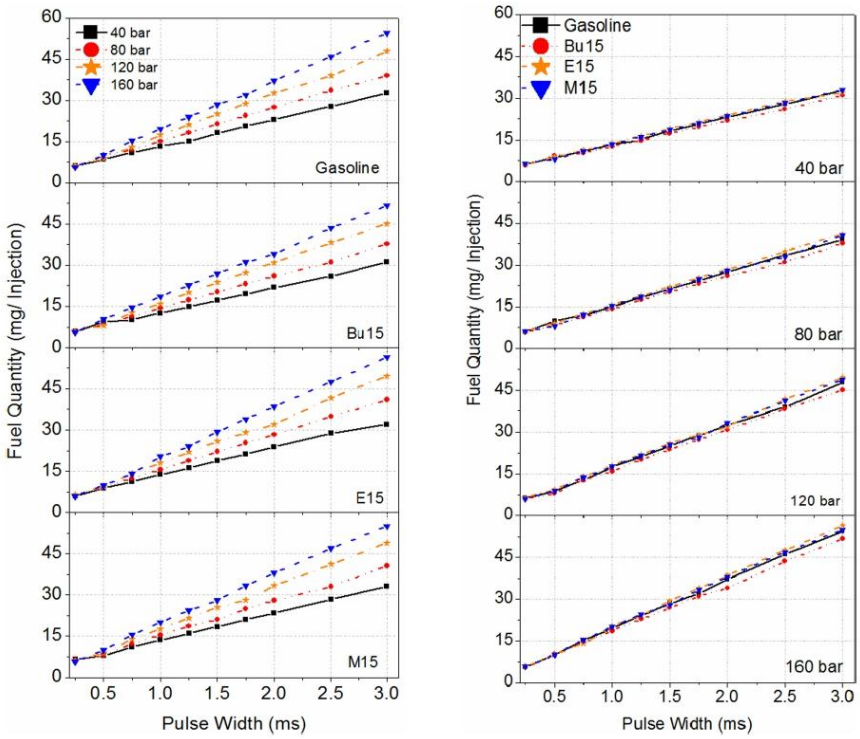

Fig. 5. Injector calibration curves showing a direct relationship between the quantity of fuel injected and the pulse width of the injector.

gasoline under non-evaporative conditions. Thereafter experimental measurements were done on an engine operating at 2000 rpm after it achieved thermal steady-state. The engine load was varied from no load to full load in steps of 20% for making the measurement of different parameters. An engine management system (EMS) from MoTeC was configured to find MBT timing. This was performed by varying the ST from 16 to 32 CA° bTDC as per the method prescribed by Heywood [19]. Optimum SoI timing of 270 CA° bTDC was used, and stoichiometric fuel–air mixture was inducted into the engine throughout the experiments. Table 4 shows the experimental test matrix.

During the engine experiments, soot was collected on a 47 mm quartz filter paper, which was conditioned and then placed inside the filter holder assembly of the partial flow dilution tunnel. Soot sample collection duration was d ~ 15 min at each engine operating condition, and exhaust gas dilution ratio was maintained ~ 15. The dilution ratio was calculated using the following formula:

$$\text{Dilution ratio (r)} = \frac{[\text{undiluted exhaust } CO_2]}{[\text{diluted } CO_2 - \text{ ambient } CO_2]}$$

Prior to soot loading, filter papers were conditioned by placing them in a desiccator for 48 h in order to remove trace moisture content, if any. After soot loading, the soot laden quartz filters were analyzed using field emission scanning electron microscopic (FE-SEM) imaging. FE-SEM (SUPRA 40VP; NTS GmbH) was used to determine the particulate morphology of the soot sample collected on the filter paper from various test fuels under varying engine experimental conditions. Soot is essentially non-conductive in nature, which may collect charge during scanning by the electron beam. Therefore particulate matter (PM) samples were made conductive by applying a thin layer of gold coating on them using a sputter coater (Mini Sputter Coater Quorum Technology; SC7620), which prevents accumulation of electrostatic charge and helps achieve excellent images. Thereafter, soot samples were mounted on a carbon tape, which was put on to the surface of the stub for imaging. Finally, images were captured at variable pressure mode operating conditions in the FE-SEM, and scanning electron micrographs were captured for further analysis.

4. Results and discussion

Results of the experiments are discussed under three headings, namely: (a) Macroscopic spray characterization; (b) Combustion characterization; and (c) Particulate morphology characterization.

4.1. Macroscopic spray characterization

Distillation curve of test-fuels and fuel quantity injected per cycle are critically important parameters, which affect the spray evolution in the engine combustion chamber, fuel-air mixing characteristics, and consequent engine combustion and emission characteristics. Therefore before performing macroscopic spray investigations and spray evolution using shadowgraphy, distillation curve of different test fuels (Fig. 4) and injector calibration for finding a relationship between the fuel quantity being injected by the fuel injector and the injector pulse width (Fig. 5) was established.

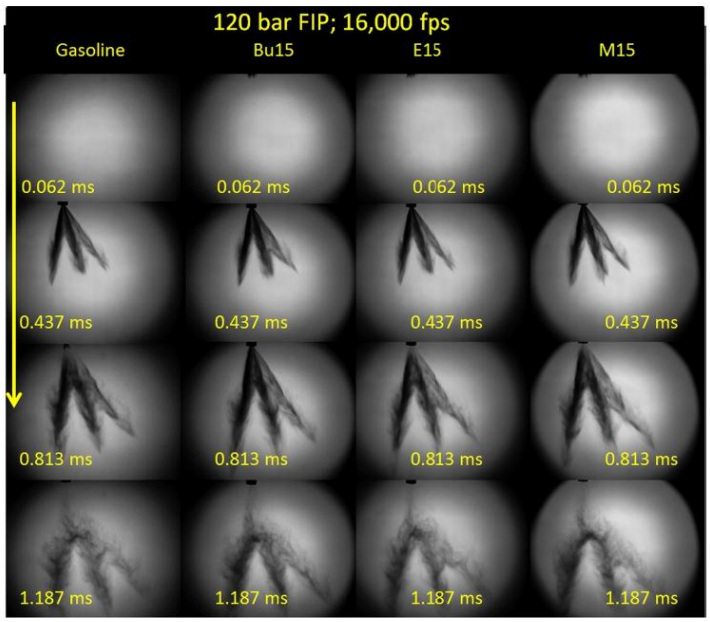

Fig. 6a. Shadowgraphy images of the evolution of spray plumes of different test fuels at 120 bar FIP.

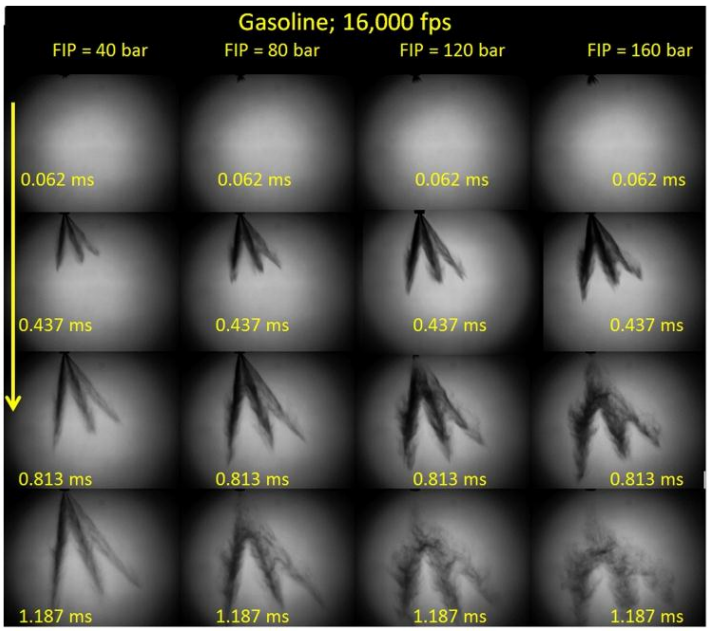

Fig. 6b. Shadowgraphy images of the evolution of spray plumes of gasoline at different FIP.

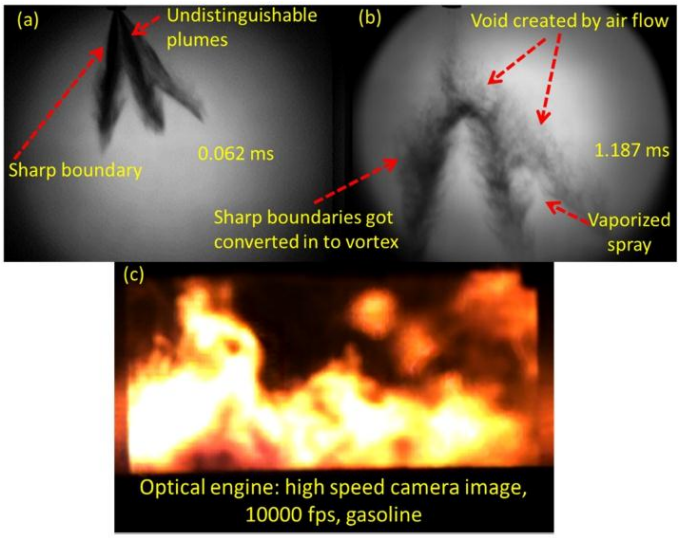

Fig. 7. Details of spray and combustion imaging.

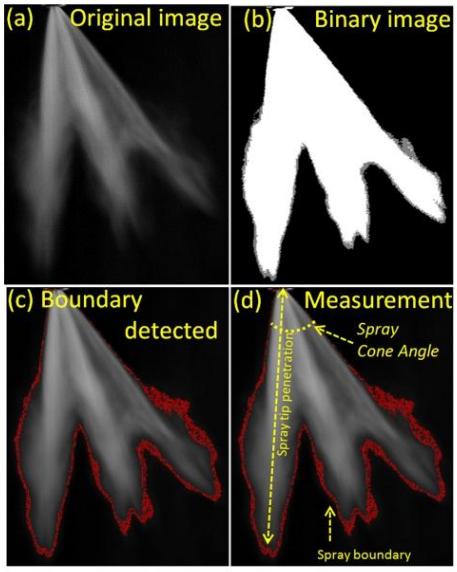

Fig. 8. Post-processing of spray images using 'Image J' software for determining macroscopic spray characteristics of gasoline spray at FIP of 160 bar.

Distillation curves for oxygenated test-fuels were below the baseline gasoline, except for Bu15. Bu15 and baseline gasoline exhibited almost similar distillation characteristics, particularly for higher fractions of the test-fuel evaporated. Presence of relatively higher oxygen content and lower boiling points of ethanol and butanol in E15 and M15 may have caused relatively earlier evaporation of lower fractions of these test fuels. All test fuels showed relatively lesser differences at lower and higher distillation temperatures, but this difference was relatively higher at intermediate fractions. This may be due to significantly higher latent heat of vaporization of primary alcohols compared to gasoline and

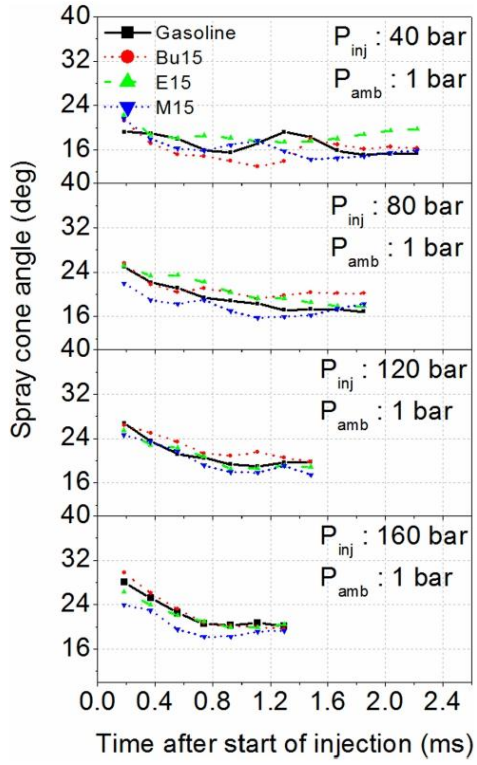

Fig. 9. Spray cone angles for gasohol at varying FIPs.

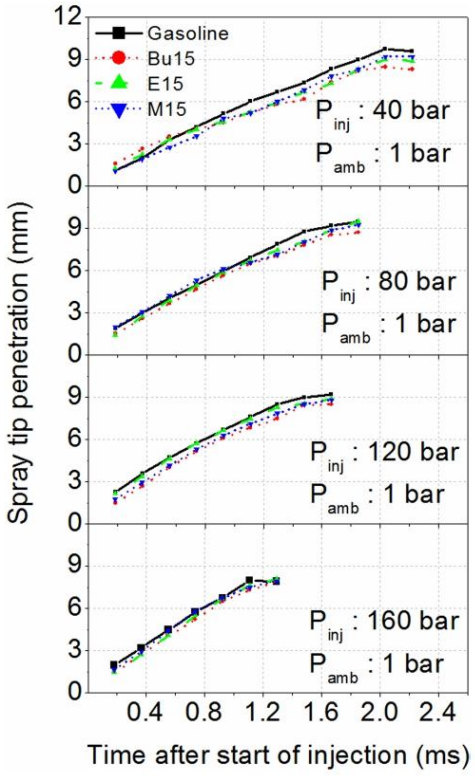

Fig. 10. Spray penetration length for gasohol at varying FIPs.

evaporation of most alcohols in the temperature range of 60–70 °C (Boiling point of primary alcohols). At higher distillation temperatures, this difference reduces to negligible levels because of complete evaporation of primary alcohols, and only gasoline remaining in the test fuel. This effect can very well be related to the HRR curves shown later in the paper (Fig. 13). In a nutshell, gasoline is a multi-component fuel with no inherent fuel oxygen; therefore, its distillation curve is characteristically different from gasohols, which contains 15% (by volume) primary alcohols. Alcohols , are single component chemicals which have a single boiling point. Different distillation curves of these test-fuels remain a critical factor responsible for different combustion behavior of these test fuels at varying engine operating conditions and these distillation curves are helpful in explaining the results of engine combustion better.

Fig. 5 shows the quantity of fuel injected at different pulse widths of the injector at four different FIPs. Mass of fuel injected in 1000 injections was weighed using a precision weighting balance, and the injection pulse width was varied from 0.2 to 3 ms. The average fuel quantity injected in each injection event was plotted for different pulse widths at different FIPs. To avoid measurement errors, each measurement was repeated thrice, and the average value was used for the injector calibration curves. For a pulse width of $\leq$ 0.5 ms, slightly irregular trends for all test fuels were obtained. However, beyond 0.5 ms pulse width, the trends were consistent and fairly linear. The injector calibration curves are important for ensuring that different test fuels with an injection of a different mass of fuel deliver the same fuel energy per injection. Thereafter, spray experiments for all test fuels were carried out for macroscopic characterization using the shadowgraphy technique, and the results of these tests are discussed in the next section.

Fig. 6(a) shows a comparative spray evolution of test fuels at ambient conditions and FIP of 120 bar. Fig. 6(b) shows spray evolution of gasoline at FIPs of 40, 80, 120, and 160 bar. Shadowgraphy was performed (for the side view) with the first appearance of fuel droplets out of the injector at 0.062 ms. In Fig. 6(a), sharp spray boundaries were visible up to 0.437 ms for all test fuels. Spray plume evolution gradually stabilized at 0.437 ms. Beyond this time, sharp spray boundaries got blurred due to vortex structures, and then spray droplets mixed with ambient air in the immediate vicinity of the spray plumes. The occurrence of these structures is rather stochastic, regardless of the test fuel used. Such a condition is highly desirable since most fuel droplets mix with ambient air, and higher surface area of droplets available encourages superior fuel vaporization and their consequent mixing with the ambient air.

Spray shadowgraphy details are shown in Fig. 7, which are helpful in understanding Fig. 6(a) and Fig. 6(b). The injected fuel starts vaporizing from the spray plume surface after the secondary spray breakup. Once the fuel vaporizes, the vapor phase expands in volume and loses its momentum due to energy exchange with the surrounding air. Due to this, the fuel vapors are pushed sidewise by the trailing spray droplets. Therefore, most fuel vapors were observed at the sides of the spray

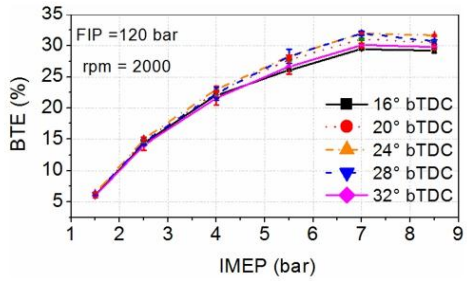

Fig. 11. BTE vs. IMEP curve of gasoline-fueled GDI engine at varying STs at FIP of 120 bar at 2000 rpm engine speed.

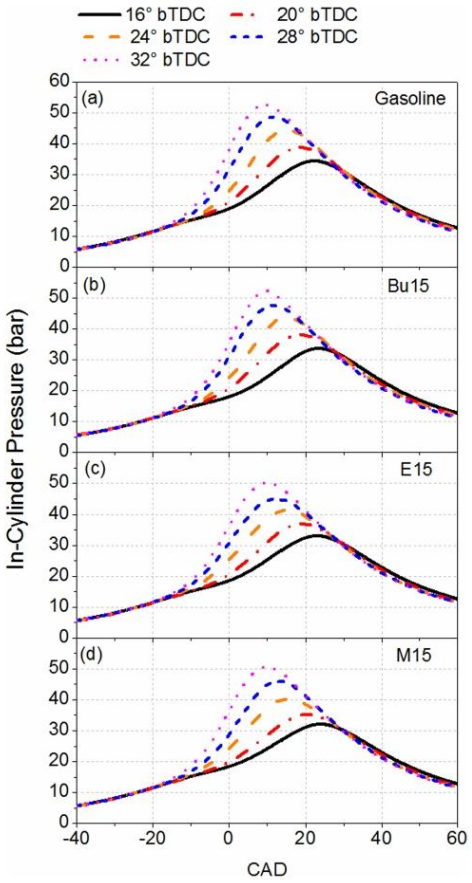

Fig. 12. In-cylinder pressure variations vs. crank angle curve at varying STs for different test fuels in the GDI engine of 120 bar FIP at 2000 rpm engine speed.

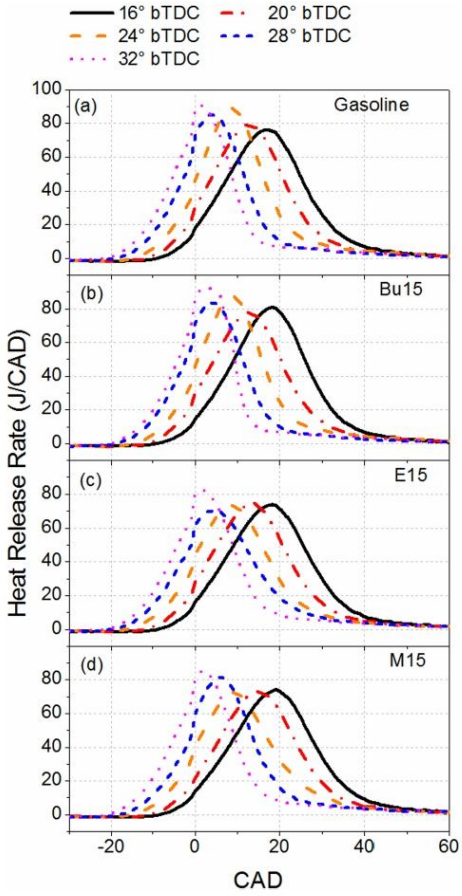

Fig. 13. HRR variations vs. crank angle curves at varying ST for different test fuels in GDI test engine.

plumes in the early stage of the injection event up to 0.813 ms. Vaporization proceeds from the periphery of the plume, and its degree of completion depends on the FIP, as seen in Fig. 6(b). The edges seem "evenly inhomogeneous," and the plumes are hardly distinguishable at 1.187 ms after the start of injection. Differences in the images at the same FIP but different test fuels were largely attributed to kinematic viscosity and surface tension of the test fuel. It is observed that the differences in sprays with changing FIP were more dominant than that due to changing test fuels. As the FIP increased, the boundaries tend to disappear. For lower FIP of 40 bar, the spray boundaries were observed to be quite sharp in all shadowgraphy images taken from 0.062 ms to 1.187 ms after the start of injection, as seen in Fig. 6(b). As the FIP increased, this sharpness of boundaries reduced, and vortices were observed on these boundaries (e.g., at FIP = 160 bar at 0.813 and 1.187 ms). These results indicate that changing FIP significantly changes the spray plume structure. It is expected that there would be a corresponding change in the fuel–air-mixing characteristics and consequent

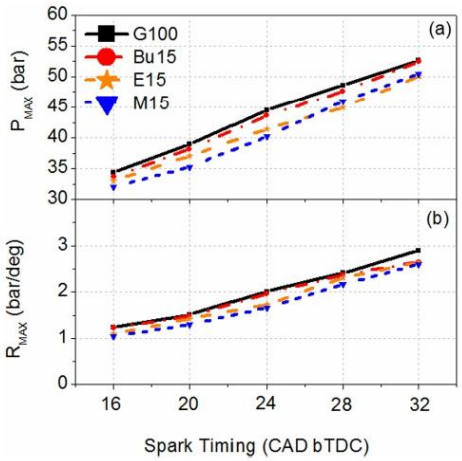

Fig. 14. P_{max} and R_{max} of different test fuels at varying STs.

changes in engine combustion and performance characteristics since larger spray droplets and ligaments get atomized further into finer droplets at higher FIPs, leading to superior vaporization and consequently improved fuel–air mixing.

With the above understanding of the spray plume boundaries and different parameters affecting it, the next step is to calculate macroscopic spray characteristics such as spray penetration length and spray cone angle at different FIPs. All these experiments were carried out at FIPs of 40, 80, 120, and 160 bar with the fuel spray under ambient conditions. In order to determine macroscopic spray characteristics, spray images were captured using a high-speed camera and were post-processed using 'Image J' software. Important steps involved in the post-processing of captured images are shown in Fig. 8.

Fig. 8(a) shows a shadowgraphy image of gasoline spray plumes at a FIP of 160 bar. This image was subsequently converted into a binary image (Fig. 8(b)). Here, the pixel value of the background region was represented as "0," and the spray region was represented as "1". After separating the background and the spray regions, boundary pixels of the spray were identified (Fig. 8(c)). To obtain images with lesser background noise and enhanced spray boundary, appropriate filters in the software were used. The enhanced image (Fig. 8(d)) was then used for determining the macroscopic spray characteristics, namely, spray tip penetration and spray cone angle. The macroscopic spray parameters were then plotted and discussed in Figs. 9 and 10.

Fig. 9 shows the temporal evolution of spray cone angle corresponding to E15, M15, and Bu15 vis-a-vis gasoline at four FIPs (40, 80, 120, and 160 bar) in the ambient environment. The evolution of the spray cone angle is highly dependent on the 'time after the start of injection' and is also dependent on the FIP. The research question to be answered is 'the importance of comparative spray cone angle in combustion for different test fuels'. At lower FIPs (40 and 80 bar), the spray cone angle was relatively lower than higher FIPs (120 and 160 bar). At higher FIPs, the spray cone angle increased, which resulted in broader sprays compared to lower FIPs. Spray cone angle obtained at FIPs of 80, 120, and 160 bars were relatively more stable and exhibited a consistent trend compared to 40 bar FIP. This was due to pneumatic pump characteristics. These pumps, when operated at significantly lower FIP, tend to exhibit relatively lower stability. Increased spray cone angle was mainly due to longer spray tip penetration. These trends were identical for all test fuels. Spray cone angle for M15 corresponding to FIP of 80, 120, and 160 bar appear to be the lowest among all test fuel. Different

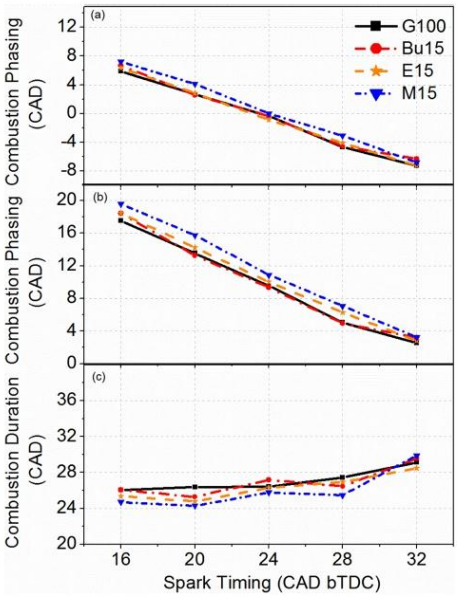

Fig. 15. SoC, CP, and CD for different test fuels at varying STs.

spray cone angles at different FIPs and different test fuels affect the radial distribution of spray droplets. It is an indicator of the extent of air entrainment in the spray plume. Wider is the spray cone angle; superior is the fuel–air mixing. A wider spray cone angle encourages more homogeneous fuel–air mixture formation. In a GDI engine, higher FIP results in superior fuel spray atomization, which improves the fuel–air mixing. On the other hand, too high FIP may lead to spray impingement on the cylinder walls. Overall, it seems that FIP is a dominant factor, when it comes to 'evolution of spray cone angle,' and the effect of different test-fuels is almost negligible compared to varying FIP. At the same FIP, the effect of the fuel type is not distinguishable and should not affect combustion. This would be discussed in greater details in the subsequent section on 'combustion characterization.'

Fig. 10 shows the spray penetration length of different test fuels at varying FIPs. As seen in this figure, spray evolves in a relatively shorter time with increasing FIP for all test fuels. Also, relatively higher FIP resulted in a larger number of smaller droplets, which increased the surface area available per unit mass of fuel injected. This helps spray droplet vaporization due to the availability of larger surface area for heat exchange. In general, spray tip penetration increases with increasing FIP for specific pulse width.

At FIP of 160 bar, spray jet penetrations for fully developed sprays were 79 mm for gasoline, 79 mm for Bu15, 80 mm for E15, and 79 mm for M15. At FIP of 40 bar, spray jet penetrations of fully developed sprays were 96 mm for gasoline, 83 mm for Bu15, 89 mm for E15, and 92 mm for M15. At lower FIPs, the spray was fully developed with a much higher pulse width, in contrast to higher FIPs. At a higher FIP of 160 bar, the difference in spray jet penetration length between the test fuels reduced, whereas, at a lower FIP of 40 bar, the difference amongst different test fuels was comparatively higher. Similar to the spray cone angle, spray tip penetration length may not necessarily play an important role for different test fuels, especially at higher FIPs (160 bar).

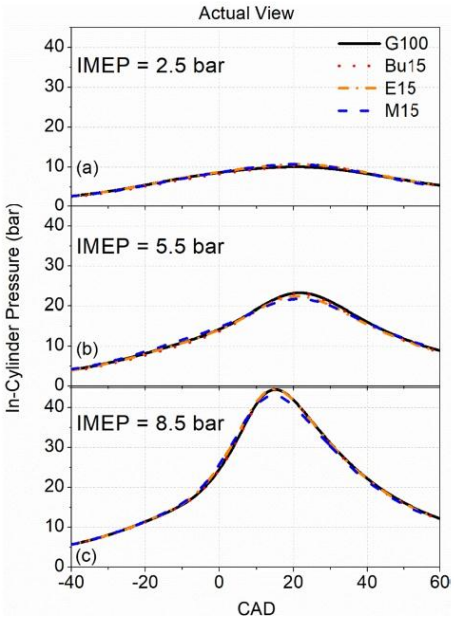

Fig. 16a. Pressure-crank angle curves for different test fuels at varying engine loads.

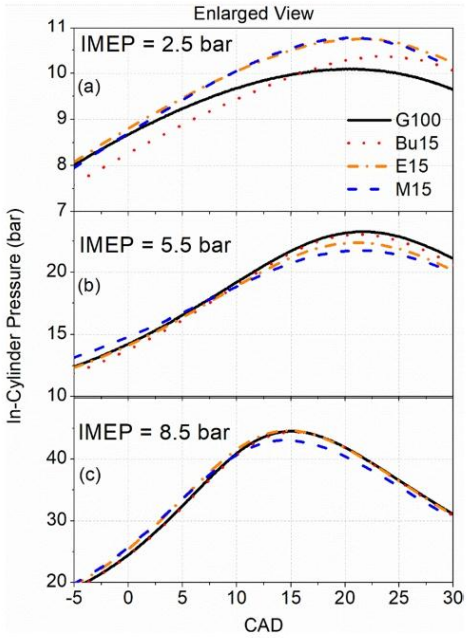

Fig. 16b. Enlarged view of pressure-crank angle curves for different test fuels at varying engine loads.

4.2. Combustion characterization

Optimum ST plays a critical role in SI engine combustion and affects their emissions and performance [19]. In order to minimize emissions and the engine knock, spark retard or knock margin technique were experimentally investigated here. Heywood and others have described this technique in detail [19,20], and the same has been implemented in these experiments. An attempt has been made to correlate results from the macroscopic spray investigation to the engine combustion characteristics for different test fuels used in this study.

Fig. 11 shows the BTE vs. IMEP curves for gasoline-fueled GDI engine at different STs varying from 16 to 32° bTDC in steps of 4° CA. BTE increased in the following sequence: 16, 32, 20, 28, 24°bTDC. The lowest BTE was observed for 16° bTDC ST, and the highest BTE was observed for 24°bTDC ST. For 24° bTDC ST, ignition of the fuel–air mixture takes place sufficiently early in the power stroke in order to extract the maximum power output. The spray cone angle and vortex from the spray images can be correlated to this trend at 24°bTDC. As seen in Figs. 6 and 7 (spray images), sharp boundaries get converted into a vortex and enhance the mixture formation process in the CVSC at atmospheric conditions. At 24°bTDC, most fuel droplets mix with ambient air, creating a high surface area per unit mass of fuel injected, which permits superior fuel vaporization. A wider spray cone angle encourages more homogeneous mixture formation, which leads to higher BTE of the engine.

Fig. 12 shows variations in the in-cylinder pressure w.r.t. crank angle degrees (CAD) at different STs. Advancing the ST resulted in relatively higher peak in-cylinder pressure and relatively earlier peak in-cylinder pressure (P_{max}). The flame evolution period shortened, whereas the flame propagation period prolonged with advanced STs. Too advanced ST (32° bTDC) slowed down the upward movement of the piston due to earlier SoC and pressure buildup, which acted against the piston movement. On the other hand, too retarded ST led to relatively lower peak pressure on the piston due to retarded combustion (16° bTDC), hence in both cases, the work done by the burning gases on the piston would reduce, lowering the BTE of the engine. As the ST advanced, peak in-cylinder pressure increased and vice-versa.

Fig. 12 showed that for 24° bTDC ST, P_{max} was positioned at 16° aTDC. For 24° bTDC ST, ignition of the fuel–air mixture takes place sufficiently early in the power stroke. By doing so, the maximum power is extracted by the piston movement. Since most fuel was gasoline (>85%) in all test fuel blends, there was a relatively very low difference in the pressure-crank angle diagrams of oxygenated fuels vis-à-vis gasoline. However, the effect of oxygenated test fuels on the HRR and CHR curves was quite significant, as seen in Fig. 13.

Fig. 13 shows the variations of the HRR vs. crank angle at different STs. Advancing ST promoted more charge to burn closer to the top dead center (TDC) during the expansion/power stroke, leading to higher HRR. Retarded ST delayed the combustion, which was clearly noticed in the HRR curves. P_{max} slightly reduced with increasing oxygen content in the test fuels. This happened due to two reasons. The first reason was the relatively lower blending ratio of oxygenate (15% v/v) in gasohol, which contributed not so significantly. The second reason was the higher latent heat of vaporization of gasohol (as discussed in Fig. 3), which reduced the peak combustion temperature due to the charge cooling effect [21–24]. Negative HRR was observed for all test fuels due to the charge cooling effect during the ignition delay period. HRR becomes positive only after the SoC.

Fig. 14 shows the variations in the P_{max} and R_{max} for different test fuels at different STs. Both P_{max} and R_{max} increased with advancing ST

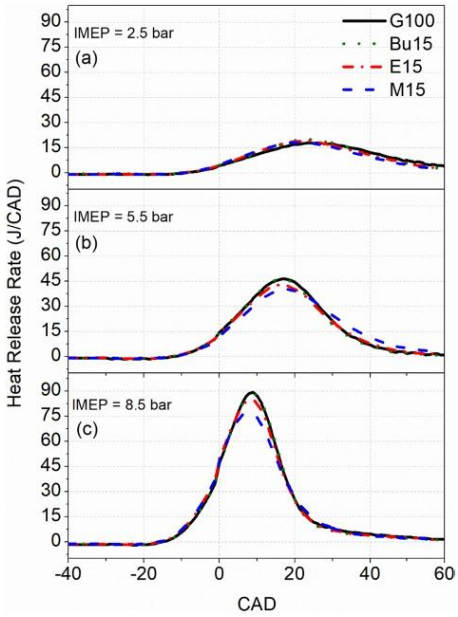

Fig. 17. HRR vs. crank angle curves for different test fuels at varying engine loads.

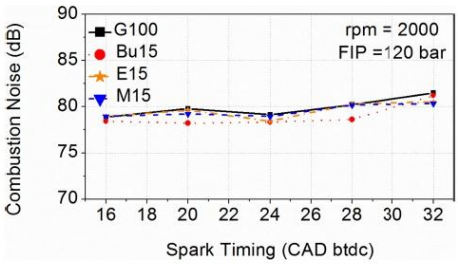

Fig. 18. Combustion noise from different test fuels at varying STs.

and reduced with increasing oxygen content in the test fuels. This could be possibly due to increased turbulence in the combustion chamber and faster fuel-air mixing at increased engine speed, leading to higher HRR. P_{max} was higher for gasoline, followed by Bu15, E15, and M15. Fuel-air mixture reactivity played an important role in combustion because increasing oxygen content of the test fuel led to increased latent heat of vaporization, which absorbed part of combustion generated heat. This reduced the rate of chemical reactions, leading to lower P_{max} and R_{max}. R_{max} reached up to ~ 3 bar/CAD at 32 °bTDC, and the minimum value of R_{max} was ~ 1 bar/CAD at 16° bTDC.

Fig. 15 shows the variations in SoC, CP, and CD for different fuels at varying STs. Crank angle position for 10% CHR (CA_{10}) is referred to as 'SoC.' SoC is dependent on ST and inherent oxygen content of the test fuel. Oxygenated fuels showed relatively retarded SoC compared to baseline gasoline due to relatively slower fuel–air mixture combustion kinetics. The presence of moisture traces in methanol and ethanol also reduced the fuel–air mixture combustion kinetics, resulting in retarded SoC. Crank angle position for 50% CHR (CA_{50}) is taken as 'CP.' CP is a measure of overall CD in an engine cycle. CP is directly linked to combustion efficiency. Combustion efficiency decreased for advanced CP as well as for retarded CP. Increasing fuel oxygen content resulted in retarded CP. CP for Bu15 and gasoline were nearly identical. Crank angle position for 90% CHR (CA_{90}) is referred to as the end of combustion (EoC). CD is estimated by subtracting EoC and SoC and is represented in °CA. As seen in the literature and observed in these experimental results, CD was relatively shorter for oxygenated fuels due to their higher laminar flame velocity compared to baseline gasoline [25–27]. In GDI engine combustion of all these test fuels, advanced ST resulted in longer CD and vice-versa. Retarded ST reduced the flame speed in the engine combustion chamber, but it increased the temperature at the end of the compression stroke, which affected the flame speed, and reduced the CD.

Fig. 16(a) shows the variations in the in-cylinder pressure vs. crank angle curves for different test fuels at varying engine loads, and Fig. 16 (b) shows an enlarged view of Fig. 16(a). As expected, P_{max} increased with increasing engine load. Among different test fuels, no significant variations were observed at lower engine loads. However, at higher engine loads, M15 exhibited relatively lower P_{max}. These results can be correlated very well with the HRR curve shown in Fig. 17.

Fig. 17 shows the variations in the HRR vs. crank angle for different test fuels at varying engine loads. The variations in the HRR curve for different test fuels were negligible because the energy content of fuel injected per cycle was identical. Amongst the test fuels, M15 showed slightly lower peak HRR. It was noticed that HRR shifted slightly towards the TDC with increasing engine load. A negative HRR curve was also noticed due to the charge cooling effect of spray droplets. HRR is largely affected by the physical properties of test fuels, including inherent fuel oxygen content. Premixed oxygenates in the test fuel improve the engine combustion [7,28].

Combustion noise is strongly influenced by the engine's combustion characteristics. These combustion characteristics depend on various engine operating parameters such as ST, engine speed, FIP, and so on. In this study, combustion noise was calculated from the cylinder pressure-crank angle data.

Combustion noise is attributed to the changes in the cylinder pressure, which makes the engine cylinder "breathe"; thus, noise is radiated outwards from the outer surface of the engine. To calculate this noise (in dB), first, a structural attenuation filter was applied to the spectrum of cylinder pressure data. This filter accounts for the stiffness of the engine cylinder. Post application of this filter, the noise spectrum was A-weighted. Fig. 18 shows the variations in combustion noise at different STs. Oxygenated fuels showed relatively lower combustion noise due to relatively lower HRR. For baseline gasoline, combustion noise was relatively higher, which was due to relatively earlier SoC. Earlier combustion caused a pressure rise before the TDC; hence more work was required to compensate for this loss. Unsteady flow processes in the engine combustion chamber and increased cylinder pressure rise rate were the possible sources of this combustion noise. Combustion noise also fluctuated, when engine operating conditions such as ST, engine speed, and FIP changed. As discussed in the previous graphs, HRR for gasohol was relatively lower; hence the combustion noise was also relatively lower. Fluctuations in the HRR in the engine combustion chamber was responsible for high-frequency combustion noise as well. Methanol fuelled engine also exhibited increased unregulated emissions. Regulated and unregulated gaseous emissions from these test fuels have been explored in another paper from our group [29].

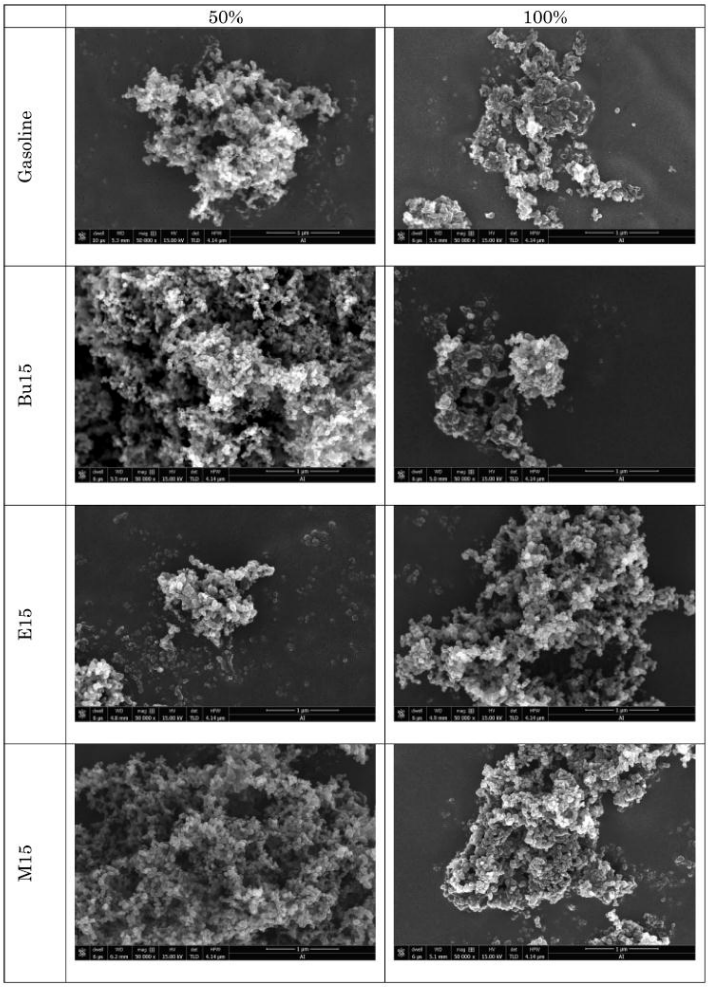

Fig. 19a. FE- SEM images of particulates collected from a GDI engine using different test fuels at 50,000x magnification at 50 and 100% engine load.

4.3. Particulate morphology characterization

Figs. 19a, b show the FE-SEM images of particulates collected from a GDI engine using different test fuels at 50,000× and 400,000× magnification at 50 and 100% engine load, and Fig. 19(c) shows energy dispersive X-Ray spectroscopy (EDS) of soot particulates. FE-SEM images showed that soot particle boundaries were overlapping with each other, and no clear individual particle boundaries were seen. However, one could distinguish between the boundaries of primary particles, which were on the top layer/ surface. A clear difference in particle concentration and agglomeration was seen in FE-SEM images of gasohol vis-à-vis baseline gasoline-fueled engine. Gasoline origin particulates were relatively less agglomerated, and the lump of these particulates was relatively smaller than gasohol origin particulates at all engine loads. This may be due to the agglomeration of soot particles, which formed coherent structures either in the combustion chamber or in the exhaust manifold before the sampling. In all particulate samples, light and dark contrast was clearly visible at both magnifications. It was observed that most particles were not perfectly spherical, and a chain-like structure was formed by some of these particles. Oxygenated fuels had a significant effect on the soot morphology and reactivity because more reactive soot particles tend to burn at the boundaries. Relatively higher fuel quantity injected at higher engine loads may have resulted in increased soot concentration from oxygenated fuels. Higher in-cylinder temperature and pressure in the combustion chamber are responsible for reducing soot particle size distribution and for agglomeration.

Trace metals have been investigated earlier also and its results are shown in the open literature, which indicate that trace metals play a

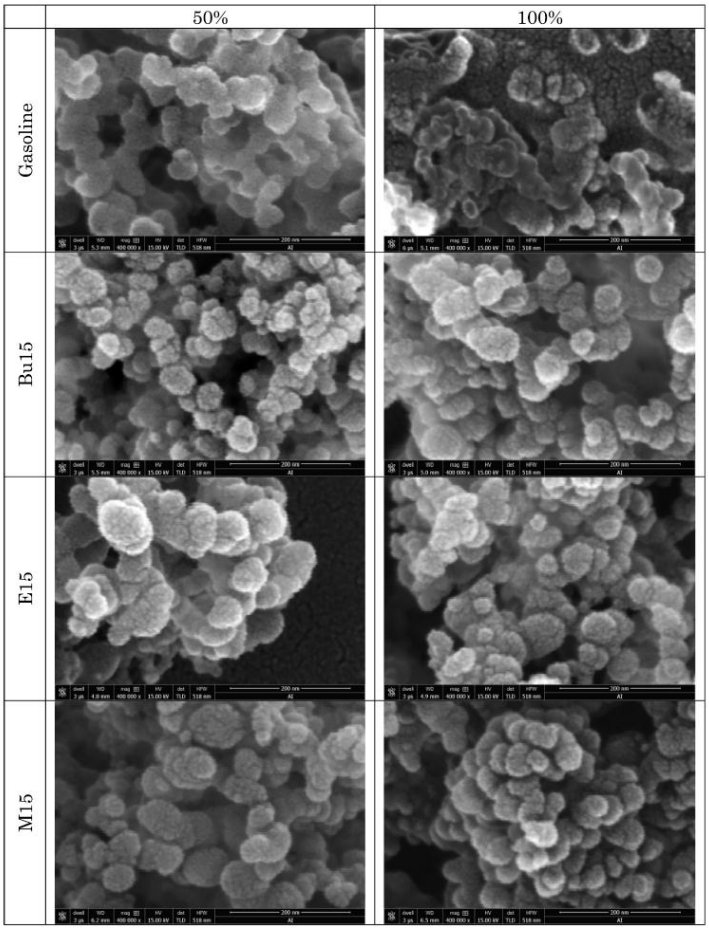

Fig. 19b. FE- SEM images of particulates collected from a GDI engine using different test fuels at 400,000x magnification at 50 and 100% engine load.

vital role in understanding the composition of soot [30,31]. EDS was used to quantitatively detect the elemental composition of particulates. EDS spectra were collected for 50s to minimize the influence of radiation exposure and potential beam damage. It is important to investigate trace metals in particulates because they can enter the human respiratory system and can possibly cross the cell membrane to cause greater damage to the human health. There are three key sources of trace metals in the particulates. The first is the fuel, the second is the organo-metallic additives of the lubricating oil used for enhancing its desirable properties, and the third is the engine wear debris. Table 5 shows important elements detected by EDS from the FE-SEM images of the soot particles. In all these soot samples, C and K were found in the highest concentration. Therefore they exhibited the highest peak in the EDS spectra. Similar results are reported in the open literature [31] as well. The trace metals may look the same in different test fuels, but they vary in distribution among different test fuels. This could be because of the fact that a minimum of 85% gasoline was still present in each test fuels, which may have contributed to distinguishable trace metal distributions in these particulate spectra.

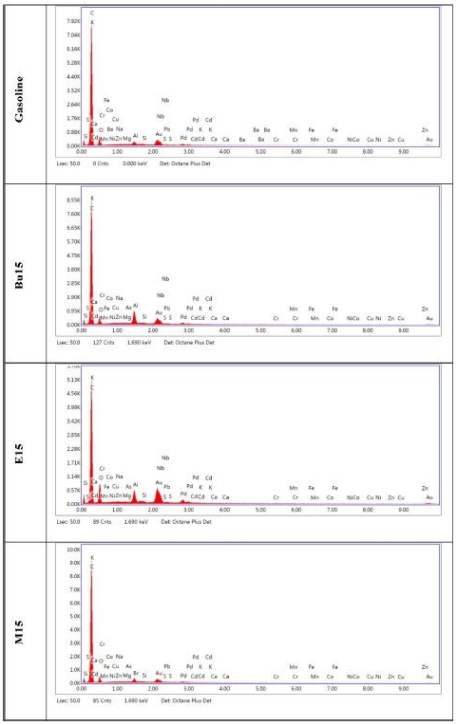

Fig. 19c. EDS for test fuels at different engine loads.

Table 5
Trace metals in particulates.

Test Fuel	Trace metals
Gasoline	Al, Au, Ba, C, Ca, Cd, Co, Cr, Cu, Fe, K, Mg, Mn, Na, Nb, Ni, O, Pb, Pd, Si, Zn
Bu15	Al, As, Au, C, Ca, Cd, Co, Cr, Cu, Fe, K, Mg, Mn, Na, Nb, Ni, O, Pb, Pd, S, Si, Zn
E15	Al, As, Au, C, Ca, Cd, Co, Cr, Cu, Fe, K, Mg, Mn, Na, Ni, O, Pd, S, Si, Zn
M15	As, Au, Br, C, Ca, Cd, Co, Cr, Cu, Fe, K, Mn, Na, Ni, O, Pb, S, Si, Zn

5. Conclusions

Few important conclusions from this study involving macroscopic spray, combustion, and particulate morphology characterizations of gasohol fueled GDI engines are as follows: FIP was a dominant factor, which affected the spray cone angle and spray penetration length to a great degree, in comparison to different test fuels and pulse widths. The variations among different test fuels at the same FIP was insignificant. At relatively higher FIPs, spray cone angle increased, which resulted in broader sprays compared to lower FIPs. As a result, a wider spray cone angle produced a more homogeneous fuel–air mixture. The test engine was optimized for ST, and 24° bTDC was found to be optimum ST. Both P_{max} and R_{max} increased with advancing ST and reduced with increasing oxygen content of the test fuels. Gasohol was found to have relatively lesser combustion noise because of a relatively longer ignition delay. In addition, combustion noise correlated very well with HRR and CHR curves. PM morphology changed with engine operating conditions; however, some key similarities and differences among PM emitted from different test fuels were observed in this study.

Overall, the results of this investigation offer new technological insights to oxygenated fuel operated GDI engine developers and help understand the effect of spray characteristics of these oxygenated fuels on engine combustion and particulate morphology, compared to conventional gasoline.

CRediT authorship contribution statement

Nikhil Sharma: Data curation, Formal analysis, Investigation, Writing - original draft. **Avinash Kumar Agarwal:** Conceptualization, Methodology, Project administration, Resources, Supervision, Validation, Writing - review & editing.

Declaration of Competing Interest

The authors declare that they have no known competing financial interests or personal relationships that could have appeared to influence the work reported in this paper.

References

[1] Sharma N, Agarwal AK. Particle characterization of soot aggregates emitted by gasohol fueled direct injection engine. Energy Fuels 2018;33(1):420–8.
[2] Sharma N, Agarwal AK. Effect of the fuel injection pressure on particulate emissions from a gasohol (E15 and M15)-fueled gasoline direct injection engine. Energy Fuels 2017;31(4):4155–64.
[3] Su T, Chang C, Reitz RD, Farrell P, Pierpont A, Tow T. Effects of injection pressure and nozzle geometry on spray SMD and DI emissions. SAE Int J Fuels Lubr 1995;4 (0148–7191):975–84.
[4] Agarwal AK, Shukla PC, Gupta JG, Patel C, Prasad RK, Sharma N. Unregulated emissions from a gasohol (E5, E15, M5, and M15) fuelled spark ignition engine. Appl Energy 2015;154:732–41.
[5] Maurya RK, Agarwal AK. Experimental investigations of particulate size and number distribution in an ethanol and methanol fueled HCCI engine. J Energy Res Technol 2015;137:(1).
[6] Gupta JG, Agarwal AK, Aggarwal SK. In Particulate emissions from Karanja biodiesel fuelled turbocharged CRDI SUV engine, ASME 2014 Internal Combustion Engine Division Fall Technical Conference, 2014; American Society of Mechanical Engineers Digital Collection; 2014.
[7] Yanju W, Shenghua L, Hongsong L, Rui Y, Jie L, Ying W. Effects of methanol/gasoline blends on a spark ignition engine performance and emissions. Energy Fuels 2008;22(2):1254–9.
[8] He X, Ratcliff MA, Zigler BT. Effects of gasoline direct injection engine operating parameters on particle number emissions. Energy Fuels 2012;26(4):2014–27.
[9] Bilgin A, Sezer I. Effects of methanol addition to gasoline on the performance and fuel cost of a spark ignition engine. Energy Fuels 2008;22(4):2782–8.
[10] Nauwerck A, Pfeil J, Velji A, Spicher U, Richter B. A basic experimental study of gasoline direct injection at significantly high injection pressures; 0148-7191. SAE J Engines 2005;114:218–26.
[11] Patel C, Agarwal AK, Tiwari N, Lee S, Lee CS, Park S. Combustion, noise, vibrations and spray characterization for Karanja biodiesel fuelled engine. Appl Therm Eng 2016;106:506–17.
[12] Agarwal AK, Park S, Dhar A, Lee CS, Park S, Gupta T, et al. Review of experimental and computational studies on spray, combustion, performance, and emission characteristics of biodiesel fueled engines. J Energy Res Technol 2018;140:(12).
[13] Chen Z, Yang F, Xue S, Wu Z, Liu J. Impact of higher n-butanol addition on combustion and performance of GDI engine in stoichiometric combustion. Energy Convers Manage 2015;106:385–92.
[14] Cooney C, Wallner T, McConnell S, Gillen JC, Abell C, Miers SA, Naber JD. In Effects of blending gasoline with ethanol and butanol on engine efficiency and emissions using a direct-injection, spark-ignition engine, ASME 2009 Internal Combustion Engine Division Spring Technical Conference, 2009; American Society of Mechanical Engineers; 2009. p. 157–165.
[15] Wallner T, Miers SA, McConnell S. A comparison of ethanol and butanol as oxygenates using a direct-injection, spark-ignition engine. J Eng Gas Turbines Power 2009;131(3):032802.
[16] Thewes M, Muther M, Brassat A, Pischinger S, Sehr A. Analysis of the Effect of Bio-Fuels on the Combustion in a Downsized DI SI Engine. SAE International Journal of Fuels and Lubricants; 2011, 5, (2011-01-1991), 274-288.
[17] Charoenphonphanich C, Ormman P, Karin P, Kosaka H, Chollacoop N. Experimental Investigation in Combustion Characteristics of Ethanol-Gasoline Blends for Stratified Charge Engine. 2011-32-0551 SAE Technical Paper 2011.
[18] Lee KO, Seong H, Sakai S, Hageman M, Rothamer D. Detailed morphological properties of nanoparticles from gasoline direct injection engine combustion of ethanol blends; 0148–7191. SAE Technical Paper 2013. 2013-24-0185.
[19] Heywood J. Internal combustion engine fundamentals. McGraw-Hill Education; 1988.

[20] Stone R. Introduction to internal combustion engines. Palgrave Macmillan; 2012.
[21] Agarwal AK. Biofuels (alcohols and biodiesel) applications as fuels for internal combustion engines. Prog Energy Combust Sci 2007;33(3):233–71.
[22] Zhuang Y, Hong G. Primary investigation to leveraging effect of using ethanol fuel on reducing gasoline fuel consumption. Fuel 2013;105:425–31.
[23] Yoon S, Ha S, Roh H, Lee C. Effect of bioethanol as an alternative fuel on the emissions reduction characteristics and combustion stability in a spark ignition engine. Proc Inst Mech Eng, Part D: J Automobile Eng 2009;223(7):941–51.
[24] Yoon SH, Lee CS. Effect of undiluted bioethanol on combustion and emissions reduction in a SI engine at various charge air conditions. Fuel 2012;97:887–90.
[25] Hara T, Tanoue K. Laminar flame speed of ethanol, n-heptane, iso-octane air mixtures. JSAE paper 2006, 20068518.
[26] Beeckmann J, Röhl O, Peters N. Numerical and experimental investigation of laminar burning velocities of iso-octane, ethanol and n-butanol; 0148–7191. SAE Technical Paper 2009. 2009-01-2784.
[27] Farrell J, Johnston R, Androulakis I. Molecular structure effects on laminar burning velocities at elevated temperature and pressure; 0148–7191. SAE J Engines 2004;3:0148–7191.
[28] Zhao H, Ge Y, Hao C, Han X, Fu M, Yu L, et al. Carbonyl compound emissions from passenger cars fueled with methanol/gasoline blends. Sci Total Environ 2010;408(17):3607–13.
[29] Sharma N, Agarwal AK. Effect of fuel injection pressure and engine speed on performance, emissions, combustion, and particulate investigations of gasohols fuelled gasoline direct injection engine. J Energy Res Technol 2020;142:(4).
[30] Patel C, Chandra K, Hwang J, Agarwal RA, Gupta N, Bae C, et al. Comparative compression ignition engine performance, combustion, and emission characteristics, and trace metals in particulates from Waste cooking oil, Jatropha and Karanja oil derived biodiesels. Fuel 2019;236:1366–76.
[31] Sharma N, Agarwal RA, Agarwal AK. Particulate bound trace metals and soot morphology of gasohol fueled gasoline direct injection engine. J Energy Res Technol 2019;141, (2):022201.

ARTICLE IN PRESS
JID: CNF [m5G;September 28, 2021;21:32]
Combustion and Flame xxx (xxxx) xxx

Contents lists available at ScienceDirect

Combustion and Flame

journal homepage: www.elsevier.com/locate/combustflame

A flamelet LES of turbulent dense spray flame using a detailed high-resolution VOF simulation of liquid fuel atomization

Jian Wen[a,*], Yong Hu[b], Takayuki Nishiie[c], Jun Iino[c], Assaad Masri[d], Ryoichi Kurose[a]

[a] Department of Mechanical Engineering and Science, Kyoto University, Kyoto daigaku-Katsura, Nishikyo-ku, Kyoto 615-8540, Japan
[b] State Key Laboratory of Fire Science, University of Science and Technology of China, Hefei, Anhui 230026, China
[c] Numerical Flow Designing Ltd., Higashigotanda, 1-10-10, Shinagawa City, Tokyo 141-0022, Japan
[d] School of Aerospace Mechanical and Mechatronic Engineering, The University of Sydney, NSW 2006, Australia

ARTICLE INFO

Article history:
Received 8 May 2021
Revised 6 September 2021
Accepted 6 September 2021
Available online xxx

Keywords:
Atomization
Dense spray combustion
LES
Flamelet
E-L transformation
Needle spray burner

ABSTRACT

A numerical framework used to model dense spray flames is proposed. In this framework, the liquid fuel (acetone) atomization is solved by a detailed high-resolution VOF simulation, and the Eulerian components of liquid droplets are transformed into Lagrangian droplets, which are stored in a database at a certain downstream cross-section. Then, the combustion process is solved by a LES/FPV (flamelet progress variable) adopting the pre-stored database of Lagrangian droplets (i.e., the position, size, and velocity of each droplet) as the inlet boundary conditions. This framework is a one-way coupling between a VOF simulation and a combustion simulation. The validity of this approach is investigated by comparing the computations with the experiments of the Sydney Piloted Needle Spray Burner. The VOF simulation shows that the volume flux of the droplets at the nozzle exit fluctuates both temporally and spatially and the larger droplets tend to be located away from the center axis compared to the small droplets. The computed breakup length is in good agreement with the empirical correlation. In the database of the Lagrangian droplets for the LES/FPV of spray flames, the location of the sampling cross-section, the sampling time, and the threshold value for Eulerian–Lagrangian (E-L) transformation strongly affect the properties of the Lagrangian droplets, and are critical for the successful use of the LES/FPV. Two spray flames with different recess distances are computed using their optimal pre-stored droplets databases and both show generally good agreement with the experiments in terms of the gas temperature and droplet size distributions. The spray flame with a longer recess distance, which is more representative of a dilute spray, is considered to have a longer and wider premixed core than that with a shorter recess distance representing a dense spray. The discrepancy in the prediction of denser spray flames becomes more evident leading to over-predictions of gas temperature further downstream. Reasons for this behavior are discussed in the text.

1. Introduction

Owing to the increasing concerns regarding global warming and a shortage of energy, it is important for energy generators to achieve a high combustion efficiency and extremely low emissions. Therefore, liquid fuel spray combustion, which is widely used in gas turbine, gasoline, diesel, and rocket engines, merits detailed investigations. Spray combustion includes extremely complex physical phenomena, starting from the liquid fuel atomization along with the droplet evaporation and evaporated fuel-air mixing, ending up with combustion. Therefore, the complexity involved makes it difficult to clarify the detailed mechanism and relevant models underlying spray atomization and combustion.

As mentioned by Masri [1], studies on spray combustion are generally classified into dense and dilute sprays. In the latter case, the spray dynamics associated with atomization is neglected. In a dense spray region where atomization occurs, many generated droplets make it difficult for experimental diagnostics to acquire sufficient information [2], thereby leaving the atomization process unclarified, and hence the dense spray region remains vague numerically [e.g., 3–30] and experimentally [e.g., 31,32–37,38]. For dilute spray flames, fuel sprays are regarded as a cluster of individual droplets and are then solved by the Lagrangian approach to

* Corresponding author.
E-mail address: wen.jen.66m@st.kyoto-u.ac.jp (J. Wen).

https://doi.org/10.1016/j.combustflame.2021.111742

consider an interaction with the surrounding gas phase. However, the Lagrangian approach still has difficulty in providing the initial droplet size distribution near the nozzle exit owing to the abundance of interplayed phenomena, namely, the processes of primary breakup, secondary breakup, and droplet coalescence/collision [e.g., 39,40–46,47].

To investigate such spray combustion located in the dense regime, Masri et al. [e.g., 48,49,50] at the University of Sydney designed a canonical platform that can supply various spray inlet conditions, which is called the Sydney Piloted Needle Spray Burner (referred to as the Sydney Burner, hereafter) to stabilize repeatable turbulent spray flames by placing two concentric tubes within the pilot annulus. By varying the recess distance, which refers to the distance between the liquid fuel jet nozzle to the pilot outlet, different types of sprays can be reproduced. However, there haven't been any attempts to use a numerical simulation to couple the combustion process with the beginning atomization process together.

The purpose of this study is, therefore, to propose a numerical framework to model the coupling of atomization and combustion of dense spray flames while maintaining reasonable computational cost. Results are compared with experimental data obtained from the Sydney needle burner [49,50]. The concept is as follows. The liquid fuel atomization is solved by a detailed numerical simulation, in which both continuum gas and liquid phases are strictly solved in a Eulerian framework, and the Eulerian components of the liquid droplets are transformed into the Lagrangian droplets at a certain downstream cross-section, i.e., sampling cross-section, whose information is stored in database. Then, the combustion process is solved by a large eddy simulation (LES) with a flamelet model adopting the pre-stored database of Lagrangian droplets, namely, by a one-way coupling between a VOF simulation and a combustion simulation.

2. Mathematical models

In this work, all computations are performed using an unstructured LES solver, i.e., the FrontFlow/Red extended by Kyoto University [23,51,52].

2.1. Governing equations for dense spray region

In the dense spray region where the atomization process occurs, liquid and gas continuum phases are treated as incompressible fluids and are both solved in a Eulerian framework. Their governing equations solved in this region include the conservation equations of mass and momentum as follows,

$$\rho \bigtriangledown \cdot \boldsymbol{u} = 0, \tag{1}$$

$$\rho\left(\frac{\partial \boldsymbol{u}}{\partial t} + \boldsymbol{u}\cdot\bigtriangledown\boldsymbol{u}\right) = -\bigtriangledown P + \bigtriangledown\cdot(2\mu\boldsymbol{S}) + \boldsymbol{F}_\sigma + g. \tag{2}$$

Here, ρ is the local density, $\boldsymbol{u}$ the velocity vector, P the pressure, μ the viscosity, $\boldsymbol{S}$ the rate-of-strain tensor $S_{ij} \equiv (\partial_i u_j + \partial_j u_i)/2$, and $\boldsymbol{F}_\sigma$ is the source term of surface tension calculated by the continuum surface force (CSF) model [53].

The high-resolution interface capturing (HRIC) scheme [54] is implemented into the volume of fluid (VOF) method in order to capture the gas-liquid interface and the atomization process, where the VOF advection function takes the following form Albadawi et al. [55],

$$\frac{\partial \psi}{\partial t} + \boldsymbol{u}\cdot\bigtriangledown\psi + \boldsymbol{u}_m(1-\psi)\bigtriangledown\psi = 0, \tag{3}$$

where, ψ is the VOF value within each grid, and $\boldsymbol{u}_m = \boldsymbol{u}_l - \boldsymbol{u}_g$ is the compressive velocity. The subscripts l and g refer to liquid and gas phases, respectively. The compressive velocity is considered only for the gas-liquid interface in the normal direction to avoid a dispersion of the VOF value. This additional compressive term helps retain the mass conservation and convergence for the VOF advection. It also facilitates the simulation of a multiphase flow with a large liquid/gas density ratio. Because the present study is performed in cylindrical coordinates with unstructured grids, the HRIC scheme is implemented instead of the coupled level-set and VOF method, which avoids the unnecessary complexity induced by the use of the level-set method.

A tagging method [56] is then utilized to transform the Eulerian liquid parts at a specific downstream cross-section into the Lagrangian spherical droplets with the droplet properties such as the position, size, and velocity, which are saved in a database (referred to as E-L tagging and E-L transformation, respectively, hereafter). Then, the stored Lagrangian droplets are utilized as the inlet boundary conditions for the combustion process.

2.2. Governing equations for dilute spray region

The combustion process occurring in the dilute spray region is modeled by a LES, utilizing the governing equations for the mass, momentum, and energy, and the detailed information can be found in studies [24,28,30]. To include the detailed chemical kinetics, a non-adiabatic version of flamelet/progress variable approach (FPV) [52,57] is used for the modeling of the turbulence-chemistry interaction, which results in the solution of the following equations,

$$\frac{\partial \bar{\rho}}{\partial t} + \bigtriangledown\cdot(\bar{\rho}\tilde{\boldsymbol{u}}) = S_\rho, \tag{4}$$

$$\frac{\partial \bar{\rho}\tilde{\boldsymbol{u}}}{\partial t} + \bigtriangledown\cdot(\bar{\rho}\tilde{\boldsymbol{u}}\tilde{\boldsymbol{u}}) = -\bigtriangledown\bar{P} + \bigtriangledown\cdot(\bar{\boldsymbol{\tau}} + \bar{\boldsymbol{\tau}}_{sgs}) + S_{\rho\boldsymbol{u}}, \tag{5}$$

$$\frac{\partial \bar{\rho}\tilde{h}}{\partial t} + \bigtriangledown\cdot(\bar{\rho}\tilde{\boldsymbol{u}}\tilde{h}) = \bigtriangledown\cdot[\bar{\rho}(\widetilde{D_h}\bigtriangledown\tilde{h})] + \bigtriangledown q_h + Q_{rad} + S_{\rho h}, \tag{6}$$

$$\frac{\partial \bar{\rho}\tilde{Z}}{\partial t} + \bigtriangledown\cdot(\bar{\rho}\tilde{\boldsymbol{u}}\tilde{Z}) = \bigtriangledown\cdot[\bar{\rho}(\widetilde{D_Z}\bigtriangledown\tilde{Z})] + \bigtriangledown q_Z + S_{\rho Z}, \tag{7}$$

$$\frac{\partial \bar{\rho}\tilde{C}}{\partial t} + \bigtriangledown\cdot(\bar{\rho}\tilde{\boldsymbol{u}}\tilde{C}) = \bigtriangledown\cdot[\bar{\rho}(\widetilde{D_C}\bigtriangledown\tilde{C})] + \bigtriangledown q_C + \bar{\rho}\tilde{\dot{\omega}}_C, \tag{8}$$

where, the overbar, $-$, denotes the filtered mean value, and the tilde, $\sim$, denotes the Favre averaged value. $\tau_{sgs} = \bar{\rho}(\widetilde{\boldsymbol{u}\boldsymbol{u}} - \tilde{\boldsymbol{u}}\tilde{\boldsymbol{u}})$ is the subgrid term of the stress tensor, h the enthalpy, Z the mixture fraction. The mixture fraction is defined as the mass fraction of fuel stream, such that $Z = 1$ means a fuel stream and $Z = 0$ means an oxidizer stream. Following the work [52,57], the progress variable C is defined as the summation of combustion products, i.e., $C = Y_{H_2O} + Y_{H_2} + Y_{CO_2} + Y_{CO}$. Y is the mass fraction of chemical species. D_h, D_Z, and D_C are diffusion coefficients of h, Z, and C, respectively. D_h is the gaseous thermal diffusivity given by $D_h = \lambda/(\rho c_p)$, D_Z and D_C are obtained by assuming the unity Lewis number. λ is the heat conductivity, c_p is the specific heat capacity at constant pressure. q_h, q_Z, and q_C are the subgrid-scale (SGS) scalar fluxes, $q_\phi = \bar{\rho}(\widetilde{\boldsymbol{u}\phi} - \tilde{\boldsymbol{u}}\tilde{\phi})$, $(\phi = h, Z, C)$. Q_{rad} is the radiation heat loss modeled by the weighted sum of gray gases (WSGG) model [58]. $\dot{\omega}_C$ is the source term of reaction progress variable. The eddy viscosity approximation is used to determine the τ and q as follows,

$$\bar{\tau}_{sgs} = \mu_t[(\bigtriangledown\tilde{\boldsymbol{u}}) + (\bigtriangledown\tilde{\boldsymbol{u}})^T)], \tag{9}$$

$$q_\phi = \bar{\rho}\alpha_t\bigtriangledown\tilde{\phi}, \tag{10}$$

where, μ_t and α_t denote the turbulent viscosity and eddy diffusivity, respectively, and are generally related in the formulation as $\alpha_t = \mu_t/(\bar{\rho} Sc)$ with a constant Schmidt number of $Sc = 0.4$ [59], where μ_t is determined by the dynamic Smagorinsky–Lilly model [60].

A non-adiabatic flamelet/progress variable approach (FPV), which can consider the effect of the heat loss caused by the latent heat of spray vaporization and radiation, is used. In order to generate the flamelet library, the following flamelet equations depending on the unity Lewis number assumption with heat loss are solved as follows,

$$\rho \frac{\partial Y_k}{\partial t} - \frac{\rho \chi}{2} \frac{\partial^2 Y_k}{\partial Z^2} - \dot{\omega}_k = 0, \tag{11}$$

$$\rho \frac{\partial T}{\partial t} - \frac{\rho \chi}{2} \left(\frac{\partial^2 T}{\partial Z^2} + \frac{1}{c_p} \frac{\partial c_p \partial T}{\partial Z \partial Z} \right) + \sum_k \frac{\rho \chi}{2} \left(\frac{\partial Y_k}{\partial Z} + \frac{Y_k}{W} \frac{\partial W}{\partial Z} \right) \left(1 - \frac{c_{p,k}}{c_p} \right) \frac{\partial T}{\partial Z} + \frac{1}{c_p} \sum_k h_k \dot{\omega}_k + q'_{loss} = 0, \tag{12}$$

$$q'_{loss} = -\frac{\alpha}{c_p} \sum_k h_k \dot{\omega}_k, \tag{13}$$

where, the subscript k denotes the chemical species, χ is the scalar dissipation rate, $\dot{\omega}_k$ the reaction rate of species k, T the gas temperature, W the mean molecular weight of mixture, $c_{p,k}$ the specific heat capacity of species k at constant pressure, q'_{loss} the heat loss, α the heat loss rate parameter which can be varied from 0 to 1. Then a four dimensional flamelet library is obtained as,

$$\tilde{\varphi} = \tilde{\varphi}(\tilde{Z}, \widetilde{Z''^2}, \tilde{C}, \widetilde{\triangle h}), \tag{14}$$

where, Z''^2 is the variance of mixture fraction, $\triangle h$ is the enthalpy defect due to heat loss, φ is the flame properties such as gas temperature, species mass fraction, and reaction rate. Here, the adiabatic enthalpy h_a is calculated by Eq. (16) by assuming $\triangle h = 0$, i.e., $h_a = \tilde{h}(\tilde{Z}, \widetilde{Z''^2}, \tilde{C}, \widetilde{\triangle h} = 0)$, and thus the enthalpy defect $\triangle h$ can be calculated by $\triangle h = h_a - h$, where h is determined with Eq. (6).

The influence of the evaporating droplets on the carrier gas flow is considered using the Particle-Source-In Cell (PSI-Cell) method [61]. S_ρ, $S_{\rho \boldsymbol{u}}$, $S_{\rho h}$, and $S_{\rho Z}$, which are the source terms for the mass, momentum, enthalpy, and mixture fraction originating from the dispersed droplets, respectively, are given as follows,

$$S_\rho = -\frac{1}{\triangle V} \sum_N \frac{dm_d}{dt}, \tag{15}$$

$$S_{\rho \boldsymbol{u}} = -\frac{1}{\triangle V} \sum_N \frac{dm_d \boldsymbol{u_d}}{dt}, \tag{16}$$

$$S_{\rho h} = -\frac{1}{\triangle V} \sum_N \frac{dm_d h_d}{dt}, \tag{17}$$

$$S_{\rho \tilde{Z}} = -\frac{1}{\triangle V} \sum_N \frac{dm_d}{dt} \quad \text{for fuel}, \tag{18}$$

where, $\triangle V$ is the volume of the unit grid, N is the number of droplets in the grid, and m_d, $\boldsymbol{u}_d$, and h_d are the mass, velocity, and specific enthalpy of the droplet, respectively.

Considering the non-equilibrium Langmuir–Knudsen evaporation model [24,62], the governing equations used to track the droplet profiles such as the position, x_d, velocity, $\boldsymbol{u}_d$, temperature, T_d, and mass, m_d, are given,

$$\frac{dx_d}{dt} = \boldsymbol{u}_d, \tag{19}$$

$$\frac{d\boldsymbol{u}_d}{dt} = \frac{f_1}{\tau_d} (\tilde{\boldsymbol{u}} - \boldsymbol{u}_d), \tag{20}$$

$$\frac{dT_d}{dt} = \frac{Nu}{3Pr} \left(\frac{\tilde{c}_p}{c_{p,d}} \right) \left(\frac{f_2}{\tau_d} \right) (\tilde{T} - T_d) + \frac{1}{m_d} \left(\frac{dm_d}{dt} \right) \frac{L_V}{c_{p,d}}, \tag{21}$$

$$\frac{dm_d}{dt} = -\frac{Sh}{3Sc} \frac{m_d}{\tau_d} ln(1 + B_M), \tag{22}$$

Here, f_1 and f_2 are the correction coefficients for the Stokes drag and heat transfer for the evaporating fuel droplet, τ_d is the particle response time [13,63], T the gas temperature, L_V the latent heat of evaporation at T_d, c_p and $c_{p,d}$ the specific heat of gas and fuel droplet, the Nusselt number and Prandtl number $Nu = 2 + 0.522 Re_{sl}^{1/2} Pr^{1/3}$ and $Pr = \mu c_p/\lambda$, the Sherwood number and Schmidt number $Sh = 2 + 0.552 Re_{sl}^{1/2} Sc^{1/3}$ and $Sc = \mu/(\rho D_k)$, the mass transfer number $B_M = (Y_{F,s} - Y_F)/(1 - Y_{F,s})$. The detailed information of the droplet evaporation model can be found in our previous studies [24,46,64,65]. The employed secondary breakup model is the Taylor analogy breakup (TAB) model [66].

3. Computational setup

3.1. Computational domains

A numerical framework is proposed in the present study, where the spray atomization and the subsequent combustion are simulated using different methods following an assumption that these two sub-processes usually occur in separated domains. Therefore, two computational domains are adopted and are marked as atomization and combustion domains, respectively, as shown in Fig. 1. In Fig. 1(a), the part depicted by the black line is the Sydney Burner, which consists of two concentric tubes, 1 and 2, surrounded by a pilot tube, 3. The inner tube, 1, is the liquid fuel nozzle with an inner diameter of $D_l = 0.686$ mm and wall thickness of 0.381 mm, and the outer tube, 2, is the air stream nozzle for the liquid fuel atomization with an inner diameter of $D_g = 10$ mm and wall thickness of 0.5 mm. The pilot tube, 3, is used to supply the hot combustion products through an inner diameter of $D_p = 25$ mm and wall thickness of 0.2 mm. The concentric tubes are adjustable such that the distance from the liquid fuel nozzle to the pilot outlet is variable, enabling the Sydney Burner to supply a dense or dilute spray for the combustion. The distance is called the recess distance and is referred to as Lr in the present and related studies [e.g., 48,49,50], ranging from 0 to 80 mm. The present study selected two different flame cases, N-AF8-25 and N-AF8-80 which hold different Lr values, $Lr = 25$ and 80 mm, respectively.

However, for the atomization computation, the case of $Lr = 80$ mm requires a much higher computational cost than that of $Lr = 25$ mm. Therefore, only the N-AF8-25 case atomization process is calculated, which is depicted by the solid and dotted blue lines in Fig. 1(a), and is shown in Fig. 1(b) in detail. The atomization domain consists of a region with a wall boundary having a length of 25 mm corresponding to the experimental recess distance and a free boundary of 25 mm. Two atomization-combustion coupling (ACC) planes are set in the atomization domain. These are utilized to transform the Eulerian components into the Lagrangian droplets and serve as the inlet boundary conditions for the combustion simulation. To investigate the influence of different ACC positions on the E-L transformation, one plane is set at 5 mm upstream of the pilot outlet (ACC1) and the other is 5 mm downstream of the pilot outlet (ACC2).

The combustion domain is depicted by the red line in Fig. 1(a), the details of which are presented in Fig. 1(c). The entire combustion domain holds a diameter of $D_c = 104$ mm. In the axial direction, the inlet boundary is placed at the ACC plane, whose distance

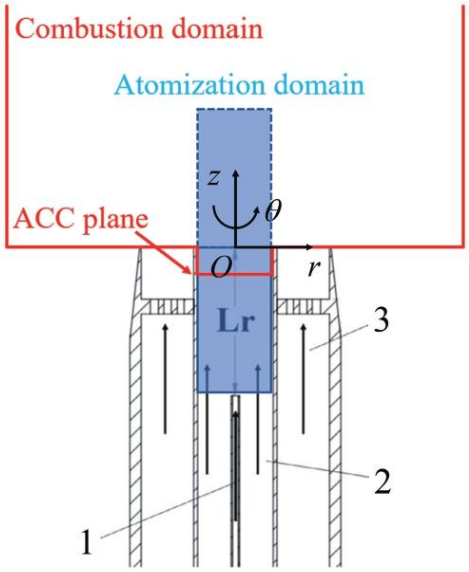

(a) Computational domains of atomization and combustion. 1, 2, and 3 refer to liquid fuel nozzle, air stream nozzle, and pilot tube, respectively and ACC refers to atomization-combustion coupling plane

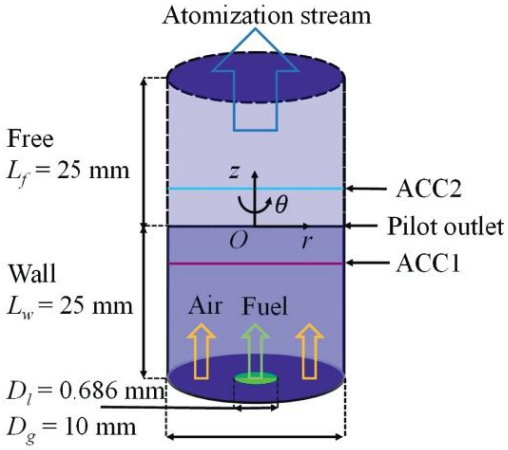

(b) Computational domain of atomization

Fig. 1. Schematics of computational domains.

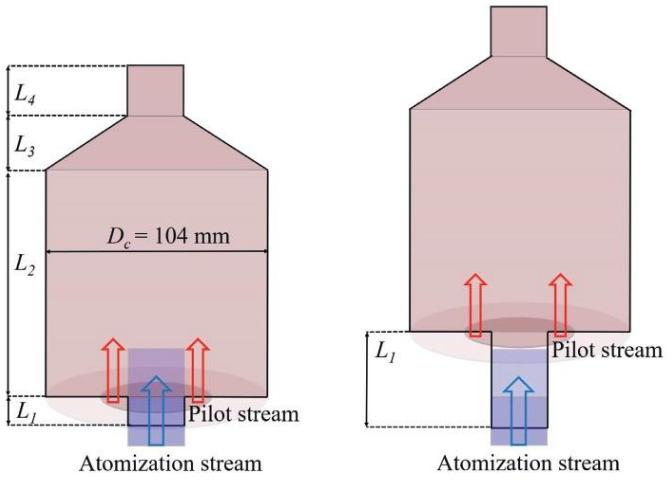

(c) Computational domains of combustion (left: N-AF8-25; right: N-AF8-80)

Fig. 1. Continued

to the pilot outlet is marked as L_1. Since the recess distance of N-AF8-25 and N-AF8-80 are adjusted to 25 and 80 mm to produce dense and dilute sprays, L_1 holds two values of 10 and 65 mm for N-AF8-25 and N-AF8-80, respectively, and the other parameters $L_2 = 1000$ mm, $L_3 = 75$ mm, and $L_4 = 135$ mm are kept the same in both cases.

The cylindrical coordinate system with the unstructured grids is utilized for both atomization and combustion simulations. The atomization computational domain has a total of 24.6 million grid points, with a non-uniform mesh size ranging from 8 to 100 μm in the radial direction, and a uniform mesh size of 100 μm in the axial direction. The combustion computational domain has a total of 18 million grid points, with an increasing mesh size of 0.13 to 3 mm in the radial direction, and a variable mesh size of 0.15 to 3.5 mm in the axial direction. In addition, the Hinze scale $\eta_H = \sigma/(\rho_g U_g^2)$ in the atomization computation is estimated to be 8.54 μm and the mesh size holds 1–10 η_H. As suggested in our previous study [46] and regarding this simulation reaches to the experimental scale, it could be considered as a high-resolution VOF simulation.

Table 1
Parameters for atomization simulation.

Physical properties	
Liquid fuel	Acetone
Gas&Air	
Liquid nozzle diameter, D_l (mm)	0.686
Liquid jet velocity, u_l (m/s)	2.57
Liquid jet viscosity, μ_l (Pa s)	3.33×10^{-4}
Liquid jet density, ρ_l (kg/m^3)	786
Liquid jet temperature, T_l (K)	300
Liquid jet Reynolds number, Re_l (−)	4161
Gas jet diameter, D_g (mm)	10
Gas jet velocity, u_g (m/s)	48
Gas jet viscosity, μ_g (Pa s)	1.81×10^{-5}
Gas jet density, ρ_g (kg/m^3)	1.20
Gas jet temperature, T_g (K)	300
Gas jet Reynolds number, Re_g (−)	31, 823
Liquid-gas surface tension, σ (N/m)	2.37×10^{-2}
Ambient pressure, P (MPa)	0.1
Aerodynamic Weber number, We (−)	80

3.2. Computational conditions

For the atomization computation, the temperature and pressure are set to room temperature and atmospheric pressure, and hence, both the liquid fuel and air have a temperature of 300 K, which can be regarded as a cold state for only atomization, neglecting the evaporation effect. Therefore, the air viscosity, μ_g, is 1.81×10^{-5} Pa s, and liquid viscosity, μ_l, is 3.33×10^{-4} Pa s, the liquid-gas surface tension, σ, is 2.37×10^{-2} N/m. At the inlet, both the liquid and carrier gas velocities, u_l and u_g, are assigned as 2.57 m/s and 48 m/s with a flat laminar velocity profile, respectively, according to the experiments [49,50]. Thus, in both configurations, i.e., N-AF8-25 and N-AF8-80, the dimensionless parameters, including the aerodynamic Weber number, $We = \rho_g u_g^2 D_l/\sigma$, evaluated as 80, the liquid jet Reynolds number, $Re_l = 4161$, as well as the carrier gas Reynolds number, $Re_g = 31,823$, are close to the experimental conditions, as shown in Thomas and Lowe's works [49,50]. The parameters used in the atomization computation are shown in Table 1.

After the atomization computation, the droplets are transformed into the Lagrangian droplets, which are stored in a database for the following combustion computation. Droplets recorded at the ACC plane of the atomization domain are directly injected into the combustion domain at the ACC plane at a fixed time step determined by satisfying the step interval of the combustion computation, which are explained in the following section. When these cold Lagrangian fuel droplets flow out of the nozzle and face the hot pilot gases, combustion occurs after the evaporation and mixing with the combustion products from the pilot that is in the stoichiometric condition and has a velocity of 1.5 m/s. Two different gas velocity profiles: (1) a uniform flat gas velocity that equals to 48 m/s; (2) a gas velocity profile extracted from the

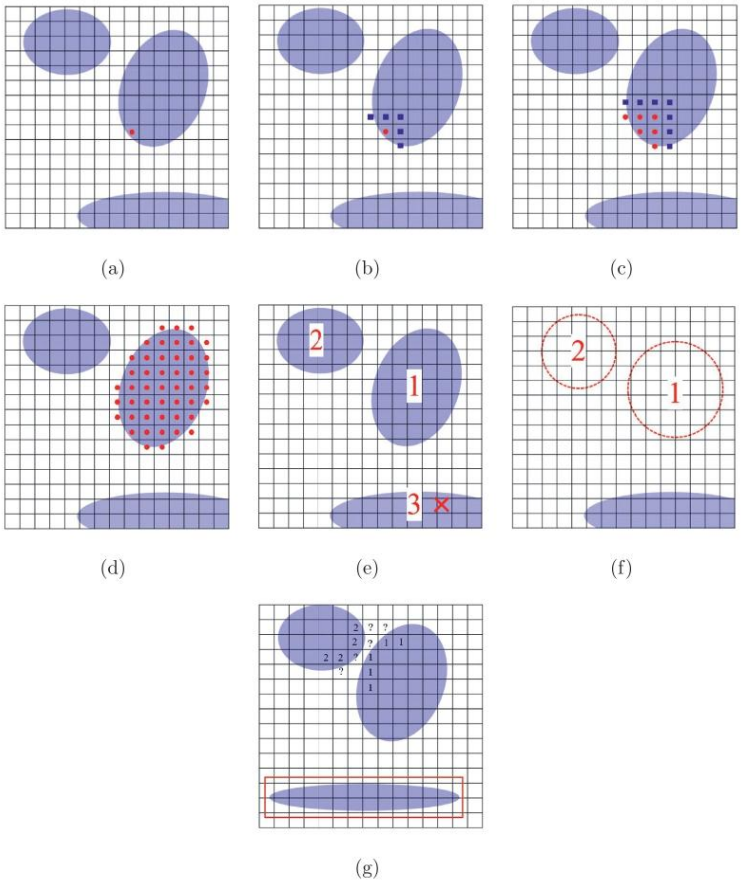

Fig. 2. Algorithm of E-L tagging method.

atomization computation, are performed to study the influence of different inlet gas velocity profiles.

The flamelet calculations for the flamelet library generation are conducted with FlameMaster code [67]. The numbers of grids set for $\tilde{Z}$, $\widetilde{Z''^2}$, $\tilde{C}$, and $\widetilde{\triangle h}$ are $100 \times 20 \times 100 \times 10$. The reaction mechanism for acetone/air combustion proposed by Pichon et al. [68] is employed, which consists of 81 species and 416 reactions.

The computational cost for single realization of atomization and combustion simulations, performed on the Kyoto University Supercomputer (Cray XC40), are around 430k core·hours (840 h in real time using 512 cores) and 250–370k core·hours (230–340 h in real time using 1088 cores), respectively.

4. Results and discussion

4.1. Atomization and E-L transformation

In the experiments of the dense sprays, it is difficult to acquire confident droplet size distribution owing to the diagnostics limitation. In fact, Lowe et al. [50] reported that large numbers of ligaments and irregular shaped objects are formed before secondary breakup. Those ligaments and irregular shaped objects are considered to more likely increase the turbulence in the flow field. Although such liquid ligaments and irregular shaped objects are also observed in the present simulation, those are forced to be transformed into Lagrangian sphere droplets using a E-L tagging method owing to the limitation of the consideration of those shapes. The influence of this will be discussed later.

The E-L tagging method is used to recognize the dispersed Eulerian components generated by the primary breakup during the atomization process and transfer their properties into the Lagrangian droplets, which are later directly placed in the computational domain to replace the Eulerian components. To simply explain the E-L tagging method employed in the present study, 2-dimensional schematics are given as shown in Fig. 2. First, a threshold for the tagging method should be artificially given, with which the cells satisfying the criterion would be tagged and then become one part of a transformed Lagrangian droplet. In the present study, the

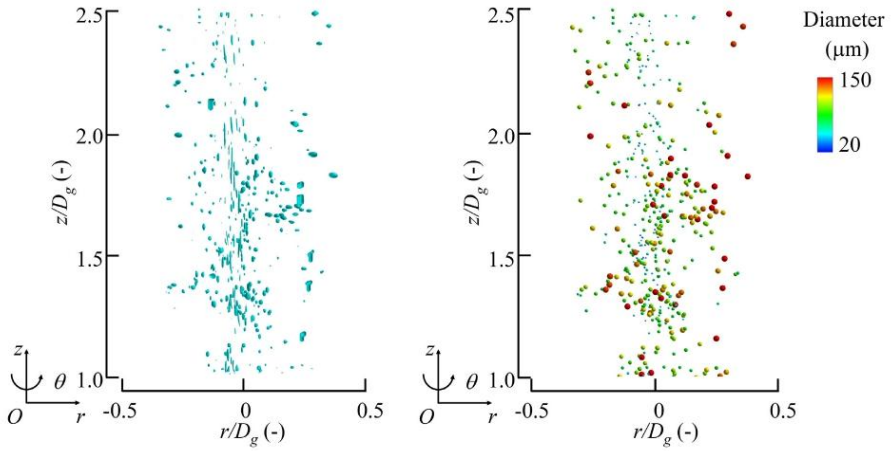

(a) Eulerian components (b) Lagrangian droplets

Fig. 3. Comparison of droplet position and size distributions between Eulerian components and Lagrangian droplets at $1.0 \le z/D_g \le 2.5$ and $-0.5 \le r/D_g \le 0.5$ (Lagrangian droplets are colored and scaled by diameter size).

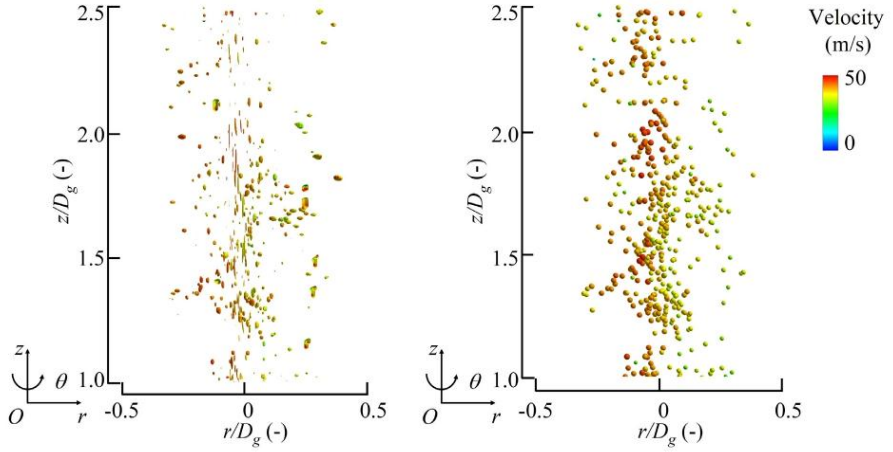

(a) Eulerian components (b) Lagrangian droplets

Fig. 4. Comparison of axial velocity and position distributions between Eulerian components and Lagrangian droplets at $1.0 \le z/D_g \le 2.5$ and $-0.5 \le r/D_g \le 0.5$ (Eulerian components and Lagrangian droplets are colored by velocity).

volume fraction of gas phase $VOID = 1 - \psi$, is used for the tagging method, and hence the threshold for the $VOID$ value is set as $VOID_{cri}$.

For a cell satisfying $VOID < VOID_{cri}$, it would be tagged by a red marker as shown in Fig. 2(a). The surrounding cells are then checked and also the cells satisfying $VOID < VOID_{cri}$ are tagged by blue markers, which represent the edge of the tagged droplet as shown in Fig. 2(b). Later on, the cells neighboring the edge of the tagged droplet are checked and tagged by blue markers to represent the new edge of the tagged droplet, and the original blue markers are switched to red markers to represent the inside of the tagged droplet as shown in Fig. 2(c). By looping the steps from (b) to (c), a droplet would be filled by red markers and no further neighboring cells could be tagged by blue markers, then all markers are switched to red markers as shown in Fig. 2(d), which would later be tagged by a specific marker such as 1 shown in Fig. 2(e). By employing the steps from (a) to (d), all the dispersed Eulerian components would be tagged by the specific markers such as 1, 2, and 3, as shown in Fig. 2(e). Then the details of each tagged Eulerian component would be further checked. For example, for 3 in

Fig. 2(e), some cells in it are neighboring the wall boundary such that the detailed information could not be further checked, which makes 3 unable to be recognized as a Lagrangian droplet as shown in Fig. 2(f). Some more complex situations are provided in Fig. 2(g), for example, how to deal with the cells marked by the question marks since they should belong to two individual droplets, or how to deal with the dispersed component with extremely slim structure marked by the red rectangle. Therefore, for more interests of this tagging method, please refer to the work of Herrmann [56], Zuzio et al. [69] as well as our previous work [46].

In the present study, the E-L transformation is triggered only if the Eulerian droplet passes through the ACC plane, as shown in Fig. 1(b), which is a cross-section at the downstream region in the atomization computational domain. Therefore, a buffer region is created upstream of the ACC plane, and the Eulerian components in this buffer region that can pass through the ACC plane within one sampling time interval are transformed into Lagrangian droplets and then saved in the database for subsequent combustion. Because the computational time interval used for the combustion simulation is 1×10^{-5} s, and that for the atomization simulation is 5×10^{-8} s, the sampling time interval is thus set as 200 steps of the atomization computation, that is, 1 step of the combustion simulation.

Figures 3 and 4 show comparisons of the position, size, and axial velocity between the Eulerian components and the transformed Lagrangian droplets. Generally, a good agreement is observed. Specifically, it can be seen that the Lagrangian droplets with a red color match the large Eulerian components in both the droplet position and size. A good match is also shown for the small droplets with a green color. Such an agreement of the axial velocity profiles can also be found in Fig. 4. Therefore, the present E-L tagging method can work properly to transform Eulerian components into the Lagrangian droplets.

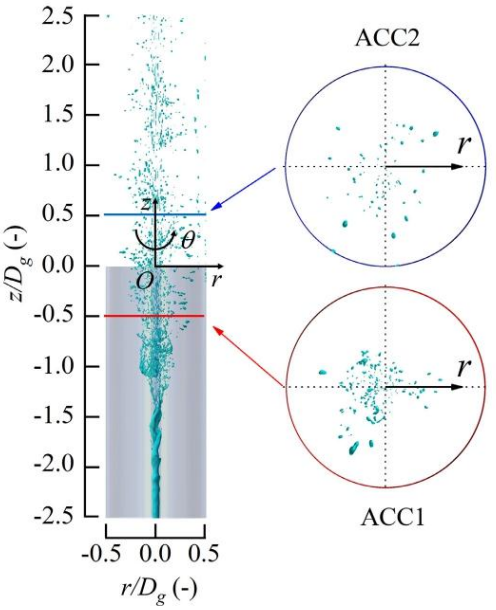

Fig. 5. Atomization behavior and the Eulerian components distributions at ACC1 and ACC2 ($VOID_{cri} = 0.9$).

4.2. Atomized droplets database

4.2.1. Database concept and droplet size distribution

To confidently build a database serving as the inlet boundary conditions for the combustion computation, the critical factors affecting the atomization properties should be carefully checked. The present E-L tagging method includes three important parameters, i.e., the downstream distance from the fuel nozzle to the ACC plane, Z_0, the threshold value of the E-L tagging method, and the total sampling time for recording the droplets profiles. Regarding the downstream distance Z_0, with a smaller Z_0, where the liquid jet is not fully developed, the E-L tagging method cannot transform the ligaments and irregular shaped objects into larger Lagrangian blobs, which is unrealistic, resulting in mass loss; however, with a larger Z_0, where less ligaments exist and Eulerian droplets are easily transformed into the Lagrangian droplets, the E-L tagging method also loses its accuracy owing to the numerical diffusion since the cells might hold diffused VOF values and the unexpected transformed Lagrangian droplets. Therefore, two different ACCs, i.e., one is 5 mm upstream of the pilot outlet (ACC1) and another is 5 mm downstream of the pilot outlet (ACC2), which are shown in Fig. 1(b), are exhibited to check the confidence of the position. On the other hand, considering the threshold values used in the E-L tagging method, a larger threshold, which can recognize the tiny Eulerian droplets, increases the risk of numerical error caused by numerical diffusion, some of which are simply numerical noise and referred to as fake droplets. However, a smaller threshold neglects those droplets with a small scale in comparison to the local grid size, losing realistic small droplets, which have a significant influence on the subsequent evaporation and combustion properties. Thus, three different thresholds, $VOID_{cri} = 0.9$, 0.95, and 0.99, are selected and their validities are examined. Hence, four different databases can be acquired, as presented in Table 2. Note that the atomization simulation is only calculated once under the condition shown in Table 1, and the droplet databases are obtained during the simulation by setting different ACCs and thresholds.

Figure 5 shows the atomization behavior in the front view and at the cross-sections of ACC1 and ACC2, the colored surface of which is the iso-surface of the E-L tagging method threshold of 0.9, i.e., the liquid-phase volume fraction of the grids is larger than 10%. The liquid column starts to show instability around the downstream at $z/D_g = -2.25$, and twists at approximately $z/D_g = -1.75$. When it passes $z/D_g = -1.5$, a breakup behavior can be observed. The liquid column becomes discontinuous, and smaller droplets and some ligaments and irregular shaped objects can be found around the $z/D_g = -1.0$. Beyond $z/D_g = -0.5$, most of the visible liquid phase is due to dispersed droplets, which tend to flow away from the center axis. By comparing the cross-sections of ACC1 and ACC2, the existing droplets are found to be denser at ACC1, and the downstream droplets at ACC2 reach further in the radial direction.

Figure 6 shows the droplet profiles in different databases, plotted with droplet diameters which are binned over 10 μm interval for droplets up to 50 μm, 20 μm interval for droplets from 50 to 150 μm, and 50 μm interval for droplets with size above 150 μm. For Fig. 6(a), with the ACC plane going downstream and increasing the threshold of the E-L tagging method, the peak of the PDF value changes from 70 to 30 μm. By comparing the droplet size distributions of A1 and A2 in three different clusters, i.e., 0–50 μm, 50–150 μm, and 150–200 μm, there are few differences between both cases, indicating occurrences of further breakup. Moreover, the threshold of the E-L tagging method seems to have a more significant influence on the droplet size distribution than the ACC position by comparing the differences between A2 and A4 as well as A1 and A2. By applying a larger threshold, more droplets with the

Table 2
Databases acquired in atomization simulation.

Database	ACC plane	Threshold for E-L transformation	Volumetric particle loading
A1	ACC1	0.9	7.40
A2	ACC2	0.9	9.28
A3	ACC2	0.95	9.84
A4	ACC2	0.99	11.22

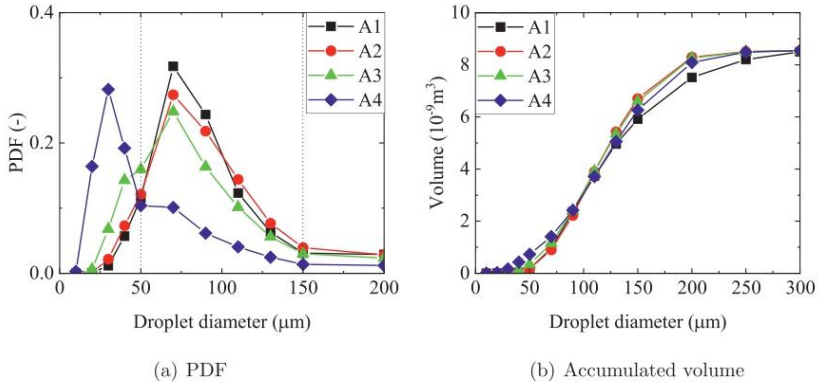

Fig. 6. Droplet size distribution in terms of (a) PDF and (b) accumulated volume of different atomization databases (A1–A4).

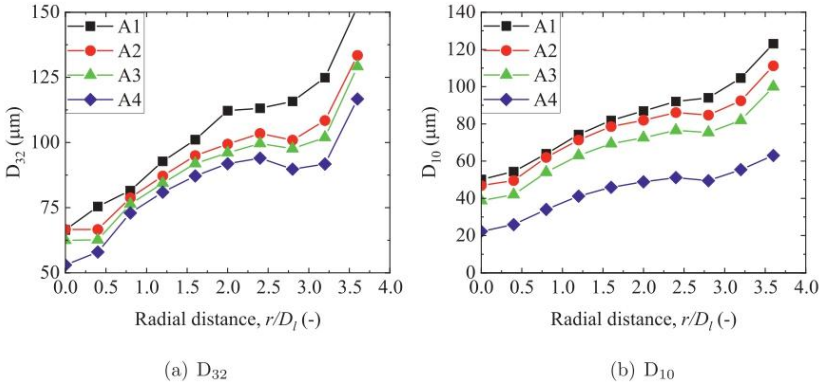

Fig. 7. Radial distributions of droplet size in (a) D_{32} and (b) D_{10} for different atomization databases (A1–A4).

diameter less than 50 μm seem to be captured with the value of 0.99. By comparing the total droplet volume of different databases shown in Fig. 6(b), all databases show a similar total droplet mass, which means that almost of the Eulerian components are captured by the present E-L tagging method. In addition, one thing worth noting is that for a large Lagrangian droplet, which might be comparable to the mesh size, the mass and momentum interactions between gas phase and the Lagrangian droplet are decided by the surrounding cells instead of the local cell such that the Lagrangian droplet could be still considered as a point by the PSI-Cell method.

Because this study is focused on dense spray, the volumetric particle loading of droplets in the computational domain is further checked, as shown in Table 2. Here, the ratio of droplet distance and droplet diameter is presented instead of simple volume fraction, which can refer to as S/d in Elghobashi's work [70], where, S indicates the distance between the centers of two neighboring droplets, and d denotes the diameter of droplet. With $S/d \geq 10$, the two-way coupling method could be employed in this study instead of four-way coupling. When the ACC plane is set further downstream, the droplets can reach further in the radial direction, which can refer to the cross-sections of ACC1 and ACC2 in Fig. 5, and thus A2 shows a larger value than A1, indicating a more dilute spray compared with A1.

4.2.2. Droplet spatial and temporal size distributions

In traditional combustion simulations, the sizes of droplets issued from the inlet boundary are often given using a simple atomization model or a presumed droplet size distribution. In this study, on the other hand, those are taken from a database resulting from the atomization computation. Therefore, the sampling time of

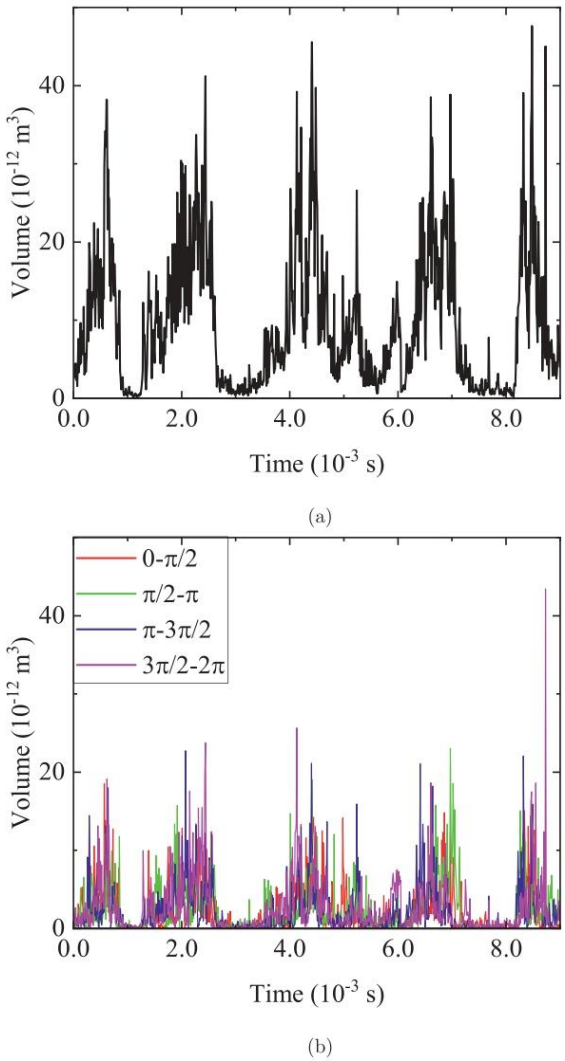

Fig. 8. Time variations of droplet volume through ACC1 plane for the database A1: (a) in total, (b) each quadrant.

atomization computation should be carefully discussed. To obtain a symmetrical flame structure without any preferences in any directions, the spatial distribution of the droplets must be checked such that the position profile should be spatially homogeneous without any biases in any directions. For example, many more larger droplets can be found in $\pi \leq \theta < 3\pi/2$ and fewer droplets can be found in $0 \leq \theta < \pi/2$ at ACC1, and larger droplets are observed on the right side at ACC2, as shown in Fig. 5, thus the droplets distribution shows some preferences if the sampling time is insufficient.

The complexity of the azimuthal homogeneity analysis increases if the droplet size is further considered. Figure 7 shows the Sauter mean diameter (D_{32}) and arithmetic mean diameter (D_{10}) radial distributions obtained from the different databases. The droplet size for either D_{32} or D_{10} increases as the droplets flow further away from the central axis, which means that the droplet size has a strong correlation with the radial distribution, and thus it is sufficient to base the analysis for azimuthal homogeneity on investigating the droplet size with different angles θ in the radial plane. The droplet size can be used to represent the radial distance between the droplet and the center axis, and the angle θ can be used to represent different radial directions. In addition, referring to the experimental study [50] based on the Sydney Burner

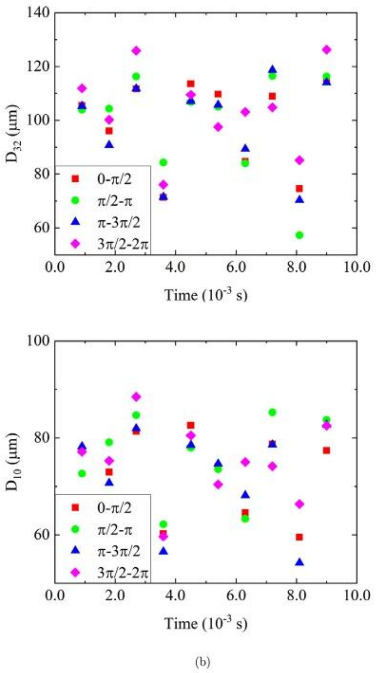

Fig. 9. Time variations of D_{32} and D_{10} of droplets through each quadrant of ACC1 plane for the database A1: (a) D_{32}, (b) D_{10}.

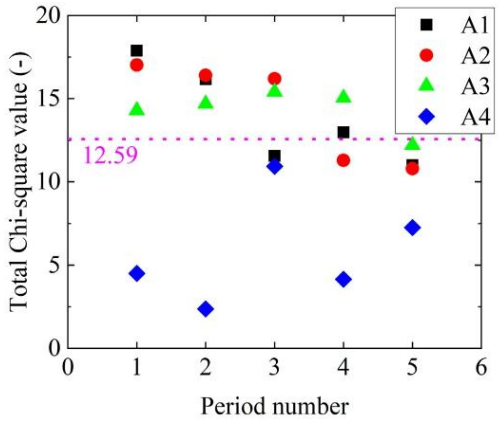

Fig. 10. Total values of different databases A1–A4 with different sampling time.

of N-AF8-25 and N-AF8-80, which only supplies the D_{32} distributions along the center axis (see Fig. 12), D_{32} is always less than 60 μm. Given that the database of A4 holds the D_{32} value less than 60 μm, whereas those of other three cases are larger than 60 μm, the database A4 provides a better droplet size distribution according to the experiment.

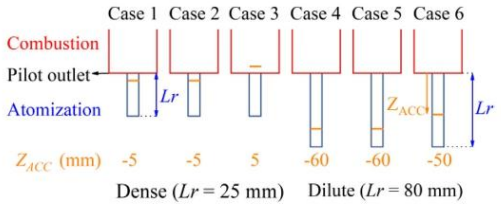

Fig. 11. Conducted cases and schematic of locations of recess distance, *Lr*, and ACC planes, Z_{ACC}, for combustion in detail.

To obtain a sufficient number of reliable data for a homogeneous analysis, the sampling time and interval are discussed. The sampling interval is set 1×10^{-5} s, which is 200 steps for the atomization computation and 1 step for the combustion computation, and thus the combustion simulation can simply read the data in a step-by-step manner. Figure 8 shows the time variations of droplet volume through ACC1 plane and through each quadrant of ACC1 plane, from the 120,000th step, in which the liquid jet is thought to be fully developed and starts to steadily breakup, to the 300,000th step, which is thought to be long enough for sampling. Five periods can be observed in Fig. 8(a) showing that the atomization process holds a periodic characteristic with breakup and non-breakup periods. In Matas's study [71,72], the frequency of the liquid jet breakup is found to have a strong relation to the gas and liquid velocities as well as the nozzle size, and the empirical correlations are shown as follows.

$$f = \left(\sqrt{\frac{\rho_g \delta_l}{\rho_l \delta_g}} u_g + u_l\right) / D_g, \tag{23}$$

$$\delta = \nu_0 / \max\left(\frac{d\nu}{dr}\right). \tag{24}$$

where δ is the thickness of the vorticity layer, ν denotes the radial velocity, and ν_0 is the radial velocity measured near the Sydney Burner nozzle, e.g., $z/D_g = 0$. The thickness of the vorticity layer of liquid and gas phases, δ_l and δ_g are directly acquired in the simulation. By this correlation, the calculated result is 547 Hz, and the mean period shown in Fig. 8(a) is simply calculated as 556 Hz. Therefore, the present detailed numerical simulation and the E-L tagging method are considered to be reasonable to reproduce the atomization phenomena. Figure 8(b) shows the variations of droplet volume through each quadrant of ACC1 plane, and it could be observed that the droplet volume of each quadrant shows totally different values in different breakup periods. For example, for the quadrant of $3\pi/2 - 2\pi$, it holds larger values in the later time in each breakup period except for the 3rd period between 3 and 5 ms. Figure 9 also shows the time variations of D_{32} and D_{10} through each quadrant of ACC1 plane in each a half breakup period. It could be observed that the values of D_{32} and D_{10} in each a half breakup period are totally different such that the droplet sampling time for acquiring a homogeneous distribution need to be further checked.

By comparing the D_{32} and D_{10} distributions in Fig. 7, the droplet size has a strong correlation with the radial distance, that is, the closer the droplets to the center axis, the smaller the droplets are. Therefore, the angle θ in the radial plane and the droplet size can be used to analyze the droplet spatial distribution by the Chi-square homogeneity check, the detail of which can be found in Appendix A.

Table 3 shows the calculated chi-square values of the database A1 with a sampling time starting at the 120,000th step and ending up with the 300,000th step, covering five full-breakup peri-

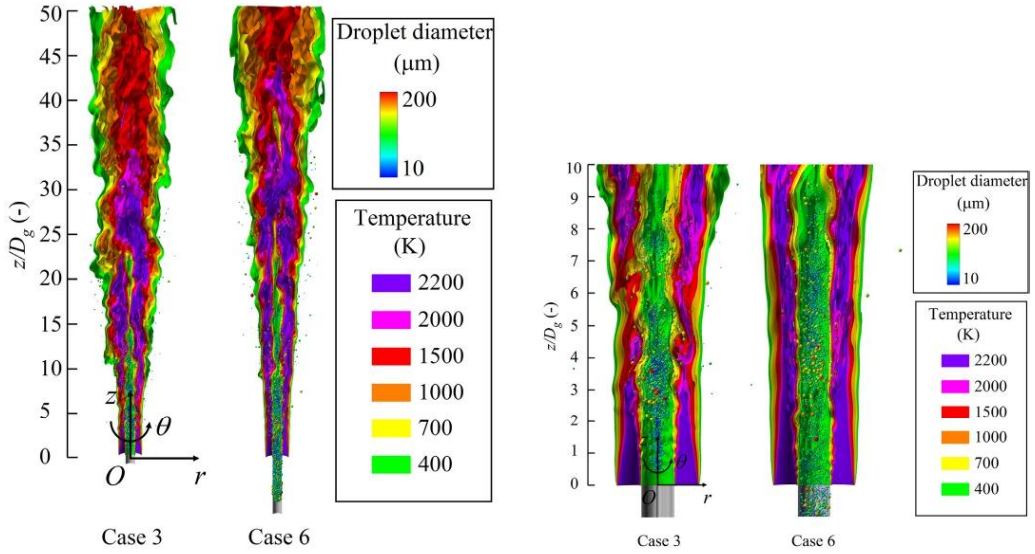

Fig. 12. Instantaneous gas temperature iso-surface and droplet distribution for Cases 3 and 6.

Table 3
Chi-square homogeneity check for the database A1.

A1	$0-\pi/2$	$\pi/2-\pi$	$\pi-3\pi/2$	$3\pi/2-2\pi$	Total
0–50 μm	0.12	0.27	4.88	1.77	7.04
50–150 μm	0.11	0.02	0.78	0.16	1.07
150–300 μm	0.56	0.22	0.80	1.32	2.9
Total	0.79	0.51	6.46	3.25	11.01

ods. Compared to other cells, there is an odd value particularly larger than the others, which is marked as red in $\pi \leq \theta < 3\pi/2$ with a diameter of less than 50 μm. It means that in the region $\pi \leq \theta < 3\pi/2$, more droplets with a diameter of less than 50 μm exist compared to the other three regions. Because the number of droplets with diameter of less than 0–50 μm is very small in the database A1 (see Fig. 6(a), black line), it is reasonable to observe such a bias that some region holds a different number of droplets because the droplets generated by the breakup fluctuate spatially and temporally. However, the total value of this case is 11.01, which is less than the critical value of 12.59, ensuring that the spatial distribution of the droplets has no obvious bias by sampling the five breakup periods from the 120,000th step to the 300,000th step.

Figure 10 shows the total values of each database by employing different sampling times from one to five periods. The total values of A1 and A2 continue decreasing when the sampling time is increased from one to five periods, out of which the total values of A4 continue fluctuating because the number of small droplets with a diameter of 0–50 μm of A4 is larger than those of the other three cases, thus those odd values (an example is shown in red in Table 3) are decreased such that the total value is much smaller than those of the other three cases. By sampling five breakup periods, all four databases hold reasonable total values to ensure the azimuthal homogeneity, and the sampling time is thus selected to be five breakup periods from the 120,000th step to the 300,000th step.

In total, for the atomization computation, the physical time is 15 ms, in which the first 6 ms is used for the liquid jet development to reach a steady state, and the last 9 ms is used for the droplet database sampling discussed in this section. For the combustion computation, the physical time is 100 ms such that the particle injection is cycled about 11 times.

4.3. Combustion characteristics

4.3.1. Simulation cases and flame features

As mentioned in Section 3.1, two different configurations, N-AF8-25 and N-AF8-80, are utilized with representative recess distance of 25 mm and 80 mm. In addition, two different inlet gas velocity profiles, one flat and the other extracted from the atomization computation, are incorporated to study the sensitivity of the dense spray flame to the inlet boundary conditions. Further, considering the computational cost, out of the four databases of A1 to A4 two databases, A1 and A4, are selected to investigate the influence of the droplet inlet boundary conditions on the flame characteristics because A1, A2, and A3 display similar droplet size profiles of D_{32} and D_{10}, whereas A1 holds different gas velocity compared to A2–A4. Therefore, a total of six cases are discussed as shown in Table 4, Fig. 11 provides a clear schematic of the conducted six cases. The orange lines depicted in the figure indicate the ACC planes, where the droplets are recorded in the atomization computation and are applied in the combustion computations as the inlet boundary conditions. In addition, the axial distance of the ACC plane Z_{ACC} relative to the pilot outlet, is displayed for a better understanding.

In dense sprays, laser diagnostic measurements are difficult owing to the co-existence of liquid fragments and abundant atomized droplets, which reflect and absorb the light. Therefore, a chirped-

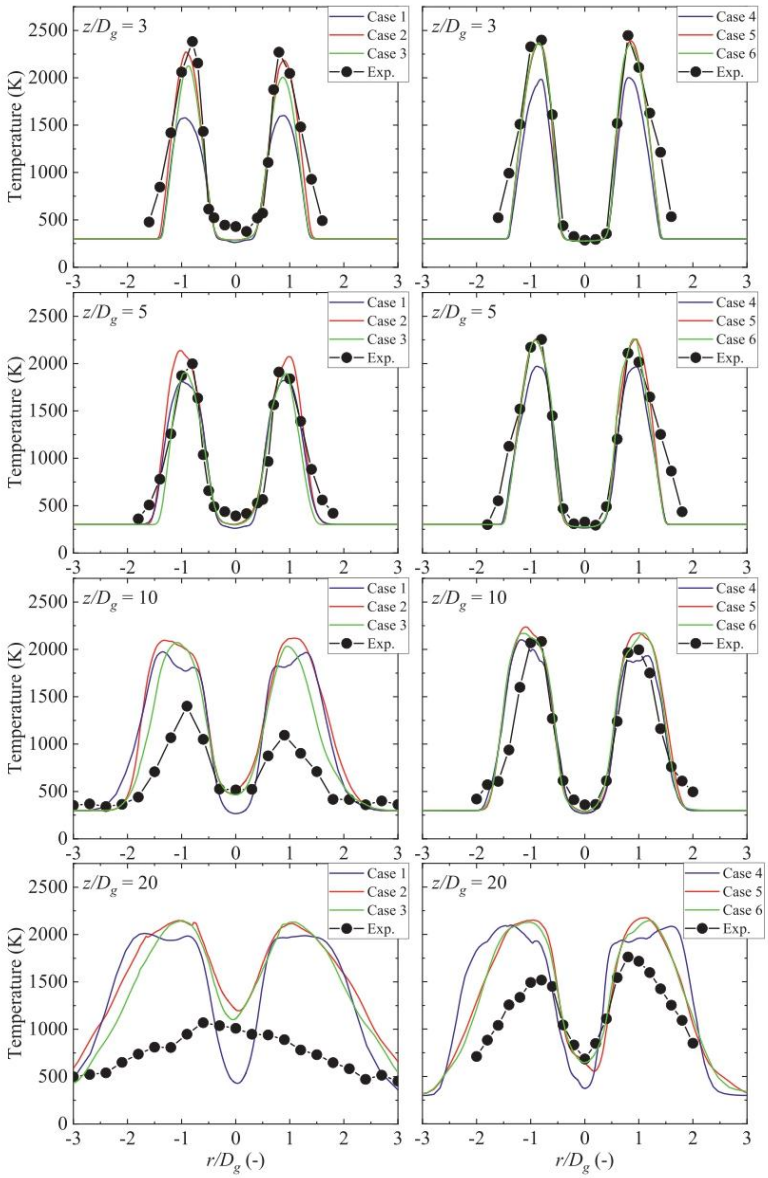

Fig. 13. Comparison of radial distributions of time-averaged of gas temperature at different axial downstream locations of $z/D_g = 3$, 5, 10, and 20 between combustion simulation and experiment for Cases 1–6. Left is for dense spray and right is for dilute spray.

probe-pulse femtosecond coherent anti-Stokes Raman spectroscopy (CPP-fs-CARS) with a repetition rate of 5 kHz was employed by Thomas and Lowe [49,50] to measure the gas temperature distribution based on the platform of the Sydney Burner, which supplies various gas temperature profiles ranging from dense to dilute sprays with ethanol and acetone fuels. The gas temperature distributions in both the dense and dilute sprays with the acetone fuel are considered in this work to validate the proposed numerical simulations.

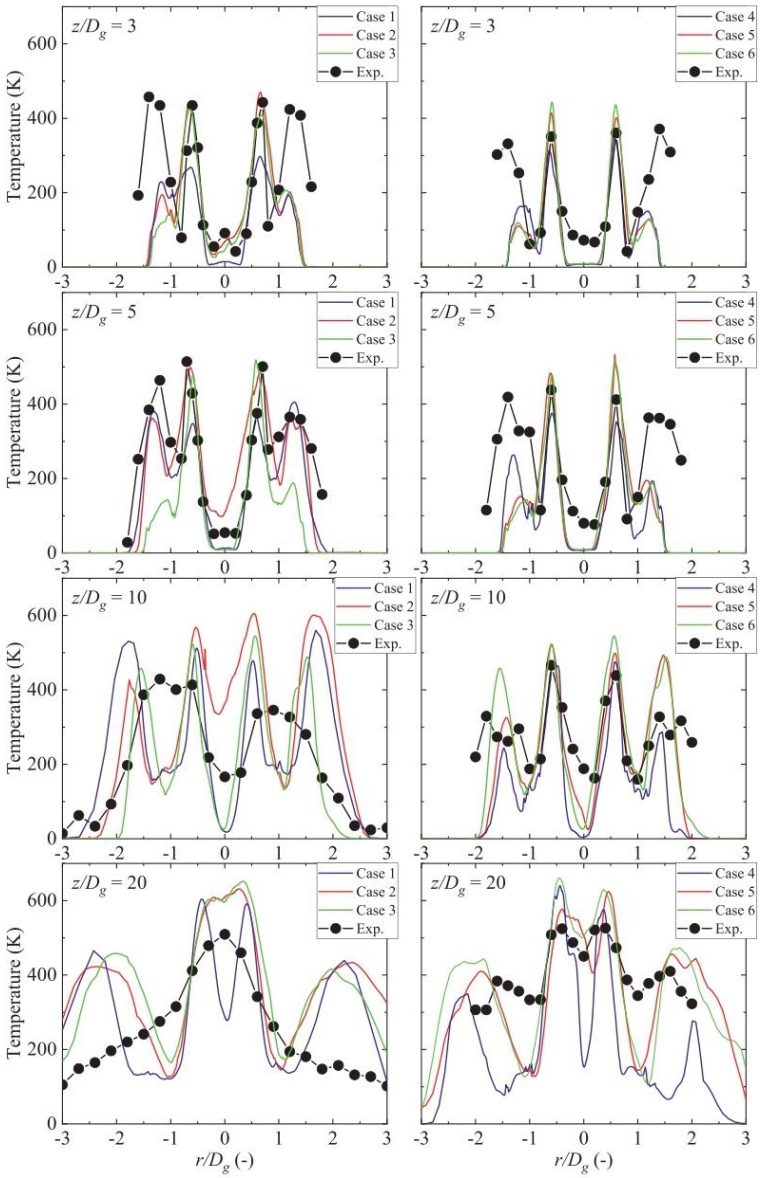

Fig. 14. Comparison of radial distributions of RMS of gas temperature at different axial downstream locations of z/D_g = 3, 5, 10, and 20 between combustion simulation and experiment for Cases 1–6. Left is for dense spray and right is for dilute spray.

Table 4
Conducted cases for combustion simulation.

Case	Velocity profile	Atomization database	Configuration
1	Flat	A1	Dense
2	Atomization	A1	(N-AF8-25)
3	Atomization	A4	
4	Flat	A1	Dilute
5	Atomization	A1	(N-AF8-80)
6	Atomization	A4	

Figure 12 shows the instantaneous gas temperature profiles and fuel droplets distribution for Cases 3 and 6. The double reaction zone, where a premixed core is inside a surrounding non-premixed zone, can be observed. The premixed cores are extended in both the span and axial directions despite the recess distance changes from 25 to 80 mm. Meanwhile, each temperature iso-surface in Case 3 is shorter than that of Case 6, which means that the dilute spray (Case 6) with a longer recess distance can enhance the mixing and combustion processes.

4.3.2. Comparisons with experiments

Figures 13 and 14 show the radial distributions of the time-averaged and RMS of gas temperature at different axial downstream locations, $z/D_g = 3$, 5, 10, and 20, where the experimental data are compared with simulations of Cases 1–6 detailed in Table 4. The influences of the inflow gas velocity profiles and inflow droplet profiles are discussed.

The computed results of the mean gas temperature depict a symmetric unimodal distribution at different axial locations, and at the downstream of $z/D_g = 20$, the peak temperature is suppressed. However, based on the experiments at $z/D_g = 20$, the symmetric unimodal distribution is absent for the dense case, and is still distinguished in the dilute case. The reason for this difference is thought to be the result of a higher proportion of fragments and filaments presented in the dense case [49,50], which leads to a less stable and lower mean temperature. By contrast, at the upstream locations of $z/D_g = 3$, the flame is more dominated by the pilot flame such that the reaction zone is less affected by the spray properties and a similar temperature profile is observed for both dense and dilute flame cases. Regarding the simulation results, the atomization velocity presents its priory in comparison to the flat one, showing a good agreement with experiments at the upstream region. Even for the $z/D_g = 10$ of the dilute cases, the temperature distribution still matches very well. For both cases with atomization velocity profiles, the temperature distributions do not show much difference though the D_{32}, D_{10}, and PDF distribution of droplet diameter show a significant difference (see Figs. 6(a) and 7(b)). However, some discrepancies can still be observed, i.e., cases with atomization gas velocity and smaller droplets (Cases 3 and 6) have intermediate values between the cases with flat gas velocity and larger droplets (Cases 1 and 4), and cases with atomization gas velocity and larger droplets (Cases 2 and 5). This is because the turbulence generated by the primary breakup during the atomization process of Cases 3 and 6 (5 mm downstream of the pilot outlet) is weaker than that of Cases 2 and 5 (5 mm upstream of the pilot outlet), but stronger than the flat ones. In addition, the difference disappears when the recess distance is increased from 25 to 80 mm based on a comparison of the differences between a dense spray (Cases 2 and 3) and a dilute spray (Cases 5 and 6) because the ACCs, where the turbulence in the atomization computation is recorded, are 5 mm upstream and 5 mm downstream of the pilot outlet for a dense spray, but are 60 and 50 mm upstream of the pilot outlet for a dilute spray, as shown in Fig. 11. Therefore, the difference in turbulence owing to different ACCs finally disappears at the pilot outlet for a dilute spray.

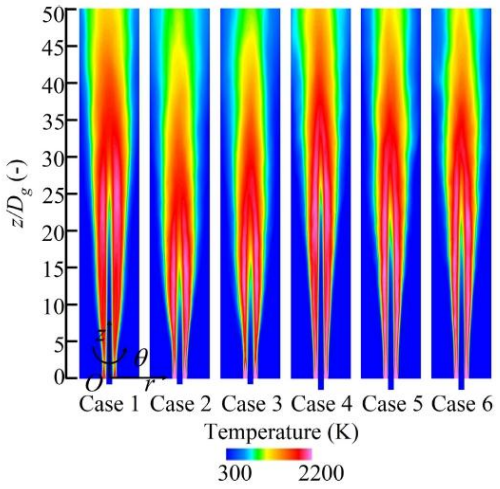

Fig. 15. Comparison of distribution of time-averaged of gas temperature for Cases 1–6.

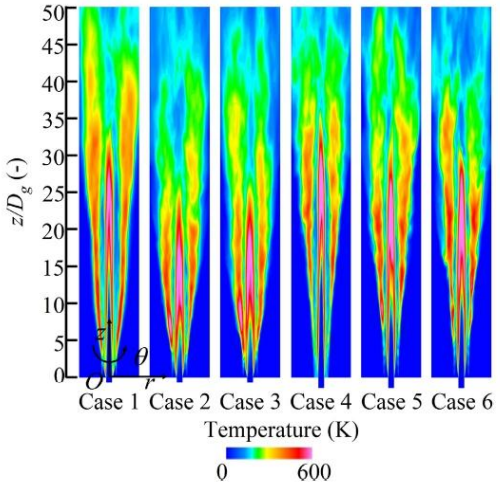

Fig. 16. Comparison of distribution of RMS of gas temperature for Cases 1–6.

An obvious discrepancy is seen between the simulation results and the experimental data at the downstream location of $z/D_g = 20$ of a dense spray, where the temperatures of simulation are overpredicted. In contrast to which, in a dilute spray, the temperature profiles of simulation match those of experiment very well and only drift away at the downstream location of $z/D_g = 20$, which is still not that obvious compared to that in a dense spray. The good agreement in the upstream region is due to the well-controlled boundary conditions which are also the interest of the present study. In addition, a suitable flamelet model or a better combustion mechanism may help to improve the difference observed in the downstream region for the dilute spray. However, for the great discrepancy in the dense spray, the situation is totally

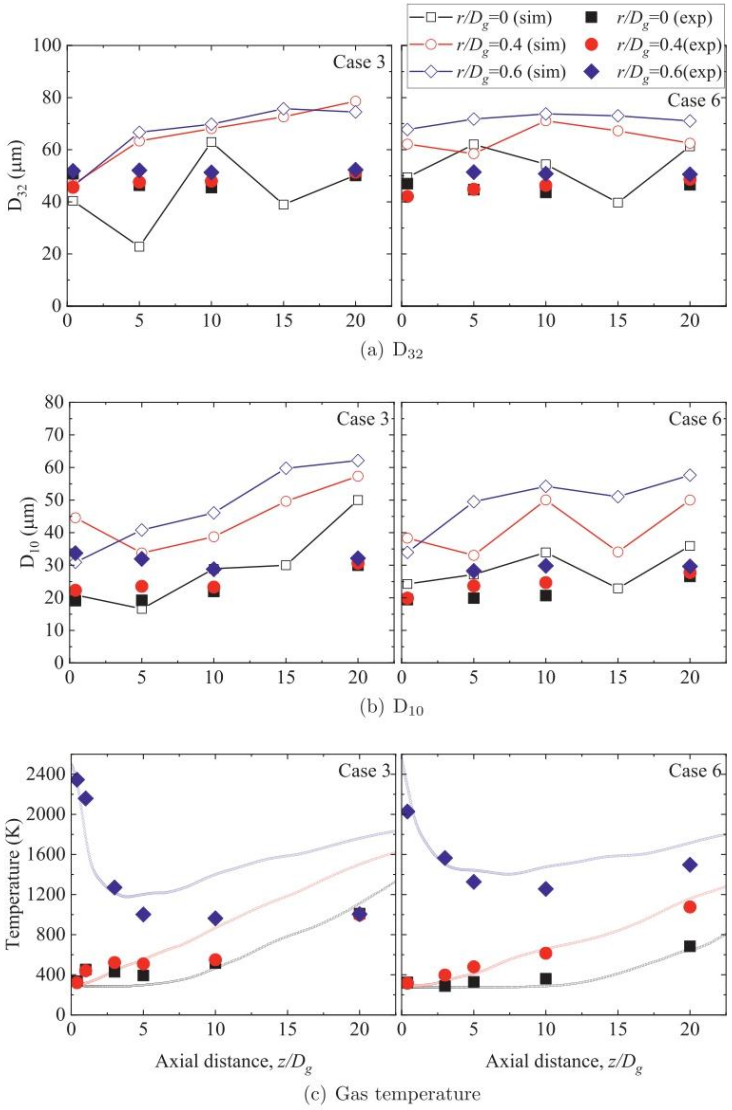

Fig. 17. Comparison of streamwise distributions of time-averaged droplet sizes (D_{32} and D_{10}) and gas temperature at different radial locations of $r/D_g = 0$, 0.4, and 0.6 between combustion simulation and experiment for Cases 3 and 6. Only droplets diameter less than 0.1 mm are counted.

different. According to the experiment [50], a speculation is proposed that the combustion is finished in the downstream location of $z/D_g = 20$ even there exists fuel droplets such that the temperature distribution does not present the symmetric unimodal distribution. On the other hand, the combustion is still happening in the simulation such that an overestimation as well as a totally different structure could be observed. The dense spray region has much more larger ligaments and irregular shaped objects that cannot be consumed, and those larger liquid components generated by the primary breakup easily cause more unpredicted turbulence when they flow downstream and breakup into smaller droplets. Therefore, the local flow field is extremely unstable in the downstream region, which is different from the upstream region where the disturbances of those ligaments and irregular shaped objects have not developed. Therefore, the burning process might not occur much or just be finished, while the fuel is still present there, resulting in a

lower local temperature distribution. However, in the present simulation, the larger ligaments and irregular shaped objects are just simply transformed into Lagrangian droplets, failing to consider the realistic interaction between the gas phase and liquid fuel, as well as the further breakup behavior. Therefore, the Lagrangian droplets continue to be consumed when they reach further downstream, ensuring a continuous burning without any negative influences on the combustion, and thus a higher temperature distribution could be observed. However, the unstable flow field caused by those ligaments and irregular shaped objects may have significant influences on the fuel droplet evaporation and fuel vapor heat release. Another possibility is that the larger ligaments and irregular shaped objects tend to disperse further in the radial direction and thus the heavier ligaments and irregular shaped objects finally fall when they flow out of the flame zones. However, the total energy of the simulation is conserved such that the temperature distribution of the experiment is lower than that of the simulation.

The profiles of the RMS of gas temperature show a twin peak on the both sides of the centerline until $z/D_g = 10$, which is less distinct for the dense case. This twin peak structure is also well-captured by the present study for all six cases, and the Cases 3 and 6 still have the intermediate values. The computational results show a reasonable match with the experiments near the center axis, and some discrepancies away from the center axis. In the experiment work, the temperature is strongly affected by the pilot flame in the outer space, such that the temperature distribution out of $-1.25 \leq r/D_g \leq 1.25$, outside the edge of the pilot flame, presents some discrepancies. In addition, owing to the larger ligaments and irregular shaped objects mentioned in the last paragraph, it is difficult to capture the accurate temperature distributions in the dense spray cases. Therefore, the discrepancies tend to become eliminated when the recess distance is increased from 25 to 80 mm around the nozzle centerline from $r/D_g = -1$ to $r/D_g = 1$, except for the location at $z/D_g = 20$, where the combustion of dense spray in the experiment is considered to be completed.

Figures 15 and 16 show the distributions of the time-averaged and RMS of gas temperature until the downstream location of $z/D_g = 50$ for all six cases. It can be seen that, compared to the results on the assumption of a uniform inlet boundary condition, the use of inlet velocities determined from the atomization computation can enhance the mixing and establish the combustion at the most upstream locations. On the other hand, the profiles of the fluctuating temperature indicate that the differences of droplets in databases A1 and A4 may not have a significant influence on the combustion characteristics when comparing Cases 2 and 3 as well as Cases 5 and 6. In addition, the symmetrical flame structures in all cases prove that the droplet databases sampled from the atomization computation have no biases in any directions. This confirms that the proposed sampling method coupling the atomization and combustion computations is successful.

Figure 17 shows the streamwise distributions of the time-averaged droplet sizes (D_{32} and D_{10}) and gas temperature of Cases 3 and 6 at different radial locations of $r/D_g = 0$, 0.4, and 0.6 in comparison with the experiment results. Due to the limitation of the experiment measurement of Phase Doppler Anemometry (PDA), the measured droplet size is limited to 100 μm. Therefore, the calculations of D_{32} and D_{10} omit the Lagrangian droplets with a diameter of larger than 100 μm. However, the droplet size distributions between simulation and experiment still show large discrepancies, and the discrepancies might result from two reasons from the views of simulation and experiment. From the view of simulation, the E-L transformation utilized in the present study might improperly transform the larger ligaments and irregular shaped objects into Lagrangian droplets leading to an increment in droplet size. From the view of experiment, the PDA has severe criterion to measure sphere droplets and most sphere droplets holds relatively smaller diameter to maintain the shape, which leads to a decrease in droplet size. However, there are still some shared properties for the droplet size in simulation and experiment. Both D_{32} and D_{10} increase from center to side despite increasing the recess distance from 25 to 80 mm. For the dense spray, the D_{32} values increase slightly further downstream from $z/D_g = 0.4$–20, whereas for the dilute spray, the D_{32} values decrease slightly from $z/D_g =$ 10–20, which also match the experiment results at the radial locations of $r/D_g = 0.4$ and 0.6. The D_{10} values of the simulation keep increasing in a dense spray and keep fluctuating in a dilute spray, whereas the D_{10} values of the experiment keep fluctuating in a dense spray and keep increasing in a dilute spray. This opposite development is considered to be a result of omitting the larger Lagrangian droplets artificially. Since D_{10} is more affected by the portion of small droplets, and the measured droplets in the experiment tend to hold smaller diameter whereas the transformed droplets in the simulation may hold larger diameter, hence it is difficult for the simulation to predict the D_{10} values. Regarding the temperature development along with the axial direction, the dilute spray is considered to have a good agreement with the experiment at different radial locations. Whereas, for the dense spray, even good agreement can be observed at the center axis, it fails to capture the downstream temperatures especially for the outer locations of $r/D_g = 0.6$. This is probably because of insufficiency of the consideration of effect of liquid ligaments and irregular shaped objects existing away from the center axis, as mentioned before.

5. Conclusions

In this study, a numerical framework which is a one-way coupling between a VOF simulation and a combustion simulation was proposed, and the validity was investigated for the dense spray flames. Atomization was simulated by a detailed high-resolution VOF simulation, in which both continuum gas and liquid phases were strictly solved in a Eulerian framework, and the Eulerian components of the liquid droplets were transformed into the Lagrangian droplets at a certain downstream cross-section, i.e., sampling cross-section, whose information was stored in the database. Then, the combustion process was solved by a LES/FPV adopting the pre-stored database of Lagrangian droplets (i.e., the position, size, and velocity of each droplet) as the inlet boundary conditions. Computations were validated against measurement made in the Sydney Piloted Needle Spray Burner, which can generate both dilute and dense spray flames by varying the recess distance from the liquid fuel jet nozzle to the pilot outlet.

Regarding the detailed high-resolution VOF simulation of liquid fuel atomization, the volume flux of the droplets at the exit of the nozzle was observed to fluctuate both temporally and spatially, which meant that there exist periods of breakup and non-breakup during the atomization process. It was also found that the breakup period was in good agreement with an existing empirical correlation, and that, compared to the small droplets, larger droplets tended to be located away from the center axis. Meanwhile, in the database of the Lagrangian droplets for the LES/FPV of spray flames, the location of the sampling cross-section, sampling time, and threshold value for a Eulerian–Lagrangian (E-L) transformation were found to strongly affect the properties of the Lagrangian droplets, and to be critical for the success of the use of the LES/FPV of present spray flames.

By use of the optimal pre-stored droplets database, the results of LES/FPV of two flame cases with different recess distances showed generally similar trends with the experiment in terms of the gas temperature and droplet size distributions. The spray flame with a longer recess distance, which represents a dilute spray, was considered to have a longer and wider premixed core than that

with a shorter recess distance representing a dense spray. This behavior is believed to be due to the enhanced mixing between the evaporated fuel and oxidizer. For the dense spray flame, the discrepancy in the gas temperature between the prediction and experiment tended to become more evident, and when moving downstream, the over-predictions were observed. This was considered to be attributed to the fact that for the LES/FPV of the dense spray flame, the relatively large and non-spherical liquid components were regarded as the Lagrangian spherical droplets in the present E-L transformation, and therefore, their further breakup and influence on the turbulence development and flame evolution were neglected.

In summary, the numerical framework proposed in this study is capable of reproducing the spray atomization and the gas temperature distributions in dilute spray flames of Sydney Piloted Needle Burner with a relatively low computational cost and without any atomization model or presumed initial droplet size distribution. Some failures of gas temperature distributions in dense spray flames and droplet size distributions are discussed in detail which requires further investigations. The improvement of the E-L tagging method in generating droplet databases for relatively dense sprays merits future work.

Declaration of Competing Interest

The authors declare that they have no known competing financial interests or personal relationships that could have appeared to influence the work reported in this paper.

Acknowledgments

This work was partially supported by MEXT as "Program for Promoting Researches on the Supercomputer Fugaku" (Digital Twins of Real World's Clean Energy Systems with Integrated Utilization of Super-simulation and AI) and by JSPS KAKENHI Grant number 19H02076. YH acknowledges the support of the National Natural Science Foundation of China (Grant no. 52006151) and "the Fundamental Research Funds for the Central Universities" (YJ201943). AM is supported by the Australian Research Council. The authors also thank Dr. A. Lowe for providing us the detailed configuration of the Sydney Burner.

Appendix A. Details of Chi square homogeneity check for droplet spatial distribution analysis

The homogeneity analysis for droplet spatial distribution is discussed in details. As mentioned in Section 4.2.2, the angle θ in the radial plane and the droplet size can be used to analyze the droplet spatial distribution. The space can be divided into four mathematical quadrants, i.e., $0 \le \theta < \pi/2$, $\pi/2 \le \theta < \pi$, $\pi \le \theta < 3\pi/2$, and $3\pi/2 \le \theta < 2\pi$, to check the preference in different radial directions, and the droplet size can be divided into three clusters, i.e., 0–50 μm, 50–150 μm, and 150–300 μm to check the distance bias in a certain radial direction. The Chi-square homogeneity validation is a method generally used to analyze the data homogeneity in different clusters, and the data can be regarded as homogeneous if the accumulated value is satisfied. First, the degree of freedom for the Chi-square is calculated as $df = (\text{row} - 1) \times (\text{col} - 1)$, where df indicates the degree of freedom, row is the number of rows, with three droplet size clusters herein; col is the number of columns, i.e., the 4 mathematical quadrants, as shown in Table 3. Therefore, the degree of freedom is $df = (3-1) \times (4-1) = 6$. The critical value (with 95% confidence level) under a degree of freedom of 6 can be found to be 12.59 according to the statistics, which means that if the total value of all cells is less than 12.59, then the data can be confirmed to have a 95% possibility to ensure the azimuthal homogeneity of the droplet distribution. The calculation algorithm is very simple, which is briefly introduced. For the cell i in a certain row and column, there is a statistic F_i by counting the number of droplets which satisfy the conditions (i.e., droplet size and angle), and thus a total value of the row or column can be calculated. Based on the statistic of cell i and total values of rows and columns, the expected value of cell i could be calculated as E_i. Then, the total value of all cells, X^2, of one database can be calculated as $X^2 = \sum_{i=1}^{n}((E_i - F_i)^2/E_i^2)$. By using this Chi-square homogeneity check, if the total value is less than the critical value of 12.59, it can be said that the droplets are homogeneously distributed in the four mathematical quadrants ($0 \le \theta < \pi/2$, $\pi/2 \le \theta < \pi$, $\pi \le \theta < 3\pi/2$, and $3\pi/2 \le \theta < 2\pi$) with smaller droplets close to the center axis and larger droplets away from the center axial such that the database can be considered to have no special preferences existing in a specific direction.

References

[1] A.R. Masri, Turbulent combustion of sprays: from dilute to dense, Combust. Sci. Tech. 188 (2016) 1619–1639.
[2] M. Linne, Imaging in the optically dense regions of a spray: a review of developing techniques, Prog. Energy Combust. Sci. 39 (2013) 403–440.
[3] H. Chiu, T. Liu, Group combustion of liquid droplets, Combust. Sci. Tech. 17 (1977) 127–142.
[4] A. Umemura, Interactive droplet vaporization and combustion: approach from asymptotics, Prog. Energy Combust. Sci. 20 (1994) 325–372.
[5] S. Li, Spray stagnation flames, Prog. Energy Combust. Sci. 23 (1997) 303–347.
[6] E. Gutheil, W. Sirignano, Counterflow spray combustion modeling with detailed transport and detailed chemistry, Combust. Flame 113 (1998) 92–105.
[7] A.Y. Klimenko, R.W. Bilger, Conditional moment closure for turbulent combustion, Prog. Energy Combust. Sci. 25 (1999) 25–62.
[8] V. Gopalakrishnan, J. Abraham, Effects of multicomponent diffusion on predicted ignition characteristics of a n-heptane diffusion flame, Combust. Flame 136 (2004) 557–566.
[9] H. Pitsch, M. Ihme, An Unsteady/Flamelet Progress Variable Method for LES of non-Premixed Turbulent Combustion, AIAA Paper No. 2005–557.
[10] J. Reveillon, L. Vervisch, Analysis of weakly turbulent dilute-spray flames and spray combustion regimes, J. Fluid. Mech 537 (2005) 317–347.
[11] M. Nakamura, F. Akamatsu, R. Kurose, M. Katsuki, Combustion mechanism of liquid fuel spray in a gaseous flame, Phys. Fluids 17 (2005) 1–14.
[12] J. Reveillon, F.X. Demoulin, Evaporating droplets in turbulent reacting flows, Proc. Combust. Inst. 31 (2007) 2319–2326.
[13] H. Watanabe, R. Kurose, S.M. Huang, F. Akamatsu, Characteristics of flamelets in spray flames formed in a laminar counterflow, Combust. Flame 148 (2007) 234–248.
[14] N. Abani, A. Munnannur, R.D. Reitz, Reduction of numerical parameter dependencies in diesel spray models, J. Eng. Gas Turbines Power 130 (2008) 032809.
[15] Y. Baba, R. Kurose, Analysis and flametlet modelling for spray combustion, J. Fluid. Mech. 612 (2008) 45–79.
[16] M. Ihme, Y.C. See, Prediction of autoignition in a lifted methane / air flame using an unsteady flamelet/progress variable model, Combust. Flame 157 (2010) 1850–1862.
[17] R. Bilger, A mixture fraction framework for the theory and modeling of droplets and sprays, Combust. Flame 158 (2011) 191–202.
[18] K. Luo, H. Pitsch, M.G. Pai, O. Desjardins, Direct numerical simulations and analysis of three-dimensional n-heptane spray flames in a model swirl combustor, Proc. Combust. Inst. 33 (2011) 2143–2152.
[19] M.R. Turner, S.S. Sazhin, J.J. Healey, C. Crua, S.B. Martynov, A breakup model for transient diesel fuel sprays, Fuel 97 (2012) 288–305.
[20] C. Bajaj, M. Ameen, J. Abraham, Evaluation of an unsteady flamelet progress variable model for autoignition and flame lift-off in diesel jets, Combust. Sci. Tech. 185 (2013) 454–472.
[21] S. Ukai, A. Kronenburg, O.T. Stein, LES-CMC of a dilute acetone spray flame, Proc. Combust. Inst. 34 (2013) 1643–1650.
[22] S. De, S.H. Kim, Large eddy simulation of dilute reacting sprays: droplet evaporation and scalar mixing, Combust. Flame 160 (2013) 2048–2066.
[23] S. Tachibana, K. Saito, T. Yamamoto, M. Makida, T. Kitano, R. Kurose, Experimental and numerical investigation of thermos-acoustic instability in a liquid–fuel aero-engine combustor at elevated pressure: validity of large-eddy simulation of spray combustion, Combust. Flame 162 (2015) 2621–2637.
[24] T. Kitano, K. Kaneko, R. Kurose, S. Komori, Large-eddy simulations of gas- and liquid-fueled combustion instabilities in back-step flows, Combust. Flame 170 (2016) 63–78.
[25] L. Ma, D. Roekaerts, Numerical study of the multi-flame structure in spray combustion, Proc. Combust. Inst. 36 (2017) 2603–2613.
[26] B. Wang, A. Kronenburg, G.L. Tufano, O.T. Stein, Fully resolved DNS of droplet array combustion in turbulent convective flows and modelling for mixing filed in inter-droplet space, Combust. Flame 189 (2018) 347–366.
[27] A. Pillai, R. Kurose, Combustion noise analysis of a turbulent spray flame using a hybrid DNS/APE-RF approach, Combust. Flame 200 (2019) 168–191.

[28] Y. Hu, R. Kurose, Nonpremixed and premixed flamelets LES of partially premixed spray flames using a two-phase transport equation of progress variable, Combust. Flame 188 (2018) 227–242.
[29] Y. Hu, R. Kurose, Partially premixed flamelet in LES of acetone spray flames, Proc. Combust. Inst. 37 (2019) 3327–3334.
[30] Y. Hu, R. Kai, R. Kurose, E. Gutheil, H. Olguin, Large eddy simulation of a partially pre-vaporized ethanol reacting spray using the multiphase DTF/flamelet model, Int. J. Multiph. Flow 125 (2020) 103216.
[31] Y. Hardalupas, A. Taylor, J.H. Whitelaw, Mass flux, mass fraction and concentration of liquid fuel in a swirl-stabilized flame, Int. J. Multiph. Flow 20 (1994) 233–259.
[32] G. Chen, A. Gomes, Dilute laminar spray diffusion flames near the transition from group combustion to individual droplet burning, Combust. Flame 110 (1997) 392–404.
[33] M. Alden, J. Bood, Z. Li, M. Richter, Visualization and understanding of combustion processes using spatially and temporally resolved laser diagnostic techniques, Proc. Combust. Inst. 33 (2011) 69–97.
[34] D. Cavaliere, J. Kariuki, E. Mastorakos, A comparison of the blow-off behaviour of swirl-stabilized premixed, non-premixed and spray flames, Flow Turbul. Combust. 91 (2013) 347–372.
[35] M. Chrigui, J. Gounder, A. Sadiki, J. Janicka, A.R. Masri, Acetone droplet behavior in reacting and non reacting turbulent flow, Flow Turbul. Combust. 90 (2013) 419–447.
[36] H. Luo, K. Nishida, S. Uchitomi, Y. Ogata, W. Zhang, T. Fujikawa, Effect of temperature on fuel adhesion under spray-wall impingement condition, Fuel 234 (2018) 56–65.
[37] A. Verdier, J.M. Santiago, A. Vandel, G. Godard, G. Cabot, B. Renou, Local extinction mechanisms analysis of spray jet flame using high speed diagnostics, Combust. Flame 193 (2018) 440–452.
[38] I.A. Mulla, G. Godard, G. Cabot, F. Grisch, B. Renou, Quantitative imaging of nitric oxide concentration in a turbulent -heptane spray flame, Combust. Flame 203 (2019) 217–229.
[39] D.R. Guildenbecher, C. Lopez-Rivera, P.E. Sojka, Secondary atomization, Exp. Fluids 46 (2009) 371–402.
[40] X. Jiang, G. Siamas, K. Jagus, T. Karyiannis, Physical modelling and advanced simulations of gas-liquid two-phase jet flows in atomization and sprays, Prog. Energy Combust. Sci. 36 (2010) 131–167.
[41] M. Herrmann, Detailed numerical simulations of the primary atomization of a turbulent liquid jet in crossflow, J. Eng. Gas Turbines Power 132 (2010) 061506.
[42] N. Ashgriz, Atomization of a liquid jet in a crossflow, AIP Conf. Proc. 1440 (2012) 33–46.
[43] X. Li, M.C. Soteriou, Detailed numerical simulation of liquid jet atomization in crossflow of increasing density, Int. J. Multiph. Flow 104 (2018) 214–232.
[44] A. Umemura, J. Shinjo, Detailed SGS atomization model and its implementation to two-phase flow LES, Combust. Flame 195 (2018) 232–252.
[45] T.-W. Lee, J.E. Park, R. Kurose, Determination of the drop size during atomization and liquid jets in cross flows, At. Sprays 28 (2018) 241–254.
[46] J. Wen, Y. Hu, A. Nakanishi, R. Kurose, Atomization and evaporation process of liquid fuel jets in crossflows: a numerical study using Eulerian/Lagrangian method, Int. J. Multiph. Flow 129 (2020) 103331.
[47] A. Pillai, J. Nagao, R. Awane, R. Kurose, Influences of liquid fuel atomization and flow rate fluctuations on spray combustion instabilities in a backward-facing step combustor, Combust. Flame 220 (2020) 337–356.
[48] J.D. Gounder, A. Kourmatzis, A.R. Masri, Turbulent piloted dilute spray flames: flow fields and droplet dynamics, Combust. Flame 159 (2012) 3372–3397.
[49] L.M. Thomas, A. Lowe, A. Satija, A.R. Masri, R.P. Lucht, Five kHz thermometry in turbulent spray flames using chirped-probe pulse femtosecond CARS, part I: processing and interference analysis, Combust. Flame 200 (2019) 405–416.
[50] A. Lowe, L.M. Thomas, A. Satija, R.P. Lucht, A.R. Masri, Five kHz thermometry in turbulent spray flames using chirped-probe pulse femtosecond CARS, part II: structure of reaction zones, Combust. Flame 200 (2019) 417–432.
[51] H. Moriai, R. Kurose, H. Watanabe, Y. Yano, F. Akamatsu, S. Komori, Large-eddy simulation of turbulent spray combustion in a subscale aircraft jet engine combustor-predictions of NO and soot concentrations, J. Eng. Gas Turbines Power 135 (2013) 091503.
[52] A. Kishimoto, H. Moriai, K. Takenaka, T. Nishiie, M. Adachi, A. Ogawara, R. Kurose, Application of a non-adiabatic flamelet/progress-variable approach to large eddy simulation of H_2/O_2 combustion under a pressurized condition, J. Heat Transf. 139 (2017) 124501.
[53] J.U. Brackbill, D.B. Kothe, C. Zemach, A continuum method for modeling surface tension, J. Comput. Phys. 100 (1992) 335–354.
[54] S. Muzaferija, M. Peric, Computation of free-surface flows using interface–tracking and interface-capturing methods, in: O. Mahrenholtz, M. Markiewicz (Eds.), Nonlinear Water Wave Interaction, Computational Mechanics Publications, Southampton (1998), pp. 59–100.
[55] A. Albadawi, D.B. Donoghue, A.J. Robinson, D.B. Murray, Y.M.C. Delauré, Influence of surface tension implementation in volume of fluid and coupled volume of fluid with level set methods for bubble growth and detachment, Int. J. Multiph. Flow 53 (2013) 11–28.
[56] M. Herrmann, A parallel Eulerian interface tracking/Lagrangian point particle multi-scale coupling procedure, J. Comput. Phys. 229 (2010) 745–759.
[57] C.D. Pierce, P. Moin, Progress-variable approach for large-eddy simulation of non-premixed turbulent combustion, J. Fluid Mech. 504 (2004) 73–97.
[58] N. Lallemant, A. Sayre, R. Weber, Evaluation of emissivity correlations for H_2O-CO_2-N_2/air mixtures and coupling with solution methods of the radiative transfer equation, Prog. Energy Combust. 22 (1996) 543–574.
[59] H. Pitsch, H. Steiner, Large-eddy simulation of a turbulent piloted methane/air diffusion flame (Sandia flame D), Phys. Fluids 12 (2000) 2541.
[60] D.K. Lilly, A proposed modification of the Germano subgridscale closure method, Phys. Fluids A 4 (1992) 633–635.
[61] C.T. Crowe, M.P. Sharma, D.E. Stock, The particle-source-in cell (PSI-CELL) model for gas-droplet flows, J. Fluid Eng. Trans. ASME 99 (1977) 325–332.
[62] R.S. Miller, K. Harstad, J. Bellan, Evaluation of equilibrium and non-equilibrium evaporation models for many-droplet gas-liquid flow simulations, Int. J. Multiph. Flow 24 (1998) 1025–1055.
[63] R. Kurose, H. Makino, S. Komori, M. Nakamura, F. Akamatsu, M. Katsuki, Effects of outflow from the surface of a sphere on drag, shear lift, and scalar diffusion, Phys. Fluids 15 (2003) 2338–2351.
[64] T. Kitano, J. Nishio, R. Kurose, S. Komori, Evaporation and combustion of multicomponent fuel droplets, Fuel 136 (2014) 219–225.
[65] T. Kitano, J. Nishio, R. Kurose, S. Komori, Effects of ambient pressure, gas temperature and combustion reaction on droplet evaporation, Combust. Flame 161 (2014) 551–564.
[66] P.J. O'Rourke, A.A. Amsden, The TAB Method for Numerical Calculation of Spray Droplet Breakup, SAE Paper, 1987.
[67] H. Pitsch, Flamemaster: a C++ computer program for 0D combustion and 1D laminar flame calculations, Cited in, 1998, p. 81.
[68] S. Pichon, G. Black, N. Chaumeix, M. Yahyaoui, J.M. Simmie, H.J. Curran, R. Donohue, The combustion chemistry of a fuel tracer: measured flame speeds and ignition delays and a detailed chemical kinetic model for the oxidation of acetone, Combust. Flame 156 (2009) 494–504.
[69] D. Zuzio, J.E. ezes, B. DiPierro, An improved multiscale Eulerian–Lagrangian method for simulation of atomization process, Comput. Fluids 176 (2018) 285–301.
[70] S. Elghobashi, Particle-laden turbulent flows: direct simulation and closure models, Appl. Sci. Res. 48 (1991) 301–314.
[71] J.-P. Matas, S. Marty, A. Cartellier, Experimental and analytical study of the shear instability of a gas-liquid mixing layer, Phys. Fluids 23 (2011) 094112.
[72] J.-P. Matas, A. Delon, A. Cartellier, Shear instability of an axisymmetric air-water coaxial jet, J. Fluid Mech. 843 (2018) 575–600.

Combustion and Flame 220 (2020) 337–356

Contents lists available at ScienceDirect

Combustion and Flame

journal homepage: www.elsevier.com/locate/combustflame

Influences of liquid fuel atomization and flow rate fluctuations on spray combustion instabilities in a backward-facing step combustor

Abhishek L. Pillai*, Jun Nagao, Ryo Awane, Ryoichi Kurose

Department of Mechanical Engineering and Science, Kyoto University, Kyoto daigaku-Katsura, Nishikyo-ku, Kyoto 615-8540, Japan

ARTICLE INFO

Article history:
Received 5 June 2019
Revised 18 June 2020
Accepted 21 June 2020
Available online 20 July 2020

Keywords:
Spray combustion instability
Turbulent spray combustion
LES

ABSTRACT

Combustion instabilities occurring in spray combustion fields inside a backward facing step combustor have been investigated by performing large-eddy simulations (LES). In this study, the influence of fluctuations in the incoming oxidizer air velocity (caused by drastic pressure oscillations in the combustor during combustion instability) on the droplet diameter distribution (due to atomization) of the injected liquid fuel spray, as well as the influence of pressure oscillations on the fuel flow rate have been taken into consideration using appropriate models. For the temporal fluctuations in fuel droplet diameter distribution, a model for the Sauter Mean Diamter (SMD) of atomized droplets, obtained as a function of spray injection parameters and gas/liquid properties, is incorporated in the LES. Additionally, to consider the temporal fluctuations in fuel flow rate along with its phase difference with the pressure oscillations, a model derived from Bernoullis principle is proposed and employed in the LES. The objective is to examine in detail, the impacts of the fluctuations in fuel droplet diameter distribution and the fluctuations in fuel injection rate individually, as well as the impact of the mutual interaction of these two fluctuations, on the spray combustion instability characteristics. Results of the LES reveal that the temporal fluctuations in fuel droplet diameter distribution resulting from combustion instability, lead to a reduction in the intensity of pressure oscillations and hence the combustion instability's strength. Additionally, the temporal fluctuations in liquid fuel flow rate strongly influence the intensity of spray combustion instability, and it is observed that the combustion instability intensity increases with the increase in phase difference between the fuel flow rate fluctuations and pressure oscillations. Furthermore, the effect of the temporal fluctuations in fuel droplet diameter distribution resulting in the reduction of combustion instability intensity, becomes more pronounced as the phase shift between the fuel flow rate fluctuations and pressure oscillations becomes larger. It is clarified that the above-mentioned behavior of spray combustion instability, results from the change in the correlation between heat release rate fluctuations and pressure oscillations near the combustor's dump plane, which is caused by the change in the local residence time of fuel droplets and the local fuel droplet evaporation rate.

1. Introduction

The global civil air traffic has grown steadily over the last decade, and the demand for passenger and cargo transportation is expected to increase even further in the near future. This is evidenced by the International Civil Aviation Organization's (ICAO) annual global statistics [1], according to which 4.1 billion passengers were carried on scheduled services in 2017 alone (a 7.2% rise than its predecessor year). Therefore, the need for clean and environmentally friendly gas turbine engines with better combustion efficiency has become ever so important. In particular, the regulations on toxic nitrogen oxide (NOx) emissions are becoming increasingly stringent, making the development of gas turbine engines that produce low levels of NOx highly desirable and mandatory [1]. Methods such as spraying fuel as a fine mist, pre-mixing air and fuel, and lean premixed prevaporized (LPP) combustion have attracted attention [2] as NOx regulatory compliance measures. Although the reduced combustion temperature of LPP combustion has the advantages of lower emissions of NOx and soot, this type of combustion also has increased unsteadiness, which increases the risk of occurrence of combustion instability [3–5].

Combustion instability is a form of unstable combustion generated inside the combustors of gas turbine engines, and is a

* Corresponding author.
E-mail address: pillai.abhisheklakshman.2e@kyoto-u.ac.jp (A.L. Pillai).

https://doi.org/10.1016/j.combustflame.2020.06.031

primary cause of combustor damage [4,5] and loud combustion noise. Hence, accurate prediction and control of this phenomenon is crucial for designing and developing efficient next generation engines. High amplitude pressure oscillations at discrete frequencies occur inside a combustor during such unstable combustion. Theoretically, combustion instability increases when there is a significant correlation between the heat release rate fluctuations and the pressure oscillations, i.e., the phase difference between the two fluctuations is small [6], because the energy of acoustic waves propagating in a combustor is increased as a consequence of the unsteady heat release (which means the pressure oscillations are amplified). However, the conditions leading to such an occurrence, its amplitude characteristics, and detailed mechanism are yet to be elucidated in depth. Currently, many studies are being conducted worldwide to clarify the mechanism of combustion instability and for its accurate prediction [e.g., [5],[7–11], [12]. In particular, compared to turbulent gaseous combustion with fuels such as natural gas, the combustion instability arising in spray combustion fields using liquid fuels such as kerosene, exhibits a more sophisticated phenomenon in which the dispersion and evaporation of liquid fuel droplets, and mixing of the evaporated fuel with the oxidizer followed by chemical reaction occur simultaneously and interactively, making the underlying physics very difficult to elucidate. In previous experimental studies, Lee et al. [9] determined that combustion instabilities can be actively controlled by modifying the properties of liquid fuel spray. Moreover, García et al. [10] reported that the evaporation of liquid fuel affects the frequency of combustion instability generated. However, because the data that can be collected from experiments are limited, the various factors affecting combustion instability characteristics have yet to be comprehensively clarified.

However, the remarkable improvement in computer performance and development of schemes/solvers capable of accurately and stably capturing the pressure perturbations in a combustion field in recent years, has allowed numerical analysis which can provide an abundance of data, to be used in studies on combustion instabilities [11–15]. Tachibana et al. [11], applied large-eddy simulation (LES) to the turbulent spray combustion field inside a liquid-fuel aero-engine combustor, and were the first to successfully reproduce combustion instability in a spray combustion field, as observed in their experiment performed at the Japan Aerospace Exploration Agency (JAXA). Later, Kitano et al. [12] performed LESs of turbulent spray combustion fields in a back-step flow combustor, to investigate the effect of initial droplet diameter of the liquid fuel spray injected into the combustor, on the combustion instability characteristics. It was clarified that the intensity of pressure oscillations during combustion instability is strongly affected by the initial fuel droplet diameter (the average droplet diameter d_{avg} for a fixed size distribution). However, they did not take into consideration the influence of temporal fluctuations in the fuel droplet size distribution and fuel flow rate on combustion instability. During combustion instability inside a back-step flow combustor, the velocity of incoming air fluctuates due to the pressure oscillations, which causes the fuel droplet size distribution to fluctuate as well (effect of varying level of atomization). Furthermore, the pressure oscillations also lead to fluctuations in the fuel flow rate.

Therefore, the purpose of this study is to elucidate the effects of temporal fluctuations in the droplet diameter distribution and the flow rate of liquid fuel into the combustor, on the spray combustion instability characteristics. In particular, a model capable of accounting for the temporal fluctuations in droplet diameter distribution of the injected fuel, due to secondary atomization of the liquid fuel is employed, and a model to account for the temporal fluctuations in fuel injection rate is proposed. By applying LES incorporating these models to the turbulent spray combustion fields in a back-step flow combustor, the effects of the individual models as well as the effects of their mutual interaction, on the characteristics of combustion instability can be investigated in detail.

2. Large-eddy simulation

Combustion instability is a transient phenomenon in which turbulent flow, combustion reaction and acoustic resonance are intertwined in a complex manner. Therefore, in order to realize its precise prediction, it is necessary to perform computations in a large domain that includes not only the targeted combustor region, but also the sections upstream and downstream of the combustor. Moreover, the computational grid must be sufficiently fine in the regions where combustion reaction occurs, and the simulation must be performed over a long time period to acquire time series data for analyzing the oscillation frequency. Hence, Large-eddy Simulation (LES) is adopted as the computation strategy for this work. The effect of liquid fuel atomization on combustion instability characteristics is investigated in detail, for turbulent spray combustion field in a back-step flow combustor. Additionally, the influence of temporal fluctuations in liquid fuel mass flow rate due to pressure fluctuations inside the combustor (arising from combustion instability itself) on the combustion instability characteristics are also examined. Furthermore, the influence on combustion instability characteristics is examined when phase differences are applied to the temporal fluctuations of the liquid fuel mass flow rate.

2.1. Governing equations

For LES of the gas-phase, which is treated as an Eulerian continuum, the Favre-filtered form of the conservation equations of mass, momentum, energy and mass fraction of chemical species are solved along with the state equation for ideal gas. Details of these governing equations can be found in the previous work [12]. For evaluation of the unresolved subgrid-scale (SGS) terms, the dynamic Smagorinsky model [16,17] is employed, and the spatial filter function used in the LES is a Gaussian filter. In order to resolve the flame-front on the computational grid of the LES [18–22] by artificially thickening it, the flame thickening factor F defined below, is introduced in the Favre-filtered conservation equations of enthalpy and species mass fraction [12]

$$F = (F_{max} - 1)\Omega + 1. \tag{1}$$

where the maximum flame thickening coefficient is $F_{max} = 12$. The term Ω in the above equation is called the flame sensor [18,21,22] which is used to detect the flame-front position. Ω varies from zero in fully burnt or unburnt regions to unity inside the reaction zone and is defined as

$$\Omega = \tanh\left(\alpha \frac{q}{q_{max}}\right). \tag{2}$$

where, q is the local heat release rate, and q_{max} is the maximum heat release rate computed from a one-dimensional laminar flame simulation. The thickness of the transition layer between non-reacting and reacting zones is regulated by the parameter α, and in the present simulations $\alpha = 5$ is used [12]. Thus, the dynamic version of Thickened Flame Model (TFM) is applied which smoothly modulates the thickening factor F from unity in the regions away from the flame front to large values inside the flame. Thickening is applied only in the vicinity of the reaction zones, and fuel droplet evaporation is active in the regions away from the flame front as well. As described later in Fig. 8, high rates of fuel droplet evaporation occur mainly in regions away from or outside the reaction zones. Hence, it is assumed that the influence of dynamically TFM

on fuel droplet evaporation is small enough to warrant any corrections for heat and mass exchanges between the dispersed- and gas-phases in the present LESs. Artificial thickening of the flame-front suppresses its interaction with the SGS turbulence, therefore, an efficiency function E is also introduced in the transport equations of enthalpy and species mass fraction [12], which serves as a correction for the loss of flame surface wrinkling due to artificial flame thickening, and is computed using the procedure described in [19,21].

Evolution of the fuel spray is governed by a set of Lagrangian equations describing the dynamics of individual fuel droplets which are treated as point masses. These are the governing equations for droplet trajectory $\boldsymbol{x}_d$, velocity $\boldsymbol{u}_d$, temperature T_d, and mass m_d, whose details can be found in previous works [12,23,24]. A non-equilibrium Langmuir-Knudsen model [25–27] is employed for droplet evaporation. Source terms appearing in the governing equations of the gas-phase, which represent the interactions between dispersed-phase (fuel droplets) and gas-phase [12] are calculated using the Particle-Source-In-Cell (PSI-Cell) approach [28], thereby realizing two-way coupling. Detailed calculation procedures of these source terms and the dispersed-phase are described in [23,24,29], and are not repeated here for the sake of brevity.

2.2. Reaction model

Fuel for the liquid spray considered in this work is kerosene (hereafter referred to as KERO), originally composed of $C_{10}H_{22}$ (76.7 wt%), C_9H_{12} (13.2 wt%) and C_9H_{18} (10.1 wt%). However, KERO is assumed to be an equivalent single species ($C_{9.7396}H_{20.0542}$) of these three species [30]. A two-step reduced chemical scheme proposed by Franzelli et al. [30] is used to model the combustion of gaseous KERO. The reduced chemical scheme takes into account six species (KERO, O_2, H_2O, CO_2, CO and N_2) and the following two reactions.

$$\mathrm{KERO} + 10\mathrm{O_2} \xrightarrow{\dot{\omega}_{f,1}} 10\mathrm{CO} + 10\mathrm{H_2O}, \tag{3}$$

$$\mathrm{CO} + 0.5\mathrm{O_2} \underset{\dot{\omega}_{r,2}}{\overset{\dot{\omega}_{f,2}}{\rightleftharpoons}} \mathrm{CO_2}. \tag{4}$$

Where, $\dot{\omega}_{f,1}$ is the forward reaction rate for the oxidation of KERO in Eq. (3), and $\dot{\omega}_{f,2}$ and $\dot{\omega}_{r,2}$ are the forward and reverse reaction rates, respectively for the reversible CO oxidation reaction in Eq. (4). Calculation procedure for the reaction rates $\dot{\omega}_{f,1}$, $\dot{\omega}_{f,2}$ and $\dot{\omega}_{r,2}$ are described in [30,31]. The local equivalence ratio required to calculate these reaction rates are estimated using the standard Bilger's definition, and its calculation method is the same as that detailed in a previous work [32]. Furthermore, to estimate the reaction rates $\dot{\omega}_{f,1}$, $\dot{\omega}_{f,2}$ and $\dot{\omega}_{r,2}$ in a given computational cell, the temperature and the molar concentration of species corresponding to that computational cell are used [30–32]. This reaction model is capable of accurately reproducing important combustion quantities, such as laminar flame speed, adiabatic flame temperature, equilibrium CO levels, and ignition delays for a wide range of equivalence ratio, fresh gas temperature and pressure [30]. Moreover, it has also been validated for the accurate prediction of flame propagation characteristics of fuel droplet arrays [31].

2.3. Atomization model

One of the objectives of the present study is to analyze the influence of combustion instability on the atomization (diameter distribution) of liquid fuel spray being injected into the back-step combustor. Recently, Lee et al. [33] used the integral from of the conservation equations of mass, momentum and energy to theoretically derive a cubic relation for the droplets' Sauter Mean Diameter (SMD) post-atomization, for liquid sprays in cross-flows. Hence, this approach does not involve any ad-hoc modeling or unphysical descriptions of the atomization process [33]. Moreover, this model has been extensively validated against experimental data for spray atomization in cross-flow configuration [33], which makes it suitable for application in the present study where fuel spray is injected into air cross-flow (described later in Section 2.5). The expression for calculating the SMD (referred to as Lee model or SMD modulation hereafter) of injected fuel droplets, which relates the SMD to a cubic function of gas-phase velocity ratio is given by

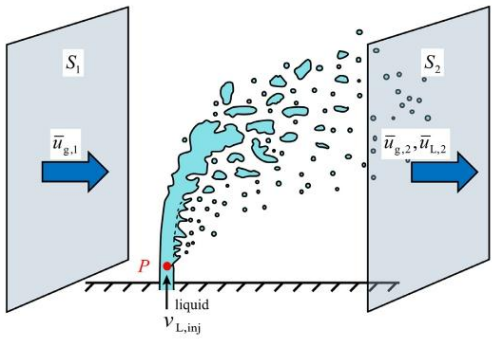

Fig. 1. Schematic of liquid jet atomization in crossflow. (For interpretation of the references to color in this figure legend, the reader is referred to the web version of this article.)

$$SMD = \frac{3\sigma + \sqrt{9\sigma^2 + \frac{\kappa\mu_L \overline{u}_{L,2}^2}{\overline{\eta}_{L,inj} A_{inj}} \left(\frac{\rho_L}{2} \left(\overline{v}_{L,inj}^2 - \overline{u}_{L,2}^2 \right) + \frac{A_c}{\overline{\eta}_{L,inj} A_{inj}} \frac{\rho_{g,1}}{2} \left(\overline{u}_{g,1}^3 - \overline{u}_{g,2}^3 \right) \right)}}{\left(\frac{\rho_L}{2} \left(\overline{v}_{L,inj}^2 - \overline{u}_{L,2}^2 \right) + \frac{A_c}{\overline{\eta}_{L,inj} A_{inj}} \frac{\rho_{g,1}}{2} \left(\overline{u}_{g,1}^3 - \overline{u}_{g,2}^3 \right) \right)}, \tag{5}$$

$$Ac = \left[3.44 d_{inj} \sqrt{\frac{\rho_L \overline{v}_{L,inj}^2}{\rho_{g,1} \overline{u}_E Sg, 1^2}} \right] \times \left[7.86 d_{inj} \left(\frac{\rho_L \overline{v}_{L,inj}^2}{\rho_{g,1} \overline{u}_{g,1}^2} \right)^{0.17} \times 8.06^{0.33} \right], K = 0.112. \tag{6}$$

here, $\rho_{g,1}$ and $\overline{u}_{g,1}$ are the cross-sectional plane averaged gas-phase density and velocity, respectively, upstream of the fuel injection point (cross-section S_1 in Fig. 1). $\overline{u}_{g,2}$ is the downstream cross-sectional plane (S_2 in Fig. 1) averaged gas-phase velocity, $\overline{v}_{L,inj}$ is the injection velocity of fuel droplets, and $\overline{u}_{L,2}$ is the mean velocity of fuel droplets after secondary atomization. The schematic in Fig. 1 also illustrates these quantities. Furthermore, σ represents the surface tension of liquid fuel, ρ_L is the liquid fuel density, μ_L is the dynamic viscosity of liquid fuel, A_{inj} is the injector exit area, d_{inj} is the injector exit diameter, A_c is the cross-sectional area of the spray given by Eq. (6), and K is a proportionality constant for the viscous dissipation term which is the only adjustment parameter in this model, and is determined based on the flow velocity and the value of SMD. Figure 2 shows the variation of SMD of liquid fuel droplets with the cross-sectional plane averaged air velocity $\overline{u}_{g,1}$, calculated using the Lee model. It can be seen that as the inflow air velocity increases, the resulting droplet size (SMD) decreases and vice-versa. When combustion instability occurs, the resulting pressure fluctuations inside the combustor cause the incoming air flow velocity to fluctuate accordingly, which in

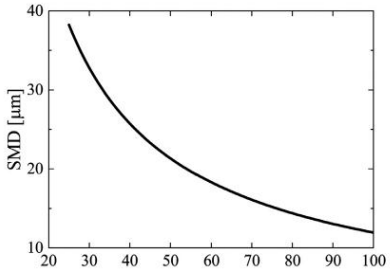

Fig. 2. Effect of incoming air-velocity $u_{g,1}$ on SMD using Lee model [33].

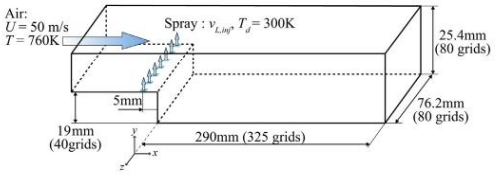

Fig. 3. Computational domain and conditions.

turn produces fluctuations in the SMD of fuel droplets as a consequence of the varying degree of atomization. In the present simulations, the SMD computed using Eq. (5) with instantaneous gas- and liquid-phase injection parameters and properties, is used to calculate the size distribution of fuel droplets to be injected (described in Section 2.5). So, with this atomization model, it is assumed that the spray is already established at the fuel injection positions, meaning the atomization process is assumed to be instantaneous and this is a limitation of the Lee/atomization model. However, such an assumption is reasonable in the context of the present LESs, since combustion starts occurring after the backward-facing step downstream of the fuel injection positions (as will be evident later from Figs. 7 and 8 and their accompanying discussion in Section 3.1). Furthermore, the computational cost of modeling primary atomization is still quite prohibitive, hence, the Lee model has been chosen for this study.

2.4. Variable Mass Flow Rate model (VMFR model)

The influence of pressure fluctuations inside the back-step combustor (caused by combustion instability) on the incoming air flow, and the injected fuel spray is also considered in this study. In the LESs, incoming air in the combustor has a sufficiently large inflow area (see Fig. 3), hence, its velocity fluctuations adjust automatically to the pressure fluctuations. On the other hand, fluctuations in the injection velocity of the liquid fuel spray which is an incompressible fluid, are considered using the following Variable Mass Flow Rate model (hereafter referred to as VMFR model), that can be derived from the Bernoulli's equation.

$$\overline{v}_{L,inj} = \begin{cases} \overline{v}_{ave} \times \sqrt{\frac{P_0 - P\left(t_{now} - T\frac{\phi_{ph}}{2\pi}\right)}{P_0 - P_{ave}}}, & for \;\; P_0 > P\left(t_{now} - T\frac{\phi_{ph}}{2\pi}\right) \\ \overline{v}_{min}, & for \;\; P_0 \le P\left(t_{now} - T\frac{\phi_{ph}}{2\pi}\right) \end{cases} \tag{7}$$

Here $\overline{v}_{L,inj}$ is the instantaneous fuel injection velocity, $\overline{v}_{ave}$ is the mean fuel injection velocity ($\overline{v}_{ave} = 2$ m/s), P_{ave} is the time averaged pressure at the fuel injection position (represented by point P in red color in Fig. 1, just above the fuel injection port exit), T is the period of pressure oscillation, t_{now} is the current time, $P(t)$ is the transient pressure just above the fuel injection position's exit (point P in Fig. 1 at the injection port exit) at time instance t, ϕ_{ph} is the phase difference between fuel flow rate fluctuations and pressure oscillations, and P_0 is the fuel injection pressure expressed as the summation of pump pressure P_{pump} and P_{ave}. In Eq. (7) above, it is assumed that when the instantaneous value of pressure at the fuel injection position $P(t_{now} - T\frac{\phi_{ph}}{2\pi})$ becomes greater than or equal to P_0, $\overline{v}_{L,inj}$ is equal to a small value $\overline{v}_{min}$ (10% of $\overline{v}_{ave}$). Ideally, the fuel injection should be cut-off when the transient pressure $P(t)$ exceeds the fuel injection pressure P_0. However, in the initial test runs for the various cases in which VMFR model is applied, it was observed that if the fuel injection velocity $\overline{v}_{L,inj}$ is made zero for the duration when $P(t_{now} - T\frac{\phi_{ph}}{2\pi})$ exceeds P_0, the overall equivalence ratio computed using the fuel and air mass flow rates over the time period of one oscillation cycle could not be maintained at 1.0. Hence, some initial trial runs of the simulations were conducted to optimize the value of $\overline{v}_{min}$. and it was found that $\overline{v}_{min} = 10\%$ of $\overline{v}_{ave}$ worked well to maintain the overall equivalence ratio close to 1.0 in all cases. The pump pressure P_{pump} is obtained from Bernoulli's equation as

$$P_{pump} = \frac{1}{2}\rho_L \overline{v}_{ave}^2. \tag{8}$$

It has been confirmed in a previous experimental investigation conducted by Ghoniem et al. [34] that when combustion instability occurs, the velocity fluctuations of incoming air are 90° out of phase with the pressure fluctuations. Moreover, one can also expect fluctuations in the liquid fuel spray's flow rate, since it is susceptible to the pressure fluctuations inside the combustor. However, it is difficult to accurately measure the liquid fuel flow rate fluctuations due to limitations of measuring equipment. Additionally, many experimental studies have been carried out to suppress combustion instabilities in spray combustion fields by actively controlling the fuel injection rate [e.g., [9],[35,36],[37]. Most of the previous studies analyze the fluctuations in pressure, velocity and heat release rate, but rarely investigate the influences of spatial distributions of liquid fuel droplets, evaporation rate, fuel, and their temporal variations on combustion instability. Furthermore, studies using numerical simulations to explore the aforementioned physical parameters are also scarce to the best of the authors' knowledge. Therefore, in addition to considering fluctuations in the flow rate of liquid fuel spray due to combustion instability in the present study, the active control of liquid fuel injection rate is also considered via. the phase difference ϕ_{ph}, and LESs of various cases are performed with different values of ϕ_{ph}, to investigate the impact of temporal variations of fuel injection rate on combustion instability.

2.5. Computation details and calculation conditions

The computational domain of the combustor section is shown in Fig. 3, while the entire computational domain is illustrated in Fig. 4. The computational domain-size and the conditions are set in accordance with the previous study by Kitano et al. [12], except for the combustor length l and the injection velocity of liquid fuel $\overline{v}_{L,inj}$. The combustor length has been increased from $l =$ 200 mm in the previous study [12] for spray combustion simulations to $l = 290$ mm in the present study. The reason for increasing the combustor length in this study is the modification made to the fuel injection configuration. In the LESs performed by Kitano et al. [12], fuel droplets were injected 5 mm upstream of the back-step similar to the present LESs, however, they were injected along a continuous slit (see Fig. 12 in [12]). In the present configuration, fuel droplets are injected from 7 injection ports arranged

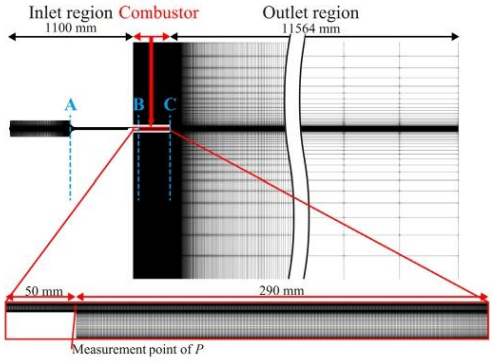

Fig. 4. Computational grid.

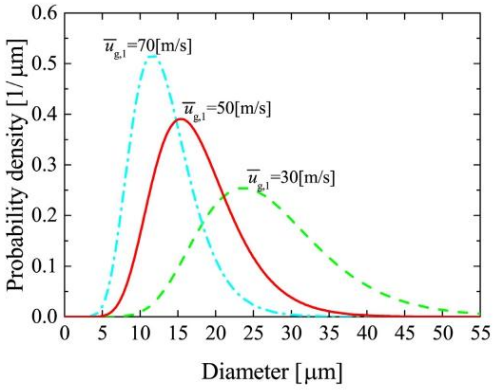

Fig. 5. Effect of air-velocity $\overline{u}_{g.1}$ on injected fuel droplet size distribution.

at equal intervals as depicted in Fig. 3. Initial test run with this fuel injection configuration and the same combustor length as the previous study [12] yielded very weak nonlinear limit cycle oscillation/combustion instability. This was caused by the alteration of heat release rate topology due to change in the fuel injection configuration, and a consequent weakening of the phase relationship/coupling between heat release rate fluctuations and pressure oscillations. The combustor length was then gradually increased in the test runs until a strong enough combustion instability occurred for a combustor length of $l = 290$ mm.

The computational geometry used in this study as well as that of Kitano et al. [12] is similar to the experimental test rig of Smith and Zukoski [38]. In Fig. 4, the section up to location A from the left end of the inlet region is the plenum chamber. The left end of the plenum chamber has a small inlet area through which air supply enters into the domain. Incoming air temperature is $T_{in} = 760$ K and the mass flow rate of incoming air $\dot{m}_{air}$ is kept constant. At the inlet boundary, Neumann condition is applied for the inlet pressure P_{in} and inlet density ρ_{in} is calculated using ideal gas law as $\rho_{in} = P_{in}/RT_{in}$. Incoming air velocity at the inlet boundary u_{in} fluctuates in accordance with the fluctuations of P_{in}. The air mass flow rate can be expressed as $\dot{m}_{air} = \rho_{in}A_{in}u_{in}$, where A_{in} is the inlet area. Using the ideal gas equation, the air mass flow rate equation can be recast as follows to yield the solution for u_{in}.

$$u_{in} = \frac{\dot{m}_{air}}{\rho_{in}A_{in}} = \frac{\dot{m}_{air}RT_{in}}{A_{in}P_{in}} \tag{9}$$

Since $\dot{m}_{air}$, R, T_{in} and A_{in} are constant values, u_{in} varies depending on the variation of P_{in} as per the above equation. No-slip boundary condition is applied at the wall surfaces, and the walls are assumed to be isothermal with their temperature fixed at 760 K. The x, y, and z axes correspond to the main channel/flow direction, vertical direction, and span direction, respectively (as shown in Fig. 3), and the step's streamwise position is set to $x = 0$ mm. Air is introduced into the combustor through the inflow section, and fuel droplets (KERO) are injected vertically upwards with velocity $\overline{v}_{Inj}$ from the position 5 mm upstream of the step. The injection rate of fuel droplets is adjusted such that, the overall equivalence ratio is 1.0 over the time period of one oscillation cycle (as explained in Section 2.4), and the initial temperature of fuel droplets is 300 K. Figure 2 shows an example of the change in SMD of injected fuel droplets with respect to the cross-sectional plane averaged air velocity $\overline{u}_{g.1}$. The probability density function (PDF) for droplet diameter distribution of the liquid fuel is defined using a modified Nukiyama-Tanasawa function [39]. Figure 5 shows the droplet size distributions of liquid fuel spray at the time of injection, corresponding to various values of the cross-sectional plane averaged air velocity $\overline{u}_{g.1}$. The SMDs required to compute these droplet size distributions (since, the modified Nukiyama-Tanasawa function [39] uses SMD as a parameter) that vary in time depending on the value of $\overline{u}_{g.1}$, are obtained using the Lee model [Eq. (5)]. As $\overline{u}_{g.1}$ increases, the SMD decreases, and the droplet size distribution gets biased towards smaller size and vice versa. The droplet diameter distribution of the injected fuel spray for cases without the Lee model, i.e., Cases NA-1 to NA-5 (summarized in Table 1 and explained below) in which SMD modulation is not applied, is based on the measured droplet diameter distribution of a previous experiment conducted by Moriai et al. [40] for a real gas turbine combustor. Fitting parameters of the modified Nukiyama-Tanasawa distribution function are calculated so as to obtain a best fit curve to this measured droplet diameter distribution. The average droplet diameter d_{avg} corresponding to this droplet size distribution is 18 μm and the corresponding SMD is 22.5 μm. The reason for choosing this droplet size distribution with $d_{avg} = 18$ μm is that, in the previous study by Kitano et al. [12], the influence of d_{avg} of injected fuel spray on the strength of combustion instability (intensity of pressure oscillations) was investigated, and it was found that combustion instability was strongest for a specific value of d_{avg}, and that d_{avg} corresponded to this exact droplet size distribution based on Moriai et al.'s measurements [40] (with $d_{avg} = 18$ μm).

Table 1
Cases investigated in this study (× : Model is not applied, ○: Model is applied). ϕ_{ph} is the phase shift angle by which the fuel mass flow rate fluctuations lag the combustor pressure oscillations.

Case	Lee model (SMD modulation)	VMFR model	Phase shift angle ϕ_{ph}
NA-1	×	×	-
NA-2	×	○	0°
NA-3	×	○	90°
NA-4	×	○	180°
NA-5	×	○	270°
A-1	○	×	-
A-2	○	○	0°
A-3	○	○	90°
A-4	○	○	180°
A-5	○	○	270°

Table 1 summarizes the cases that have been examined and compared in this study. First, in Section 3.1, Case NA-1 and Case A-1 are examined and compared, and the influence of fluctuations

in initial droplet size distribution of liquid fuel on the combustion instability characteristics is investigated. Next, in Section 3.2, Cases NA-2 to NA-5 (i.e., cases without the Lee model) are compared and examined to investigate the effect of fluctuations of liquid fuel flow rate (along with the phase difference ϕ_{ph} applied in the VMFR model) on the combustion instability characteristics. In Cases NA-1 to NA-5, the atomization/Lee model is not applied and a presumed droplet size distribution with SMD = 22.5 μm as explained above is imposed. Hence, Cases NA-1 to NA-5 are referred to as cases "without SMD modulation" or cases "without Lee model" for the remainder of this article. Finally, in Section 3.3, the cases with Lee model (or cases with SMD modulation), i.e., Cases A-2 to A-5 are examined and compared against the cases without Lee model (i.e., Cases NA-2 to NA-5), in order to investigate the influence of temporal fluctuations of both the droplet size distribution and the liquid fuel flow rate, and their interaction on the combustion instability characteristics. The phase difference ϕ_{ph} applied between the temporal fluctuations of liquid fuel flow rate and the pressure oscillations in each case, is set as shown in Table 1.

The LESs of all the spray combustion cases listed in Table 1 are performed using an in-house thermal flow analysis code FK^3 [12,24,29,31,41–47]. This code's solver employs a pressure-based semi-implicit (fractional-step) algorithm for compressible flows [48]. The computational domain is discretized using a non-uniform staggered Cartesian grid, with fine grid-spacing near the walls. There are approximately 2.4 million grid points in the combustor section, and the total number of grid points in the whole computational domain including the outflow is about 21.5 million. The spatial derivatives in the governing equations of the gas-phase are approximated using a second-order accurate central difference scheme, except for the convection terms in the governing equations of the gas-phase enthalpy and chemical species mass fractions which are evaluated using the WENO scheme [49]. The third-order explicit TVD Runge-Kutta scheme is used for time integration of the convection terms. All thermodynamic properties and transport coefficients are calculated according to CHEMKIN [50,51] taking temperature dependence into account. The validity of the present LES for predicting the combustion instabilities has been confirmed by comparison with an experiment [38] for gas combustion instability in the previous work by Kitano et al. [12]. The in-house code FK^3 has also been successfully applied for simulating spray combustion problems in the past and also validated [52]. The CPU time required per case of this computation is approximately 480,000 h (about 470 h of real time) by parallel computation using 1024 cores on a SGI:ICE X supercomputer (with Intel Xeon E5-2670 processor) at the Central Research Institute of Electric Power Industry (CRIEPI), Japan.

3. Results and discussion

3.1. Influence of time variations of liquid fuel droplet diameter distribution on combustion instability

First, Case NA-1 (without SMD modulation) and Case A-1 (with SMD modulation) are considered, and the occurrence of combustion instability in these Cases is confirmed. Figure 6 shows the time variations of pressure P, heat release rate Q, streamwise velocity $\tilde{u}$, fuel droplet evaporation rate $\dot{m}$, and SMD of injected fuel droplets, in Case NA-1 and Case A-1. Here, P represents the value of pressure measured at a point on the dump plane (i.e., the interface between the combustor and inlet duct) as shown in Fig. 4, $\tilde{u}$ represents the cross-sectional ($y-z$ plane)-averaged value of the streamwise velocity at the dump plane, Q and $\dot{m}$ represent the total values of heat release rate and fuel droplet evaporation rate, respectively, inside the combustor, and SMD represents the value computed using the Lee model in Eq. (5) (note that the SMD is constant in Case NA-1, since the atomization/Lee model is not applied and the injected droplet size distribution does not vary in time). The inspection cross-section for $\tilde{u}$ used in the Lee model to compute $\overline{u}_{g.1}$ (see Fig. 1), is located 8 mm upstream of the fuel injection ports. Ideally the inspection cross-section for computing $\overline{u}_{g.1}$ should be placed close to the fuel injection ports' position, to get an accurate estimate of the incoming air's kinetic energy. However, when combustion instability occurs, the pressure oscillations induce fluctuations in the velocity of incoming air/gas-phase which in turn induces fluctuations in the velocity of injected fuel droplets. As a result of the pressure oscillations, some droplets are pushed backwards and get displaced upstream of the fuel injection ports. Therefore, the rationale for placing the inspection cross-section for computing $\overline{u}_{g.1}$ 8 mm upstream of the fuel injection ports, is to ensure that no fuel droplets cross or are present at this cross-section, otherwise the estimate for $\overline{u}_{g.1}$ will not be correct, since it will include the effect of momentum exchange between the gas- and dispersed-phases.

The phase ϕ shown in Fig. 6(a) is defined using the time variation of pressure P as a reference. $\phi = 0^\circ$ is defined as the instance when P reaches atmospheric pressure value P_{atm} as it increases during its oscillations, $\phi = 90^\circ$ is defined as the instance when P reaches its maximum value P_{max}, $\phi = 180^\circ$ is defined as the instance when P reaches the atmospheric pressure P_{atm} as it decreases during its oscillations, and $\phi = 270^\circ$ is defined as the instance when P reaches its minimum value P_{min}. The figure shows that the various physical quantities oscillate with a period that is approximately constant in both Case NA-1 and Case A-1. It can be seen that the phase difference between the variations of P and $\tilde{u}$ is approximately 90°. This phase difference was also observed in a previous experiment [34], and is caused by classical air column vibration mechanism (where fluid acceleration is governed by the pressure gradient). Moreover, in Case A-1, the SMD varies in time and corresponds to the fluctuations of $\tilde{u}$. This is apparent from Fig. 6(b) as well as Fig. 6(c). In Fig. 6(c), $\tilde{u}$ represents the streamwise air velocity computed 8 mm upstream of the fuel injection position (which is the inspection cross-section used for computing $\overline{u}_{g.1}$, required for the Lee/atomization model), and at the center of the inlet duct. The phase difference between the variations of SMD and $\tilde{u}$ in both Fig. 6(b) and (c) is 180°, and in accordance with the Lee model (SMD decreases with increasing air inflow velocity and vice-versa, see Fig. 2). Additionally, the phase of the variations of $\dot{m}$ lags that of $\tilde{u}$ by approximately 90° in Case NA-1, and 120° in Case A-1. The phase difference between $\dot{m}$ and $\tilde{u}$ depends on the distance from the fuel injection location to the combustion reaction region, the evaporation properties of the fuel, and the combustion properties.

To understand more about the flow-fields and the nature of the flames obtained from the LESs, instantaneous distributions of gas-phase temperature and Flame Index (FI), on the central $x-y$ plane of Case NA-1 are illustrated in Fig. 7, at various time instances/phases ranging from $\phi = 0^\circ - 270^\circ$. The left column shows the instantaneous distributions of gas-phase temperature along with the dispersed fuel droplets (represented by grey entities), while the right column shows the instantaneous distributions of FI. Here, the standard definition of FI is used, i.e. $FI = \nabla Y_F \cdot \nabla Y_O$, where Y_F and Y_O are the mass fractions of fuel and oxidiser, respectively. Furthermore, FI distributions shown in Fig. 7 have been weighted by the heat release rate, in order to avoid the influence of regions with pure droplet evaporation and pure mixing (i.e., regions without reactions). The instantaneous distributions of gas-phase temperature and fuel droplets indicate that, as the injected fuel droplets convect downstream with the flow, they disperse and evaporate. Subsequent combustion of the evaporated fuel occurs and flame is formed behind the back-step.

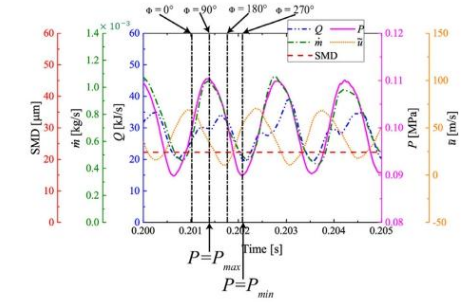

(a) Case NA-1

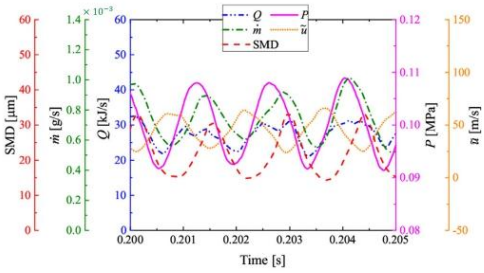

(b) Case A-1

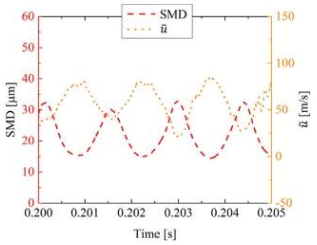

(c) Time variations of SMD and incoming air's streamwise velocity $\tilde{u}$ computed 8mm upstream of the fuel injection position at the center of the inlet duct for Case A-1.

Fig. 6. Comparisons of time variations of pressure P, heat release rate Q, streamwise velocity $\tilde{u}$, droplet evaporation rate $\dot{m}$, and droplet Sauter Mean Diameter (SMD), between cases without (Case NA-1) and with (Case A-1) SMD modulation.

Droplet count reduces with increasing downstream distance from the dump plane as a consequence of evaporation and combustion. For Cases NA-1, the droplet relaxation time τ_d is in the range of $\tau_d = 5.53 \times 10^{-8} - 8.48 \times 10^{-4}$ s (depending upon the instantaneous droplet size and properties of the gas-phase surrounding it). The droplet relaxation time values presented this study, include the correction to Stokes drag for droplet motion and evaporation as explained in [24,27,29]. The turbulent time scale τ_t is approximately 7.44×10^{-3} s. Here, τ_t is defined as the ratio of the streamwise integral length scale value computed at the location 40 mm downstream of the back-step (at the center of the combustor's cross-section), to the standard deviation of gas-phase streamwise velocity at that location. Stokes number St, based on the above-defined droplet relaxation time τ_d and turbulent time scale τ_t is thus, $\mathrm{St} = \tau_d/\tau_t$ and is in the range of $7.42 \times 10^{-6} - 0.114$. Therefore, fuel droplets get entrained into the large vortical structures that are periodically generated behind the back-step (due to oscillations of $\tilde{u}$), and this is more clearly visible in Fig. 7(a) and (b). Judging from the distributions of fuel droplets, gas-phase temperature and *FI* at different phases ϕ, it is evident that the dispersed droplet clusters and the gas-phase experience periodically pulsating motion due to the influence of combustion instability (i.e., pressure oscillations). As for the nature of flame generated, the distributions of *FI* shown in the right column of Fig. 7 at different phases ϕ are predominantly positive (although some small regions with negative *FI* do exist). This indicates that premixed combustion is dominant in Case NA-1, with the exception of some minor zones with non-premixed combustion. Similar tendencies

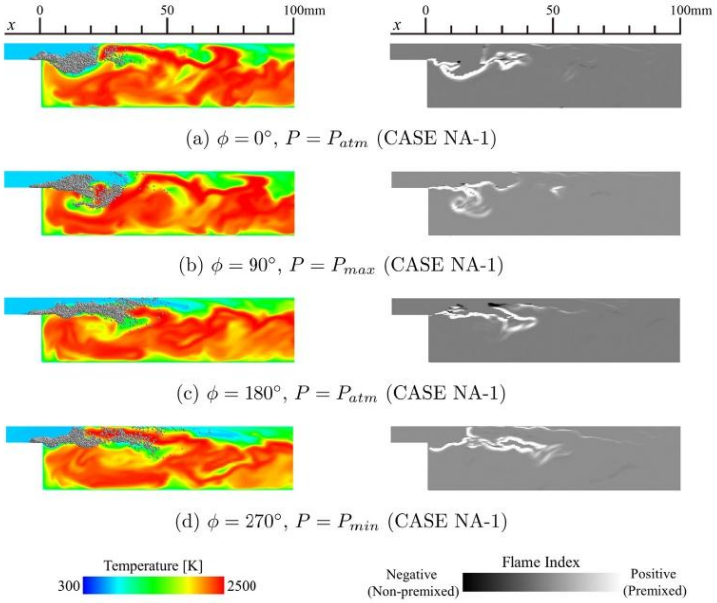

Fig. 7. Instantaneous distributions of gas-phase temperature along with dispersed fuel droplets (left column), and Flame Index (right column), on the central $x - y$ plane for Case NA-1 at different values of phase ϕ.

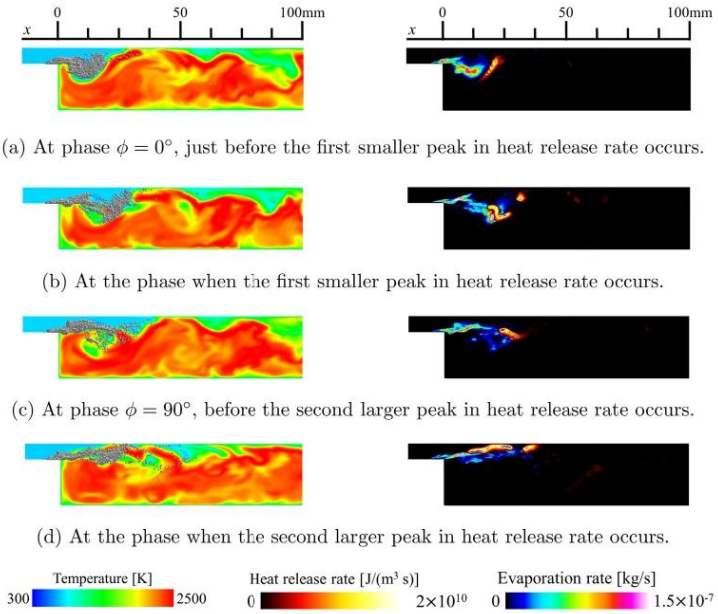

Fig. 8. Instantaneous distributions of gas-phase temperature along with dispersed fuel droplets (left column), and heat release rate and fuel droplet evaporation rate (right column), on the central $x - y$ plane for Case NA-1.

were observed for all the other cases investigated in this study, and hence their results are not shown for the sake of brevity.

Moreover, the temporal variations of total heat release rate Q inside the combustor, depicted in Fig. 6 have a double peak feature. The general trend observed in Fig. 6(a) for Case NA-1 is that, the first peak of Q (smaller in magnitude) occurs during the time period when pressure rises from P_{min} to P_{max} (i.e. during $\phi = 270^\circ - 90^\circ$), soon after the phase $\phi = 0^\circ$ ($P = P_{atm}$), and the second peak of Q (larger in magnitude) occurs during the time period when pressure falls from P_{max} to P_{min} (i.e., during $\phi = 90^\circ - 270^\circ$), right before the phase $\phi = 180^\circ$ ($P = P_{atm}$). To analyze the mechanism responsible for this double peak behavior of Q, Fig. 8 illustrates the instantaneous distributions of gas-phase temperature (along with fuel droplets) on the left column, and those of fuel droplet evaporation rate and heat release rate on the right column, for Case NA-1 at different phases/time instances. The temperature and fuel droplet distributions shown in Fig. 8(a) at the phase $\phi = 0^\circ$, correspond to the instance when the streamwise velocity $\bar{u}$ of incoming air is maximum, and the vortex shedding process is occurring. Consequently, during the period $\phi = 270^\circ - 90^\circ$, fuel droplets get entrained into this large vortex near the back-step, and they have sufficient residence time to evaporate. As a result, the evaporation rate in the vortex region becomes large, as shown in Fig. 8(a) (right) which subsequently leads to ignition of the fuel-air mixture, thereby causing an increase in the heat release rate (around $x \approx 25$ mm) as depicted in Fig. 8(b), which corresponds to the phase when the first smaller peak of Q occurs. After the first peak of Q occurs, the vortex that is periodically shed during $\phi = 270^\circ - 90^\circ$ is conveyed downstream as depicted by the temperature and fuel droplet distributions at the phase $\phi = 90^\circ$ in Fig. 8(c), all the while fuel droplets have been evaporating (Fig. 8(c) right). The fuel that has evaporated during the period $\phi = 270^\circ - 90^\circ$ and convected downstream of the dump plane without reacting, suddenly ignites and leads to a rise in the heat release rate just prior to the phase $\phi = 180^\circ$ (during the period $\phi = 90^\circ - 270^\circ$), as shown in Fig. 8(d) (right) and thus, the second larger peak of Q occurs. The temporal variation of Q in Case A-1 also has a similar double peak feature (see Fig. 6(b)), but, the magnitude of the second peak is nearly the same as that of the first peak. The reason for this reduction in magnitude of the second peak of Q compared to that in Case NA-1, is the consideration of varying degree of fuel spray atomization via. the Lee model in Case A-1. The influence of this model on fuel droplet evaporation, heat release rate and combustion instability is clarified later in the discussion that follows. It is also worth noting that interaction of flame with the wall is present, which is discernable from the FI distributions in Fig. 7 and the heat release rate distribution in Fig. 8(d). Flame-wall interaction occurs in all the cases investigated in this study. As mentioned previously in Section 2.5, the walls are assumed to be isothermal and their temperature is fixed at 760 K (same as the inlet air temperature). Therefore, as in any practical combustor, heat loss to the walls is considered in the present LESs, even though the isothermal wall boundary condition is a simplification.

Figures 9 and 10 show the spectra of pressure oscillations and the streamwise distributions of the amplitude of peak frequency components of pressure oscillations, respectively, for Case NA-1 and Case A-1. The locations A, B, and C shown in Fig. 10 correspond to the same locations shown in Fig. 4. The sampling time and period for calculating the statistics are approximately 0.05 s and 0.02 ms, respectively. Figure 9 shows that the spectra of pressure oscillations for Cases NA-1 and A-1 have a clear peak at 699 Hz, and that the peak amplitude is larger for Case NA-1. Moreover, Fig. 10 shows that the oscillation mode of the pressure variations' peak frequency component occurring in Case NA-1 and Case A-1, consists of the combustion chamber's fundamental oscillation mode (1/4 wavelength mode), with the oscillation antinode occurring at B and the oscillation node occurring at C. These results indicate that combustion instabilities indeed occur in both Case NA-1 and Case A-1. Next, the effect of time variations of the liquid fuel droplet diameter distribution upon injection, which are considered via. the Lee model, on the intensity of the pressure oscillations caused by combustion instability is investigated. Figure 11 presents the root mean square (RMS) values of pressure fluctuations in Case NA-1 and Case A-1. The figure shows that the RMS value of pres-

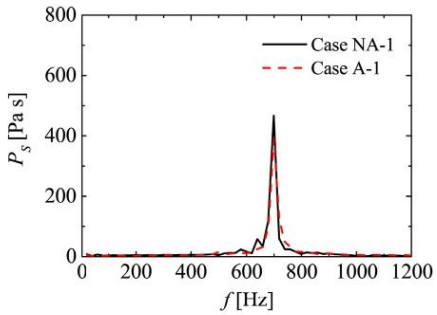

Fig. 9. Comparison of the spectra of pressure oscillations between cases without (Case NA-1) and with (Case A-1) SMD modulation.

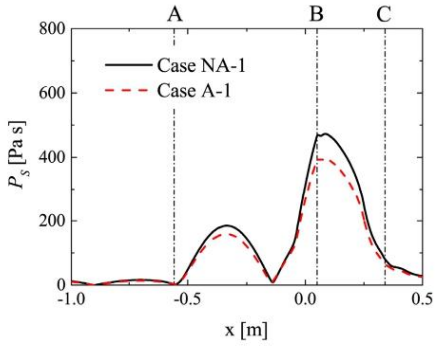

Fig. 10. Comparison of the streamwise profiles of amplitude of peak frequency components of pressure oscillations, between cases without (Case NA-1) and with (Case A-1) SMD modulation.

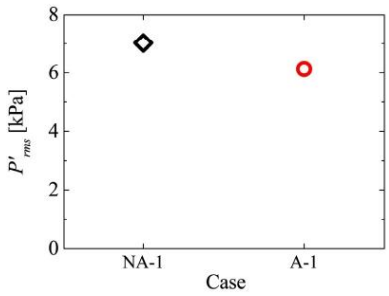

Fig. 11. Comparison of the intensities of pressure oscillations P'_{rms}, between cases without (Case NA-1) and with (Case A-1) SMD modulation.

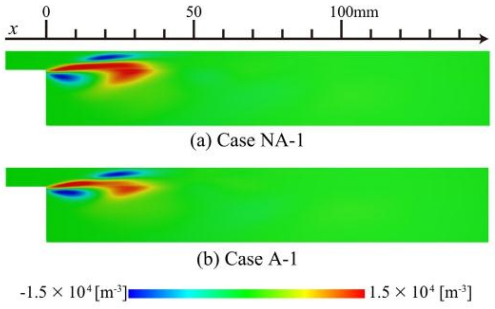

Fig. 12. Comparison of distributions of the spanwise-averaged local Rayleigh Index RI on the $x-y$ plane, between cases without (Case NA-1) and with (Case A-1) SMD modulation.

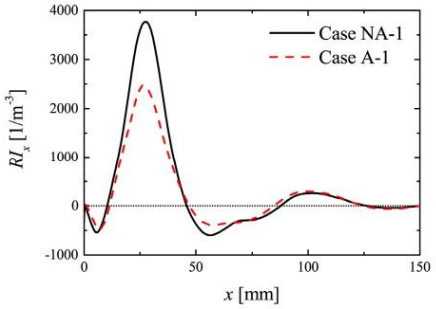

Fig. 13. Comparison of streamwise distributions of the cross-sectional ($y-z$)-averaged local Rayleigh Index RI_x, between cases without (Case NA-1) and with (Case A-1) SMD modulation.

sure fluctuations in Case NA-1 is approximately 10% larger in comparison with that in Case A-1. It is apparent that the time variations of the liquid fuel droplet diameter distribution upon injection (considered using the Lee model), influence the intensity of combustion instability. To identify the factors causing the difference in the RMS values of pressure fluctuations, the Rayleigh Index (RI) has been computed for each case. Here, the RI is defined as follows

$$RI = \frac{1}{t_s}\int \frac{P'q'}{P'_{rms}Q_{ave}}\,dt. \tag{10}$$

where P' and q' represent the fluctuations in pressure P and heat release rate Q, respectively, Q_{ave} represents the time-averaged value of total heat release rate inside the combustor, t_s represents the sampling time, and P'_{rms} represents the RMS value of pressure fluctuations. In the regions where RI is positive, the pressure oscillations are driven by the heat release, whereas, in the regions where RI is negative, the pressure oscillations are damped by the heat release. The $x-y$ planar distributions of spanwise-averaged (z-direction) value of local RI for Case NA-1 and Case A-1 are shown in Fig. 12, while the streamwise (x-direction) distributions of the cross-sectional ($y-z$)-averaged value of Rayleigh Index RI_x are shown in Fig. 13. Figure 12 shows that the value of RI is positive in the region near the combustion chamber's dump plane, for both Case NA-1 and Case A-1. This indicates that the pressure oscillations are driven by the heat release in this region. Additionally, Fig. 13 shows that RI_x is smaller in the vicinity of the position at a distance of $x = 25$ mm from the combustion chamber's dump plane, for Case A-1 in comparison with Case NA-1. This is the reason for the RMS value of pressure oscillations in Case NA-1 being larger than that in Case A-1.

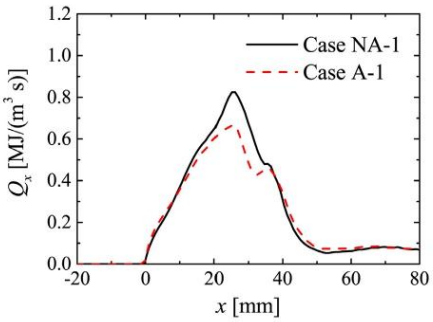

Fig. 14. Comparison of the streamwise distributions of phase- and cross-sectional ($y-z$ plane) averaged heat release rate Q_x, at phase of $\phi = 90^\circ$ (when $P = P_{max}$) between cases without (Case NA-1) and with (Case A-1) SMD modulation.

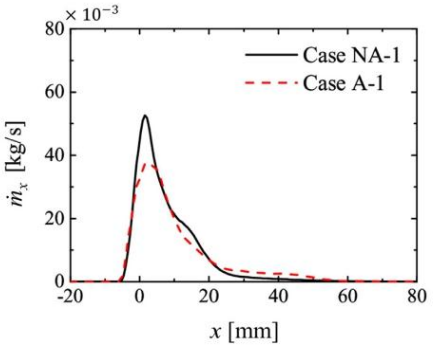

Fig. 15. Comparison of the streamwise distributions of phase- and cross-sectional ($y-z$ plane)-averaged evaporation rate $\dot{m}_x$, at phase of $\phi = 0^\circ$ between cases without (Case NA-1) and with (Case A-1) SMD modulation.

Next, the reason for the difference in the distributions of RI_x is investigated in further detail. The positive RI_x distributions are strongly influenced by the heat release rate at the phase when pressure reaches its maximum value i.e., $\phi = 90^\circ$. The streamwise distributions of the $y-z$ cross-sectional-averaged heat release rate Q_x with phase averaging at the phase $\phi = 90^\circ$ when pressure reaches its maximum value ($P = P_{max}$), are shown in Fig. 14 for Case NA-1 and Case A-1. The figure shows that the heat release rate at the phase when pressure is at its maxima, is greater in Case NA-1. The distribution of heat release rate at a particular phase is influenced by the distribution of evaporation rate of the fuel droplets immediately beforehand. Therefore, the streamwise distributions of the $y-z$ cross-sectional-averaged evaporation rate $\dot{m}_x$, with phase averaging at $\phi = 0^\circ$ are shown in Fig. 15 for Cases NA-1 and A-1.

Figure 15 shows that the evaporation rate at the phase before the phase when pressure reaches its maximum value (see Fig. 6(a)), is higher for Case NA-1 in comparison with Case A-1. Moreover, the figure also shows that the fuel droplets evaporate mostly in the vicinity of the dump plane above the step (near $x = 0$ mm). The behavior of fuel droplets after being injected was investigated in detail by post-processing the LES data. The results revealed that the fuel droplets required approximately one half of a

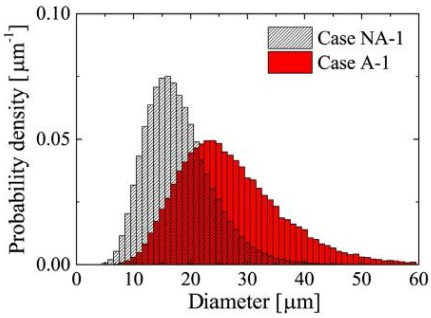

Fig. 16. Comparison of phase-averaged fuel droplet size distributions at the phase of $\phi = 180^{\circ}$, between cases without (Case NA-1) and with (Case A-1) SMD modulation.

period (i.e., phase difference of 180°) to traverse from the fuel injection ports to the location directly above the step/dump plane (distance of 5 mm). Therefore, the decrease in the evaporation rate at phase $\phi = 0^{\circ}$ in Case A-1 is influenced by the droplet diameter distribution of the injected liquid fuel, at the phase that occurs approximately one half of a period earlier (in other words, at $\phi = 180^{\circ}$).

Figure 16 shows the Probability Density Functions (PDF) of droplet diameter distribution of the injected liquid fuel droplets, with phase averaging at $\phi = 180^{\circ}$ for Case NA-1 and Case A-1. The figure shows that the number of fuel droplets with large diameters at $\phi = 180^{\circ}$ increased in Case A-1 in comparison with Case NA-1. As mentioned previously, the SMD and hence, the size distribution of injected fuel droplets are fixed in time for Case NA-1, while they vary in time for Case A-1. The fuel injection rate at any given phase is the same in both cases, meaning the volume of fuel injected is the same. However, the total droplet surface area available for evaporation is different between these two cases, which follows from the fundamental definition of Sauter Mean Diameter. For a fixed volume of fuel spray injected, its total surface area is inversely proportional to the SMD. Therefore, a shift to larger SMD implies a decrease in the total surface area available for evaporation. Therefore, the injection of relatively larger fuel droplets at phase $\phi = 180^{\circ}$ in Case A-1, leads to a reduction in the peak evaporation rate near the dump plane at the subsequent phase of $\phi = 0^{\circ}$ (see Fig. 15).

These results reveal that the temporal fluctuations of liquid fuel droplet size distribution (considered using the atomization/Lee model in Case A-1), which are caused by the velocity fluctuations of incoming air that accompanies the combustion instability, lead to the injection of fuel droplets with larger diameters in Case A-1, even though the mass/volume of fuel injected is the same in both cases. This leads to a decrease in the evaporation rate locally, which in turn decreases the heat release rate near the dump plane at the phase when pressure reaches its maximum value. Consequently, the correlation between heat release rate fluctuations and pressure oscillations is weakened (as indicated by the difference in the RI_x distributions in Fig. 13), which decreases the intensity of combustion instability.

3.2. Influence of temporal variations of liquid fuel flow rate on combustion instability

First, it is confirmed whether or not combustion instabilities are excited in the cases where the time variations of liquid fuel flow rate are considered, but the time variations of droplet size distribution are not (i.e., without SMD modulation). The phase shift ϕ_{ph} between the fuel flow rate variations and the pressure oscillations (used in the VMFR model) in Cases NA-2, NA-3, NA-4, and NA-5 is set to 0°, 90°, 180°, and 270°, respectively. Figure 17 shows the time variations of pressure P, heat release rate Q, streamwise velocity $\tilde{u}$, fuel droplet evaporation rate $\dot{m}$, and Fuel Mass Flow Rate (Fuel M.F.R) for Cases NA-2, NA-3, NA-4, and NA-5. The quantities P, $\tilde{u}$, Q and $\dot{m}$ shown in the figure are defined the same way as those in Fig. 6(a) and (b) of Section 3.1. The new quantity appearing in Fig. 17 is Fuel M.F.R (Mass Flow Rate) which represents the total value of fuel injection rate from all 7 ports. Figure 17 shows that these various physical quantities clearly oscillate with a period that is approximately constant in each case, except for Case NA-2. The phase difference between the variations of P and $\tilde{u}$ is approximately 90° in all cases except for Case NA-2. Moreover, the figure also shows that in all cases, the peaks in the variations of Fuel M.F.R occur approximately at $180^{\circ} \sim 270^{\circ}$ after the peaks in the variations of $\dot{m}$. Additionally, the phase shift between the variations of fuel flow rate and that of pressure, matches the value of phase difference ϕ_{ph} set for all the cases (see Table 1).

Figures 18 and 19 illustrate the pressure oscillation spectra and the streamwise distributions of the peak frequency component amplitudes of the pressure oscillations, respectively, for all the cases. The locations A, B, and C in Fig. 19 correspond to the same locations as shown in Fig. 4. The sampling time and period for calculating the statistics are approximately 0.05 s and 0.02 ms, respectively. Figure 18 shows that for all cases, the spectra of pressure oscillations have clear peaks within the frequency range of 600 Hz–750 Hz, and that the frequency corresponding to peak amplitude becomes smaller, as the phase shift ϕ_{ph} applied to the fuel flow rate variations becomes larger. Additionally, Fig. 19 shows that the oscillation mode of the peak frequency component of the pressure variations occurring in all cases, consists of the fundamental oscillation mode (1/4-wavelength mode) of the combustion chamber, with the oscillation antinode occurring at B and the oscillation node occurring at C. These results reveal that combustion instabilities occur in the cases that consider the temporal fluctuations in liquid fuel flow rate.

The effect of liquid fuel flow rate fluctuations accounted for by the VMFR (Variable Mass Flow Rate) model, on the intensity of pressure oscillations arising from combustion instabilities is investigated next. In Case NA-5, flashback (a phenomenon wherein flames and fuel droplets flow upstream) and a particularly unstable combustion instability phenomenon occurred. Therefore, only Case NA-2, Case NA-3, and Case NA-4 are primarily discussed in this section. Figure 20 shows the RMS values of the pressure oscillations for all cases. The RMS value of pressure oscillations for Case NA-1, wherein the VMFR model is not applied, is also plotted for comparison. The figure shows that the phase shift ϕ_{ph} applied between the fluctuations in liquid fuel flow rate and the pressure oscillations using the VMFR model, influences the RMS value of the pressure oscillations (and hence, the intensity of combustion instabilities). It is evident that, as the phase shift ϕ_{ph} applied to the fuel flow rate fluctuations increases, the RMS value of pressure oscillations also increases. It is also apparent from Fig. 17 that, as the value of phase shift ϕ_{ph} increases, the amplitude of fuel mass flow rate (Fuel M. F. R) fluctuations also increases, which would influence the local fuel droplet evaporation rate. This would in turn influence the heat release rate, and consequently the coupling between heat release rate fluctuations and pressure oscillations, which would ultimately dictate the intensity of combustion instabilities. These factors are discussed in detail in the following.

To investigate the factors causing this increase in the RMS value of pressure oscillations, the Rayleigh Index RI for each case is calculated. Figure 21 shows the $x - y$ planar distributions of the spanwise-averaged (z-direction) value of RI for each case. The fig-

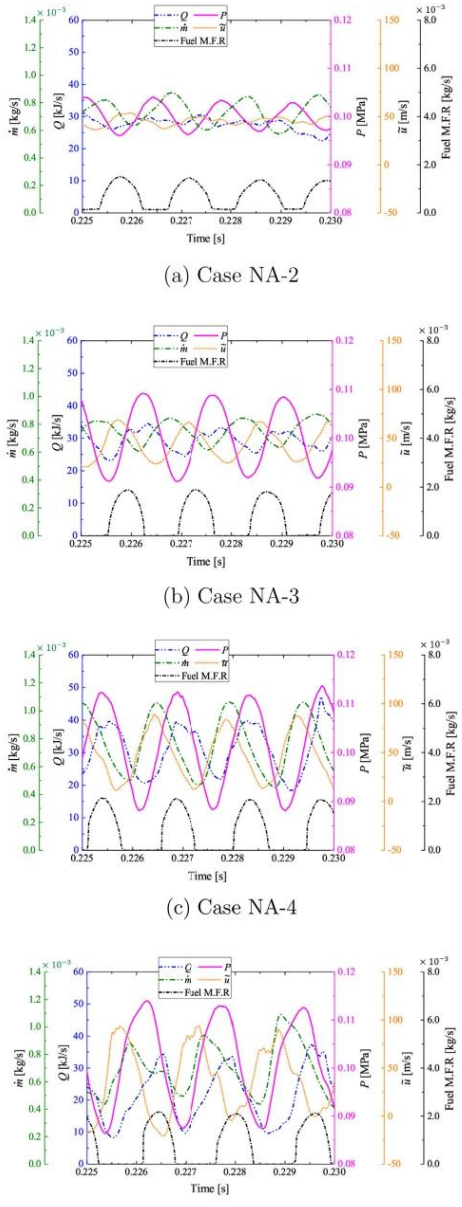

Fig. 17. Comparisons of time variations of pressure P, heat release rate Q, streamwise velocity $\tilde{u}$, droplet evaporation rate $\dot{m}$, and fuel mass flow rate (Fuel M.F.R), among cases with different phase shift angle ϕ_{ph} and without SMD modulation (Cases NA-2 to NA-5).

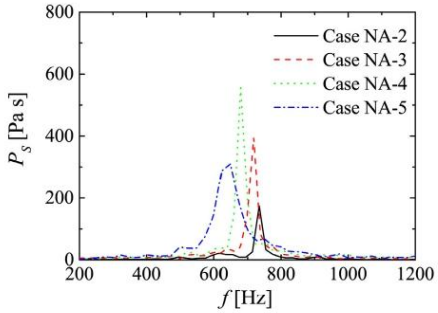

Fig. 18. Comparison of the spectra of pressure oscillations among cases with different phase shift angle ϕ_{ph} and without SMD modulation (Cases NA-2 to NA-5).

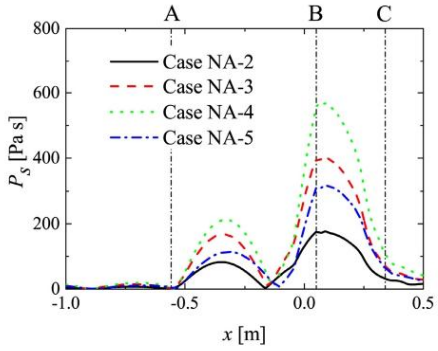

Fig. 19. Comparison of the streamwise profiles of amplitude of peak frequency components of pressure oscillations, among cases with different phase shift angle ϕ_{ph} and without SMD modulation (Cases NA-2 to NA-5).

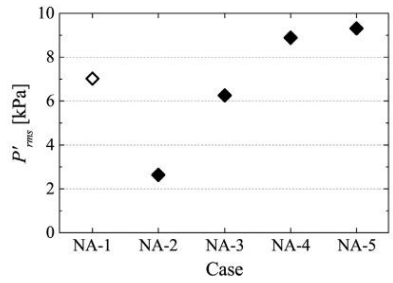

Fig. 20. Comparison of the intensities of pressure oscillations P'_{rms}, among cases with different phase shift angle ϕ_{ph} and without SMD modulation (Cases NA-1 to NA-5).

ure shows that as the phase shift ϕ_{ph} increases, the region in which the RI is positive becomes larger, and the region wherein RI is negative becomes smaller. Figure 22 shows the streamwise distributions of RI_x, which is the cross-sectional $(y-z)$-averaged value of the RI, for each case. The figure shows that in Case NA-2, Case NA-3, and Case NA-4, the positive peak position of RI_x approaches the vicinity of the combustion chamber's dump plane (upstream side) as the phase shift ϕ_{ph} increases. The antinodes

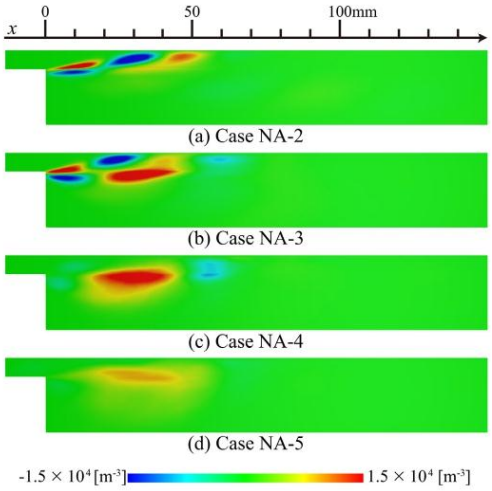

Fig. 21. Comparison of distributions of the spanwise-averaged local Rayleigh Index on the $x - y$ plane, among cases with different phase shift angle ϕ_{ph} and without SMD modulation (Cases NA-2 to NA-5).

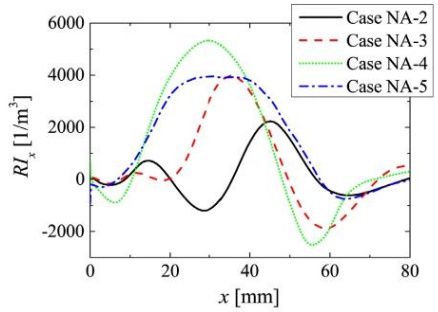

Fig. 22. Comparison of the streamwise distributions of cross-sectional $(y - z)$-averaged local Rayleigh Index RI_x, among cases with different phase shift angle ϕ_{ph} and without SMD modulation (Cases NA-2 to NA-5).

of pressure oscillations corresponding to the peak frequency components of Cases NA-2 to NA-5 are located near the combustor's dump plane, as shown in Fig. 19. Therefore, the positive peak of RI_x shifting upstream, closer to the dump plane would enhance the pressure oscillation amplitude. Hence, the difference in the RI_x distributions among Cases NA-2 to NA-5 is the reason behind the increasing RMS value of pressure oscillations, with increasing phase shift ϕ_{ph} applied to the temporal fluctuations of liquid fuel flow rate.

Next, the reasons for the differences in the distributions of RI_x are investigated in further detail. The positive RI_x distributions are strongly influenced by the heat release rate at the phase when pressure reaches its maximum value ($\phi = 90^\circ$). The streamwise distributions of the cross-sectional $(y - z)$-averaged heat release rate Q_x, with phase averaging at the phase $\phi = 90^\circ$ (when $P = P_{max}$), are shown in Fig. 23 for Case NA-2, Case NA-3, and Case NA-4. The figure shows that as the phase shift ϕ_{ph} increases, the peak value of Q_x distribution also increases and its position moves

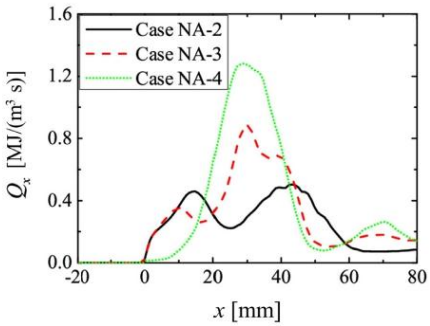

Fig. 23. Comparison of the streamwise distributions of phase- and cross-sectional $(y - z)$-averaged local heat release rate Q_x, at the phase of $\phi = 90^\circ$ among cases with different phase shift angle ϕ_{ph} and without SMD modulation (Cases NA-2 to NA-4).

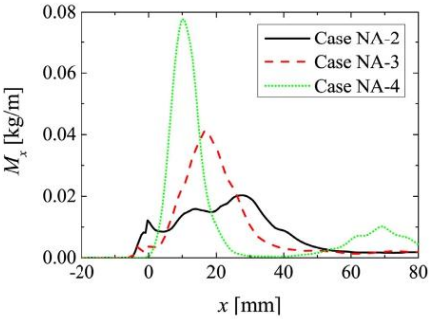

Fig. 24. Comparison of the streamwise distributions of phase-averaged local fuel mass M_x, at the phase of $\phi = 0^\circ$ among cases with different phase shift angle ϕ_{ph} and without SMD modulation (Cases NA-2 to NA-4).

upstream. Moreover, the position of the peak in Q_x distribution approximately coincides with the position of positive peak in the RI_x distribution for each case (see Fig. 22). Therefore, the fact that the position of peak in the heat release rate at the phase when pressure reaches its maximum value, is moving upstream as the phase shift ϕ_{ph} applied to the fluctuations of liquid fuel flow rate increases, is the reason for the difference in the RI_x distributions.

In the following, reasons for the upstream shift in the position of peak heat release rate (i.e., peak values of Q_x distributions in Fig. 23) at the phase when pressure reaches its maximum value (i.e., $\phi = 90^\circ$), with increasing phase shift ϕ_{ph} are investigated further. The spatial distribution of heat release rate at a particular phase (or time instance) is strongly influenced by the spatial distribution of gaseous fuel at the phase occurring immediately beforehand. Therefore, the streamwise distributions of the gaseous fuel mass M_x with phase averaging at $\phi = 0^\circ$, which will dictate the distributions of Q_x at phase $\phi = 90^\circ$, are shown in Fig. 24 for Case NA-2, Case NA-3, and Case NA-4. The figure shows that as the phase shift ϕ_{ph} increases, the peak value of M_x also increases and its position moves upstream. The distribution of the gaseous fuel at a particular phase is also strongly influenced by the distribution of fuel droplet evaporation rate at the phase occurring immediately beforehand. Hence, the streamwise distributions of the cross-sectional $(y - z)$-averaged evaporation rate $\dot{m}_x$ with phase

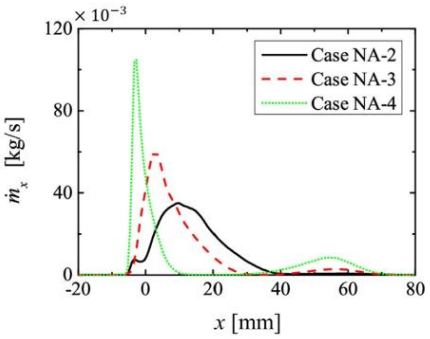

Fig. 25. Comparison of the streamwise distributions of phase- and cross-sectional ($y-z$)-averaged local evaporation rate $\dot{m}_x$, at the phase of $\phi = 270^\circ$ among cases with different phase shift angle ϕ_{ph} and without SMD modulation (Cases NA-2 to NA-4).

averaging at $\phi = 270^\circ$, which will govern the distributions of M_x at $\phi = 0^\circ$, are shown in Fig. 25 for Case NA-2, Case NA-3, and Case NA-4. Similar to the trends in the distributions of Q_x and M_x, the figure shows that as the phase shift ϕ_{ph} that is applied to the time variations of the liquid fuel flow rate increases, the peak value of $\dot{m}_x$ increases, its position moves upstream, and becomes more localized. Therefore, the reason for the position of peak heat release rate moving towards the upstream side of the combustor with increasing phase shift ϕ_{ph}, is the change in the relationship between the phase of temporal fluctuations of the liquid fuel flow rate, and the phase of time variations of the incoming oxidizing air's streamwise velocity, that leads to an increase in the residence time of the fuel droplets in the vicinity of the combustor's dump plane, causing an increase in the supply of gaseous fuel at the phase when pressure reaches its maximum value.

The results presented above indicate that the flow rate time variations of the liquid fuel injected into the combustion chamber, have a strong influence on the intensity of combustion instability. Moreover, as the phase shift ϕ_{ph} between the fuel flow rate variations and the pressure oscillations increases, the intensity of combustion instability also increases. This is due to the fact that the residence time and local evaporation rate of the fuel droplets increase as the phase shift ϕ_{ph} increases, which causes an increase in the heat release rate in the vicinity of the combustion chamber's dump plane, and also increases the strength of the correlation between the heat release rate fluctuations and the pressure oscillations.

3.3. Influences of temporal variations of droplet diameter distribution and liquid fuel flow rate on combustion instability

The excitation of combustion instabilities in the cases where temporal variations of both the fuel droplet diameter distribution (atomization/Lee model) and the fuel flow rate (VMFR model) are considered, is first confirmed. The phase shift ϕ_{ph} between the fuel flow rate variations and the pressure oscillations in Cases A-2, A-3, A-4, and A-5 is set to 0°, 90°, 180°, and 270°, respectively. Figure 26 shows the time variations of pressure P, heat release rate Q, streamwise velocity $\tilde{u}$, fuel droplet evaporation rate $\dot{m}$, SMD (Sauter Mean Diameter), and Fuel M.F.R for Cases A-2, A-3, A-4, and A-5. Once again, these quantities bear the same definitions as those in Figs. 6 and 17 of Sections 3.1 and 3.2, respectively. Figure 26 shows that these various physical quantities oscillate with a period that is approximately constant in each case, and

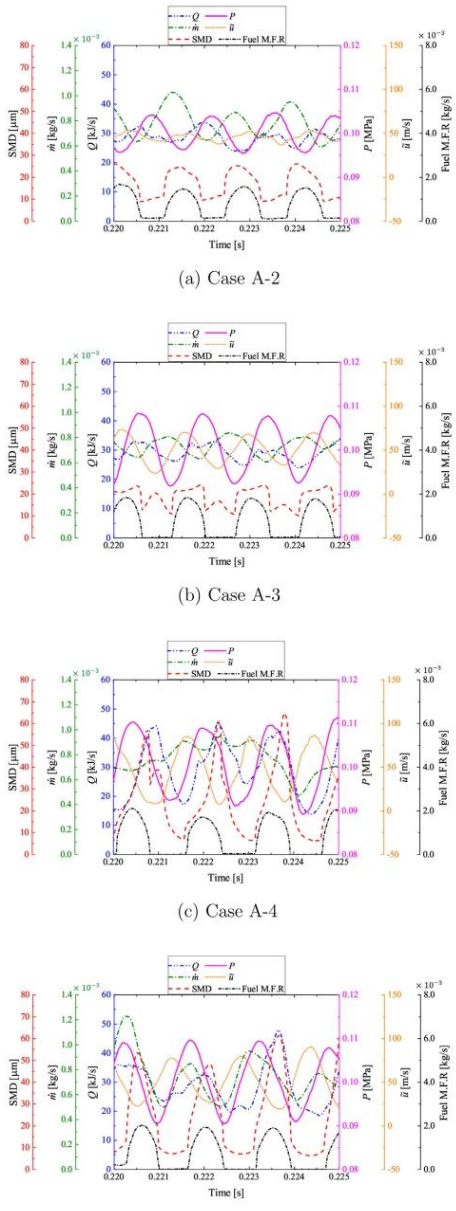

Fig. 26. Comparisons of time variations of pressure P, heat release rate Q, streamwise velocity $\tilde{u}$, droplet evaporation rate $\dot{m}$, droplet Sauter Mean Diameter (SMD), and fuel mass flow rate (Fuel M.F.R), among cases with different phase shift angle ϕ_{ph} and with SMD modulation (Cases A-2 to A-5).

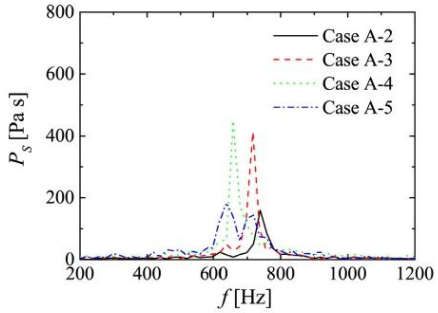

Fig. 27. Comparison of the spectra of pressure oscillations among cases with different phase shift angle ϕ_{ph}, and with SMD modulation (Cases A-2 to A-5).

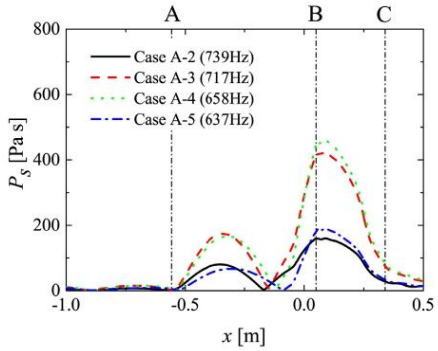

Fig. 28. Comparison of streamwise profiles of the amplitude of peak frequency components of pressure oscillations, among cases with different phase shift angle ϕ_{ph} and with SMD modulation (Cases A-2 to A-5).

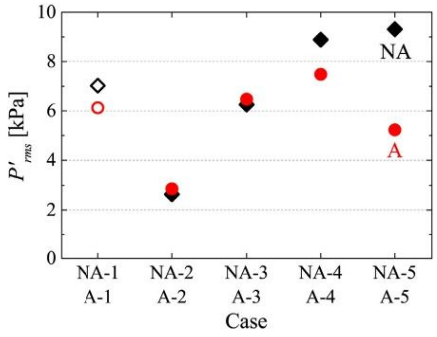

Fig. 29. Comparison of the intensities of pressure oscillations P'_{rms}, among cases with different phase shift angle ϕ_{ph}, without (Cases NA-1 to NA-5) and with (Cases A-1 to A-5) SMD modulation.

that combustion instabilities are excited in all cases. Moreover, the phase difference between the variations of P and $\tilde{u}$ is 90°. Additionally, the phase shifts ϕ_{ph} between the variations of fuel flow rate and the pressure oscillations match the settings in Table 1.

Figures 27, 28, and 29 show the spectra of pressure oscillations, the streamwise distributions of the amplitude of peak frequency components of the pressure oscillations, and the intensity of pressure oscillations P'_{rms}, respectively, for Cases A-2, A-3, A-4, and A-5 (Fig. 29 also shows the comparison of P'_{rms} with Case A-1 and the cases without SMD modulation i.e., Cases NA-1 to NA-5). Locations A, B, and C shown in Fig. 28 correspond to the same locations depicted in Fig. 4. The sampling time and period are approximately 0.05 s and 0.02 ms, respectively, for calculation of statistics. Figure 27 shows that the spectra of pressure oscillations have clear peaks in the frequency range of 600 Hz to 750 Hz for all cases. Additionally, Fig. 28 shows that the oscillation mode of the peak frequency component of pressure variations that occurs in all cases, consists of the fundamental oscillation mode (1/4-wavelength mode) of the combustion chamber, with the oscillation antinode and node occurring at B and C, respectively. These results indicate that combustion instabilities occur in the cases considering the time variations of both liquid fuel flow rate and fuel droplet diameter distribution (i.e., Cases A-2 to A-5).

Next, the effects of time variations of droplet diameter distribution and liquid fuel flow rate (i.e., when both variations are considered simultaneously), on the intensity of pressure oscillations caused by the combustion instabilities are investigated. Figure 29 shows the RMS values of pressure oscillations P'_{rms} for all cases (including the ones in which the Lee model is not used). The RMS values of pressure oscillations for Case NA-1 and Case A-1, wherein the VMFR model is not applied, are also plotted for comparison. The figure shows that, contrary to the trend for the cases in which only the time variations of fuel flow rate are considered (i.e., Cases NA-2 to NA-5 wherein only the VMFR model is applied, but not the Lee model), Cases A-4 and A-5 show an opposite trend in the intensity of pressure oscillations (P'_{rms}) with increasing ϕ_{ph}. In these cases, the temporal fluctuations of fuel droplet diameter distribution (considered using the Lee/atomization model) have the effect of decreasing the pressure oscillation intensity P'_{rms} (and hence the intensity of combustion instabilities), upon its mutual interaction with the fluctuations in liquid fuel flow rate (VMFR model). Additionally, as the phase shift ϕ_{ph} between the temporal fluctuations in fuel flow rate and the pressure oscillations becomes larger, the effect of the temporal fluctuations of fuel droplet diameter distribution on reducing P'_{rms} becomes more pronounced.

In the following, reasons for the reduction in the values of P'_{rms} at larger values of phase shift ϕ_{ph}, due to the influence of fluctuations in fuel droplet diameter distribution, and its interaction with the fluctuations in fuel flow rate are investigated. Figure 30 shows the $x-y$ planar distributions of the spanwise-averaged (z-direction) value of the Rayleigh Index RI for each case. By comparing Figs. 21 and 30, it can be seen that for the cases in which the phase shift ϕ_{ph} is large, i.e., Case A-4 ($\phi_{ph}=180°$) and Case A-5 ($\phi_{ph}=270°$), the region wherein RI is positive becomes smaller compared to that in the planar distributions of spanwise-averaged RI of the corresponding cases in Fig. 21 (i.e., Case NA-4 and Case NA-5, respectively, with corresponding phase shifts ϕ_{ph}). This difference in the RI distributions causes the pressure oscillations' RMS value to become smaller in Case A-4 and Case A-5. However, from Figs. 21 and 30, it is evident that the distributions of RI in Case A-2 and Case A-3 are virtually the same as those in Case NA-2 and Case NA-3, respectively. But, the intensity of pressure oscillations P'_{rms} of Case A-2 and Case A-3 are marginally higher than those of the corresponding cases without the Lee model (without SMD modulation), i.e., Case NA-2 and Case NA-3 as shown in Fig. 29. The phase shift ϕ_{ph} applied to Cases NA-2 and A-2 is $\phi_{ph}=0°$, and that applied to Cases NA-3 and A-3 is a relatively small value of $\phi_{ph}=90°$. Figure 31 illustrates the comparison of streamwise distributions of cross-sectional ($y-z$)-averaged local Rayleigh Index RI_x between Cases NA-2 and A-2, and between Cases NA-3 and A-3. The RI_x dis-

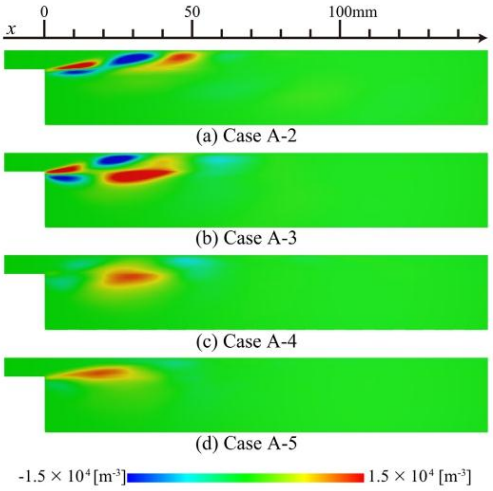

Fig. 30. Comparison of distributions of the spanwise-averaged local Rayleigh Index on the x-y plane, among cases with different phase shift angle ϕ_{ph}, and with SMD modulation (Cases A-2 to A-5).

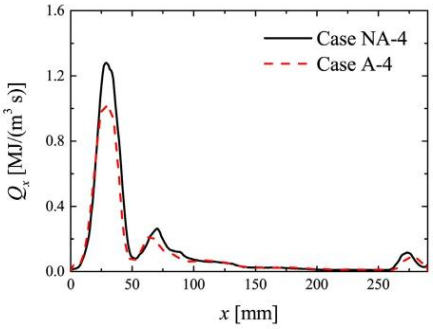

Fig. 32. Comparison of the streamwise distributions of phase- and cross-sectional (y-z)-averaged heat release rate Q_x, at the phase of $\phi = 90^\circ$ (when $P = P_{max}$), between cases without (Case NA-4) and with (Case A-4) SMD modulation.

tributions of Cases NA-2 and A-2 in Fig. 31(a) are similar in shape, but the positive RI_x distribution of Case A-2 has slightly larger values at certain streamwise locations, especially close to the dump plane. Similar tendency is observed in the RI_x distributions of Cases NA-3 and A-3 in Fig. 31(b). In the vicinity of the dump plane, the positive RI_x distribution of Case A-3 also has slightly larger values compared to that of Case NA-3. Therefore, the P'_{rms} values of Case A-2 and Case A-3 are marginally higher (although the difference is virtually insignificant) than those of the corresponding cases without the Lee model (without SMD modulation), i.e., Case NA-2 and Case NA-3, respectively.

The cause for the RMS value of pressure oscillations in Case A-4 being smaller than that in Case NA-4 is examined next. Since the positive RI spatial distributions are strongly influenced by the heat release rate at the phase when pressure reaches its maximum value (i.e., $\phi = 90^\circ$), the streamwise distributions of the cross-sectional ($y - z$)-averaged heat release rate Q_x with phase averaging at the phase $\phi = 90^\circ$ are shown in Fig. 32 for Cases NA-4 and A-4. The figure shows that the value of Q_x in the vicinity of the combustion chamber's dump plane is smaller in Case A-4 compared to Case NA-4. The distribution of heat release rate at $\phi = 90^\circ$ is governed by the distribution of fuel droplet evaporation rate at the phase occurring previously. Hence, the $x - y$ planar distributions of phase- and spanwise-averaged (z-direction) fuel droplet evaporation rate $\dot{m}_x$ at various phases are examined in Fig. 33 for Cases NA-4 and A-4. The figure shows that the evaporation rate in the vicinity of the combustor's dump plane is smaller for Case A-4 in comparison with Case NA-4 during $\phi = 270^\circ - 0^\circ$. Therefore, the decrease in heat release rate at phase $\phi = 90^\circ$ in Case A-4 is caused by the decrease in its evaporation rate during $\phi = 270^\circ - 0^\circ$.

The behavior of fuel droplets after being injected was analyzed in detail by post-processing the LES data, to investigate the reason behind the decrease in evaporation rate during $\phi = 270^\circ - 0^\circ$ in Case A-4. The results revealed that many of the droplets in the region where the evaporation rate for Case A-4 was lower in comparison with Case NA-4 during $\phi = 270^\circ - 0^\circ$, were injected at phase $\phi \approx 90^\circ$ when the fuel mass flow rate is largest (this can be confirmed from Figs. 17(c) and 26(c)). In Cases NA-4 and A-4, fuel injection starts around $\phi = 0^\circ$ and lasts up to $\phi = 180^\circ$, with the fuel injection rate peaking at $\phi \approx 90^\circ$ (see Figs. 17(c) and 26(c), respectively). Furthermore, the inlet air mass flow rate is fixed in both cases and the overall equivalence ratio is also maintained at 1.0 in both cases. From Fig. 26(c), it is evident that the

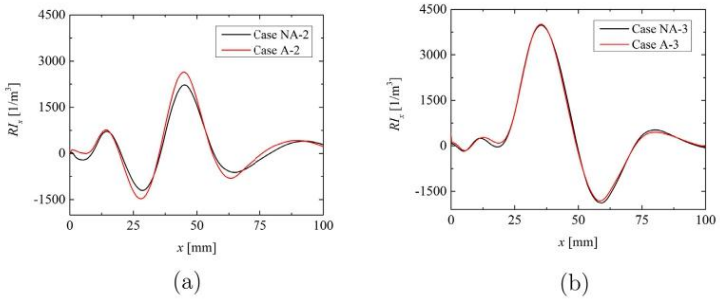

Fig. 31. Comparison of the streamwise distributions of cross-sectional ($y - z$)-averaged local Rayleigh Index RI_x between (a) Cases NA-2 and A-2, and (b) Cases NA-3 and A-3.

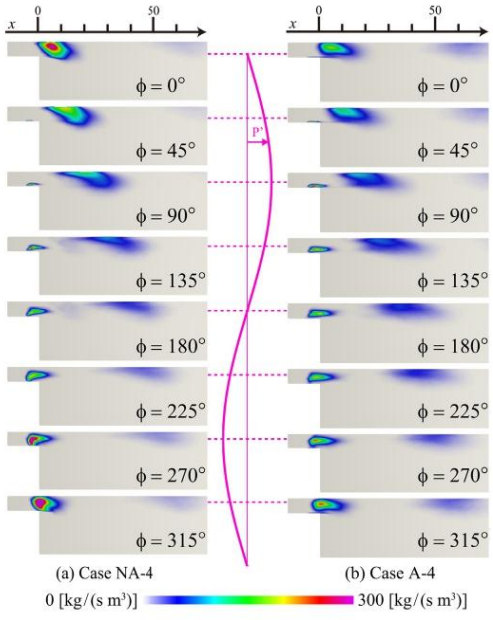

Fig. 33. Comparison of the distributions of phase- and spanwise-averaged evaporation rate, between cases without (Case NA-4) and with (Case A-4) SMD modulation.

SMD of injected fuel spray in Case A-4 is mostly large compared to the constant SMD value of 22.5 μm of the injected fuel spray in Case NA-4, during the fuel injection period of $\phi = 0^\circ - 180^\circ$. The total mass/volume of fuel spray injected during the period $\phi = 0^\circ - 180^\circ$ is nearly the same in both Cases NA-4 and A-4, but in Case A-4, the injected spray comprises of larger diameter droplets compared to Case NA-4. For the same volume of fuel spray injected, the total droplet surface area available for evaporation is inversely proportional to the SMD. The droplet relaxation time τ_d and the turbulent time scale τ_t (defined in Section 3.1) estimates for Case NA-4 are, $\tau_d = 5.72 \times 10^{-8} - 7.89 \times 10^{-4}$ s and $\tau_t = 6.04 \times 10^{-3}$ s, yielding Stokes number (defined here as the ratio τ_d/τ_t) in the range $\mathrm{St} = 9.47 \times 10^{-6} - 0.131$. Similarly, for Case A-4, $\tau_d = 5.69 \times 10^{-8} - 8.78 \times 10^{-4}$ s and $\tau_t = 4.46 \times 10^{-3}$ s, which implies St ranges from 1.28×10^{-5} to 0.197. A lot of the fuel droplets injected during $\phi = 0^\circ - 180^\circ$ reside in the vicinity of the dump plane in both cases (due to the application of phase shift $\phi_{ph} = 180^\circ$ between the fuel flow rate fluctuations and the pressure oscillations), which can be qualitatively discerned from the distributions of evaporation rate at the corresponding phases ϕ in Fig. 33 (although there will be some time delay between fuel spray injection and evaporation). Since the fuel mass flow rate is maximum at $\phi = 90^\circ$, the decrease in fuel droplet evaporation rate in the vicinity of combustor's dump plane in Case A-4, will be influenced by the droplet diameter distribution of liquid fuel at $\phi \approx 90^\circ$. Figure 34 shows the size distributions of fuel droplets with phase averaging at $\phi = 90^\circ$ for Cases NA-4 and A-4. The droplet size distribution PDFs shown in this figure are computed at the phase $\phi = 90^\circ$, using all the droplets within the control volume ranging from the fuel injection ports' location to the combustor's dump plane. This implies that the fuel droplets that were injected starting at the phase $\phi = 0^\circ$ till the phase $\phi = 90^\circ$,

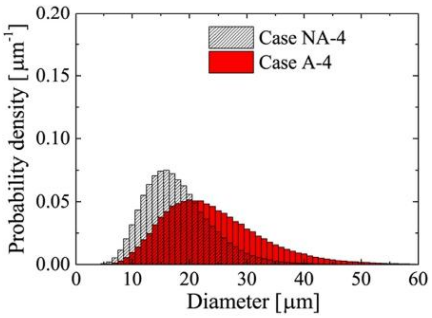

Fig. 34. Comparison of phase-averaged droplet size distributions, at the phase of $\phi = 90^\circ$ (when $P = P_{max}$), between cases without (Case NA-4) and with (Case A-4) SMD modulation.

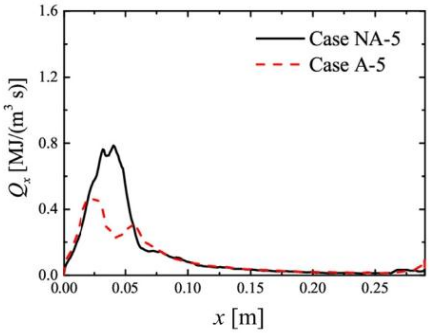

Fig. 35. Comparison of the streamwise distributions of phase- and cross-sectional (y-z)-averaged heat release rate Q_x, at the phase of $\phi = 90^\circ$ (when $P = P_{max}$), between cases without (Case NA-5) and with (Case A-5) SMD modulation.

and that are still residing within the aforementioned control volume, are included in the droplet size distribution PDFs depicted in Fig. 34. This figure shows that the droplet diameter distribution becomes wider in Case A-4 at phase $\phi = 90^\circ$, resulting in a larger SMD of the fuel spray for Case A-4. Hence, the evaporation rate near the dump plane is lower in Case A-4 compared to Case NA-4 during $\phi = 270^\circ - 0^\circ$. These results reveal that the reason for the RMS value of pressure oscillations becoming smaller in Case A-4, is the mean droplet diameter of the fuel spray becoming larger (owing to the application of Lee/atomization model), which subsequently causes the evaporation rate to decrease. This in turn leads to a reduction in the heat release rate in the vicinity of the combustion chamber's dump plane, that ultimately weakens the correlation between the heat release rate fluctuations and the pressure oscillations.

The reason for P'_{rms} becoming smaller for Case A-5 in comparison with Case NA-5 is also investigated. Similar to the situation between Cases A-4 and NA-4, the region wherein RI is positive becomes smaller in Case A-5 (see Fig. 30) compared to Case NA-5 (see Fig. 21), which causes the decrease in its pressure oscillation intensity P'_{rms}. Therefore, the heat release rate at the phase when pressure reaches its maximum value ($\phi = 90^\circ$) is examined. Figure 35 shows the streamwise distributions of the cross-sectional ($y - z$)-averaged heat release rate Q_x, with phase averaging at $\phi = 90^\circ$ for Cases NA-5 and A-5. The figure shows that the value of

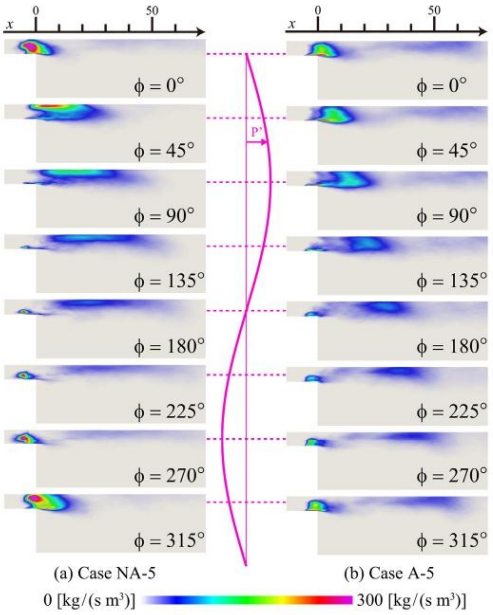

Fig. 36. Comparison of the distributions of phase- and spanwise-averaged evaporation rate, between cases without (Case NA-5) and with (Case A-5) SMD modulation.

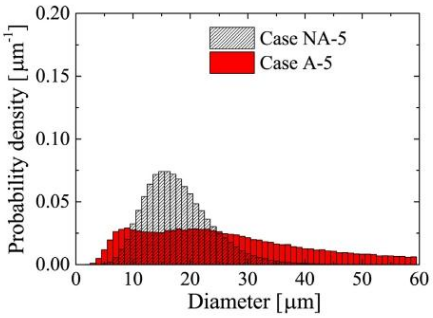

Fig. 37. Comparison of phase-averaged droplet size distributions, at the phase of $\phi = 180^\circ$ (when $P = P_{atm}$), between cases without (Case NA-5) and with (Case A-5) SMD modulation.

Q_x in the vicinity of the dump plane is smaller in Case A-5 compared to Case NA-5. Since the distribution of heat release rate at $\phi = 90^\circ$ is influenced by the distribution of fuel droplet evaporation rate at the previous phase, the $x - y$ planar distributions of the phase- and spanwise-averaged (z-direction) fuel droplet evaporation rate $\dot{m}_x$ at various phases of Case NA-5 and Case A-5 are shown in Fig. 36. The figure shows that the evaporation rate in the vicinity of the combustor's dump plane is smaller for Case A-5 in comparison with Case NA-5 during $\phi = 270^\circ - 0^\circ$. Therefore, the decrease in the heat release rate at $\phi = 90^\circ$ is caused by the decrease in the evaporation rate during $\phi = 270^\circ - 0^\circ$.

Upon examining the behavior of fuel droplets after being injected in both the cases, using their post-processed LES data, it was observed that many of the droplets in the region wherein the evaporation rate was lower for Case A-5 in comparison with Case NA-5 during $\phi = 270^\circ - 0^\circ$, were injected at $\phi \approx 180^\circ$ when the fuel mass flow rate is maximum (which can be confirmed from Figs. 26(d) and 17(d)). Fuel injection starts around $\phi = 90^\circ$ and ends at $\phi = 270^\circ$, with the peak fuel mass flow rate occurring at $\phi \approx 180^\circ$ in Cases NA-5 and A-5 (see Figs. 17(d) and 26(d)). The SMD of injected fuel spray in Case A-5 increases rapidly during $\phi = 90^\circ - 180^\circ$, and attains maxima around phase $\phi = 180^\circ$, as apparent from Fig. 26(d). Therefore, the injected fuel spray in Case A-5 is mostly comprised of large diameter fuel droplets compared to Case NA-5 in which the injected fuel spray's SMD (or droplet size distribution) is constant in time (SMD = 22.5 μm). For Case NA-5, droplet relaxation time is in the range of $\tau_d = 5.6 \times 10^{-8} - 8.34 \times 10^{-4}$ s, and turbulent time scale $\tau_t = 5.18 \times 10^{-3}$ s, hence $\mathrm{St} = 1.08 \times 10^{-5} - 0.161$. Similarly, for Case A-5, $\tau_d = 5.53 \times 10^{-8} - 8.5 \times 10^{-4}$ s and $\tau_t = 7.44 \times 10^{-3}$ s, which means $\mathrm{St} = 7.44 \times 10^{-6} - 0.114$. Additionally, due to the application of phase shift $\phi_{ph} = 270^\circ$ in Cases NA-5 and A-5, the phase relationship between the fluctuations of incoming air's streamwise velocity $\tilde{u}$ and fuel flow rate is altered (Figs. 17(d) and 26(d)), and most of the fuel droplets injected during $\phi = 90^\circ - 270^\circ$ reside near the dump plane, as indicated by the distributions of evaporation rate in Fig. 36. Moreover, in both Case NA-5 and Case A-5, the air mass flow rates are the same and the overall equivalence ratio is maintained at 1.0. So once again, following the same reasoning applied to Cases NA-4 and A-4 using the aforementioned details, the total droplet surface area of the injected fuel spray available for evaporation should be smaller in Case A-5 compared to Case NA-5, since it is inversely proportional to the SMD. Hence, the evaporation rate near the dump plane becomes smaller for Case A-5 compared to Case NA-5 during the subsequent phases, i.e., $\phi = 270^\circ - 0^\circ$.

To get an idea of the droplet sizes encountered in Cases NA-5 and A-5, the phase-averaged droplet size distributions of the fuel sprays calculated at $\phi = 180^\circ$ (maximum fuel injection rate) are shown in Fig. 37. Similar to Cases NA-4 and A-4, the phase-averaged droplet size distribution PDFs in Fig. 37 have been computed using all the droplets within the control volume ranging from the injection ports' position to the dump plane. As mentioned before, the application of the phase shift $\phi_{ph} = 270^\circ$ using the VMFR model to Cases NA-5 and A-5, will result in many of the fuel droplets injected during $\phi = 90^\circ - 180^\circ$ to still reside within this control volume at the phase $\phi = 180^\circ$, and they are also included in the droplet size distribution PDFs in Fig. 37. The figure indicates that the droplet diameter distribution at $\phi = 180^\circ$ becomes much wider for Case A-5, implying that its corresponding SMD also becomes larger. Since this droplet size distribution of fuel spray will influence the evaporation rate near the dump plane, Case A-5 has lower evaporation rate compared to Case NA-5. These results reveal that the reason for the pressure oscillations' RMS value becoming smaller for Case A-5 in comparison with Case NA-5, is the same as that for Cases A-4 and NA-4 discussed above.

The droplet size distribution PDF of Case A-5 in Fig. 37 is much wider or flatter than that of Case A-4 in Fig. 34. In Case A-5 the injected fuel spray consists mostly of large droplets owing to the generally large SMD values during the fuel injection period (see Fig. 26(d)). But, these injected droplets will simultaneously undergo evaporation as well and reduce in diameter during $\phi = 90^\circ - 180^\circ$. Therefore, when this cluster of fuel droplets is used to calculate the size distribution PDF at phase $\phi = 180^\circ$, a flatter PDF shape is obtained for Case A-5 due to some of the previously injected (during $\phi = 90^\circ - 180^\circ$) large droplets having already evaporated to some extent and reduced in size. This is made possible by the longer residence time of fuel droplets in Case A-5 compared to that in Case A-4 within the above-mentioned control volume,

as a consequence of the larger value of phase shift $\phi_{ph} = 270^{\circ}$ applied in Case A-5. The residence time of fuel droplets will be longer in Case A-5 compared to that in Case A-4, because the peak fuel injection rate in Case A-5 occurs around the phase when the incoming air's streamwise velocity is minimum (see Fig. 26(d)). Such tendency is not observed in the droplet size distribution PDF of Case NA-5 (even though droplet evaporation is active during the residence period), since the Lee model (SMD modulation) is not applied and the fuel droplets are injected with a size distribution PDF that remains fixed in time (corresponding to a constant SMD of 22.5 μm). The above results reveal that the effect of temporal variations in the droplet diameter distribution of liquid fuel on the intensity of combustion instability, becomes more significant as the phase shift ϕ_{ph} between the fuel flow rate fluctuations and the pressure oscillations increases. This happens because the droplet diameter distribution of the injected fuel spray becomes wider as the phase shift ϕ_{ph} increases, which enhances the strength of its effect on suppressing the increase in local evaporation rate and the accompanying increase in heat release rate, owing to the time variations of liquid fuel flow rate as discussed in Section 3.2.

4. Conclusions

In this study, LES was applied to the turbulent spray combustion field inside a back-step flow combustor to investigate the effects of temporal fluctuations in droplet diameter distribution and the flow rate of liquid fuel entering the combustor, on the spray combustion instability characteristics. For the LESs performed in this study, the average Reynolds number at the inlet of the combustor was kept constant at 4000, the initial pressure inside the combustor was 0.1 MPa, the length of the combustor was 290 mm, the overall equivalence ratio was 1.0, and the average fuel droplet diameter for the cases without SMD modulation (i.e., without Lee model) was kept constant at 18 μm (SMD = 22.5 μm). A total of 10 cases were setup and investigated in a systematic manner, by changing the conditions in the models to take into consideration the influences of fuel spray atomization (Lee model), and fuel flow rate fluctuations along with its phase difference ϕ_{ph} with the pressure oscillations (VMFR model). The following conclusions were drawn from this study:

(1) Cases NA-1 and A-1 are first considered to investigate the influence of temporal fluctuations in droplet size distribution of injected fuel spray alone, on combustion instability. With the application of the Lee model in Case A-1, the droplet diameter distribution of liquid fuel entering the combustor varies in time, depending on the fluctuations in incoming oxidizing air velocity caused by combustion instability. Moreover, this temporal fluctuation in the droplet diameter distribution tends to lower the intensity of combustion instability. The reason for this is a weakening of the correlation between heat release rate fluctuations and pressure oscillations. This results from the reduction in heat release rate near the dump plane of the combustor, caused by the broadening of droplet size distribution of liquid fuel (in Case A-1) due to the temporal fluctuations in the SMD (considered via. the Lee/atomization model). Consequently, larger diameter fuel droplets are injected which leads to a localized reduction in the evaporation rate.

(2) For the cases in which only the VMFR model is applied, but not the Lee model (i.e., Cases NA-2 to NA-5), the temporal fluctuations in the flow rate of liquid fuel injected into the combustor strongly influence the combustion instability intensity. Moreover, the combustion instability intensity increases with increasing phase shift ϕ_{ph} between the fuel flow rate fluctuations and pressure oscillations. The reason for this is the strengthening of the correlation between the heat release rate fluctuations and the pressure oscillations. As the phase shift ϕ_{ph} increases, the heat release rate near the dump plane also increases as a consequence of increased fuel droplet residence time, and the subsequent localized increase in fuel droplet evaporation rate.

(3) For the cases in which both the VMFR model and the Lee model are applied simultaneously (i.e., Cases A-2 to A-5), the effect of temporal fluctuations in the liquid fuel droplet diameter distribution on reducing the combustion instability intensity, becomes more significant with increasing phase shift ϕ_{ph} between the liquid fuel flow rate fluctuations and the pressure oscillations. This is caused by a localized reduction in the fuel droplet evaporation rate (even though the fuel droplet residence time increases with increase in ϕ_{ph} as mentioned above), as a result of the widening in the droplet diameter distribution of the injected fuel spray (increased SMD and hence injection of larger diameter droplets) with increasing phase difference ϕ_{ph}. Hence, a localized decrease in the heat release rate is observed near the dump plane, which leads to the weakening of the correlation between heat release rate fluctuations and pressure oscillations.

The results in this study, were obtained using LES under limited conditions (mentioned above), and it is likely that the combustion instability behavior will change upon varying said conditions. This warrants further studies in the future, to investigate the effects of varying those conditions on the spray combustion instability characteristics.

Declaration of Competing Interest

The authors declare that they have no known competing financial interests or personal relationships that could have appeared to influence the work reported in this paper.

Acknowledgments

The authors are grateful to Dr. Kazuaki Matsuura of Japan Aerospace Exploration Agency (JAXA) and Prof. Taewoo Lee of Arizona State University for many useful discussions. This research was partially supported by MEXT (Ministry of Education, Culture, Sports, Science, and Technology – Japan) as "Priority issue on Post-K computer" (Accelerated Development of Innovative Clean Energy Systems), and by JSPS KAKENHI Grant Number 19H02076.

References

[1] International civil aviation organization, 2017, URL http://www.icao.int/Pages/default.aspx
[2] Japan aerospace exploration agency, 2003 URL http://www.jaxa.jp/article/special/aviation.
[3] T. Lieuwen, K. McManus, Introduction: combustion dynamics in lean-premixed prevaporized (LPP) gas turbines, J. Propuls. Power 19 (5) (2003) 721.
[4] A.P. Dowling, S.R. Stow, Acoustic analysis of gas turbine combustors, J. Propuls. Power 19 (2003) 751–764.
[5] T. Lieuwen, V. Yang, Combustion instabilities in gas turbine engines: operational experience, fundamental mechanisms, and modeling, Prog. Astronaut. Aeronaut. 210 (2005) 3–26.
[6] L. Rayleigh, The explanation of certain acoustical phenomena, Nature 18 (1878) 319–321.
[7] F. Culick, M.V. Heitor, J.H. Whitelaw, Unsteady combustion, Springer Science & Business Media, 1996.
[8] M. Zhu, A.P. Dowling, K.N.C. Bray, Self-excited oscillations in combustors with spray atomizers, J. Eng. Gas Turbines Power 123 (4) (2001) 779–786.
[9] J.-Y. Lee, E. Lubarsky, B.T. Zinn, Slow active control of combustion instabilities by modification of liquid fuel spray properties, Proc. Combust. Inst. 30 (2) (2005) 1757–1764.
[10] M. de la Cruz García, E. Mastorakos, A.P. Dowling, Investigations on the self-excited oscillations in a kerosene spray flame, Combust. Flame 156 (2) (2009) 374–384.

[11] S. Tachibana, K. Saito, T. Yamamoto, M. Makida, T. Kitano, R. Kurose, Experimental and numerical investigation of thermo-acoustic instability in a liquid–fuel aero-engine combustor at elevated pressure: validity of large-eddy simulation of spray combustion, Combust. Flame 162 (6) (2015) 2621–2637.
[12] T. Kitano, K. Kaneko, R. Kurose, S. Komori, Large-eddy simulations of gas- and liquid-fueled combustion instabilities in back-step flows, Combust. Flame 170 (2016) 63–78.
[13] K. Sato, E. Knudsen, H. Pitsch, Study of combustion instabilities imposed by inlet velocity disturbance in combustor using les, ASME Turbo Expo 2009: Power for Land, Sea, and Air, American Society of Mechanical Engineers (ASME) (2009), pp. 87–99.
[14] P. Wolf, G. Staffelbach, L.Y.M. Gicquel, J.-D. Muller, T. Poinsot, Acoustic and large eddy simulation studies of azimuthal modes in annular combustion chambers, Combust. Flame 159 (11) (2012) 3398–3413.
[15] B. Franzelli, E. Riber, L.Y.M. Gicquel, T. Poinsot, Large eddy simulation of combustion instabilities in a lean partially premixed swirled flame, Combust. Flame 159 (2) (2012) 621–637.
[16] P. Moin, K.D. Squires, W.H. Cabot, S. Lee, A dynamic subgrid-scale model for compressible turbulence and scalar transport, Phys. Fluids 3 (1991) 2746–2757.
[17] C.D. Pierce, P. Moin, A dynamic model for subgrid-scale variance and dissipation rate of a conserved scalar, Phys. Fluids 10 (12) (1998) 3041–3044.
[18] J.-P. Legier, T. Poinsot, D. Veynante, Dynamically thickened flame LES model for premixed and non-premixed turbulent combustion, Summer program 2000, CTR, Stanford University (2000), pp. 157–168.
[19] F. Charlette, C. Meneveau, D. Veynante, A power-law flame wrinkling model for LES of premixed turbulent combustion part I: non-dynamic formulation and initial tests, Combust. Flame 131 (1–2) (2002) 159–180.
[20] P.A. Strakey, G. Eggenspieler, Development and validation of a thickened flame modeling approach for large eddy simulation of premixed combustion, J. Eng. Gas Turbines Power 132 (7) (2010) 071501.
[21] F. Proch, A.M. Kempf, Numerical analysis of the Cambridge stratified flame series using artificial thickened flame LES with tabulated premixed flame chemistry, Combust. Flame 161 (10) (2014) 2627–2646.
[22] A. Rittler, F. Proch, A.M. Kempf, LES of the Sydney piloted spray flame series with the PFGM/ATF approach and different sub-filter models, Combust. Flame 162 (4) (2015) 1575–1598.
[23] M. Nakamura, F. Akamatsu, R. Kurose, M. Katsuki, Combustion mechanism of liquid fuel spray in a gaseous flame, Phys. Fluids 17 (12) (2005) 123301.
[24] A.L. Pillai, R. Kurose, Combustion noise analysis of a turbulent spray flame using a hybrid DNS/APE-RF approach, Combust. Flame 200 (2019) 168–191.
[25] J. Bellan, M. Summerfield, Theoretical examination of assumptions commonly used for the gas phase surrounding a burning droplet, Combust. Flame 33 (1978) 107–122.
[26] J. Bellan, K. Harstad, Analysis of the convective evaporation of nondilute clusters of drops, Int. J. Heat Mass Transf. 30 (1) (1987) 125–136.
[27] R.S. Miller, K. Harstad, J. Bellan, Evaluation of equilibrium and non-equilibrium evaporation models for many-droplet gas-liquid flow simulations, Int. J. Multiph. Flow 24 (6) (1998) 1025–1055.
[28] C.T. Crowe, M.P. Sharma, D.E. Stock, The Particle-Source-In Cell (PSI-CELL) model for gas-droplet flows, J. Fluids Eng. 99 (2) (1977) 325–332.
[29] T. Kitano, J. Nishio, R. Kurose, S. Komori, Effects of ambient pressure, gas temperature and combustion reaction on droplet evaporation, Combust. Flame 161 (2) (2014) 551–564.
[30] B. Franzelli, E. Riber, M. Sanjosé, T. Poinsot, A two-step chemical scheme for kerosene–air premixed flames, Combust. Flame 157 (7) (2010) 1364–1373.
[31] Y. Haruki, A.L. Pillai, T. Kitano, R. Kurose, Numerical investigation of flame propagation in fuel droplet arrays, Atom. Sprays 28 (4) (2018) 357–388.
[32] T. Hara, M. Muto, T. Kitano, R. Kurose, S. Komori, Direct numerical simulation of a pulverized coal jet flame employing a global volatile matter reaction scheme based on detailed reaction mechanism, Combust. Flame 162 (2015) 4391–4407.
[33] T.-W. Lee, J.E. Park, R. Kurose, Determination of the drop size during atomization of liquid jets in cross flows, Atom. Sprays 28 (3) (2018) 241–254.
[34] A.F. Ghoniem, S. Park, A. Wachsman, A. Annaswamy, D. Wee, H.M. Altay, Mechanism of combustion dynamics in a backward-facing step stabilized premixed flame, Proc. Combust. Inst. 30 (2) (2005) 1783–1790.
[35] K.R. Mcmanus, J.C. Magill, M.F. Miller, Combustion instability suppression in liquid-fueled combustors, AIAA Paper AIAA-98-0642, 1998(1998).
[36] S. Murugappan, E.J. Gutmark, S. Acharya, M. Krstic, Extremum-seeking adaptive controller for swirl-stabilized spray combustion, Proc. Combust. Inst. 28 (2000) 731–737.
[37] K. Yu, K.J. Wilson, T.P. Parr, K.C. Schadow, An experimental study on actively controlled dump combustors, RTO AVT Symposium on "Active Control Technology for Enhanced Performance Operational Capabilities of Military Aircraft, Land Vehicles and Sea Vehicles", Braunschweig, Germany, 2000.
[38] D.A. Smith, E.E. Zukoski, Combustion instability sustained by unsteady vortex combustion, AIAA Paper 85, (1985) 1248, https://apps.dtic.mil/sti/citations/ADP011178.
[39] P. González-Tello, F. Camacho, J. Vicaria, P.A. González, A modified Nukiyama–Tanasawa distribution function and a Rosin-Rammler model for the particle–size-distribution analysis, Powder Technol. 186 (2008) 278–281.
[40] H. Moriai, R. Kurose, H. Watanabe, Y. Yano, F. Akamatsu, S. Komori, Large-eddy simulation of turbulent spray combustion in a subscale aircraft jet engine combustor–predictions of NO and soot concentrations, J. Eng. Gas Turbines Power 135 (9) (2013) 091503.
[41] R.N. Roy, M. Muto, R. Kurose, Direct numerical simulation of ignition of syngas (H_2/CO) mixtures with temperature and composition stratifications relevant to HCCI conditions, Int. J. Hydrogen Energy 42 (41) (2017) 26152–26161.
[42] A.L. Pillai, R. Kurose, Numerical investigation of combustion noise in an open turbulent spray flame, Appl. Acoust. 133 (2018) 16–27.
[43] Y. Hu, R. Kurose, Nonpremixed and premixed flamelets LES of partially premixed spray flames using a two-phase transport equation of progress variable, Combust. Flame 188 (2018) 227–242.
[44] Y. Hu, R. Kurose, Partially premixed flamelet in les of acetone spray flames, Proc. Combust. Inst. 37 (3) (2019) 3327–3334.
[45] Y. Hu, R. Kurose, Large-eddy simulation of turbulent autoigniting hydrogen lifted jet flame with a multi-regime flamelet approach, Int. J. Hydrogen Energy 44 (12) (2019) 6313–6324.
[46] C.T. d'Auzay, U. Ahmed, A.L. Pillai, N. Chakraborty, R. Kurose, Statistics of progress variable and mixture fraction gradients in an open turbulent jet spray flame, Fuel 247 (2019) 198–208.
[47] U. Ahmed, C.T. d'Auzay, M. Muto, N. Chakraborty, R. Kurose, Statistics of reaction progress variable and mixture fraction gradients of a pulverised coal jet flame using Direct Numerical Simulation data, Proc. Combust. Inst. 37 (3) (2019) 2821–2830.
[48] V. Moureau, C. Bérat, H. Pitsch, An efficient semi-implicit compressible solver for large-eddy simulations, J. Comput. Phys. 226 (2) (2007) 1256–1270.
[49] G.-S. Jiang, C.-W. Shu, Efficient implementation of weighted ENO schemes, J. Comput. Phys. 126 (1996) 202–228.
[50] R.J. Kee, D.-L. Graham, J. Warnatz, M.E. Coltrin, J.A. Miller, A Fortran computer code package for the evaluation of gas-phase, multicomponent transport properties, SANDIA Report No. SAND86-8246, Sandia National Laboratories, Albuquerque NM, Livermore CA, 1986.
[51] R.J. Kee, F.M. Rupley, J.A. Miller, Chemkin-II: a FORTRAN chemical kinetics package for the analysis of gas-phase chemical kinetics, SANDIA Report No. SAND89-8009B, Sandia National Laboratories, Albuquerque NM, Livermore CA, 1989.
[52] R. kurose, 2019, URL http://www.tse.me.kyoto-u.ac.jp/members/kurose/link_e.php

Applied Mathematical Modelling 40 (2016) 268–283

Contents lists available at ScienceDirect

Applied Mathematical Modelling

journal homepage: www.elsevier.com/locate/apm

Modeling the atomization of high-pressure fuel spray by using a new breakup model

Yusong Yu *, Guoxiu Li, Yong Wang, Jiawei Ding

The School of Mechanical, Electronic and Control Engineering, Beijing Jiaotong University, Beijing 100044, China

ARTICLE INFO

Article history:
Received 28 August 2013
Received in revised form 30 July 2014
Accepted 17 April 2015
Available online 6 June 2015

Keywords:
Atomization
Cavitation
Nozzle internal flow
Spray near angle

ABSTRACT

The main objective of this research is to develop a new breakup model and investigate the influence of cavitation, turbulence on processes of high-pressure diesel sprays. The model distinguishes between jet primary atomization and droplet secondary atomization. The primary atomization was simulated based on a modified turbulence induced atomization model taken into account the coupling effects of the relaxation of the velocity profile, cavitation and turbulent fluctuation based on the principle of conservation of energy. The growth time scale of surface waves was provided by Kelvin–Helmholtz (K–H) instability theory on an infinite length cylinder for an inviscid liquid jet. The time scale of initial surface waves based on K–H instability theory on an infinite plane jet is much larger than that based on infinite length cylindrical jet. Based on the present modified model, the weighting coefficients of turbulence and cavitation on the overall atomization can be distinguished clearly. There was remarkable variation in simulated spray shape with present models. It could be seen that the original turbulence induced atomization model results in a shorter spray penetration and smaller drops near the spray core than the modified model. When applying the turbulent weighting coefficient C_t in the determination of the spray angle, the resultant value of spray angle gradually drops due to the reduction of C_t. However, the spray angle increases with increasing the cavitation weighting coefficient C_{cav}. Comparing the experimental results (such as spray angle, tip penetration and spray shape) with the theoretical ones for different injection pressure, gives a reasonable agreement.

1. Introduction

The atomization of fuel spray plays a key role in the mixing of diesel fuel vapor and air, ignition, combustion, and the formation of pollutant emissions. The detailed understanding of the spray formation process has been recognized as an significant step for the increase of combustion efficiency and the reduction of pollutant emissions for D.I. Diesel engines.

Knowledge of atomization near the spray nozzle is important and basic to understanding the spray mechanisms, as characteristics in this region affect the atomization performance achieved further downstream. Despite lots of experimental investigations have been carried out [1–11], an in-depth and quantitative understanding of the near-nozzle spray region hasn't been achieved. But a vast amount of study show that internal flow in nozzle has an important influence on the spray characteristics [12–14]. Quantitative evaluation of spray construction in this region is nearly infeasible using most of conventional techniques (e.g., visible light methods) [15]. Numerical simulation and theoretical analysis are powerful tools of

* Corresponding author. Tel.: +86 13810012475.

http://dx.doi.org/10.1016/j.apm.2015.04.046
0307-904X/

Nomenclature

α	nozzle diameter, m
L_t	integral length scale of turbulence, m
$L_{w.t}$	wavelength of surface instability, m
$L_{A.t}$	length scale of primary atomization, m
τ_t	turbulent time scale, s
U	liquid jet velocity, m/s
ρ_g	gas (ambient) density, kg/m^3
ρ_l	liquid fuel density, kg/m^3
ω	growth rate of instabilities, 1/s
r_p	radius of the product drop, m
δ	boundary thickness, m
θ	momentum thickness, m
α	spray cone angle, °
$\tau_{exp.t}$	time for the exponential growth of instabilities, s
τ_w	wave growth time scale, s
$\tau_{A.t}$	time scale of atomization, s
$\tau_{spn.t}$	time required for the spontaneous growth of instabilities, s
$E_{boundary}$	kinetic energy of relaxation of the velocity profile, m^2/s^2
E_t	kinetic energy of turbulence, m^2/s^2
E_c	kinetic energy of cavitation, m^2/s^2
υ_l	liquid kinematic viscosity, m^2/s
k	wave number of instabilities
σ	surface tension, N/m
c_d	discharge coefficient
Re	Droplet Reynolds number $2Ur_p/\upsilon_l$

Subscripts

x	x-direction
y	y-direction
l	liquid
g	gas
t	turbulent
c	cavitation

investigation of the atomization phenomena. Several theories have been proposed to explain the liquid core atomization, such as aerodynamic interaction with ambient gas, jet internal turbulence, cavitation inside the nozzle holes. Many researchers have focus on the effects of cavitation and turbulence on primary atomization. Arcoumanis et al. [16] numerically investigated the effects of nozzle flow and injection processes on the structure of diesel sprays. Huh and Gosman [17] developed a new phenomenological primary breakup model which considers the effects of turbulence on the jet breakup. Bianchi et al. [3] proposed a modified breakup model which included the effects of cavitation and turbulence in the KH model. S. Som developed a new primary breakup model named KH-ACT model. The new mode is modified to include the effects of cavitation and turbulence generated inside the injector. Rate of decrease in droplet radius scales with the ratio of length to time scale. The scales include aerodynamic-induced KH scale, cavitation and Turbulence scale. The largest ratio determines the dominant breakup process [18]. In Turner's study, the coherent liquid core is modeled as a liquid jet. The spray breakup is described using a composite model to separately address the disintegration of the liquid core into droplets and their further aerodynamic breakup. The jet breakup model uses the results of hydrodynamic stability theory to define the breakup length of the jet, and downstream of this point, the spray breakup process is modeled for droplets only [19]. But none of these theories alone can explain the complexity of the atomization phenomenon.

In an attempt to improve spray breakup predictions, many models have been proposed. The original TAB [20] spray breakup model was based on Taylor's analogy between an oscillating and distorting drop like a spring-mass system. Several studies [21–22] have revealed thought that the TAB model can produce excessive droplet breakup that is not in agreement with experimental data. This is attributed to the fact that cavitation and turbulence phenomena inside the injector nozzle and liquid core, experimentally shown to be of great importance to atomization [23–25], as well as non-linear droplet distortion effects are not accounted for in the TAB model. In the WAVE model [26–27], derived from a linear stability analysis of liquid jets, the breakup time is determined by surface instability of droplets as a function of the wavelength and the frequency of the Kelvin–Helmholtz wave. But WAVE model can't simulate the effects of nozzle internal flow (cavitation and turbulent fluctuations) on the jet atomization. In the turbulence induced atomization model [17] the jet internal

turbulence and gas inertia are thought to be the two dominant breakup forces. The turbulent fluctuations in the emerging jet are responsible of the initial surface perturbations that grow exponentially by K–H instabilities due to the interaction with surrounding gas.For high pressure Diesel spray the effects of jet turbulence, cavitation and nozzle flow on liquid core primary breakup must be considered [28]. The effects of cavitation, turbulence, and aerodynamic effect on spray characteristics have not previously been comprehensively investigated so far. The existing breakup models seldom consider the multiple factors of above effects. Furthermore, the qualitatively with varying degree of cavitation and turbulence has not been established. These provided the major motivation for the present study.

In present study, a hybrid breakup model was developed to investigate the atomization processes of high-pressure Diesel sprays. It distinguished between jet primary breakup and droplet secondary breakup. Jet primary breakup, which is the physical process that leads to the detachment of drops and ligaments from the liquid jet surface, was modeled using the modified turbulence induced atomization model. Concerning the secondary breakup, high-pressure injection systems lead to high droplet velocities and the competition between K–H instability and Rayleigh–Taylor (R–T) instability is considered. The hybrid model was added to the KIVA-3V code to simulate high-speed spray evolution. KIVA, a transient, three-dimensional, multiphase, multicomponent code for the analysis of chemically reacting flows with sprays has been under development at the Los Alamos National Laboratory. KIVA-3V used in this study is the 3d version of KIVA. The code uses an Arbitrary Lagrangian Eulerian methodology on a staggered grid. In addition, KIVA uses an implicit time-advancement with the exception of the advective terms that are second-order manner. A stochastic particle method is used to model liquid spray, including the effects of droplet collisions and aerodynamic breakups. The code allows it for easy modifications for solving a variety of hydrodynamics problems involving spray atomization, reaction and heat transfer etc. The code has a widespread application in the automotive industry. In order to validate the new model, the present model was applied to simulate the experiment of Blessing et al. [29]. Then the numerical study in the effects of injection pressure on spray characteristics were carried out.

2. Mathematical model

Jet primary breakup is the complex physical process that leads to the detachment of drops and ligaments from the continuous liquid jet. A review of literature clearly reveals that the primary atomization is the result of complex phenomena like surface wave growth, internal jet turbulence fluctuations and cavitation inside the injection nozzle [19]. Since, none of the previous theories alone is able to describe the whole spray dynamics, a more accurate breakup model taken into account much of factors should be presented. In this study, a modified turbulence induced atomization model is given. For the secondary droplet breakup, the KH–RT model is used. After liquid droplets disintegrate from continuous liquid core, breakup model should be changed from the primary breakup model to secondary breakup model.

2.1. turbulence induced atomization mode

In the turbulence induced atomization model [17] the jet internal turbulence and gas inertia are thought to be the two dominant breakup forces, i.e., liquid turbulence and aerodynamic. The turbulent fluctuations in nozzle flow are responsible of the initial surface waves that grow exponentially by K–H instabilities due to the interaction with surrounding gas.

The length and time scales of surface waves are defined and used to describe the atomization process. The wavelength of surface instability ($L_{w,t}$) is assumed to be proportional to the integral length scale of turbulence (L_t) which is the dominant length scale of primary atomization ($L_{A,t}$).

$$L_{A,t} = C_1 L_t = C_2 L_{w,t} \tag{1}$$

with $C_1 = 2$ and $C_2 = 0.5$. Huh and Gosman assumed that the atomization length scale was twice the integral length scale of liquid jet turbulence.

The time scale of atomization $\tau_{A,t}$ is assumed to be the linear sum of the turbulent time scale τ_t and the wave growth time scale τ_w.

$$\tau_{A,t} = \tau_{spn,t} + \tau_{\exp,t} = C_3 \tau_t + C_4 \tau_{w,t} \tag{2}$$

The constants C_3 and C_4 have been kept equal to 1.0 and 3.0 respectively [17]. In Eq. (2) $\tau_{spn,t}$ and $\tau_{\exp,t}$ are the time required for the spontaneous growth of instabilities and the time for their exponential growth until they detach as droplets respectively. The wave growth time scale τ_w is provided by K–H instability theory ($L_w = L_{w,t}$) on an infinite plane for an inviscid liquid jet.

$$\tau_{w,t} = \frac{1}{\sqrt{\frac{\rho_l \rho_g}{(\rho_l+\rho_g)^2}\left(\frac{U}{L_w}\right)^2 - \frac{\sigma}{(\rho_l+\rho_g)L_w^3}}} \tag{3}$$

The liquid jet average turbulent kinetic K_{avg} and its dissipation rate ε_{avg} at the nozzle exit is calculated using a simple force balance based on based on the pressure drop along the nozzle downstream length [17].

$$K_{avg} = \frac{U^2}{8L/D}\left(\frac{1}{c_d^2} - K_c - \left(1 - s^2\right)\right) \tag{4}$$

$$\varepsilon_{avg} = K_\varepsilon \frac{U^3}{2L}\left(\frac{1}{c_d^2} - K_c - (1-s^2)\right) \tag{5}$$

The velocity U is a liquid velocity at the nozzle exit. L and D are the nozzle length and diameter respectively. The discharge coefficient, the loss coefficient due to the nozzle entrance sharpness, and the downstream-to-upstream contraction area ratio of the injection nozzle are represented by c_d, K_c, and s, respectively. K_c and K_ε are model constants whose values are 0.45 and 0.27 respectively [30].

The turbulent length and time scale are related to the turbulent kinetic energy and its dissipation rate in the injection holes.

$$L_t = C_\mu \frac{\kappa_{avg}^{3/2}}{\varepsilon_{avg}} \tag{6}$$

$$\tau_t = C_\mu \frac{\kappa_{avg}}{\varepsilon_{avg}} \tag{7}$$

The constant c_μ is equal to 0.009 [17].

Owing to the droplet breakup, the diameter of the parent drop is assumed to decrease continuously with time according to the following expression:

$$\frac{dr}{dt} = -\frac{L_{A,t}}{\tau_{A,t}} \tag{8}$$

The spray cone angle is calculated as:

$$\tan\alpha/2 = \frac{L_{A,t}/\tau_{A,t}}{U} \tag{9}$$

2.2. Modified turbulence induced atomization model

For high pressure injection systems cavitation may occur in the injectors [31]. Cavitating sprays have characteristics significantly different from the non cavitating ones. Cavitation effects injection velocity, droplet size, jet turbulence and liquid core atomization characteristics [32].

According to M. Blessing's experimental study [29], the cavitating flow inside nozzle hole and the spray hole, as well as the spray exiting the nozzle was observed. In the cavitation flow, the cavitation bubbles are carried by the flow up to the spray nozzle exit. Beside hydraulic and aerodynamic forces, the decay of the cavitation bubbles leads by an increase of turbulence to an intensified spray break up in the spray jet exiting the hole. The experimental results indicated that cavitation has great influence on the micro cone angle of the spray near the nozzle exit.

Recently, several efforts of using more sophisticated numerical approaches have been performed in modeling the detailed turbulent flow fields in the liquid and gas during the atomization process. Jun Ishimoto et al. [33] computed the two-phase flows using LES-VOF method in conjunction with the CSF model [33]. According to the analysis, the atomization rate and the droplets-gas two-phase flow characteristics are found to be dominated by the turbulence fluctuations upstream of the injector nozzle, hydrodynamics instabilities at the gas–liquid interface, and shear stresses between the continuous liquid core and peripheral ambient of the jet. The results also reveal that the initial perturbations of the liquid column surface resulting from initial wave growth are due to a combination of turbulence and relaxation of the velocity profile as the liquid exits from the nozzle.

A review of the literature clearly shows that the primary atomization is involved with lots of factors, for instance cavitation inside nozzle, interaction between liquid and surrounding gas, internal jet turbulence fluctuations and relaxation of the velocity profile at nozzle exit, etc. A high-precision breakup model should be taken into account all of them. Hence, present research focuses on the formulation of the equations to account for four effects mentioned on the primary atomization. The resulting model should consider the combination of these four factors.

2.2.1. Cavitation induced initial waves

In the present study, the flow in the nozzle is modeled as a quasi-steady, zero-dimensional flow using the method of Sarre et al. [34]. The flow is divided into cavitating flow, when the fluid pressure at the vena contraction is assumed to be the vapor pressure, and non-cavitating flow. According to Sarre's method, the effective flow area A_{eff} can be calculated. Then the radius of an equivalent bubble R_{cav} and the atomization length scale L_{cav} are given by:

$$R_{cav} = \sqrt{\frac{\pi r_{geo}^2 - A_{eff}}{\pi}} \tag{10}$$

$$L_{cav} = 2\pi(r_{geo} - R_{cav}) \tag{11}$$

2.2.2. Turbulence fluctuations induced initial waves

In the work of Huh and Gosman [17], the parent drops were assumed to carry homogeneous isotropic turbulence starting at the injection nozzle exit. Assuming further that no additional internal turbulence is generated, an analytical solution of the turbulence scale through the use of the well-known $k-\varepsilon$ turbulence model was obtained. Details of this derivation can refer to [17,30]. The turbulent length L_t is calculated by Eq. (6).

2.2.3. Initial waves induced by relaxation of the velocity profile at nozzle exit

According to Blasius solution, the boundary thickness δ and momentum thickness θ in laminar flow can be expressed as

$$\frac{\delta}{x}=\frac{4.91}{(\mathrm{Re}_x)^{1/2}} \tag{12}$$

$$\frac{\theta}{x}\approx\frac{0.664}{(\mathrm{Re}_x)^{1/2}} \tag{13}$$

Based on the stability analysis of the separated boundary layer carried out by Brennen [35], the frequency of the disturbance in the actual flow is represented as

$$f=\frac{\gamma}{2\pi}\cdot\frac{U}{\theta} \tag{14}$$

where γ ($\gamma=0.175$) is non-dimensional frequency, f is the frequency of the disturbance in flow.

Assuming that the magnitude of the wave propagation velocity is equal to flow velocity, the wave length λ can be expressed as

$$\lambda=\frac{c}{f}\approx\frac{U}{f}=\frac{2\pi}{\gamma}\cdot\theta \tag{15}$$

When substituting the momentum thickness in laminar and turbulence flow into Eq. (15), the initial surface wave length at orifice exit is written as

$$L_{boundary}=\frac{2\pi}{\gamma}\frac{0.664}{(\mathrm{Re}_L)^{1/2}}\cdot L \tag{16}$$

where $\mathrm{Re}_L=\frac{U\cdot L}{\nu}$, L is the nozzle length, $L_{boundary}$ is initial surface length scale induced by separated boundary layer at orifice exit.

2.2.4. Kelvin–Helmholtz (KH) instability on infinite length cylinder jet

The growth time scale of surface waves provides by K–H instability theory on an infinite plane for an inviscid liquid jet in the original turbulence induced atomization model. Due to the different jet shape, the K–H instability theory on an infinite plane jet is inadequate to the predictions of surface stability of a cylindrical liquid jet in usual D.I. diesel engines.

In present study, the jet breakup is considered a cylindrical liquid jet issuing from a circular orifice into ambient. The stability of the liquid surface to linear perturbations ultimately leads to a dispersion Equation, which relates the growth rate ω, of an initial perturbation of infinitesimal amplitude, to its wave number k. The relationship also includes the physical and dynamical parameters of the liquid jet and the surrounding gas [36].

$$\begin{aligned}&(\omega+ik\cdot U)^2+2\nu_l k^2\left[\frac{I_1'(kr)}{I_0(kr)}-\frac{2kL}{k^2+L^2}\frac{I_1(kr)}{I_0(kr)}\frac{I_1'(Lr)}{I_1(Lr)}\right]\cdot(\omega+ik\cdot U)\\&=\frac{\sigma k}{\rho_l r^2}(1-r^2k^2)\cdot\left(\frac{L^2-k^2}{L^2+k^2}\right)\frac{I_1(kr)}{I_0(kr)}+\frac{\rho_g}{\rho_l}k^2\left(\frac{L^2-k^2}{L^2+k^2}\right)\frac{I_1(kr)}{I_0(kr)}\frac{K_0(kr)}{K_1(kr)}\omega^2\end{aligned} \tag{22}$$

where $L^2=k^2+\omega/\nu_l$, r is the radius of liquid jet, ν_l is liquid kinematic viscosity, I_n is the nth order modified Bessel function of the first kind, and K_n is the nth order modified Bessel function of the second kind, U is the relative velocity between gas and liquid phase. The above dispersion relation can be solved by using Muller's secant method, which is an iterative process.

The solution of above dispersion relation, which relates the wave growth rate ω to the wavenumber k, is complicated by the fact that the parameter L is still a function of r. It's infeasible for each liquid droplet in spray to solve dispersion relation by using Muller's secant iterative method, because of the numerous liquid droplets during atomization process. Even if the Monte Carlo method is adopted, the number of liquid particles still exceeds 10 of the third power.

When the liquid viscosity vanishes, the dispersion relation reduces to the results for an inviscid fluid.

$$(\omega+ikU)^2-\omega^2\frac{\rho_g}{\rho_l}\cdot\frac{K_0(ka)}{K_0'(ka)}\cdot\frac{I_0'(ka)}{I_0(ka)}=\frac{\sigma k}{\rho_l a^2}(1-k^2a^2)\cdot\frac{I_0'(ka)}{I_0(ka)} \tag{23}$$

The above Equation can be transformed into the following form, which is quadratic Equation of the wave growth rate ω.

$$\left(1-\frac{\rho_g}{\rho_l}\cdot\frac{K_0(ka)}{K_0'(ka)}\cdot\frac{I_0'(ka)}{I_0(ka)}\right)\omega^2+2ikU\omega-\left[k^2U^2+\frac{\sigma k}{\rho_l a^2}(1-k^2a^2)\cdot\frac{I_0'(ka)}{I_0(ka)}\right]=0 \tag{24}$$

For convenience, the analytical solution is expressed as:

$$\omega=\frac{-2ikU\pm\sqrt{-4k^2U^2+C}}{2A} \tag{25}$$

Where

$$A=1-\frac{\rho_g}{\rho_l}\cdot\frac{K_0(ka)}{K_0'(ka)}\cdot\frac{I_0'(ka)}{I_0(ka)}=1+\frac{\rho_g}{\rho_l}\cdot\frac{K_0(ka)}{K_1(ka)}\cdot\frac{I_1(ka)}{I_0(ka)} \tag{26}$$

$$C=4\cdot A\cdot\left[k^2U^2+\frac{\sigma k}{\rho_l a^2}(1-k^2a^2)\cdot\frac{I_1(ka)}{I_0(ka)}\right] \tag{27}$$

where ω is the root of positive real part ($\omega_i>0$), wavenumber $k=\frac{2\pi}{L_{initial}}$, $L_{initial}$ is length scale of initial surface wave. Due to the simplification in the dispersion relation, it is feasible to get the analytical solution for each droplet using Eq. (24).

2.2.5. Modified turbulence induced atomization model

The surface wave induced by boundary layer relaxation downstream of the orifice exit, cavitation and turbulent fluctuation has a very complex structure (board band spectrum). Therefore, the initial surface wave of liquid jet is a function of $L_{boundary}$ (using Eq. (16)), L_t (using Eq. (6)) and L_{cav} (using Eq. (11)), which denote length scale of the initial surface wave caused by relaxation of the velocity profile, cavitation and turbulent fluctuation respectively.

Using Eq. (24), the time scale of above three kinds of initial surface wave due to aerodynamics will be derived. Hence the time scale can be expressed as:

$$\tau_i=f(L_i)\quad i\in(boundary,t,cav) \tag{28}$$

For the present primary breakup model, the radius of the product drops is formulated with $L_{boundary}$, L_t and L_{cav}. The reciprocal of the product drop radius is expressed by the sum of the reciprocals of the length scales associated with the surface wave induced by relaxation of the velocity profile, cavitation and turbulent fluctuation with the inclusion of the respective weighting factors as follows:

$$\frac{1}{L_A}=\frac{C_{boundary}}{L_{boundary}}+\frac{C_t}{L_t}+\frac{C_{cav}}{L_{cav}} \tag{29}$$

The weighting coefficients $C_{boundary}$, C_t and C_{cav} are determined by the kinetic energy ratio of the relaxation of the velocity profile, cavitation and turbulent fluctuation. L_A is the atomization length scale.

Since the weighting coefficients represent degrees of the contributions of a particular physical phenomenon to the overall one [26], it is logical to assign a unity relation between them as:

$$C_{boundary}+C_t+C_{cav}=1 \tag{30}$$

where

$$C_i=\frac{E_i}{E_{boundary}+E_t+E_{cav}} \tag{31}$$

$$E_i=\left(\frac{L_i}{\tau_{A,i}}\right)^2\ i=boundary,t,cav \tag{32}$$

The kinetic energy of the three factors is E_i. The time scale of the surface waves is $\tau_{A,i}$. The radius of the product drop r_p is proportional to L_A.

$$r_p=A_0\cdot L_A \tag{33}$$

A_0 is a model constant which can affect the radius of the product drops. Its value is set equal to 1.0 for the present study.The size of the unstable drops is allowed to change continuously following the rate Equation

$$\frac{dr}{dt}=-\left(\frac{L_{boundary}}{\tau_{A,b}}+\frac{L_t}{\tau_{A,t}}+\frac{L_{cav}}{\tau_{A,cav}}\right) \tag{34}$$

$$\tau_{A,b}=\tau_b+A_1\cdot\tau_{w,b} \tag{35}$$

$$\tau_{A,t}=\tau_t+A_2\cdot\tau_{w,t} \tag{36}$$

$$\tau_{A,c} = \tau_{cav} + A_3 \cdot \tau_{w,c} \tag{37}$$

where the time scales associated with the surface wave induced by relaxation of the velocity profile, cavitation and turbulent fluctuation are $\tau_{w,b}$, $\tau_{w,t}$ and $\tau_{w,c}$ respectively, which can be calculated according to the above Eqs (35)–(37). A_1, A_2 and A_3 are time scale constants, which show the inhibition effect of liquid viscosity on the growth rate of surface waves. In order to simplify mathematical model, we assume the liquid viscosity have identical influence on the growth rate of surface waves. Then it is reasonable that three time scale constants are equal, i.e. $A_1 = A_2 = A_3 = A$. The time scale of initial surface waves is unknown due to lack of understanding of boundary layer relaxation near orifice exit. The effect of boundary layer relaxation, which has little influence on jet atomization for high injection pressure situation, is not considered, i.e. $\frac{L_{boundary}}{\tau_{A,b}} = 0.0$.

The modified turbulence induced atomization model takes into account the effects of the relaxation of the velocity profile, cavitation and turbulent fluctuation. Therefore, above breakup model can simulate laminar, turbulent and cavitating flow cases. In this study, we model the breakup processes of fuel jet into droplets using above new breakup model and incorporate this model into the KIVA 3V code.

3. Model behavior and validation

3.1. Comparison of instability characteristics between an infinite plane and cylindrical jet

A test case was selected to illustrate clearly the effect of jet shape on the development of surface waves. Injection parameters, liquid property and ambient conditions are summarized in Table 1.

In Fig. 1 the development characteristics of surface waves based on K–H instability theory on an infinite plane and cylindrical jet for an inviscid liquid were compared. Computations were carried-out using Muller's method at different conditions, as summarized in Table 1, for different initial surface wave length (ranges from 1.0 μm to 1000.0 μm). The time scale of initial surface waves were increased when the length of initial surface waves is increased from 0.1 μm to 1.0 mm based on above two K–H instability theories. However, the time scale of initial surface waves based on K–H instability theory on an infinite plane jet (the time scale of initial surface waves was between 0.0 s and 0.00009 s, as shown in Fig. 1(a)) was much larger than that based on K–H instability theory on infinite length cylindrical jet (the time scale of initial surface waves was between 0.0 s and 0.000026 s, as show in Fig. 1(b)). The results demonstrate that the liquid jet with the same configuration of the surface waves is much stable when the assumption of infinite plane was used. Therefore, the assumption of liquid cylinder jet has a great influence on the instability of surface waves.

Table 1
Test case parameters.

Jet diameter	0.18 mm
Injection velocity	300 m/s
Liquid kinematic viscosity	0.00000595 m^2/s
Liquid density	840 kg/m^3
Liquid and ambient temperature	293 K
Ambient pressure	0.1 MPa
Ambient gas	Air

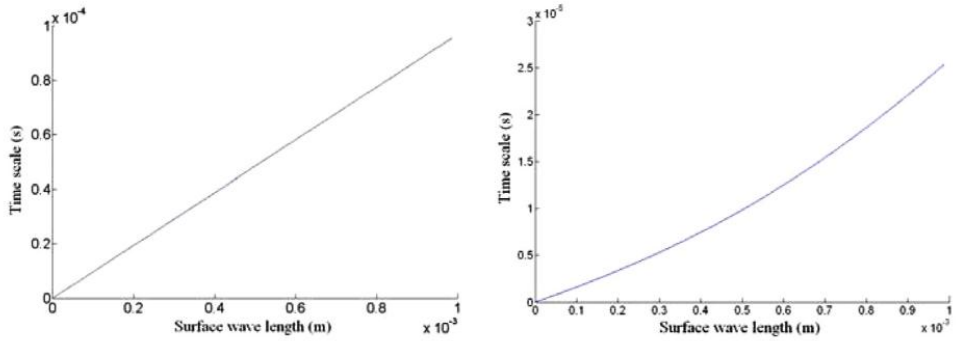

(a) Infinite plane jet (b) Infinite length cylindrical jet

Fig. 1. Calculated growth rate of surface waves based on K–H instability theory on different jet shape.

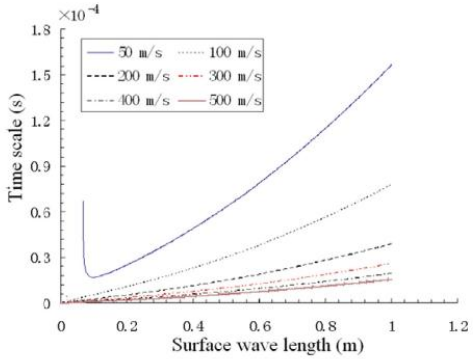

Fig. 2. Jet velocity effect on jet instability characteristics.

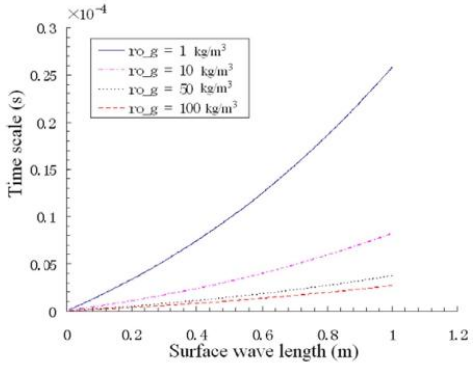

Fig. 3. Jet velocity effect on jet instability characteristics.

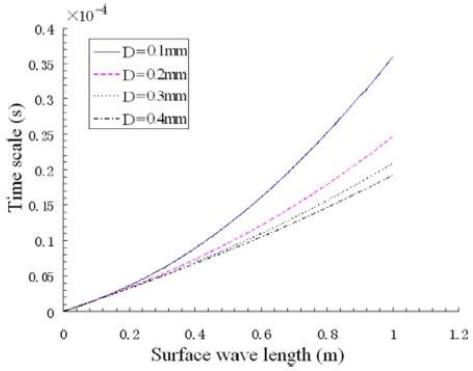

Fig. 4. Jet diameter effect on jet instability characteristics.

The features of the dispersion Eq. (24) with an assumption of infinite length cylinder inviscid liquid jet were discussed in detail. Figs. 2–4 showed the variations of the time scale versus surface wave length at different jet velocity, ambient density and jet diameter. As the jet velocity, ambient density and jet diameter increased (the Reynolds number increases), the time

Table 2
Experimental conditions [29].

Rail pressure	80 MPa
Injection duration	2.7 ms
Liquid density	840 kg/m^3
Liquid and ambient temperture	293 K
Ambient pressure	0.1 MPa
Ambient gas	Air
Conical shaper factor, K	0.0

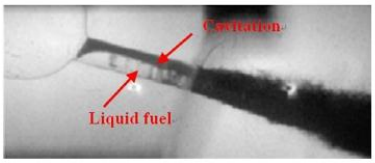

Fig. 5. Experimental results at 400 μs after start of injection (aSOI) [29].

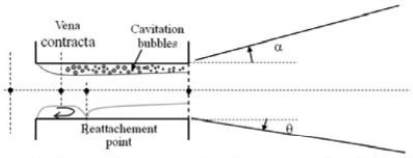

(a) Internal nozzle flow and spray angle close to nozzle exit [24]

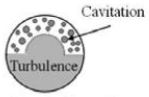

(b) Cavitating and turbulent flow at nozzle exit

Fig. 6. Schematic diagram of the spray when the asymmetric spatial distribution of cavitation is considered.

scale of surface waves decreased dramatically. It was evident that the above three factors played a significant role in the evolution of the liquid jet.

3.2. Validation of the modified breakup model

In order to validate the modified model, the present model was applied to simulate the experiment of Blessing et al. [29], which investigated the cavitating nozzle flow with transparent nozzles in real size geometry under high pressure conditions. The experiment conditions are listed in Table 2. Details of experiments are in Blessing et al. [29].

In Fig. 5 an image showing the cavitating flow inside the sac hole and the spray hole, as well as the spray exiting the nozzle is represented. The liquid fuel flows into the spray hole from the sac hole. The dark areas in the spray hole mark thereby the cavitating flow outgoing from the edge of the spray hole to the sac hole. The resulting micro cone angle of the spray close to the nozzle hole exit shows the dependence on cavitation phenomena. According to the experimental results, the spray angle close to nozzle exit is found to be asymmetric. The cavitating area increases the half spray angle, which is about 7°. At the non-cavitating side, the half spray angle is about 3°. So the global spray angle near the nozzle exit is 10°.

The regime of internal nozzle flow is a hydraulic flip flow that is partly reattached on the wall (See Fig. 5). Since this kind of flow is usually asymmetrical, a one-dimensional analysis is not possible. Therefore, the effects of turbulence and cavitation on the spray evolution have been considered in the modified breakup model using a 3D-dimensional model, the sketch of the asymmetric internal nozzle flow and spray has been shown as Fig. 6(a). According to the flow characteristics at nozzle exit (See Fig. 6(b)), the atomization length scale L_A (Based on Eq. (30)) at the cavitating flow side should consider the effects of cavitation, turbulence and boundary layer relaxation. However, at the non-cavitating flow side L_A is only a function of turbulence fluctuations and boundary layer relaxation.

Figs. 7 and 8 show the results of simulation by increasing the constant A in the modified turbulence induced atomization model, the calculated spray angles decrease gradually. The model constant A is determined by matching the experimental results. When $A = 2.8$, the simulated global spray angle is same to the experimental data (See Fig. 7) and micro spray-angle ($\alpha \approx 6.7°$ and $\theta \approx 3.3°$) have been obtained. The computed results show that the asymmetrical spray is reproduced by the modified model.

In the cavitation zone (See Fig. 6), both turbulence fluctuations and cavitation bubbles have significant influence on atomization. Based on the present modified model, the weighting coefficients of turbulence and cavitation on the overall

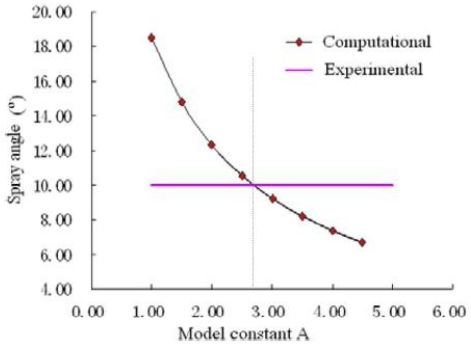

Fig. 7. Model constant A and global spray angle.

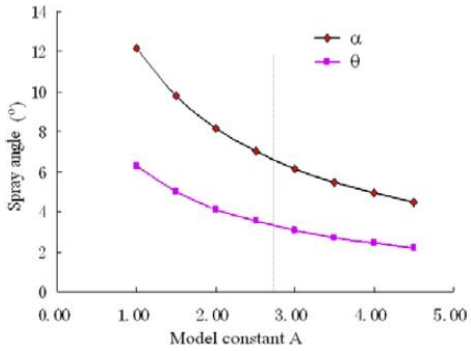

Fig. 8. Model constant A and half spray angle.

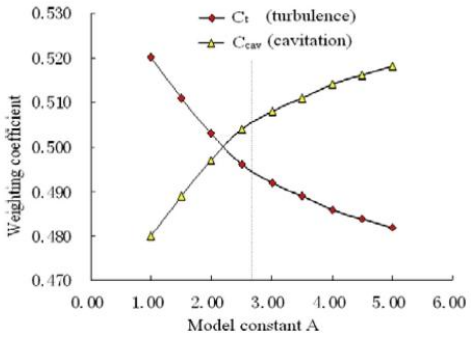

Fig. 9. Model constant A and weighting coefficient.

atomization can be distinguished clearly (See Fig. 9). When constant A is equal to 2.8, the weighting coefficient C_t and C_{cav} are approximately 0.495, 0.505 respectively. The results indicate that primary breakup at the initial primary breakup stage is dominated by cavitation. However, the effects of turbulence on primary breakup are also remarkable. The relation of model constant A and the time scale of surface waves is graphically displayed in Fig. 10. While keeping A 2.8, the time scale of

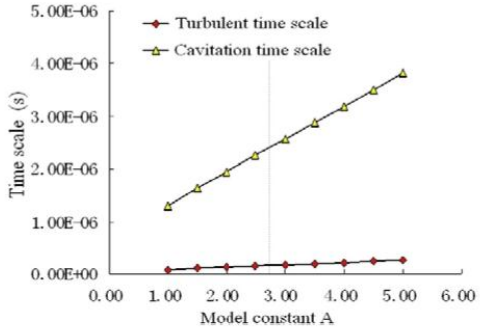

Fig. 10. Model constant A and time scale of surface waves.

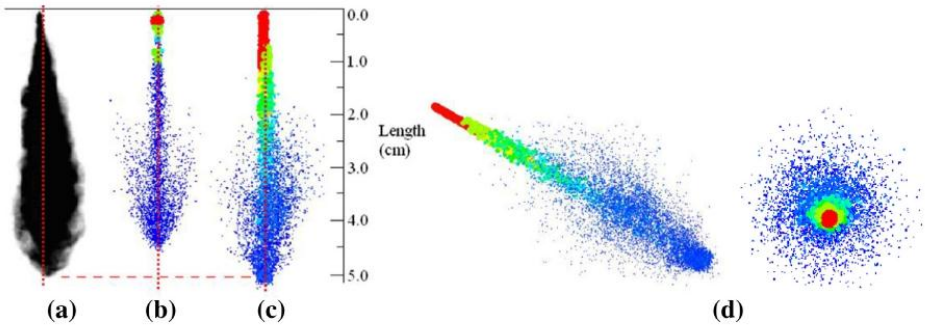

Fig. 11. Experimental and simulated spray shape(t = 1.1 ms ASOI).

turbulence and cavitation is about $2.0e^{-7}$ s, $2.3e^{-6}$ s respectively. It implies that the size of product droplets induced by cavitation is much larger than that induced by turbulence.

The computed spray shapes (1.1 ms aSOI) simulated by the present models and experiment are illustrated in Fig. 11 ((a) Experimental spray shape [29], $t = 1.1$ ms aSOI, $K = 0.0$; (b) Simulated spray shape based on the original turbulence induced atomization model; (c) Simulated spray shape based on the modified turbulence induced atomization model; (d) A vertical view of (c)). All simulated sprays consist of a spray core and a mushroom like hat or a certain around the core (See Fig. 11(b) and (c)). The actual spray looks more like a gradually growing cone with a static cone angle (See Fig. 11(a)). There is remarkable variation in simulated spray shape with present models. It can be seen that the original turbulence induced atomization model results in a shorter spray penetration and smaller drops near the spray core than the modified model. This is a consequence of un-consideration of the coupling effects between cavitation and turbulence. Due to the cavitating flow, the decay of the cavitation bubbles leads by an increase of turbulence to an intensified spray breakup in the spray jet exiting the hole. Therefore, the resulting spray angle is asymmetric. The spray angle at the cavitating flow side is much larger than that at the other non-cavitating flow side (See Fig. 11(a)). Obviously, the modified model can simulate this phenomena (See Fig. 11(c) and (d)).

In Fig. 12 the spray tip penetrations from the nozzle exit into the ambient gas based on different models and experiment are plotted as a function of time. The simulated penetration based on the original turbulence induced atomization model is much shorter than the experimental results. The modified turbulence induced atomization model results in good spray shape and penetration at the early stage of injection. Nearly straight lines of the tip penetration curves at the beginning indicate that the tip velocity of the liquid jets remains almost constant. Once the jet is fully converted into droplets, its speed is subsequently reduced due to greater aerodynamic force and drag. Hence, the penetration curve has a smaller slope at the later time. In comparison with experiments, the tip penetration is slightly over-predicted with the modified model at the later time (after about 1.2 ms ASOI). Overall, the computational results show a close agreement with the experimental data. However, the tip penetration is under-estimated with the original atomization model.

Fig. 13 reveals that the product drop size predicted from the modified turbulence induced atomization model is approximately four times larger than the one from the original model. The main reason is present model take into account the effect of cavitation. The drop size estimated from present model is consistent with the Huu Phuoc Trinh's results [36].

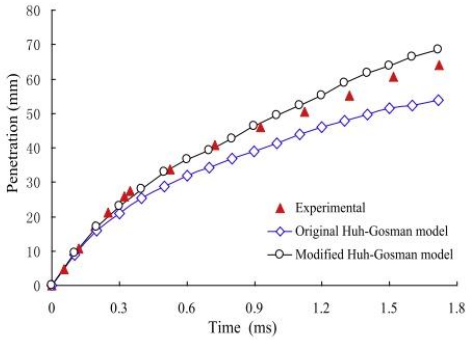

Fig. 12. Experimental [29] and simulated spray penetration.

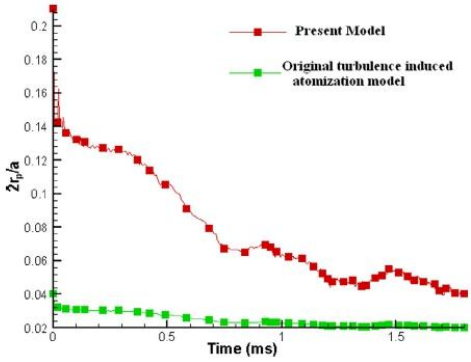

Fig. 13. Drop size predicted by different atomization model.

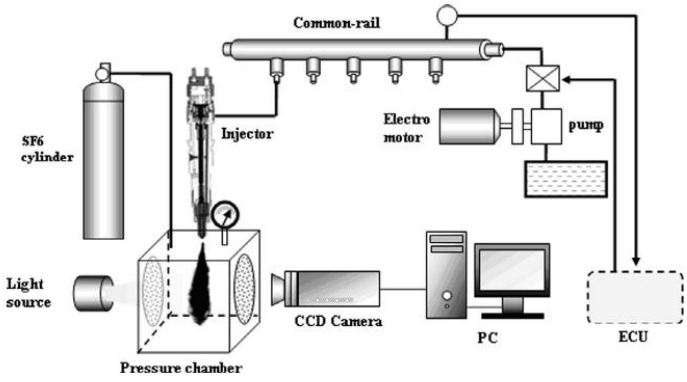

Fig. 14. Schematic diagram of the experimental system.

3.3. Effects of injection pressure on spray characteristics

Spray characteristics were investigated in a spray chamber which could be pressurized by filling nitrogen or other inert gases. The pressure chamber with constant volume allows optical accesses through two circular windows of 100 mm diameter. Fig. 14 shows schematic layout of experimental setup. High speed CCD camera was used to scatter the image with less than 200 μs. Spray penetrations and angles were measured from macroscopic scattered images.

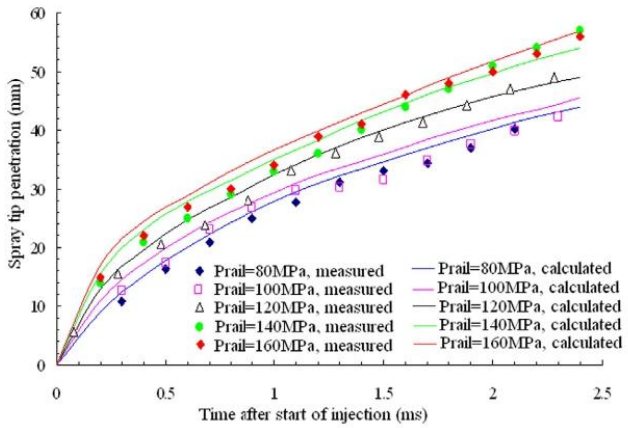

Fig. 15. Measured and computed spray tip penetration with different injection pressure.

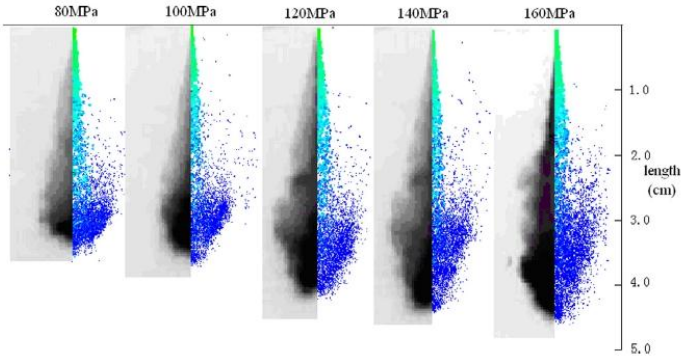

Fig. 16. Experimental and computed spray shape with different injection pressure at 1.6 ms ASOI.

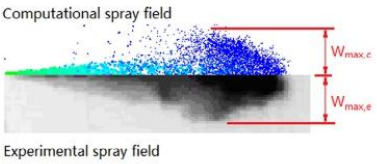

Fig. 17. Definition of computational and experimental spray maximum width (Wmax,c and Wmax,e).

The injection pressure was varied from 80 MPa to 160 MPa. SF_6 gas is filled with the constant volume chamber to simulate the high ambient pressure, because of the high density (about 5.3 times higher than nitrogen gas at the atmosphere conditions). In present experiment, the ambient gas temperature was set at room temperature and the ambient pressure was to be constant 2.0 MPa. Injection nozzle is single nozzle hole. Nozzle hole diameter was 0.18 mm. The nozzle hole L/d was 4.0. The density of diesel fuel and SF_6 gas were 843 kg/m^3 and 6.164 kg/m^3, respectively. The kinetic viscosity of fuel and SF_6 gas were 5.952×10^{-6} m^2/s and 2.61×10^{-6} m^2/s, respectively. The coefficience of surface tension fore was 0.0261 m/s.

In Fig. 15 the spray tip penetration were plotted for the five injection pressure. The tip penetration were compared with experiments. The results revealed that the present model provided a fairly good agreement with experimental data. There was tiny underestimation of the spray tip penetration before 1.6 ms after injection. In comparison with experiments, the tip penetration is slightly over-predicted with the modified model at the later time (after about 1.6 ms ASOI).

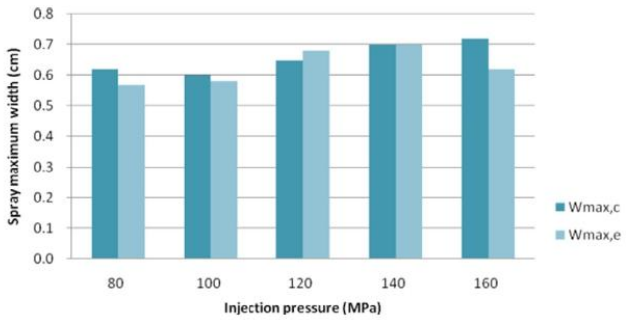

Fig. 18. Comparision between computational and experimental spray maximum width with different injection pressure at 1.6 ms ASOI.

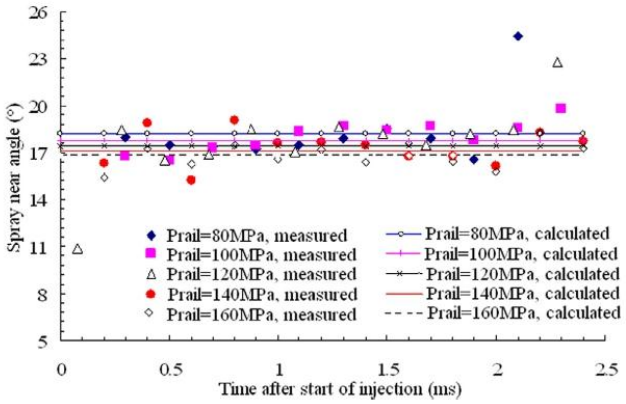

Fig. 19. Experimental and computed spray near angle with different injection pressure.

In Fig. 16 the effect of injection pressure (80 MPa, 100 MPa, 120 MPa, 140 MPa and 160 MPa) on spray shapes were compared. The left side of the images was experimental results, and the computed spray shapes were put at the right side. The results showed that present atomization model could correctly predict the spray shape and tip penetration. Whereas there were some of predicted satellite droplets near the nozzle using present model. There were no visible satellite droplets near the nozzle on experimental spray images. The reason may be that the droplet at the edge of the spray was so small that the high speed CCD camera couldn't scatter them. The spray tip penetration was increased with the higher injection pressure. In order describe the shape of spray better, we create a new spray quantitative parameters called spray maximum width (Wmax), as seen in Fig. 17.

After measuring the spray field, comparision between computational and experimental spray maximum width under different injection pressure is made (Fig. 18). As shown in Fig. 18, the spray maximum width has different value (0.55–0.72 cm) under injection pressure (80–160 MPa) at 1.6 ms ASOI. The comparison of results indicates that there is no significant difference between computational and experimental spray maximum width.

The effects of the injection pressure on spray near angle (close to the nozzle exit) were presented using present model and experimental method in Fig. 19. According to calculated results, the spray near angle kept constant during injection and increased gradually when injection pressure decreased. Hereby the highest spray core angle of approx. 18.2°when injection pressure was 80 MPa. However, the measured near spray angles were fluctuated remarkably during injection. This can be attribution to the strong instabilities and fluctuations in the internal flow. The numerical model in present study assumed the internal flow is one-dimensional and non-transient.

4. Conclusion

A hybrid breakup model to account for the primary and secondary breakup processes of atomization in sprays has been presented. The turbulence induced atomization model has been modified to model primary atomization. The growth time

scale of surface waves provides by K–H instability theory on an infinite length cylinder for an inviscid liquid jet in the modified turbulence induced atomization model, in which the jet internal turbulence and gas inertia are thought to be the two dominant breakup forces. The turbulent fluctuations in the emerging jet are responsible of the initial surface perturbations that grow exponentially by K–H instabilities due to the interaction with surrounding gas. The modified turbulence induced atomization model takes into account the effects of the relaxation of the velocity profile, cavitation and turbulent fluctuation. Therefore, this new model can simulate laminar, turbulent and cavitating flow cases.

Based on the present modified model, the weighting coefficients of turbulence and cavitation on the overall atomization can be distinguished clearly. There was remarkable variation in simulated spray shape with present models. It could be seen that the original turbulence induced atomization model results in a shorter spray penetration and smaller drops near the spray core than the modified model. When applying the turbulent weighting coefficient C_t in the determination of the spray angle, the resultant value of spray angle gradually drops due to the reduction of C_t. However, the spray angle increases with increasing the cavitation weighting coefficient C_{cav}.

The computed results show that the asymmetrical spray is reproduced by present hybrid breakup model coupling a modified turbulence induced atomization model. The original turbulence induced atomization model can't simulate the asymmetrical cases.

From the results of this investigation, the simulated penetration based on the original turbulence induced atomization model was much shorter than the experimental results. Results revealed that the present model provided a fairly good agreement with experimental data. There was tiny underestimation of the spray tip penetration before early stage after injection. In comparison with experiments, the tip penetration was slightly over-predicted with the modified model at the later time (after about 1.6 ms ASOI).

The effect of injection pressure on spray shapes was compared. There were some of predicted satellite droplets near the nozzle using present model. Whereas few visible satellite droplets near the nozzle could be distinguished on experimental images. The spray near angle kept constant during injection and increased gradually when injection pressure decreased. Hereby the highest spray core angle of approx. 18.2° when injection pressure was 80 MPa. However, the measured near spray angles were fluctuated remarkably during injection.

Acknowledgments

This work was supported by the National Natural Science Foundation of China (Grant No. 51306014).

References

[1] H. Hiroyasu, M. Arai, Fuel spray penetration and spray angle on diesel engines, Trans. JSAE 21 (1980) 5.
[2] D.L. Siebers, Liquid-phase penetration in diesel sprays, SAE Paper 980809, 1998.
[3] G.M. Bianchi, P. Pelloni, F.E. Corcione, L. Alloca, F. Luppino, Modeling atomization of high-pressure diesel sprays, J. Eng. Gas Turbines Power 123 (2) (2001) 419.
[4] P.K. Wu, R.F. Miranda, G.M. Faeth, Effects of initial flow conditions on primary breakup of nonturbulent and turbulent round liquid jets, Atomization Sprays 5 (1995) 175–196.
[5] Jean Arrègle, José V. Pastor, Santiago Ru, The Influence of Injection Parameters on Diesel Spray Characteristics, SAE Paper 1999-01-0200, 1999.
[6] T.F. Su, C.T. Chang, R.D. Reitz, P.V. Farrell, Effects of injection pressure and nozzle geometry on spray SMD and D.I. Emissions, SAE Paper 952360, 1995.
[7] Choongsik Bae, Jun Yu, Jinsuk Kang, Jangsik Kong, Effect of nozzle geometry on the common-rail diesel spray, SAE Paper 2002-01-1625, 2002.
[8] Lyle M. Pickett, Julien Manin. Transient rate of injection effects on spray development. SAE 2013-24-0001, 2013.
[9] R. Payri, F. Salvador, J. Gimeno, J. de la Morena, Macroscopic behavior of diesel sprays in the near- nozzle field, SAE Int. J. Engines 1 (1) (2008) 528–536.
[10] J. Kostas, D. Honnery, J. Soria, Time resolved measurements of the initial stages of fuel spray penetration, Fuel 88 (11) (2009) 2225–2237.
[11] J. Manin, M. Bardi, L.M. Pickett, R.N. Dahms, J.C. Oefelein, Microscopic investigation of the atomization and mixing processes of diesel sprays injected into high pressure and temperature environments, Fuel 134 (15) (2014) 531–543.
[12] Hyun Kyu Suh, Chang Sik Lee (Effect of cavitation in nozzle orifice on the diesel fuel atomization characteristics), Int. J. Heat Fluid Flow 29 (4) (2008) 1001–1009.
[13] M.I. Karamangil, R.A. Taflan, Experimental investigation of effect of corrosion on injected fuel quantity and spray geometry in the diesel injection nozzles, Fuel 112 (2013) 531–536.
[14] J. Manin, M. Bardi, L.M. Pickett, R.N. Dahms, J.C. Oefelein, Microscopic investigation of the atomization and mixing processes of diesel sprays injected into high pressure and temperature environments, Fuel 134 (15) (2014) 531–543.
[15] M.C. Lai, T.C. Wang, X. Xie, J. Han, N.A. Henein, E. Schwarz, W. Bryzik, Microscopic Characterization of Diesel Sprays At Vco Nozzle Exit, SAE paper No. 982542, 1998.
[16] C. Arcoumanis, M. Gavaises, B. French. Effect of fuel injection processes on the structure of diesel sprays. SAE Technical Paper 970799, 1997.
[17] K. Huh, A.D. Gosman, A phenomenological model of diesel spray atomization, in: Proceedings of The International Conference on Multiphase Flows, Tsukuba, Japan, 1991.
[18] S. Som, S.K. Aggarwal, Effects of primary breakup modeling on spray and combustion characteristics of compression ignition engines, Combust. Flame 157 (2010) 1179–1193.
[19] M.R. Turner, S.S. Sazhin, J.J. Healey, C. Crua, S.B. Martynov, A breakup model for transient Diesel fuel sprays, Fuel 97 (2012) 288–305.
[20] P.J. O'Rouke, A.A. Amsden, The TAB method for numerical calculation of spray droplet breakup, SAE Paper 872089, 1987.
[21] D. Assanis, M. Gavaises, G. Bergeles, Galibration, Validation of the taylor analogy breakup model for diesel spray calculation, ASME Paper 93-ICE-N11, 1993.
[22] F.X. Tanner, Liquid jest atomization and droplet breakup modeling of non-evaporating diesel fuel spray, SAE Paper 970050, 1997
[23] N. Tamaki, M. Shimizu, K. Nishida, H. Hiroyasu, Effects of cavitation and internal fow on atomization of liquid jet, Atomization Sprays 8 (2) (1998) 179–197.
[24] M. Otendal, O. Hemberg, T.T. Tuohimaa, H.M. Hertz, Microscopic high-speed liquid-metal jets in vacuum, Exp. Fluids 39 (5) (2005) 799–804.
[25] C. Crua, T. Shoba, M. Heikal, M. Gold, et al. High-speed microscopic imaging of the initial stage of diesel spray formation and primary breakup. SAE Technical Paper 2010-01-2247, 2010.
[26] R.D. Reitz, F.V. Bracco, Mechanism of atomization of liquid jets, Phys. Fluids 25 (1982) 1730.

[27] R.D. Reitz, Modeling atomization process in high-preusse vaporizing spray, Atomization Spray Technol. 309–337 (1987).
[28] R. Rotondi, C. Grimaldi, L. Postrioti, Atomizatoin of high-pressure diesel spray: experimental validation of a new breakup model, SAE Paper 2001-01-1070, 2001.
[29] M. Blessing, G. König, C. Krüger, U. Michels, V. Schwarz, Analysis of flow and cavitation phenomena in diesel injection nozzles and its effects on spray and mixture formation, SAE Paper 2003-01-1358, 2003.
[30] G.M. Bianchi, P. Pelloni, Modeling the diesel fuel spray breakup by using a hybrid model, SAE Paper 1999-01-0226, 1999.
[31] D.P. Schmidt, C.J. Rutland, M.L. Corradini, P. Roosen, O. Genge, cavitation in two-dimensional asymmetric nozzles, SAE Paper 1999-01-0518, 1999.
[32] C. Arcoumanis, H. Flora, M. Gaivaises, M. Kampanis, R. Horrocks, Investigations of cavitation in a vertical multi-hole injector, SAE Paper 1999-01-0524, 1999.
[33] Jun Ishimoto, Hidehiro Hoshina, Tadashi Tsuchiyama, Hideyuki Watanabe (Integrated simulation of the atomization process of a liquid jet through a cylindrical nozzle), Interdiscip. Inf. Sci. 13 (1) (2007) 7–16.
[34] C. Sarre, S.C. Kong, R.D. Reitz, Modeling the effects of injector nozzle geometry on diesel sprays, SAE Paper No. 1999-01-0912, 1999.
[35] C. Brennen (Cavity surface wave patterns and general appearance), J. Fluid Mech. 44 (1) (1970) 33–49.
[36] Huu Phuoc Trinh, Modeling of turbulence effect on liquid jet atomization, Paper for the Degree of Doctor of Philosophy, The University of Alabama in Huntsville, 2004.